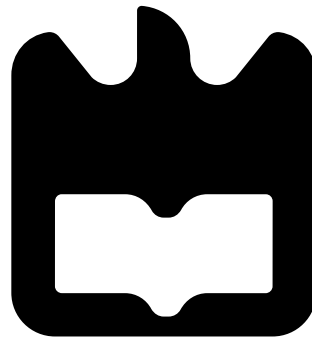




**Fernando Pedro  
Pereira Guiomar**

**Digital Nonlinear Equalization for Optical  
Transmission Systems**

**Equalização Digital Não Linear Para Sistemas de  
Transmissão Ótica**







**Fernando Pedro  
Pereira Guiomar**

**Digital Nonlinear Equalization for Optical  
Transmission Systems**

**Equalização Digital Não Linear Para Sistemas de  
Transmissão Ótica**





**Fernando Pedro  
Pereira Guiomar**

## **Digital Nonlinear Equalization for Optical Transmission Systems**

### **Equalização Digital Não Linear Para Sistemas de Transmissão Ótica**

Tese apresentada à Universidade de Aveiro para cumprimento dos requisitos necessários à obtenção do grau de Doutor em Engenharia Eletrotécnica, realizada sob a orientação científica do Doutor Armando Humberto Moreira Nolasco Pinto, Professor Associado do Departamento de Electrónica, Telecomunicações e Informática da Universidade de Aveiro.

Apoio financeiro da Fundação para a Ciência e a Tecnologia (FCT) através da bolsa SFRH/BD/74049/2010 e do projeto PTDC/EEI-TEL/3283/2012 (DiNEq), e do Fundo Europeu de Desenvolvimento Regional (FEDER) através do Programa Operacional Factores de Competitividade (COMPETE) e do Quadro de Referência Estratégico Nacional (QREN) no âmbito do projeto PANORAMA II (ref. 23301).

**FCT** Fundação para a Ciência e a Tecnologia

MINISTÉRIO DA CIÊNCIA, TECNOLOGIA E ENSINO SUPERIOR Portugal



**o júri / the jury**

presidente / president

**Doutor Paulo Jorge de Melo Matias Faria de Vila Real**

Professor Catedrático da Universidade de Aveiro

vogais / examiners committee

**Doutor Henrique José Almeida da Silva**

Professor Associado da Faculdade de Ciências e Tecnologia da Universidade de Coimbra

**Doutor Henrique Manuel de Castro Faria Salgado**

Professor Associado da Faculdade de Engenharia da Universidade do Porto

**Doutor Adolfo da Visitação Tregeira Cartaxo**

Professor Associado com Agregação do Instituto Superior Técnico da Universidade de Lisboa

**Doutor Paulo Miguel Nepomuceno Pereira Monteiro**

Professor Associado da Universidade de Aveiro

**Doutor Armando Humberto Moreira Nolasco Pinto**

Professor Associado da Universidade de Aveiro (orientador)



## agradecimentos / acknowledgements

Quatro anos passados, é difícil lembrar-me em 2011 a decidir-me por iniciar esta aventura, *quase* certo do que perseguia, *quase* confiante. Quatro anos depois, sobra uma nostalgia das indefinições de *quase*, fica uma certeza saborosa do passo certo. Fica também um percurso repleto de experiências, de viagens, de aprendizagens, de conquistas e compromissos. Na base de tudo isso, um grupo de pessoas a quem devo um agradecimento especial.

Pelo precioso suporte científico, pelo constante processo de aprendizagem e pela compreensão nos momentos mais difíceis, devo um sentido agradecimento ao professor Armando Pinto, meu orientador de doutoramento. Por sempre acreditar no meu trabalho e pelas diversas oportunidades de colaboração internacional que me proporcionou, devo igual agradecimento ao professor António Teixeira. Destaco também a contribuição preponderante para este trabalho dada pelo Dr. Andrea Carena e Dra. Gabriella Bosco, professores do Politecnico di Torino, cujo apoio científico nas várias colaborações estabelecidas foi determinante para melhorar a qualidade do trabalho desenvolvido. Agradeço ainda ao meu amigo Jacklyn Reis, pelo seu papel motivador e inspirador para o meu doutoramento, primeiro como colega de trabalho no Instituto de Telecomunicações e depois como orientador de estágio no Centro de Pesquisa e Desenvolvimento em Telecomunicações, em Campinas, Brasil.

A todos os meus colegas de luta diária, agradeço terem partilhado o seu tempo comigo, e com ele as conversas, as gargalhadas, e todas as distrações que tanto facilitam o trabalho. Não posso deixar de destacar as assíduas reuniões do “Trio d’Ataque” (Gil Fernandes, Álvaro Almeida e eu próprio), que apimentavam um pouco os almoços mais insossos na cantina com a análise criteriosa (nem sempre) dos casos futebolísticos da semana. Devo também um agradecimento sentido a todos os colegas que contribuíram diretamente no meu trabalho, com ideias e discussões estimulantes, de onde destaco a Sofia Amado, o Ali Shahpari, o Ricardo Ferreira, o Celestino Martins e o Nelson Muga. O trabalho desenvolvido não seria o mesmo sem as vossas contribuições. Aos meus pais, à minha família, devo todo o investimento de amor e suor na minha educação, que me permitiu chegar até aqui.

Finalmente, a ti, Vera, devo a força para acordar diariamente com a mesma determinação, para concluir este projeto definido pelos dois e para os dois. Contigo aprendi a coragem de sonhar a 1500 km de distância e o suporte incondicional de quem não sabe o significado da palavra *quase*.



**palavras-chave**

Sistemas de comunicação ótica, detecção coerente, processamento digital de sinal, equalização não linear, propagação digital inversa, séries de Volterra.

**resumo**

A presente tese foca-se no tema da equalização digital de distorções não lineares da fibra em sistemas coerentes de transmissão ótica. Tirando partido de modelos físicos bem conhecidos para a propagação de sinal em fibras óticas mono-modo, novas técnicas de equalização não linear são propostas, testadas numericamente e validadas por demonstração experimental. A estrutura dos algoritmos propostos é fortemente condicionada pela otimização do compromisso entre complexidade e desempenho, tendo em conta a sua futura implementação prática em transdutores comerciais operando em tempo-real.

O trabalho desenvolvido foca-se inicialmente na mitigação das distorções não lineares intra-canal, aplicando o conceito de propagação digital inversa realizado através de filtros de Volterra. Após uma análise sistemática do núcleo de Volterra de terceira ordem, é identificado um conjunto de simplificações críticas, culminando no desenvolvimento de algoritmos de equalização não linear de baixa complexidade, formulados no domínio do tempo e frequência. A complexidade de implementação das técnicas propostas é analiticamente descrita em termos de esforço computacional e latência de processamento, através da determinação do número de multiplicações reais por amostra e do número de multiplicações realizadas em série, respetivamente. O desempenho da equalização é avaliado recorrendo a simulação numérica e validação experimental através da medição da taxa de erros.

Por fim, a questão da compensação não linear inter-canal é abordada no contexto da propagação de supercanais 400G para sistemas de transmissão metro e longa distância. Nesse âmbito são experimentalmente testadas diferentes configurações de supercanal e estratégias de equalização não linear, demonstrando assim que a implementação de equalização inter-subportadora permite estender consideravelmente o alcance, requerendo apenas um esforço computacional ligeiramente superior.



**keywords**

Optical communication systems, coherent detection, digital signal processing, nonlinear equalization, digital backpropagation, Volterra series.

**abstract**

This thesis focuses on digital equalization of nonlinear fiber impairments for coherent optical transmission systems. Building from well-known physical models of signal propagation in single-mode optical fibers, novel nonlinear equalization techniques are proposed, numerically assessed and experimentally demonstrated. The structure of the proposed algorithms is strongly driven by the optimization of the performance versus complexity tradeoff, envisioning the near-future practical application in commercial real-time transceivers.

The work is initially focused on the mitigation of intra-channel nonlinear impairments relying on the concept of digital backpropagation (DBP) associated with Volterra-based filtering. After a comprehensive analysis of the third-order Volterra kernel, a set of critical simplifications are identified, culminating in the development of reduced complexity nonlinear equalization algorithms formulated both in time and frequency domains. The implementation complexity of the proposed techniques is analytically described in terms of computational effort and processing latency, by determining the number of real multiplications per processed sample and the number of serial multiplications, respectively. The equalization performance is numerically and experimentally assessed through bit error rate (BER) measurements. Finally, the problem of inter-channel nonlinear compensation is addressed within the context of 400 Gb/s (400G) superchannels for long-haul and ultra-long-haul transmission. Different superchannel configurations and nonlinear equalization strategies are experimentally assessed, demonstrating that inter-subcarrier nonlinear equalization can provide an enhanced signal reach while requiring only marginal added complexity.



*“Não importa descobrir as razões,  
O que eu gosto mesmo é de as procurar,  
E creio que isso chega para escrever  
Meu livro.”*

Supernada - “O Meu Livro”  
**Manuel Cruz**



# Contents

<b>Contents</b>	<b>i</b>
<b>List of Figures</b>	<b>v</b>
<b>List of Tables</b>	<b>xi</b>
<b>List of Acronyms</b>	<b>xiii</b>
<b>List of Symbols</b>	<b>xix</b>
<b>1 Introduction</b>	<b>1</b>
1.1 Coherent Detection in Optical Fiber Systems . . . . .	2
1.1.1 Digital coherent receiver architecture . . . . .	2
1.1.2 Post-detection DSP subsystems . . . . .	3
1.1.3 Progress on coherent optical transmission systems . . . . .	6
1.2 Motivation and Objectives . . . . .	9
1.3 Thesis Outline . . . . .	12
1.4 Main Contributions . . . . .	13
1.5 List of Publications . . . . .	14
References . . . . .	19
<b>2 Signal Propagation in Single-Mode Optical Fibers</b>	<b>29</b>
2.1 Scalar Nonlinear Schrödinger Equation . . . . .	30
2.1.1 Group velocity dispersion . . . . .	31
2.1.2 Kerr nonlinearities . . . . .	32
2.2 Coupled Nonlinear Schrödinger Equation . . . . .	34
2.2.1 Manakov equation . . . . .	35
2.3 Propagation Regimes . . . . .	36
2.4 Numerical Methods for Approximate Solutions . . . . .	37
2.4.1 Split-step Fourier method . . . . .	37
2.4.2 Volterra series transfer function . . . . .	39
2.5 Summary . . . . .	46
References . . . . .	46

<b>3</b>	<b>Nonlinear Equalization via Digital Backpropagation</b>	<b>51</b>
3.1	The Concept of Digital Backpropagation . . . . .	51
3.2	DBP Using the Split-Step Fourier Method . . . . .	55
3.2.1	Single-polarization optical systems . . . . .	55
3.2.2	Dual-polarization optical systems . . . . .	58
3.2.3	Implementation complexity . . . . .	59
3.3	DBP Using the Inverse Volterra Series Transfer Function . . . . .	61
3.3.1	Single-polarization optical systems . . . . .	61
3.3.2	Dual-polarization optical systems . . . . .	64
3.3.3	Implementation complexity . . . . .	67
3.4	Numerical Assessment . . . . .	70
3.4.1	Single-polarization optical systems . . . . .	70
3.4.2	Dual-polarization optical systems . . . . .	79
3.5	Experimental Validation . . . . .	82
3.5.1	Laboratorial setup and DSP subsystems . . . . .	82
3.5.2	Experimental results . . . . .	84
3.6	Summary . . . . .	89
	References . . . . .	90
<b>4</b>	<b>Frequency Domain Volterra Series Nonlinear Equalizer</b>	<b>97</b>
4.1	Symmetric VSNE . . . . .	98
4.1.1	Analytical formulation . . . . .	100
4.1.2	Implementation complexity . . . . .	103
4.2	Simplified VSNE . . . . .	107
4.2.1	Analytical formulation . . . . .	107
4.2.2	Implementation complexity . . . . .	110
4.3	Numerical Assessment . . . . .	113
4.3.1	Span-by-span equalization . . . . .	113
4.3.2	Multi-span equalization . . . . .	115
4.3.3	Computational effort and latency . . . . .	118
4.4	Experimental Validation . . . . .	119
4.4.1	Laboratorial setup and DSP subsystems . . . . .	121
4.4.2	Performance of nonlinear equalization . . . . .	122
4.4.3	Implementation complexity . . . . .	125
4.5	Summary . . . . .	126
	References . . . . .	128
<b>5</b>	<b>Time Domain Volterra Series Nonlinear Equalizer</b>	<b>133</b>
5.1	Analytical Formulation . . . . .	134
5.1.1	Time domain iXPM equalizer . . . . .	134
5.1.2	Time domain iFWM equalizer . . . . .	136
5.1.3	Weighted VSNE . . . . .	138
5.2	Implementation Complexity . . . . .	141
5.3	Numerical Assessment . . . . .	142
5.3.1	Performance of TD-VSNE versus FD-VSNE . . . . .	143

5.3.2	Performance of the W-VSNE . . . . .	144
5.3.3	Complexity reduction for hardware implementation . . . . .	148
5.3.4	Computational effort analysis . . . . .	150
5.4	Experimental Validation . . . . .	152
5.4.1	Laboratorial setup and DSP subsystems . . . . .	152
5.4.2	Performance of nonlinear equalization . . . . .	153
5.5	Summary . . . . .	157
	References . . . . .	158
<b>6</b>	<b>Nonlinear Equalization of 400G Superchannels</b>	<b>161</b>
6.1	Multi-Carrier Digital Backpropagation . . . . .	162
6.1.1	Coupled NLSE for WDM optical signals . . . . .	162
6.1.2	Adaptation of the DBP-SSFM . . . . .	164
6.2	Laboratorial Setup . . . . .	167
6.2.1	Superchannel configurations . . . . .	168
6.2.2	DSP subsystems . . . . .	169
6.2.3	Back-to-back characterization . . . . .	170
6.3	Ultra-Long-Haul Propagation Performance . . . . .	172
6.3.1	Performance and complexity of multi-carrier DBP . . . . .	172
6.3.2	Maximum signal reach . . . . .	175
6.4	Metro Propagation Performance . . . . .	177
6.4.1	Triple-carrier PM-64QAM . . . . .	177
6.5	Summary . . . . .	180
	References . . . . .	180
<b>7</b>	<b>Conclusions and Future Work</b>	<b>185</b>
7.1	Conclusions . . . . .	185
7.2	Future Work . . . . .	187
	References . . . . .	188
	<b>Appendices</b>	<b>191</b>
	<b>A Frequency Domain NLSE</b>	<b>193</b>
	<b>B Multi-Span VSTF</b>	<b>195</b>
	<b>C Full Derivation of the iFWM Filters in the TD-VSNE</b>	<b>199</b>



# List of Figures

1.1	Global IP data traffic forecast, in number of exabytes per month for the period of 2014-2019, as reported in the Cisco Visual Networking Index [1].	2
1.2	Physical structure and general DSP subsystems of a polarization-diversity digital coherent optical receiver for PM-QAM transmission systems. . . .	3
1.3	Estimated fiber capacity, $C$ , versus input power per channel, $P_{\text{tx}}$ , using the analytical formulation of [89] and considering 150 Nyquist-spaced WDM channels modulated at 28 Gbaud and propagated over $50 \times 80$ km of standard single-mode fiber. . . . .	10
2.1	Implementation diagram of a cascaded multi-span VSTF for an optical link composed of $N_{\text{sec}}N_{\text{s}}$ spans of fiber. . . . .	43
2.2	FWM efficiency indicated by the third-order VSTF kernel for single-span and multi-span SSMF and NZDSF optical links. . . . .	45
3.1	Schematic representation of the concept of optical backpropagation. . . .	52
3.2	Schematic representation of the concept of digital backpropagation in a dispersion-unmanaged multi-span optical transmission system. . . . .	54
3.3	Numerical implementation of the asymmetric scalar DBP-SSFM for a single fiber span and a single FFT block. . . . .	57
3.4	Numerical implementation of the asymmetric dual-polarization DBP-SSFM for a single fiber span and a single FFT block. . . . .	58
3.5	Implementation complexity, in number of RMs, of the DBP-SSFM algorithm, considering a total of 20 DBP steps. . . . .	60
3.6	Serial implementation of the single-polarization VSNE algorithm for a single fiber span and a single FFT block. . . . .	63
3.7	Serial implementation of the dual-polarization VSNE algorithm for a single fiber span and a single FFT block. . . . .	65
3.8	Parallel implementation of the dual-polarization VSNE algorithm for a single fiber span and a single FFT block. . . . .	67
3.9	Implementation complexity, in terms of latency and overall number of RMs, of the DBP-VSTF algorithm, considering a total of 20 DBP steps.	69
3.10	Coherent single-polarization m-QAM optical system model adopted for simulation purposes. . . . .	71
3.11	EVM after digital equalization of a 40 Gb/s QPSK signal propagated over $20 \times 80$ km of SSMF. . . . .	72

---

3.12	EVM after digital equalization of a 40 Gb/s QPSK signal, as a function of propagation length. . . . .	73
3.13	EVM after digital equalization of a 40 Gb/s QPSK signal transmitted over $20 \times 80$ km of NZDSF. . . . .	74
3.14	EVM after digital equalization of a 40 Gb/s QPSK signal, as a function of the LPF cutoff frequency. . . . .	76
3.15	a) Optical spectra of the propagated signal before and after the LPF and after down-sampling at 3 samples per symbol; b) EVM after digital equalization of a 40 Gb/s QPSK signal, as a function of the VSNE spectral support and the LPF cutoff frequency. . . . .	77
3.16	Analysis of the computational requirements associated with DBP-based impairment compensation. . . . .	78
3.17	Overlap-and-save algorithm configuration adopted for frequency domain simulations. . . . .	78
3.18	Coherent PM-QPSK optical system model adopted for simulation purposes.	79
3.19	Performance of dual-polarization nonlinear equalization in a 112 Gb/s PM-QPSK optical transmission system composed of $20 \times 80$ km of NZDSF. . .	81
3.20	Experimental setup of the long-haul 100G PM-QPSK transmission system.	83
3.21	Sequential application of DSP subsystems for offline processing of the received signal samples stored by the Tektronix DPO71604 oscilloscope. .	84
3.22	Optimization of the DBP-SSFM and DBP-VSTF methods at the optimum power level, as a function of the $\xi$ parameter, for experimental scenario <b>A.1</b> .	85
3.23	Experimental BER results obtained for a single-channel 120 Gb/s PM-QPSK signal, corresponding to scenario <b>A.1</b> . . . . .	86
3.24	Experimental results obtained for a single-channel 100 Gb/s PM-QPSK signal, corresponding to scenario <b>B</b> , composed of 50 spans of SSMF. . . .	87
3.25	Experimental BER results obtained for a 10-channel 120 Gb/s PM-QPSK signal with 66 GHz channel spacing, corresponding to scenario <b>A.2</b> . . . .	88
3.26	Experimental BER results obtained for a 10-channel 120 Gb/s PM-QPSK signal with 33 GHz channel spacing, corresponding to scenario <b>A.3</b> . . . .	89
4.1	Matrix representation of the optical field triplets, $\tilde{\mathcal{A}}_{\mathbf{x}/\mathbf{y}}$ , as a function of $n$ , for an illustrative $8 \times 8$ VSNE. . . . .	99
4.2	Illustration of the symmetric $\mathbf{K}_3$ kernel reconstruction technique for an exemplary NZDSF transfer function with $N=32$ . . . . .	104
4.3	Numerical implementation diagram of the VSNE and symVSNE algorithms in parallel with a frequency domain CDE. . . . .	105
4.4	Normalized mean squared error between the simVSNE and symVSNE coefficients as a function of the filter dimension, $N_k$ , and number of fiber spans per transfer function for an SSMF optical link. . . . .	108
4.5	Normalized mean squared error between the simVSNE and symVSNE coefficients as a function of the filter dimension, $N_k$ , and number of fiber spans per transfer function for an NZDSF optical link. . . . .	109
4.6	Figures of merit for the computational effort required by frequency domain VSNE-based algorithms. . . . .	112

---

4.7	Schematic representation of the simulated 224 Gb/s PM-16QAM transmission system for the numerical assessment of frequency domain VSNE-based equalization. . . . .	113
4.8	BER as a function of the launched power in each fiber span. Each curve corresponds to a different static equalization algorithm. . . . .	114
4.9	BER as a function of the $N_k$ parameter in the symVSNE and simVSNE filters for a set of input powers ranging from 1 dBm to 5 dBm. . . . .	115
4.10	BER as a function of the total number of DBP steps for an input power of a) 2 dBm, b) 3 dBm and c) 4 dBm. . . . .	116
4.11	Performance of the symVSNE and simVSNE filter arrays as a function of $N_k$ and $N_{\text{steps}}$ . . . . .	117
4.12	Laboratorial setup for the transmission, propagation and detection of 10.4 Gbaud PM-64QAM data. . . . .	120
4.13	Sequence of post-detection DSP subsystems employed in this work for the processing of 100G PM-64QAM. . . . .	121
4.14	BER performance and maximum signal reach of 100G PM-64QAM enabled by CDE and VSNE-based DBP. . . . .	123
4.15	Optimization of the DBP-SSFM method in terms of $N_{\text{steps}}$ and $N$ for a fixed input power of -5 dBm and recirculation over 28 fiber spans. . . . .	123
4.16	Optimization of the a) symVSNE and b) simVSNE filter arrays in terms of $N_k$ and $N_{\text{steps}}$ and c) maximum performance obtained for the optimum $N_k$ , for a fixed input power of -5 dBm and recirculation over 28 fiber spans. . . . .	125
4.17	Optimization of symVSNE and simVSNE in terms of effective spectral support, for an input power of -5 dBm and recirculation over 28 fiber spans. . . . .	126
5.1	Numerical implementation of the dual-polarization W-SSFM for a single fiber span and a single FFT block. . . . .	139
5.2	Schematic diagram for the implementation of DBP using the W-VSNE[ $N_k$ ] filter array in parallel with CDE. . . . .	140
5.3	Frequency domain implementation of CDE in the $x$ polarization and calculation of the corresponding $A_x^{\text{CD},(\pm 1)}$ signals, required for the W-VSNE{1} filter. . . . .	140
5.4	Implementation detail of the W-VSNE{0} filter branch, indicating the number of real multiplications. . . . .	141
5.5	Performance comparison between the FD-VSNE and TD-VSNE algorithms, employing the exact and approximated formulations. . . . .	144
5.6	Optimization of the nonlinear memory parameter, $N_{\text{NL}}$ , for the a) weighted SSFM (W-SSFM), b) W-VSNE[0] and c) W-VSNE[1] algorithms. . . . .	145
5.7	Optimization of the $\xi$ parameter for the W-VSNE and W-SSFM algorithms as a function of $N_{\text{steps}}$ . . . . .	146
5.8	Performance of the W-VSNE and direct comparison with the TD-VSNE and W-SSFM. . . . .	147
5.9	Application of the power-of-two approximation to the real part of the exponential factor in (5.23), considering $\Delta = 1$ and $K = 1$ . . . . .	148

---

5.10	Impact of the complexity reduction approximations of (5.30) and (5.32) on the performance of the minimum effort W-VSNE[1] ( $N_{\text{steps}} = 8$ ). . . .	149
5.11	Two-dimensional optimization procedure associated with the approximation of expression (5.32) to obtain $A_{x/y}^{\text{CD},(1)}$ . . . . .	150
5.12	Performance of the FD-VSNE as a function of $N_{\text{steps}}$ and $N_k$ . . . . .	152
5.13	Laboratorial setup for the experimental validation of the W-VSNE technique. . . . .	152
5.14	Optimization of the nonlinear memory, $N_{\text{NL}}$ , for the a) W-SSFM, b) W-VSNE[0] and c) W-VSNE[1] algorithms, in the 400G ULH transmission system under test. . . . .	154
5.15	Optimization of $\xi$ for the a) W-SSFM, b) W-VSNE[0] and c) W-VSNE[1] algorithms, in the 400G ULH transmission system under test. . . . .	154
5.16	Performance of the W-VSNE algorithm for nonlinear compensation in the ULH 400G transmission system under test, considering a fixed step-size of 500 km. . . . .	155
5.17	Estimated maximum reach as a function of the DBP step-size using the SSFM, W-SSFM and W-VSNE methods for the ULH 400G transmission system under test. . . . .	156
6.1	Schematic illustration of a WDM spectrum, in which DBP is applied over a a) dual- and b) triple-carrier superchannel. . . . .	163
6.2	Numerical implementation of a single step of the asymmetric dual-polarization CE-DBP-SSFM, considering a backpropagated signal composed of 3 channels. . . . .	166
6.3	Laboratorial setup for the experimental assessment of 400G superchannel transmission in metro and ultra-long-haul transmission systems. . . . .	167
6.4	400G superchannel configurations for metro and ULH transmission based on a) dual-carrier PM-16QAM, b) triple-carrier PM-16QAM and c) triple-carrier PM-64QAM. . . . .	169
6.5	Sequence of post-detection DSP subsystems for offline processing of 400G superchannels including a) total-field DBP and b) coupled-equations DBP. . . . .	170
6.6	Back-to-back characterization of single-channel and WDM transmission of 400G superchannels based on a) PM-16QAM and b) PM-64QAM modulation. . . . .	171
6.7	Performance and spatial resolution requirements of MC-DBP for ultra-long-haul 400G transmission based on a) dual-carrier and b) triple-carrier PM-16QAM modulation. . . . .	173
6.8	Sampling rate requirements of TF-DBP for the dual- and triple-carrier 400G configurations. . . . .	174
6.9	Ultra-long-haul 400G propagation performance as a function of the transmission distance and input power per superchannel, considering the optimum input power and a propagation length of 6000 km. . . . .	176
6.10	Estimated maximum signal reach of 400G transmission based on dual- and triple-carrier PM-16QAM modulation, after linear and nonlinear compensation. . . . .	176

---

6.11	Performance and spatial resolution requirements of MC-DBP for metro 400G transmission based on triple-carrier PM-64QAM modulation, considering an input power of 0 dBm and a propagation length of 1000 km.	178
6.12	Metro 400G propagation performance as a function of the transmission distance and input power per superchannel. . . . .	179
6.13	Estimated maximum signal reach of 400G transmission based on triple-carrier PM-64QAM modulation, after linear and nonlinear compensation.	179



# List of Tables

2.1	Time/frequency comparative analysis of the group velocity dispersion (GVD) and self-phase modulation (SPM) effects. . . . .	33
3.1	Set of numerical parameters corresponding to the simulation model of Fig. 3.10. . . . .	71
3.2	Set of simulation parameters for the system model of Figure 3.18. . . . .	80
3.3	Experimental setup parameters for the considered long-haul 100G PM-QPSK transmission systems. . . . .	82
4.1	Minimum computational effort and latency incurred by static equalization with the symVSNE and simVSNE filters at 3 dBm. . . . .	118
4.2	Computational effort of DBP using the SSFM, simVSNE and symVSNE algorithms, for the considered 100G PM-64QAM transmission system. . . . .	125
5.1	Computational effort and latency of the W-VSNE, FD-VSNE and W-SSFM corresponding to the results in Figure 5.8b and Figure 5.12. . . . .	150
5.2	Comparison of computational effort and latency with the benchmark W-SSFM implementation. . . . .	151
6.1	Main set of parameters associated with the laboratorial setup of Figure 6.3.168	



# List of Acronyms

<b>100G</b>	100 Gb/s
<b>100-GE</b>	100 gigabit Ethernet
<b>400G</b>	400 Gb/s
<b>1T</b>	1 Tb/s
<b>ADC</b>	analog-to-digital converter
<b>AOS</b>	acousto-optical switch
<b>ASE</b>	amplified spontaneous emission
<b>ASIC</b>	application specific integrated circuit
<b>B2B</b>	back-to-back
<b>BER</b>	bit error rate
<b>CD</b>	chromatic dispersion
<b>CDE</b>	chromatic dispersion equalizer
<b>CE</b>	coupled equations
<b>CM</b>	complex multiplication
<b>CMA</b>	constant modulus algorithm
<b>CMOS</b>	complementary metal-oxide-semiconductor
<b>CNLSE</b>	coupled nonlinear Schrödinger equation
<b>CO-OFDM</b>	coherent optical orthogonal frequency division multiplexing
<b>DAC</b>	digital-to-analog converter
<b>DBP</b>	digital backpropagation
<b>DCF</b>	dispersion compensation fiber

<b>DD</b>	decision-directed
<b>DFB</b>	distributed feedback
<b>DFT</b>	discrete Fourier transform
<b>DGD</b>	differential group delay
<b>DG-iFWM</b>	degenerated iFWM
<b>DP</b>	dual-polarization
<b>DPSK</b>	differential phase-shift keying
<b>DQPSK</b>	differential QPSK
<b>DSP</b>	digital signal processing
<b>ECL</b>	external cavity laser
<b>EDL</b>	electrical delay line
<b>EDFA</b>	Erbium doped fiber amplifier
<b>ENOB</b>	effective number of bits
<b>EVM</b>	error vector magnitude
<b>FD</b>	frequency domain
<b>FEC</b>	forward error correction
<b>FFT</b>	fast Fourier transform
<b>FIR</b>	finite impulse response
<b>FWM</b>	four-wave mixing
<b>GEQ</b>	gain equalizer
<b>GN</b>	Gaussian noise
<b>GVD</b>	group velocity dispersion
<b>LHS</b>	left-hand side
<b>LO</b>	local oscillator
<b>LPF</b>	low-pass filter
<b>I</b>	in-phase
<b>IFFT</b>	inverse fast Fourier transform

<b>iFWM</b>	intra-channel four-wave mixing
<b>IIR</b>	infinite impulse response
<b>IM/DD</b>	intensity modulation and direction detection
<b>IQM</b>	IQ modulator
<b>IP</b>	Internet Protocol
<b>ISI</b>	inter-symbol interference
<b>iSPM</b>	intra-channel self-phase modulation
<b>iXPM</b>	intra-channel cross-phase modulation
<b>MC</b>	multi-carrier
<b>MIMO</b>	multiple-input multiple-output
<b>MSA</b>	multiple-source-agreement
<b>MSE</b>	mean square error
<b>MVSTF</b>	modified VSTF
<b>NF</b>	noise figure
<b>NLI</b>	nonlinear interference
<b>NLPN</b>	nonlinear phase noise
<b>NLSE</b>	nonlinear Schrödinger equation
<b>NMZ</b>	nested Mach-Zehnder
<b>NZDSF</b>	non-zero dispersion-shifted fiber
<b>OBP</b>	optical backpropagation
<b>OBF</b>	optical bandpass filter
<b>ODE</b>	ordinary differential equation
<b>OFD</b>	optical frequency doubler
<b>OIF</b>	optical inter-networking forum
<b>OOK</b>	on-off keying
<b>OS</b>	overlap-and-save
<b>OSNR</b>	optical signal-to-noise ratio

<b>PBS</b>	polarization beam splitter
<b>PDL</b>	polarization-dependent loss
<b>PE</b>	post-emphasis
<b>PM</b>	polarization multiplexing
<b>PMD</b>	polarization mode dispersion
<b>PPG</b>	pulse pattern generator
<b>PRBS</b>	pseudo-random bit sequence
<b>PS</b>	polarization scrambler
<b>PSCF</b>	pure silica core fiber
<b>PSD</b>	power spectral density
<b>PSK</b>	phase-shift keying
<b>Q</b>	quadrature
<b>QAM</b>	quadrature amplitude modulation
<b>QPSK</b>	quadrature phase-shift keying
<b>RF</b>	radio frequency
<b>RHS</b>	right-hand side
<b>RM</b>	real multiplication
<b>RP</b>	regular perturbation
<b>SE</b>	spectral efficiency
<b>SPM</b>	self-phase modulation
<b>SpS</b>	samples per symbol
<b>SNR</b>	signal-to-noise ratio
<b>SSFM</b>	split-step Fourier method
<b>SSMF</b>	standard single-mode fiber
<b>simVSNE</b>	simplified Volterra series nonlinear equalizer
<b>symVSNE</b>	symmetric Volterra series nonlinear equalizer
<b>TD</b>	time domain

*List of Acronyms*

---

<b>TF</b>	total-field
<b>TOF</b>	tunable optical filter
<b>ULAF</b>	ultra large area fiber
<b>ULH</b>	ultra-long-haul
<b>ULL</b>	ultra-low-loss
<b>VOA</b>	variable optical attenuator
<b>VSNE</b>	Volterra series nonlinear equalizer
<b>VSTF</b>	Volterra series transfer function
<b>WDM</b>	wavelength-division multiplexing
<b>WS</b>	waveshaper
<b>W-SSFM</b>	weighted SSFM
<b>W-VSNE</b>	weighted VSNE
<b>XPM</b>	cross-phase modulation



# List of Symbols

Symbol	Designation
$A$	complex field envelope in time domain
$A_{\text{eff}}$	effective core area
$\tilde{A}$	complex field envelope in frequency domain
$\tilde{A}_{x/y}$	optical field triplet in the $x/y$ polarizations
$\mathbf{A}$	Jones vector
BW	bandwidth
$\mathbf{B}$	magnetic flux density vector
$c$	speed of light in vacuum
$D$	dispersion parameter
$D_p$	PMD parameter
$\text{DG}^{(K)}(n)$	DG-iFWM distortion generated at index $j = n + 2K$
$\hat{D}$	NLSE linear operator
$\hat{D}_{\text{SSFM}}$	SSFM linear step
$\hat{D}_{\text{SSFM}}^{\text{DBP}}$	DBP-SSFM linear step
$\hat{D}_{\text{SSFM}}^{\text{CE}}$	CE-DBP-SSFM linear step
$\mathbf{D}$	electric flux density vector
$\mathbf{E}$	electrical field vector
$f_s$	sampling rate
$F$	phased-array factor
$F^{\text{iXPM}}$	incoherent array factor associated with iXPM distortions
$F_n$	noise figure of the optical amplifiers
$\mathcal{F}\{\cdot\}$	Fourier transform operator
$\mathcal{F}^{-1}\{\cdot\}$	inverse Fourier transform operator
$G$	optical amplifier gain
$h$	spatial step-size
$h_{\text{eff,DBP}}$	effective step-size for DBP
$h_{\text{GVD}}(t, z)$	linear impulse response of the fiber up to coordinate $z$
$H_1$	single-span first-order (linear) Volterra kernel
$H_1^{\text{MS}}$	multi-span first-order (linear) Volterra kernel
$H_3$	single-span third-order (nonlinear) Volterra kernel
$H_3^{\text{MS}}$	multi-span third-order (nonlinear) Volterra kernel
$H_{\text{CD}}$	frequency domain transfer function for CD compensation
$\mathbf{H}$	magnetic field vector

---

$i$	imaginary unit
$I_{x/y}$	in-phase signal component in the $x/y$ polarization
$\mathbf{J}$	current density vector
$K_1$	single-span inverse first-order (linear) Volterra kernel
$K_1^{\text{MS}}$	multi-span inverse first-order (linear) Volterra kernel
$K_3$	single-span inverse third-order (nonlinear) Volterra kernel
$K_3^{\text{MS}}$	multi-span inverse third-order (nonlinear) Volterra kernel
$K_3^{\text{iXPM}}$	inverse Volterra kernel coefficients associated with iXPM distortions
$L$	fiber length
$L_B$	beat length of the fiber
$L_C$	correlation length of the fiber
$L_D$	dispersion length
$L_{\text{eff}}(z)$	effective length up to coordinate $z$
$L_{\text{NL}}$	nonlinear length
$L_s$	fiber span length
$m$	carrier index in a WDM comb
$M_{\text{CDE}}$	complexity associated with CDE
$M_{\text{FFT}}$	complexity associated with FFT/IFFT
$M_{\text{simVSNE}}$	complexity associated with simVSNE
$M_{\text{simVSNE}}^{\text{DBP}}$	complexity associated with DBP-simVSNE
$M_{\text{SSFM}}^{\text{DBP}}$	complexity associated DBP-SSFM
$M_{\text{symVSNE}}$	complexity associated with symVSNE
$M_{\text{symVSNE}}^{\text{DBP}}$	complexity associated with DBP-symVSNE
$M_{\text{VSNE}}$	complexity associated with matrix-based VSNE
$M_{\text{VSTF}}$	complexity associated with DBP-VSTF
$M_{\text{W-VSNE}}^{\text{DBP}}$	complexity associated with DBP-W-VSNE
$n_2$	nonlinear refractive index
$N_{\text{bits}}$	number of bits
$N_{\text{ch}}$	number of optical channels
$N_{\text{CMs}}$	number of complex multiplications
$N$	Fourier transform block-size
$N_k$	number of parallel VSNE filters
$N_{\text{NL}}$	time domain memory (in number of samples) for the W-VSNE
$N_{\text{pol}}$	number of polarization components
$N_{\text{RMs}}$	number of real multiplications
$N_s$	number of fiber spans
$N_{\text{sec}}$	number of sections, each composed of a given number of fiber spans
$N_{\text{spans/step}}$	number of span per step
$N_{\text{sps}}$	number of samples per symbol
$N_{\text{steps}}$	number of steps
$N_{\text{steps/span}}$	number of steps per span
$\hat{\mathcal{N}}$	NLSE nonlinear operator
$\hat{\mathcal{N}}_{\text{SSFM}}$	SSFM nonlinear step
$\hat{\mathcal{N}}_{\text{SSFM}}^{\text{DBP}}$	DBP-SSFM nonlinear step

---

List of Symbols

---

$\hat{\mathcal{N}}_{\text{SSFM}}^{\text{CE}}$	CE-DBP-SSFM nonlinear step
$\text{OSNR}_{\text{NL}}$	nonlinear OSNR
$P_0$	input peak optical power
$P_{\text{ASE}}$	ASE noise power
$P_{\text{NLI}}$	NLI noise power
$P_{\text{tx, ch}}$	average transmitted optical power per-channel
$\tilde{P}$	intra- and inter-polarization crosstalk terms in FD-VSNE
$\tilde{\mathcal{P}}$	intra- and inter-polarization crosstalk terms in TD-VSNE
$Q_{x/y}$	quadrature signal component in the $x/y$ polarization
$R_b$	bit-rate
$R_s$	symbol-rate
$t$	continuous time (retarded time-frame)
$t_n$	discrete time (retarded time-frame)
$T$	sampling period
$T_0$	symbol period
$v_g$	group velocity
$W$	spectral support
$W_{\text{off}}^{(m)}$	walk-off parameter for the $m$ -th carrier
$\hat{\mathcal{W}}^{(m)}$	walk-off operator for the $m$ -th carrier
$z$	spatial coordinate
$\alpha$	attenuation coefficient
$\alpha_{\text{roll-off}}$	roll-off factor of the raised-cosine filter
$\beta_0$	wave-number
$\beta_1$	group velocity inverse
$\beta_2$	group velocity dispersion coefficient
$\beta_3$	third-order dispersion coefficient
$\gamma$	nonlinear coefficient
$\Delta$	number of quantization levels
$\Delta f$	frequency spacing
$\Delta\nu$	laser linewidth
$\Delta\tau$	differential group delay
$\Delta\omega$	angular frequency spacing
$\lambda$	wavelength
$\lambda_0$	central wavelength
$\xi$	free DBP optimization parameter
$\xi_{\text{opt}}$	optimum $\xi$
$\xi_{\text{SPM}}$	free DBP optimization parameter for the SPM terms
$\xi_{\text{XPM}}$	free DBP optimization parameter for the XPM terms
$\rho$	charge density
$\tau$	continuous time (absolute time-frame)
$\tau_{\text{CDE}}$	latency associated with CDE
$\tau_{\text{FFT}}$	latency associated with FFT/IFFT
$\tau_{\text{simVSNE}}^{\text{DBP}}$	latency associated with DBP-simVSNE
$\tau_{\text{SSFM}}^{\text{DBP}}$	latency associated DBP-SSFM

$\tau_{\text{symVSNE}}^{\text{DBP}}$	latency associated with DBP-symVSNE
$\tau_{\text{VSTF}}$	latency associated with DBP-VSTF
$\tau_{\text{W-VSNE}}^{\text{DBP}}$	latency associated with DBP-W-VSNE
$\phi_{\text{NL}}$	nonlinear phase rotation
$\omega$	baseband angular frequency
$\omega_n$	baseband discrete angular frequency
$\Omega$	angular frequency
$\Omega_0$	central angular frequency
$\nabla$	gradient operator

# Chapter 1

## Introduction

The development of broadband telecommunication infra-structures is nowadays seen as a key strategic investment to ensure a worldwide sustainable and inclusive growth, both at the economic and societal levels. The number of Internet users has exploded in the last decade, generating an enormous amount of traffic flowing over trans-oceanic distances, where optical fibers are the enabling transmission medium. One of the latest global Internet Protocol (IP) traffic forecast, divulged by Cisco Systems in their visual networking index report [1], predicts a steady increase of about 23% per year until 2019, as depicted in Figure 1.1. Put into a simple metric, this means that by 2018 approximately 400 terabits of data will be exchanged in the Internet each second. The same amount of traffic was being exchanged hourly at the beginning of the 21<sup>st</sup> century [1], which represents an increase on bandwidth demand by more than three orders of magnitude over the course of less than 20 years. It thus becomes apparent that the optical transmission technologies deployed in the early 2000's, which were mainly driven by introduction of the Erbium doped fiber amplifier (EDFA) and by the use of wavelength-division multiplexing (WDM), are quickly reaching its capacity limits [2]. This ever increasing bandwidth demand is not only restricted to long-haul communications (>1000 km). In fact, approximately 66% of the global IP traffic by 2019 is expected to be propagated over metro and regional backbone networks [1]. Fostered by these critical needs and by its high commercial interest, a tremendous effort has been recently put into the research and development of novel future-proof optical transmission technologies for metro and core networks, involving both academic and industrial players.

Given the high costs involved in the setup of optical network infrastructures [3], the applied research on high-capacity optical transmission systems must take into account the development of low cost and low energy consumption solutions. Benefitting from the latest developments on high-speed electronics, new technologies for signal transmission and detection in optical communication systems have started to be investigated in the early 2000's [4–10] and are now being field deployed [11–17], incurring a minimal impact on the network propagation medium. The main enabler for this change of paradigm is the adoption of optical coherent detection, in which the carrier phase and amplitude are recovered at the receiver-side and down-converted to the electrical domain (in contrast to direct detection, in which only the field intensity is recovered), thus providing an additional degree of freedom to encode and transmit information

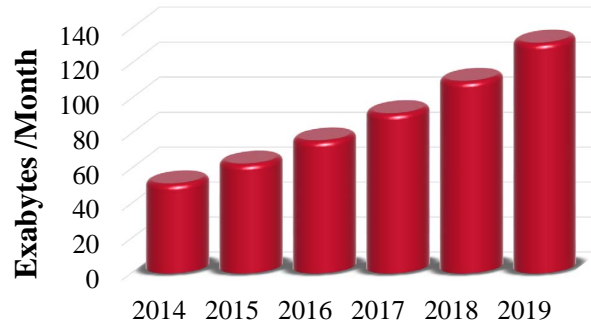


**Figure 1.1:** Global IP data traffic forecast, in number of exabytes per month for the period of 2014-2019, as reported in the Cisco Visual Networking Index [1].

[18, 19]. Most importantly, this phase-preserving optical-to-electrical signal conversion drastically boosts the applicability of post-detection digital signal processing (DSP) [4, 20–22]. The use of receiver-side DSP has provided the possibility of performing many critical operations such as phase estimation and carrier recovery entirely in the digital domain, highly reducing the complexity associated with the coherent receiver [23]. In the following, we briefly review the evolution of coherent optical transmission technologies over the last decade, focusing on the deployment of 100 Gb/s (100G) transmission systems and on the current development of novel solutions for optical transmission beyond 100G.

## 1.1 Coherent Detection in Optical Fiber Systems

### 1.1.1 Digital coherent receiver architecture

As opposed to direct detection receivers, coherent detection enables to linearly retrieve the optically encoded amplitude and phase information into the electrical domain [18]. The typical physical structure of a polarization-diversity coherent receiver, as proposed by the Optical Internetworking Forum implementation agreement [24], is schematically presented in Figure 1.2, also including the main post-detection DSP subsystems [22]. Let us consider a dual-polarization received optical field,  $\mathbf{E}_{\text{rx}}(t) = [E_{x,\text{rx}}(t) \ E_{y,\text{rx}}(t)]^T$ , where  $E_{x,\text{rx}}(t)$  and  $E_{y,\text{rx}}(t)$  are the signal components corresponding to the  $x$  and  $y$  polarizations and  $(\cdot)^T$  indicates the transpose of  $(\cdot)$ . The local oscillator (LO) laser is left in free running operation, without any hardware feedback path for frequency and/or phase synchronization. A polarization beam splitter (PBS) can be used to decompose the  $\mathbf{E}_{\text{rx}}$  and  $\mathbf{E}_{\text{LO}}$  optical fields into their orthogonal polarization components. Alternatively, a simple power splitter can be used after the LO laser to equally split the optical power into the two optical hybrids [24]. In order to facilitate monolithic integration, a coherent receiver architecture avoiding the use of PBSs both for the received signal and LO laser has also been recently proposed [25]. Since polarization demultiplexing can be performed in the digital domain [26–28], no optical dynamic control is required for polarization state alignment. A pair of  $90^\circ$  optical hybrids is used to mix the received signal with the LO reference carrier, producing four light outputs shifted by

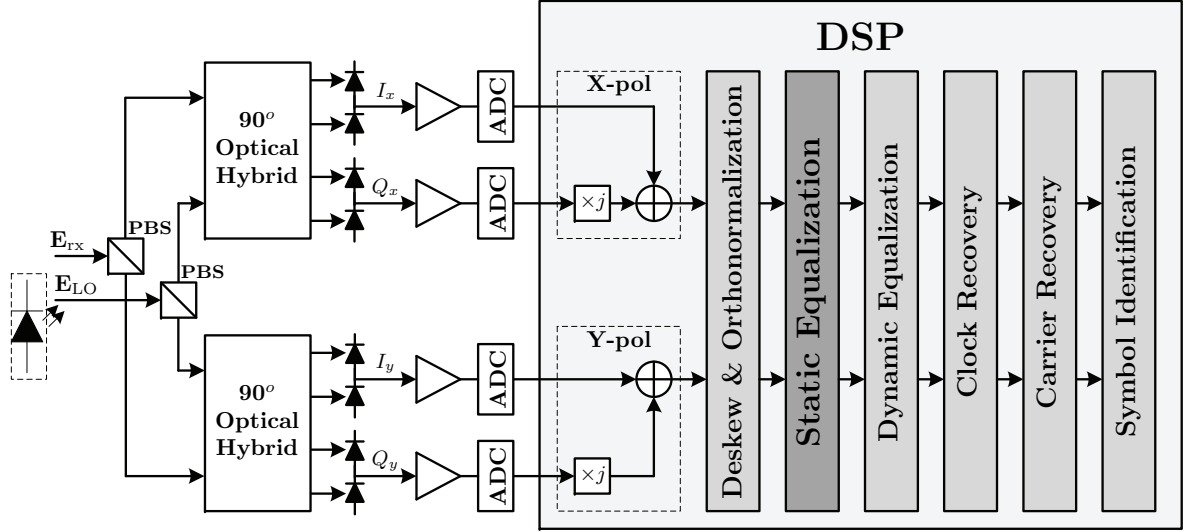


**Figure 1.2:** Physical structure and general DSP subsystems of a polarization-diversity digital coherent optical receiver for PM-QAM transmission systems.

$90^\circ$  from each other [29], containing both direct detection ( $|E_{x/y,rx}|^2$  and  $|E_{x/y,LO}|^2$ ) and coherent detection ( $\text{Re}\{E_{x/y,rx}E_{x/y,LO}\}$  and  $\text{Im}\{E_{x/y,rx}E_{x/y,LO}\}$ ) terms. The in-phase (I) information is contained in the  $\text{Re}\{E_{x/y,rx}E_{x/y,LO}\}$  terms, whereas the quadrature (Q) information is conveyed in the  $\text{Im}\{E_{x/y,rx}E_{x/y,LO}\}$  terms. Grouping the  $90^\circ$  optical hybrid outputs into  $180^\circ$  shifted optical fields, the optical-to-electrical downconversion is performed by two pairs of photodiodes operating in balanced configuration, yielding the in-phase and quadrature electrical currents,  $I_{x/y}$  and  $Q_{x/y}$ . Besides canceling out the direct detection terms, balanced detection of symmetric ( $180^\circ$  shifted) optical components allows to reduce common-mode noise, thereby enhancing the electrical signal-to-noise ratio (SNR) [30]. The electrical outputs of the balanced photodiodes are then fed to linear amplifiers in order to adjust the signal excursion entering the analog-to-digital converters (ADCs). Finally, the electrical I and Q components in both polarizations are sampled and quantized by four independent ADCs, and sent to the DSP subsystem for post-processing.

### 1.1.2 Post-detection DSP subsystems

As previously emphasized, the rebirth of optical coherent detection is strictly related with the use of post-detection DSP to simplify the hardware implementation. Supported by electronic devices capable of performing several billion operations per second, critical coherent detection tasks such as phase recovery and polarization demultiplexing [31] can be conveniently implemented through DSP, enabling a low complexity and low cost implementation with high performance and reliability. In the following, we briefly review the characteristics and functionalities of the main DSP subsystems required for baseband processing of polarization multiplexing (PM)-quadrature amplitude modulation (QAM) optical signals.

**Deskew and Orthonormalization:** Non-ideal equipment behavior within the optical demodulation and down-conversion stages may impact the analog electrical signals, possibly causing temporal misalignment, loss of orthogonality and phase/amplitude imperfections between the I and Q photocurrents. Temporal misalignment generated by different signal path lengths can be removed by a deskew algorithm [32], which may include an interpolation stage to remove fractional delays. In turn, the detrimental effect of quadrature imbalance, which is mainly caused by imperfections in the  $90^\circ$  hybrid and responsivity mismatch between the photodiodes, can be compensated by orthonormalization methods such as the Gram-Schmidt algorithm [33] and constant modulus algorithm (CMA)-based equalizers [34]. Proper compensation of the optical front end imperfections is of utmost importance, avoiding error propagation and preparing the digital signal for the subsequent DSP algorithms.

**Static Equalization:** Benefitting from the fact that the phase information is preserved during signal down-conversion in the coherent receiver, equalization of transmission impairments is possible by digitally reversing signal propagation in fiber. Employing proper equalization algorithms, both linear [35, 36] and nonlinear impairments [37, 38] can be partially removed in the digital domain. Although theoretically the digital equalization of all fiber impairments can be performed in a single DSP block, it is generally preferable to split the equalization problem into two well-defined subsystems. Deterministic effects, such as chromatic dispersion (CD) and possibly nonlinear effects, can be compensated within a static equalization block, allowing to remove the longer term memory effects, which typically require higher computational resources (e.g. more filter taps). The remaining non-deterministic effects, mostly due to polarization phenomena, can be adaptively compensated in a dedicated dynamic equalization subsystem. The static equalization subsystem represents the nuclear work of this thesis, mostly in terms of nonlinear compensation algorithms. Further details on linear and nonlinear equalization techniques will be provided in the following Chapters.

**Dynamic Equalization:** The dynamic equalization subsystem is responsible to compensate for randomly evolving phenomena such as polarization mode dispersion (PMD) and polarization-dependent loss (PDL) [28] and to eliminate residual amounts of deterministic effects that may have been under/over compensated by the static equalization stage. For PM transmission systems, polarization demultiplexing can also be implemented within the dynamic equalization block, often employing a CMA-driven equalizer (mostly for PM-quadrature phase-shift keying (QPSK) signals), which is based on a bank of  $2 \times 2$  butterfly finite impulse response (FIR) filters. The CMA criterion is optimum for constant modulus modulation formats, such as PM-QPSK. However, for multilevel modulation formats the standard CMA introduces a feedback error, thus yielding a performance penalty. Advanced CMA-based algorithms have been proposed to overcome this issue, with emphasis to the radius-directed CMA, which considers a multi-radii cost function to calculate the feedback error [31]. Alternatively, a modulation transparent approach based on Stokes-space processing has been recently proposed for adaptive polarization demultiplexing [27, 28, 39]. Hybrid CMA and Stokes-based

solutions have also been proposed [40], aiming to gather the main advantages of both approaches.

**Clock Recovery:** Due to electronic imperfections in ADCs and misalignment between the transmitter and receiver clocks, there is always some deviation from the ideal sampling instant, which may vary in time. The impact of this non-ideal sampling behavior can be reduced by a proper clock recovery subsystem, which is composed of two main blocks: a timing error detector and an interpolation stage. Due to its high performance, simplicity and carrier independency properties, the Gardner algorithm is the most widely used timing error detector approach [41, 42]. The complexity and performance of the subsequent interpolation stage can be adjusted to match the specific requirements of the received signal [43].

**Carrier Recovery:** Due to the lack of hardware phase/frequency locking between the received signal and the free-running LO laser, digital carrier recovery is required to recover the encoded phase information. In practice, carrier recovery can be partitioned into two independent blocks, comprising frequency and phase estimation. The frequency estimation block aims to determine and remove the frequency deviation between the optical received signal and the LO. Among the multitude of proposed frequency estimation techniques [44], the most commonly used for optical communications are based on:

- i) differential phase methods, where each symbol is compared with its predecessor enabling to estimate the time-varying frequency offset in a feed-forward fashion [45];
- ii) spectral methods, which are based on the observation of the maximum of the discrete spectrum [46, 47].

Most of these blind algorithms require the removal of phase modulation prior to frequency estimation. For  $M$ -phase-shift keying (PSK) formats, this can be done by raising each received symbol to the  $M^{\text{th}}$ -power. However, for QAM formats, other modulation-dependent techniques are required [48]. Alternatively, data-aided frequency estimation provides a more robust and modulation-transparent operation, at the expense of some overhead for periodic training data [49].

Once the *coarse* frequency estimation is concluded, fine carrier recovery can be applied by using proper phase estimation algorithms to remove slowly time-varying phase deviations, namely due to the non-zero laser linewidth and the residual frequency offset. A large number of feedback [50] and feed-forward [51] phase estimation algorithms have been already proposed and assessed. Similarly to the frequency estimation algorithms, phase estimation of QPSK signals can be straightforwardly achieved by removing the digital modulation with a fourth order nonlinearity and averaging the obtained phase over a given block of samples, using the Viterbi and Viterbi algorithm [52].

**Symbol Decoding:** Finally, the digitally processed signal samples are fed to a symbol-by-symbol slicer to identify the transmitted symbols.

After retrieving the binary sequence, forward error correction (FEC) is required in order to reduce the probability of error at the cost of some bit overhead [53]. Typical FEC hard-decision algorithms employed in 100G optical communication systems include 7% overhead, enabling a net coding gain of up to 9.4 dB [54]. In terms of bit error rate (BER) performance, these hard-decision FEC codes typically allow for a pre-FEC BER in the order of  $10^{-3}$  to be corrected to  $< 10^{-15}$ , thus ensuring virtually error-free transmission. More recently, due to the adoption of higher-order QAM formats where the BER performance is strongly affected, there has been a rising trend of using soft-decision FEC codes with larger overhead (typically around 20%) and enabling to correct a pre-FEC BER of in the order of  $10^{-2}$  [55].

### 1.1.3 Progress on coherent optical transmission systems

#### First developments on optical coherent detection

The application of coherent detection to optical fiber systems has been firstly proposed in the early 1980's, with homodyne [56] and heterodyne [57] demodulation schemes competing for technological supremacy. Given the absence of optical amplification solutions, the main motivation behind coherent detection during the 1980's was to improve the receiver sensitivity in comparison with the conventional direct-detection schemes, enabling to extend the transmission reach of lightwave communication links. However, limited by its high complexity and cost, the interest in coherent optical systems vanished soon after the deployment of the EDFA in the early 1990's. A very detailed review on the origins and first evolution stages of coherent optical systems can be found in [58].

#### The revival of coherent detection

With the coming of the new millennium and the continuous growth on traffic demand, the limited capacity of installed intensity modulation and direction detection (IM/DD) optical transmission systems became a primary concern for the optical telecommunications industry. Experimental attempts to migrate from per-channel bit-rates of 10 Gb/s to 40 Gb/s reusing the IM/DD systems were able to demonstrate aggregate capacities of up to 10.2 Tb/s ( $256 \times 42.7$  Gb/s) [59] over 300 km. However, the spectral efficiency (SE) and propagation performance of these systems is severely limited by the inherent characteristics of on-off keying (OOK)-based modulation formats and direct detection receivers. The revival of coherent detection emerged as the consequence of three main ingredients:

- i) capacity shortage of the deployed IM/DD optical systems;
- ii) technological advances on the electronic devices required to implement coherent detection with feasible complexity and cost;
- iii) enhanced performance and flexibility enabled by post-detection DSP.

As an intermediate solution in terms of complexity and performance, the use of differential phase-shift keying (DPSK) modulation in conjunction with differential detection has attracted significant attention in the early 2000's [60, 61]. One of the main advantages over direct detection was the possibility to employ multilevel encoding, using a differential QPSK (DQPSK) modulation format [60]. Encoding 2 bits per symbol, DQPSK formats allows to double the SE relatively to binary modulation, thus enabling to transmit 40 Gb/s within an effective support bandwidth of  $\sim 20$  GHz (20 Gsym/s). Using the two orthogonal signal polarization components as separate DQPSK channels, the SE can be doubled again, allowing to transmit 4 bits per symbol. Operating at 40 Gb/s with 10 Gb/s modulation-demodulation equipment, these PM-DQPSK systems have become an attractive solution for the industry, providing the perfect balance between performance and cost for the transmission of 40 Gb/s optical channels over moderate propagation distances [62, 63]. A field trial using commercially-ready 40-channel DQPSK transponders operating at 43 Gb/s has been reported in 2007 [64].

Despite of being an attractive solution for 40 Gb/s optical transport networks, differential detection remains a suboptimal approach. Since the photocurrents generated by differential optoelectronic conversion do not carry the absolute phase information, the performance of digital post-compensation becomes limited [18]. Besides, differential detection of higher-order modulation formats finds limited applicability due to an increased hardware complexity. In contrast, coherent detection provides an universal receiver structure with linear down-conversion of optical field into the electrical domain, enabling to fully compensate for linear impairments with digital equalizers [18]. Driven by its prominent advantages, many offline experiments employing coherent transmission of 40 Gb/s PM-QPSK were published between 2005 and 2007 [65, 66], initiating the commercial deployment of coherent optical transmission systems.

### **The deployment of 100G optical systems**

After the successful demonstration of 40 Gb/s, the standardization of 100 gigabit Ethernet (100-GE) has naturally began to push per channel bit-rates to 100G, so that a 100-GE signal could be transported by a single optical channel. Between 2007 and 2009 many 100G high-capacity and high-SE experiments were demonstrated using multilevel modulation formats such as PM-8PSK [67] and PM-16QAM [68], attaining an SE of 6.2 b/s/Hz [68] and an aggregate bit-rate of 32 Tb/s [67]. Although enabling higher SE, the propagation of dense signal constellations invariably requires enhanced SNR, thus reducing the transmission reach and the system reliability. Therefore, thanks to its high tolerance to signal impairments, long transmission reach, high resilience to optical filtering and low cost/complexity, PM-QPSK has been unanimously accepted as the best-in-class solution for commercial long-haul 100G [69]. Transmitting 4 bits per symbol, PM-QPSK enables to reach a spectral efficiency of up to 4 b/s/Hz when combined with Nyquist spectral shaping [70]. Another important advantage of this 100G solution lies on its compatibility with the currently installed 50 GHz frequency grid and commercially available 50 Gsample/s ADCs. A set of ultra-long-haul transpacific experiments has demonstrated the high reliability of 100G PM-QPSK, allowing transmission distances up to 9360 km, with SE of 3.6 b/s/Hz (channel spacing equal to the baud-rate) [71].

Meanwhile, the first commercially ready 100G transceivers have just begun to be delivered in the market in 2012. Transmission of a real-time 120 Gb/s PM-QPSK signal over 3760 km of standard single-mode fiber (SSMF) is demonstrated in [72], employing a  $5 \times 7$  inch<sup>2</sup> multiple-source-agreement (MSA) transceiver, compliant with the optical inter-networking forum (OIF) recommendations [24]. The DSP system is implemented in a 40-nm complementary metal-oxide-semiconductor (CMOS) application specific integrated circuit (ASIC), with four integrated 63 Gsample/s ADCs, performing carrier recovery and equalization of CD (tolerates up to for 60000 ps/nm of accumulated dispersion) and PMD. Soft-decision FEC is employed to guarantee error-free transmission [72].

## Beyond 100G

After the successful deployment of 100G optical systems, current research has been shifting towards the development of next-generation 400 Gb/s (400G) and 1 Tb/s (1T) optical solutions. Such a large increase in terms of bit-rate requires either increased baud-rates, higher SE or a combination of both, posing new challenges for practical implementation. On the one hand, increasing the baud-rate puts a huge pressure into the electronic hardware, primarily for the required digital-to-analog converter (DAC) and ADC processing rates. For instance, a single-carrier 400G PM-QPSK-based solution would require a symbol-rate of  $>100$  Gbaud [73]. The use of such high symbol-rates poses enormous challenges in terms of the electrical signal generation and detection, requiring very high electrical bandwidth and sampling rate [73], or the use of advanced synchronization techniques between independent electrical units [74]. On the other hand, a single-carrier 28 Gbaud 400G solution would require PM-256QAM modulation, corresponding to a required optical signal-to-noise ratio (OSNR) of  $\sim 30.4$  dB (considering a maximum BER of  $3.8 \times 10^{-3}$  for hard-decision FEC), severely limiting the signal reach in state-of-the-art optical transmission systems. This tradeoff between SE and SNR is well known from the Shannon's theory [75], which has been recently expanded to assess the fiber capacity limits, taking into account nonlinear impairments and amplifier noise [2]. Therefore, a practical solution requires a balanced tradeoff between these two main constraints.

Among the plethora of proposed modulation formats and channel configurations, the use of PM-64QAM modulation has been attracting significant attention for high-SE transmission of 100G and 400G channels, mostly targeting the application in metro optical networks. In [76] a signal reach of 1306 km is demonstrated for a  $20 \times 124.8$  Gb/s PM-64QAM signal placed in a 12 GHz WDM grid, yielding a net SE of 8.67 b/s/Hz. Targeting the 400G sector, in [77], 516 Gb/s PM-64QAM is propagated over 600 km, considering a pre-FEC BER threshold of  $2 \times 10^{-2}$ . Employing hybrid PM-32/64QAM modulation, the transmission of ten 400G channels in a 50 GHz WDM grid is demonstrated in [78], achieving a maximum signal reach of 3200 km.

Alternatively to single-carrier modulation, a promising solution for next-generation 400G and 1T optical transmission systems is the concept of "superchannel" [79]. A superchannel is composed of several tightly spaced optical subcarriers that are routed together through the network as a single entity. Many pioneer works on 400G [80] and 1T [81, 82] superchannels consider the use of coherent optical orthogonal frequency

division multiplexing (CO-OFDM) modulation as a way of enabling very high SE. Due to the orthogonality between subcarriers, coherent CO-OFDM enables baud-rate subcarrier spacing without degrading the system performance due to inter-symbol interference (ISI). However, CO-OFDM shows some disadvantages for practical implementation relatively to QAM modulation, such as the enhanced DAC requirements in terms of effective number of bits and the reduced robustness to nonlinear impairments due to the high CO-OFDM peak-to-average power ratio [83, 84]. An alternative solution that is currently being intensively investigated both by academic and industrial players with the aim of being deployed to the market in the coming years is the so-called Nyquist WDM superchannel [85]. This technique is applied over QAM subcarriers, using aggressive spectral shaping in order to enable an inter-subcarrier spacing close to the baud-rate, thus maximizing the spectral efficiency of the superchannel [79]. Because such a spectral shaping explores the Nyquist limit for ISI-free transmission, it is commonly designated in the literature as Nyquist pulse shaping. Currently, one of the stronger candidates for a commercial 400G solution is a dual-carrier PM-16QAM superchannel [86], where each subcarrier is modulated at a net baud-rate of 25 Gbaud. Using this configuration, a signal reach of 9200 km has been demonstrated in [86], where the authors consider the transmission of  $53 \times 400\text{G}$  superchannels, with 32 Gbaud gross baud-rate per subcarrier and advanced FEC with 28% overhead. Using near Nyquist pulse shaping, a subcarrier spacing of 33.33 GHz enables to achieve a net SE of 6 b/s/Hz.

## 1.2 Motivation and Objectives

Single-mode fibers are nowadays largely dominant within the fiber plant of optical core networks, including transatlantic and transpacific links. Given the tremendous costs associated with a possible renewal of the installed fiber plant, telecom operators are currently seeking for less invasive engineering solutions. Receiver-side digital equalization of fiber impairments provides a transparent and low-cost solution to optimize long-haul optical fiber links. Digital post-compensation of linear fiber impairments, such as CD and PMD, which were critical bandwidth bottlenecks, has revolutionized the design of long-haul links, avoiding the use of dispersion compensation fiber (DCF) modules. However, despite of the huge benefits that digital linear equalization has brought to backbone optical networks, including higher energy efficiency and enhanced SNR, the unstoppable growth of traffic demand has been gradually pushing optical signal propagation to the nonlinear regime. Nonlinear phenomena in long-haul and high-speed optical communications is dominated by the Kerr effect, which causes an optical power dependent variation of the refractive index, generating nonlinear distortions such as self-phase modulation (SPM), and inter-channel cross-phase modulation (XPM) and four-wave mixing (FWM). The impact of these distortions rapidly increases with the optical power and the propagation distance [87, 88], causing a progressive signal degradation and thus limiting achievable SNR for a given optical link. In this context, digital nonlinear equalization takes a prominent role as an advanced engineering solution for future backbone optical links. The modelling, prediction and mitigation of nonlinearities has become one of the most active research topics in this field, aiming

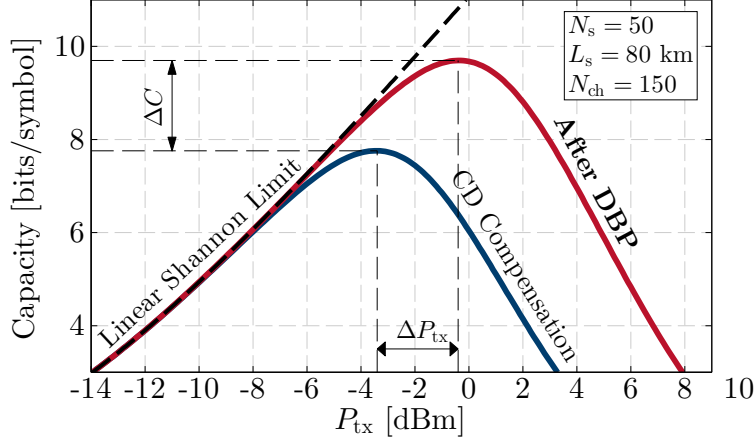


**Figure 1.3:** Estimated fiber capacity,  $C$ , versus input power per channel,  $P_{\text{tx}}$ , using the analytical formulation of [89] and considering 150 Nyquist-spaced WDM channels modulated at 28 Gbaud and propagated over  $50 \times 80$  km of standard single-mode fiber.

to maximize the fiber capacity by understanding and partially eliminating nonlinear phenomena [37, 38, 87, 89–97]. Stemming from the observation the nonlinear interference (NLI) in uncompensated optical links (links without inline dispersion compensation) takes a Gaussian-like distribution, an approximated OSNR definition accounting for nonlinear impairments has been proposed in [87, 90], yielding the so-called Gaussian noise (GN) model, which enables to define a *nonlinear OSNR* where the impact of NLI is approximated by an additive Gaussian noise process,

$$\text{OSNR}_{\text{NL}} = \frac{P_{\text{tx,ch}}}{P_{\text{ASE}} + P_{\text{NLI}}}, \quad (1.1)$$

where  $P_{\text{tx,ch}}$  represents the average optical power per-channel launched in the fiber,  $P_{\text{ASE}}$  is the amplified spontaneous emission (ASE) noise power generated by the optical amplifiers and  $P_{\text{NLI}}$  is the NLI noise power. Approximated formulas to estimate the NLI noise power are also proposed and experimentally validated in [87, 89–91]. Based on the GN model approximated formulation proposed in [89], Figure 1.3 presents an estimate of the achievable fiber capacity for an uncompensated (no inline DCF modules) optical transmission system composed of 50 SSMF spans with 80 km each, yielding a total propagation distance of 4000 km. Inline optical amplification is implemented by ideal EDFAs with 5 dB noise figure (NF) and the transmitted signal is composed of 150 Nyquist-spaced 28 Gbaud channels, approximately occupying the full C-band. On the contrary of a linear transmission system, where maximum capacity is set by the linear Shannon limit, arbitrarily high capacity in optical fiber systems cannot be obtained by using an arbitrarily high signal power. Instead, there exists an optimum signal power for which the fiber capacity is maximized. For optical powers lower than the optimum, signal degradation is dominated by added noise, whereas nonlinear distortions become dominant for higher optical powers. It is well known that nonlinear distortions can be generated both by signal–signal and signal–noise interactions [2, 98]. Fiber capacity is ultimately limited by the signal–noise interactions, which are nondeterministic and therefore cannot

be predicted and fully compensated. Nevertheless, the strength of nonlinear distortions in uncompensated fiber links is known to be largely dominated by signal–signal interactions [99], which are purely deterministic. This opens the possibility of designing an ideal post-detection nonlinear equalizer, capable of fully removing all signal–signal nonlinear distortions, given the availability of a complete physical knowledge of signal propagation in fiber. Even though the practical implementation of such an ideal nonlinear equalizer bumps into the unavoidable non-ideal behavior of real-world applications, it clearly opens the door for the development of approximate numerical techniques capable of partially compensating for the deterministic nonlinear impairments. This is the underlying idea behind the concept of digital backpropagation (DBP), in which the received optical field is virtually propagated in the backward direction resorting to iterative numerical methods [37]. The potential benefit of nonlinear equalization using DBP is qualitatively shown in Figure 1.3, effectively enabling to enhance both the optimum optical power and maximum achievable capacity. Indeed, it has been recently demonstrated that the use of post-detection DBP-based nonlinear compensation enables to reduce the effective nonlinear fiber parameter, thus extending the linear regime [100]. In addition, it has also been demonstrated that DBP allows to reduce the growth of nonlinearly-induced noise with increasing optical power: the original cubic growth is reduced to a quadratic one [101].

Driven by the possibility of extending the linear propagation regime in optical transmission systems, in recent years, there has been an increasing number of scientific contributions proposing various nonlinear equalization approaches. The pioneer works on nonlinear compensation attempted to deal signal-noise interactions, such as nonlinear phase noise (NLPN) [102], by neglecting dispersion effects and applying a constant phase rotation at the receiver [103] or determining the optimal symbol decision boundaries in the presence of NLPN [104]. However, since linear and nonlinear phenomena are tightly intertwined during propagation, these approaches find limited application in dispersion unmanaged fiber links. Provided that signal propagation in fiber can be analytically modeled by the nonlinear Schrödinger equation (NLSE), an inverse NLSE model can in principle be used for compensation purposes. Moved by this underlying idea, the first DBP algorithms have been proposed in 2008 [37, 38]. Making use of the well-known split-step Fourier method (SSFM), these DBP approaches have shown that all deterministic fiber impairments can be effectively compensated if sufficient temporal and spatial resolution are used. However, due to practical constraints in ADC technology and DSP complexity, simplified SSFM-based DBP methods have been proposed and experimentally validated, using 2 samples per symbol and several fiber spans per step [105].

Motivated by the need for high performance and low-complexity nonlinear compensation algorithms, this thesis aims at the development of novel approaches for intra- and inter-channel nonlinear compensation, assisted by a comprehensive experimental validation in high-speed and long-haul coherent optical transmission systems. The work of this thesis has therefore been planned to accomplish the following four main objectives:

- i) Develop an alternative approach for the numerical implementation of DBP with relaxed requirements in terms of spatial and temporal resolution;

- ii) Quantify and reduce the complexity of DBP-based nonlinear compensation in order to find regions of feasible practical implementation;
- iii) Develop advanced techniques, with reduced implementation complexity, for the compensation of inter-channel nonlinearities, targeting the performance optimization of next-generation 400G optical systems;
- iv) Experimentally validate the developed techniques.

### 1.3 Thesis Outline

In order to accomplish the established research objectives, this thesis is organized into seven chapters. To contextualize the problem of nonlinear compensation in optical transmission systems, Chapter 2 provides a condensed review of signal propagation in single-mode fibers, exploring the scalar and vectorial NLSE as the underlying analytical model and introducing the SSFM and the Volterra series transfer function (VSTF) as potential numerical methods to obtain approximate NLSE solutions.

The concept of DBP is thoroughly addressed in Chapter 3, where the inverse VSTF method is proposed and compared against the traditional DBP-SSFM in terms of performance and complexity. The DBP-VSTF is experimentally validated resorting to 100G PM-QPSK long-haul optical transmission systems, demonstrating its high performance and tolerance against low spatial and temporal resolution.

Building upon the DBP-VSTF method proposed in Chapter 3, an optimized frequency domain Volterra series nonlinear equalizer (VSNE) is proposed in Chapter 4, employing a symmetric kernel reconstruction technique and a frequency-flat approximation. The resulting symmetric Volterra series nonlinear equalizer (symVSNE) and simplified Volterra series nonlinear equalizer (simVSNE) algorithms benefit from an increased modularity and reduced complexity, relatively to the initial DBP-VSTF formulation. Experimental validation of the symVSNE and simVSNE techniques is performed for a 100G PM-64QAM transmission system, demonstrating important computational effort benefits associated with a high equalization performance and low processing latency.

Through an inverse Fourier analysis of the simVSNE algorithm, Chapter 5 presents a closed-form time domain formulation for Volterra-based DBP in coherent optical transmission systems. Novel time domain approximations are considered, with emphasis on the introduction of a power-weighting time window of adjustable length, yielding the weighted VSNE (W-VSNE) algorithm. The W-VSNE is experimentally validated for a dual-carrier 400G optical transmission system based on PM-16QAM modulation, enabling to demonstrate its optimized performance/complexity tradeoff.

With the aim to address the issue of inter-channel nonlinear compensation, Chapter 6 provides a comprehensive experimental assessment of dual- and triple-carrier 400G solutions for both ultra-long-haul (ULH) and metro applications, based on PM-16QAM and PM-64QAM modulation, respectively. Using SSFM-based DBP associated with a coupled-equations approach, high performance and reduced complexity inter-subcarrier nonlinear compensation is demonstrated. In addition, the triple-carrier 400G solution

is shown to enable higher linear and nonlinear performance, corroborating other recent results that point out the benefits of an evolution towards subcarrier multiplexing.

Finally, the main conclusions and suggestions for future research topics are summarized in Chapter 7.

## 1.4 Main Contributions

This thesis proposes novel digital equalization algorithms for intra- and inter-channel nonlinear compensation in high-speed coherent optical transmission systems. In order to validate the newly proposed algorithms, each contribution has been subject of experimental validation, resorting to international collaborations with top-level research institutes with state-of-the-art laboratorial facilities. The main contributions of this thesis can be summarized as follows:

- i) study of DSP subsystems and legacy DBP-based nonlinear compensation algorithms for coherent optical transmission systems [NJ1, NJ2, C1, C2, C5, C14, C26];
- ii) development, numerical assessment and experimental validation of an inverse VSTF for non-iterative implementation of DBP-based nonlinear post-compensation [J1, J2, J3, C3, C4, C6, C10, P1];
- iii) development, numerical assessment and experimental validation of the symVSNE and simVSNE algorithms for frequency domain nonlinear compensation with high modularity and reduced complexity [J4, J5, C11, C13, C15, C18, C21, C23];
- iv) development, numerical assessment and experimental validation of the W-VSNE algorithm for time domain nonlinear compensation with high modularity and reduced complexity [J6, J10, C19, C23, C24, C29];
- v) experimental assessment of inter-subcarrier nonlinear compensation in ULH 400G optical transmission systems [J11, C25].

In addition, the work directly related with the topic of this thesis, other relevant contributions were produced as a result of a tight collaboration within Optical Communications research group of Instituto de Telecomunicações. These main other contributions are:

- i) collaboration on the development and optimization of coherent technologies for future access networks [J7, J8, J9, C7, C16, C17];
- ii) collaboration on the real-time implementation of DSP algorithms and subsystems [J8, J9, C8, C12, C16, C20, P2];
- iii) collaboration on the development and experimental assessment of Stokes-based polarization demultiplexing [J12, C9, C22];

- iv) collaboration on the development of a low-complexity FIR filter for CD compensation [J13, P2];
- v) collaboration on the experimental implementation of an optical recirculating loop for long-haul laboratorial measurements [C24];
- vi) collaboration on the development of polynomial behavioral models for adaptive nonlinear mitigation in coherent optical transmission systems [C25].

## 1.5 List of Publications

The major achievements obtained from the work of this thesis were submitted for peer-review by the international scientific community through the following list of publications.

### Papers in international journals

- [J13] C. S. Martins, **F. P. Guiomar**, S. B. Amado, R. M. Ferreira, A. Shahpari, A. L. Teixeira and A. N. Pinto, “Multiplierless Distributive FIR-Based Chromatic Dispersion Equalization for Coherent Receivers,” submitted to *IEEE/OSA Journal of Lightwave Technology*, 2015.
- [J12] S. Ziaie, N. J. Muga, **F. P. Guiomar**, G. M. Fernandes, R. M. Ferreira, A. Shahpari, A. L. Teixeira and A. N. Pinto, “Experimental Demonstration of an Adaptive 3D Stokes Space PolDemux Technique for Optical Metro and Access Networks,” submitted to *IEEE/OSA Journal of Lightwave Technology*, 2015.
- [J11] **F. P. Guiomar**, S. B. Amado, J. D. Reis, S. M. Rossi, A. Chiuchiarelli, J. R. F. Oliveira, A. L. Teixeira and A. N. Pinto, “Multi-Carrier Digital Backpropagation for 400G Optical Superchannels,” to be submitted to *IEEE/OSA Journal of Lightwave Technology*, 2015. (*invited paper*)
- [J10] S. B. Amado, **F. P. Guiomar**, N. J. Muga, J. D. Reis, S. M. Rossi, A. Chiuchiarelli, J. R. F. Oliveira, A. L. Teixeira and A. N. Pinto, “Low Complexity Advanced DBP Techniques for Ultra-Long-Haul 400G Transmission Systems,” to be submitted to *IEEE/OSA Journal of Lightwave Technology*, 2015. (*invited paper*)
- [J9] R. M. Ferreira, J. D. Reis, S. M. Rossi, S. B. Amado, **F. P. Guiomar**, Ali Shahpari, J. R. F. Oliveira, A. N. Pinto and A. L. Teixeira, “Coherent Nyquist UDWDM-PON with Digital Signal Processing in Real-Time,” accepted with revisions in *IEEE/OSA Journal of Lightwave Technology*, 2015. (*invited paper*)
- [J8] R. M. Ferreira, J. D. Reis, S. B. Amado, A. Shahpari, **F. P. Guiomar**, J. R. F. Oliveira, A. N. Pinto and A. L. Teixeira, “Performance and Complexity of Digital Clock Recovery for Nyquist UDWDM-PON in Real-Time,” accepted for publication in *IEEE Photonics Technology Letters*, 2015.

## 1.5. List of Publications

---

- [J7] A. Shahpari, R. M. Ferreira, A. Sousa, V. Ribeiro, S. Ziaie, A. Tavares, Z. Vujicic, **F. P. Guiomar**, J. D. Reis, A. N. Pinto and A. Teixeira, “Coherent Ultra Dense Wavelength Division Multiplexing Passive Optical Networks,” accepted for publication in *Optical Fiber Technology*, 2015. (*invited paper*)
- [J6] **F. P. Guiomar**, S. B. Amado, C. S. Martins and A. N. Pinto, “Time Domain Volterra-Based Digital Backpropagation for Coherent Optical Systems,” *IEEE/OSA Journal of Lightwave Technology*, vol. 33, no. 15, pp. 3170–3181, 2015.
- [J5] **F. P. Guiomar**, S. B. Amado, A. Carena, G. Bosco, A. Nespola, A. L. Teixeira and A. N. Pinto, “Fully-Blind Linear and Nonlinear Equalization for 100G PM-64QAM Optical Systems,” *IEEE/OSA Journal of Lightwave Technology*, vol. 33, no. 7, pp. 1265–1274, 2015. (*invited paper*)
- [J4] **F. P. Guiomar**, and A. N. Pinto, “Simplified Volterra Series Nonlinear Equalizer for Polarization-Multiplexed Coherent Optical Systems,” *IEEE/OSA Journal of Lightwave Technology*, vol. 31, no. 23, pp. 3879–3891, 2013.
- [J3] **F. P. Guiomar**, J. D. Reis, A. Carena, G. Bosco, A. T. Teixeira and A. N. Pinto, “Experimental Demonstration of a Frequency-Domain Volterra Series Nonlinear Equalizer in Polarization-Multiplexed Transmission,” *Optics Express*, vol. 21, no. 1, pp. 276288, 2013.
- [J2] **F. P. Guiomar**, J. D. Reis, A. T. Teixeira and A. N. Pinto, “Mitigation of Intra-Channel Nonlinearities Using a Frequency-Domain Volterra Series Equalizer,” *Optics Express*, vol. 20, no. 2, pp. 1360-1369, 2012.
- [J1] **F. P. Guiomar**, J. D. Reis, A. T. Teixeira and A. N. Pinto, “Digital Post-Compensation Using Volterra Series Transfer Function,” *IEEE Photonics Technology Letters*, vol. 23, no. 19, pp. 1412-1414, 2011.

### Papers in national journals

- [NJ2] **F. P. Guiomar**, S. B. Amado, N. J. Muga, A. N. Pinto, C. Rodrigues, B. Marques, P. Costa, P. Mão-Cheia, C. Macedo, “Processamento Digital Adaptativo em Sistemas Óticos 40/100G,” *Revista Saber e Fazer Telecomunicações*, pp. 135–141, January, 2013.
- [NJ1] **F. P. Guiomar**, A. N. Pinto, C. Rodrigues and P. Mão-Cheia, “Transmissão e Recepção Coerente a 40Gb/s e 100Gb/s,” *Revista Saber e Fazer Telecomunicações*, vol. 9, pp. 128–133, December, 2011.

### Papers in conference proceedings

- [C29] S. B. Amado, **F. P. Guiomar**, N. J. Muga, J. D. Reis, S. M. Rossi, A. Chiuchiarelli, J. R. F. Oliveira, A. L. Teixeira and A. N. Pinto, “Experimental Demonstration of

- the Weighted Volterra Series Nonlinear Equalizer,” accepted for oral presentation at *10th Conference on Telecommunications (ConfTele)*, Aveiro, Portugal, September, 2015.
- [C28] J. P. Gonçalves, P. Lavrador, F. P. Guiomar, A. N. Pinto, T. R. Cunha and J. C. Pedro, “Nonlinear Behavioral Modeling Equalization Techniques for Optical Transmission Systems,” accepted for oral presentation at *10th Conference on Telecommunications (ConfTele)*, Aveiro, Portugal, September, 2015.
- [C27] S. Ziaie, **F. P. Guiomar**, R. M. Ferreira, S. B. Amado, A. Shahpari, A. L. Teixeira and A. N. Pinto, “100 Gbps DP-QPSK Transmission over 8000 km of Standard Single Mode Fiber using Recirculating Loop Technique,” accepted for oral presentation at *10th Conference on Telecommunications (ConfTele)*, Aveiro, Portugal, September, 2015.
- [C26] **F. P. Guiomar**, S. B. Amado, C. S. Martins and A. N. Pinto, “Digital Equalization of Nonlinear Fiber Impairments in Coherent Optical Transmission Systems,” accepted for oral presentation at *International OSA Network of Students (IONS)*, Valencia, Spain, September, 2015.
- [C25] **F. P. Guiomar**, S. B. Amado, J. D. Reis, S. M. Rossi, A. Chiuchiarelli, J. R. F. Oliveira, A. L. Teixeira and A. N. Pinto, “Ultra-Long-Haul 400G Superchannel Transmission with Multi-Carrier Nonlinear Equalization,” accepted for oral presentation at *41st European Conf. Optical Communication (ECOC)*, paper Th.2.2.4, Valencia, Spain, September, 2015.
- [C24] S. B. Amado, **F. P. Guiomar**, N. J. Muga, J. D. Reis, S. M. Rossi, A. Chiuchiarelli, J. R. F. Oliveira, A. L. Teixeira and A. N. Pinto, “Experimental Demonstration of the Parallel Split-Step Method in Ultra-Long-Haul 400G Transmission,” accepted for oral presentation at *41st European Conf. Optical Communication (ECOC)*, paper Th.2.6.2, Valencia, Spain, September, 2015.
- [C23] **F. P. Guiomar**, S. B. Amado, C. S. Martins, J. D. Reis, A. L. Teixeira and A. N. Pinto, “Volterra-based Digital Backpropagation: Performance and Complexity Assessment,” in *Proc. Advanced Photonics for Communications*, Boston, USA, June 2015. (*invited paper*)
- [C22] N. J. Muga, S. Ziaie, A. Shahpari, **F. P. Guiomar** and A. N. Pinto, “Optimizing Polarization Related Dynamic Equalization in Coherent Optical Communications,” in *Proc. International Conference on Transparent Optical Networks (ICTON)*, paper Mo.C1.6, Budapest, Hungary, July, 2015.
- [C21] S. B. Amado, **F. P. Guiomar**, N. J. Muga and A. N. Pinto, “Assessment of Nonlinear Equalization Algorithms for Coherent Optical Transmission Systems using an FPGA,” in *Proc. International Conference on Transparent Optical Networks (ICTON)*, paper Mo.C1.4, Budapest, Hungary, July, 2015.

## 1.5. List of Publications

---

- [C20] A. N. Pinto, S. B. Amado, C. S. Martins, S. Ziaie, N. Muga, R. Ferreira, A. L. Teixeira and **F. P. Guiomar**, “Real-Time Digital Signal Processing for Coherent Optical Systems,” in *Proc. International Conference on Transparent Optical Networks (ICTON)*, paper Mo.C1.2, Budapest, Hungary, July, 2015. (*invited paper*)
- [C19] **F. P. Guiomar**, S. B. Amado, C. S. Martins and A. N. Pinto, “Parallel Split-Step Method for Digital Backpropagation,” in *Proc. Optical Fiber Communication Conference (OFC)*, paper Th2A.28, Los Angeles, USA, March 2015.
- [C18] **F. P. Guiomar**, S. B. Amado, A. Carena, G. Bosco, A. Nespola and A. N. Pinto, “Transmission of PM-64QAM over 1524 km of PSCF using Fully-Blind Equalization and Volterra-Based Nonlinear Mitigation,” in *Proc. 40th European Conf. Optical Communication (ECOC)*, paper We.3.3.3, Cannes, France, September, 2014.
- [C17] A. Shahpari, R. Ferreira, V. Ribeiro, Z. Vujicic, A. Tavares, S. Ziaie, **F. P. Guiomar**, A. Sousa, A. N. Pinto, M. Lima, and A. L. Teixeira, “Free Space Optics Hybrid PTMP Advanced Modulation Bi-directional PON,” in *Proc. 40th European Conf. Optical Communication (ECOC)*, paper P.7.16, Cannes, France, September 2014.
- [C16] R. Ferreira, A. Shahpari, S. Amado, P. Costa, J. D. Reis, **F. P. Guiomar**, A. N. Pinto and A. L. Teixeira, “Impact of TWDM on Optional Real-Time QPSK WDM Channels,” in *Proc. 40th European Conf. Optical Communication (ECOC)*, paper P.7.19, Cannes, France, September 2014.
- [C15] A. N. Pinto, **F. P. Guiomar**, S. Amado, S. Ziaie, A. Shahpari, R. Ferreira, N. Muga and A. L. Teixeira, “Digital Equalization of Optical Nonlinearities in Very High-Speed Optical Communication Systems,” in *Proc. 16th International Conference on Transparent Optical Networks (ICTON)*, invited talk, Graz, Austria, July 2014. (*invited paper*)
- [C14] **F. P. Guiomar** and A. N. Pinto, “Terabit-Per-Second Optical Communication Systems Enabled by Digital Signal Processing,” in *Proc. European Industrial Doctoral School Summer Workshop (EIDS)*, pp. 42-43, Pardubice, Czech Republic, May, 2014.
- [C13] **F. P. Guiomar**, S. B. Amado and A. N. Pinto, “Reducing The Complexity of Digital Nonlinear Compensation for High-Speed Coherent Optical Communication Systems,” in *Proc. II International Conference on Applications of Optics and Photonics*, Aveiro, Portugal, May 2014.
- [C12] S. B. Amado, R. M. Ferreira, P. S. Costa, **F. P. Guiomar**, S. Ziaie, A. L. Teixeira, N. J. Muga and A. N. Pinto, “Clock and carrier recovery in high-speed coherent optical communication systems,” in *Proc. II International Conference on Applications of Optics and Photonics*, Aveiro, Portugal, May 2014.

- [C11] **F. P. Guiomar**, S. B. Amado, N. J. Muga, J. D. Reis, A. T. Teixeira and A. N. Pinto, “Simplified Volterra Series Nonlinear Equalizer by Intra-Channel Cross-Phase Modulation Oriented Pruning,” in *Proc. 39th European Conf. Optical Communication (ECOC)*, London, United Kingdom, paper We.3.C.6, September, 2013.
- [C10] A. N. Pinto, S. B. Amado, N. J. Muga and **F. P. Guiomar**, “Equalization of Fiber Impairments Using High-Speed Digital Signal Processing,” in *Proc. International Conference on Transparent Optical Networks (ICTON)*, Cartagena, Spain, June, 2013. (*invited paper*)
- [C9] N. J. Muga, **F. P. Guiomar** and A. N. Pinto, “Stokes Space Based Digital PolDemux for Polarization Switched-QPSK Signals,” in *Proc. Conference on Lasers and Electro-Optic (CLEO)*, San Jose, United States, June 2013.
- [C8] S. B. Amado, **F. P. Guiomar** and A. N. Pinto, “Digital Equalization of Chromatic Dispersion in an FPGA,” in *Proc. 9th Conference on Telecommunications*, Castelo Branco, Portugal, May, 2013;
- [C7] J. D. Reis, A. Shahpari, R. Ferreira, **F. P. Guiomar**, D. Neves, A. N. Pinto and A. T. Teixeira, “Analysis of Transmission Impairments on Terabit Aggregate PONs,” in *Proc. OSA Optical Fiber Communications (OFC)*, Anaheim, United States, paper OM2A5, March, 2013.
- [C6] **F. P. Guiomar**, J. D. Reis, A. Carena, G. Bosco, A. T. Teixeira and A. N. Pinto, “Experimental Demonstration of a Frequency-Domain Volterra Series Nonlinear Equalizer in Polarization-Multiplexed Transmission,” in *Proc. 38th European Conf. on Optical Communications (ECOC)*, Amsterdam, Netherlands, paper Th.1.D.1, September, 2012.
- [C5] **F. P. Guiomar** and A. N. Pinto, “Receiver-side Digital Signal Processing for 100-GE Coherent Optical Transmission Systems,” in *Proc. 17th European Conf. on Networks and Optical Communications (NOC)*, Vilanova i la Geltrú, Spain, pp. 1-6, June, 2012.
- [C4] M. Forzati, J. Martensson, H.-M. Chin, M. Mussolin, D. Rafique and **F. P. Guiomar**, “Non-Linear Compensation Techniques for Coherent Fibre Transmission,” in *Proc. Communications and Photonics Conference and Exhibition, (ACP)*, Shanghai, China, November, 2011.
- [C3] **F. P. Guiomar**, J. D. Reis, A. T. Teixeira and A. N. Pinto, “Mitigation of Intra-Channel Nonlinearities Using a Frequency-Domain Volterra Series Equalizer,” in *Proc. 37th European Conf. on Optical Communications (ECOC)*, Geneva, Switzerland, paper Tu.6.B.1, September, 2011.
- [C2] **F. P. Guiomar** and A. N. Pinto, “Impairment Compensation of a Single-Channel NRZ-QPSK Optical System through Digital Backward Propagation,” in *15th*

*European Conference on Networks and Optical Communications (NOC/OC&I)*, Faro-Portugal, June 2010.

- [C1] **F. P. Guiomar** and A. N. Pinto, “Backward Propagation Algorithms for Digital Post-Compensation of Fiber Impairments,” presented at *BONE Summer School 2010*, Budapest, 5-6th September 2010.

### Patents

- [P2] **F. P. Guiomar**, S. B. Amado, C. S. Sanches and A. N. Pinto, “Filtro Digital de Baixa Complexidade para a Compensação da Dispersão Cromática no Domínio do Tempo,” patent pending application, 2014.
- [P1] **F. P. Guiomar**, J. D. Reis, A. T. Teixeira, A. N. Pinto, C. Rodrigues and P. Mão-Cheia, “Método de Equalização Não-Linear do Canal Óptico no Domínio da Frequência,” *international patent*, EP2723004, December 2014.

### References

- [1] (2015, May) Cisco visual networking index: Forecast and methodology, 2014–2019. Cisco Systems.
- [2] R.-J. Essiambre, G. Kramer, P. J. Winzer, G. J. Foschini, and B. Goebel, “Capacity limits of optical fiber networks,” *J. Lightw. Technol.*, vol. 28, no. 4, pp. 662–701, 2010.
- [3] R. M. Morais, “Planning and dimensioning of multilayer optical transport networks,” Ph.D. dissertation, University of Aveiro, 2015.
- [4] M. G. Taylor, “Coherent detection method using DSP for demodulation of signal and subsequent equalization of propagation impairments,” *IEEE Photon. Technol. Lett.*, vol. 16, no. 2, pp. 674–676, 2004.
- [5] R. Noe, “PLL-free synchronous QPSK polarization multiplex/diversity receiver concept with digital I&Q baseband processing,” *IEEE Photon. Technol. Lett.*, vol. 17, no. 4, pp. 887–889, 2005.
- [6] —, “Phase noise-tolerant synchronous QPSK/BPSK baseband-type intradyne receiver concept with feedforward carrier recovery,” *J. Lightw. Technol.*, vol. 23, no. 2, pp. 802–808, 2005.
- [7] L. G. Kazovsky, G. Kalogerakis, and W. T. Shaw, “Homodyne phase-shift-keying systems: Past challenges and future opportunities,” *J. Lightw. Technol.*, vol. 24, no. 12, pp. 4876–4884, 2006.

- 
- [8] G. Charlet, “Progress in optical modulation formats for high-bit rate WDM transmissions,” *IEEE J. Sel. Topics Quantum Electron.*, vol. 12, no. 4, pp. 469–483, 2006.
- [9] P. J. Winzer and R.-J. Essiambre, “Advanced optical modulation formats,” *Proc. IEEE*, vol. 94, no. 5, pp. 952–985, 2006.
- [10] —, “Advanced modulation formats for high-capacity optical transport networks,” *J. Lightw. Technol.*, vol. 24, no. 12, pp. 4711–4728, 2006.
- [11] K. Roberts, M. O’Sullivan, K.-T. Wu, H. Sun, A. Awadalla, D. J. Krause, and C. Laperle, “Performance of dual-polarization QPSK for optical transport systems,” *J. Lightw. Technol.*, vol. 27, no. 16, pp. 3546–3559, 2009.
- [12] M. Birk, P. Gerard, R. Curto, L. Nelson, X. Zhou, P. Magill, T. J. Schmidt, C. Malouin, B. Zhang, E. Ibragimov, S. Khatana, M. Glavanovic, R. Lofland, R. Marcoccia, R. Saunders, G. Nicholl, M. Nowell, and F. Forghieri, “Coherent 100 Gb/s PM-QPSK field trial,” *IEEE Commun. Mag.*, vol. 48, no. 7, pp. 52–60, 2010.
- [13] M. Birk, P. Gerard, R. Curto, L. E. Nelson, X. Zhou, P. Magill, T. J. Schmidt, C. Malouin, B. Zhang, E. Ibragimov, S. Khatana, M. Glavanovic, R. Lofland, R. Marcoccia, R. Saunders, G. Nicholl, M. Nowell, and F. Forghieri, “Real-time single-carrier coherent 100 Gb/s PM-QPSK field trial,” *J. Lightw. Technol.*, vol. 29, no. 4, pp. 417–425, 2011.
- [14] G. Zhang, L. Nelson, Y. Pan, M. Birk, C. Skolnick, C. Rasmussen, M. Givehchi, B. Mikkelsen, T. Scherer, T. Downs, and W. Keil, “3760km, 100G SSMF transmission over commercial terrestrial DWDM ROADM systems using SD-FEC,” in *Proc. Optical Fiber Communication Conf. and Exposition (OFC)*, paper PDP5D.4, 2012.
- [15] Y. R. Zhou, K. Smith, R. Payne, A. Lord, G. Whalley, T. Bennett, E. Maniloff, S. Alexander, and D. Boymel, “Real-time gridless 800G super-channel transport field trial over 410km using coherent DP-16 QAM,” in *Proc. Optical Fiber Communication Conf. and Exposition (OFC)*, paper Tu2B.3, 2014.
- [16] Y. Loussouarn, E. Pincemin, M. Song, S. Gauthier, Y. Chen, and Z. Shengqian, “400 Gbps real-time coherent Nyquist-WDM DP-16QAM transmission over legacy G.652 or G.655 fibre infrastructure with 2 dB margins,” in *Proc. Optical Fiber Communication Conf. and Exposition (OFC)*, paper W3E.3, 2015.
- [17] Y. R. Zhou, K. Smith, R. Payne, A. Lord, L. Raddatz, M. Bertolini, T. Van De Velde, C. Colombo, E. Korkmaz, M. Fontana, and S. Evans, “1.4 Tb real-time alien superchannel transport demonstration over 410 km installed fiber link using software reconfigurable DP-16 QAM/QPSK,” *J. Lightw. Technol.*, vol. 33, no. 3, pp. 639–644, Feb 2015.

- [18] E. Ip, A. Lau, D. Barros, and J. M. Kahn, “Coherent detection in optical fiber systems,” *Opt. Express*, vol. 16, no. 2, pp. 753–791, 2008.
- [19] G. Li, “Recent advances in coherent optical communication,” *Advances in Optics and Photonics*, vol. 1, pp. 279–307, 2009.
- [20] G. Charlet, “Coherent detection associated with digital signal processing for fiber optics communication,” *C.R. Physique*, vol. 9, pp. 1012–1030, 2008.
- [21] M. Kuschnerov, F. N. Hauske, K. Piyawanno, B. Spinnler, M. S. Alfiad, A. Napoli, and B. Lankl, “DSP for coherent single-carrier receivers,” *J. Lightw. Technol.*, vol. 27, no. 16, pp. 3614–3622, 2009.
- [22] S. J. Savory, “Digital coherent optical receivers: Algorithms and subsystems,” *IEEE J. Sel. Topics Quantum Electron.*, vol. 16, no. 5, pp. 1164–1179, 2010.
- [23] B. Spinnler, “Equalizer design and complexity for digital coherent receivers,” *IEEE J. Sel. Topics Quantum Electron.*, vol. 16, no. 5, pp. 1180–1192, 2010.
- [24] T. J. Schmidt, D. R. Stauffer, and K. Gass, “Implementation agreement for intradyne coherent receivers,” Optical Internetworking Forum, Tech. Rep., April 2010.
- [25] C. Alonso-Ramos, P. J. Reyes-Iglesias, A. Ortega-Moñux, D. Pérez-Galacho, R. Halir, and I. Molina-Fernández, “Polarization-beam-splitter-less integrated dual-polarization coherent receiver,” *Opt. Lett.*, vol. 39, no. 15, pp. 4400–4403, Aug 2014.
- [26] K. Kikuchi, “Polarization-demultiplexing algorithm in the digital coherent receiver,” in *Proc. Digest of the IEEE/LEOS Summer Topical Meetings*, paper MC2.2, 2008, pp. 101–102.
- [27] B. Szafraniec, B. Nebendahl, and T. Marshall, “Polarization demultiplexing in Stokes space,” *Opt. Express*, vol. 18, no. 17, pp. 17 928–17 939, 2010.
- [28] N. J. Muga and A. N. Pinto, “Digital PDL compensation in 3D Stokes space,” *J. Lightw. Technol.*, vol. 31, no. 13, pp. 2122–2130, 2013.
- [29] M. Seimetz and C.-M. Weinert, “Options, feasibility, and availability of  $2 \times 4$   $90^\circ$  hybrids for coherent optical systems,” *J. Lightw. Technol.*, vol. 24, no. 3, pp. 1317–1322, 2006.
- [30] S. J. Savory, G. Gavioli, E. Torrenco, and P. Poggiolini, “Impact of interchannel nonlinearities on a split-step intrachannel nonlinear equalizer,” *IEEE Photon. Technol. Lett.*, vol. 22, no. 10, pp. 673–675, 2010.
- [31] I. Fatadin, D. Ives, and S. Savory, “Blind equalization and carrier phase recovery in a 16-QAM optical coherent system,” *J. Lightw. Technol.*, vol. 27, no. 15, pp. 3042–3049, 2009.

- 
- [32] T. Tanimura, S. Oda, T. Tanaka, T. Hoshida, Z. Tao, and J. C. Rasmussen, "A simple digital skew compensator for coherent receiver," in *Proc. 35th European Conf. Optical Communication (ECOC)*, paper 7.3.2, 2009.
- [33] I. Fatadin, S. J. Savory, and D. Ives, "Compensation of quadrature imbalance in an optical QPSK coherent receiver," *IEEE Photon. Technol. Lett.*, vol. 20, no. 20, pp. 1733–1735, 2008.
- [34] C. S. Petrou, A. Vgenis, I. Roudas, and L. Raptis, "Quadrature imbalance compensation for PDM QPSK coherent optical systems," *IEEE Photon. Technol. Lett.*, vol. 21, no. 24, pp. 1876–1878, 2009.
- [35] E. Ip and J. M. Kahn, "Digital equalization of chromatic dispersion and polarization mode dispersion," *J. Lightw. Technol.*, vol. 25, no. 8, pp. 2033–2043, 2007.
- [36] S. J. Savory, "Digital filters for coherent optical receivers," *Opt. Express*, vol. 16, no. 2, pp. 804–817, 2008.
- [37] E. Ip and J. M. Kahn, "Compensation of dispersion and nonlinear impairments using digital backpropagation," *J. Lightw. Technol.*, vol. 26, no. 20, pp. 3416–3425, 2008.
- [38] X. Li, X. Chen, G. Goldfarb, E. Mateo, I. Kim, F. Yaman, and G. Li, "Electronic post-compensation of WDM transmission impairments using coherent detection and digital signal processing," *Opt. Express*, vol. 16, no. 2, pp. 880–888, Jan 2008.
- [39] N. J. Muga and A. N. Pinto, "Adaptive 3-D Stokes space-based polarization demultiplexing algorithm," *J. Lightw. Technol.*, vol. 32, no. 19, pp. 3290–3298, 2014.
- [40] Z. Yu, X. Yi, J. Zhang, M. Deng, H. Zhang, and K. Qiu, "Modified constant modulus algorithm with polarization demultiplexing in Stokes space in optical coherent receiver," *J. Lightw. Technol.*, vol. 31, no. 19, pp. 3203–3209, Oct 2013.
- [41] F. M. Gardner, "A BPSK/QPSK timing-error detector for sampled receivers," *IEEE Transactions on Communications*, vol. 34, no. 5, pp. 423–429, May 1986.
- [42] X. Zhou and X. Chen, "Parallel implementation of all-digital timing recovery for high-speed and real-time optical coherent receivers," *Opt. Express*, vol. 19, no. 10, pp. 9282–9295, May 2011.
- [43] R. M. Ferreira, J. D. Reis, S. B. Amado, A. Shahpari, F. P. Guiomar, J. R. F. Oliveira, A. N. Pinto, and A. L. Teixeira, "Performance and complexity of digital clock recovery for Nyquist UDWDM-PON in real-time," *IEEE Photon. Technol. Lett.*, Early Access 2015.
- [44] M. Morelli and U. Mengali, "Feedforward frequency estimation for PSK: A tutorial review," *European Transactions on Telecommunications*, vol. 9, no. 2, pp. 103–116, 1998.

- [45] A. Leven, N. Kaneda, U.-V. Koc, and Y.-K. Chen, "Frequency estimation in intradyne reception," *IEEE Photon. Technol. Lett.*, vol. 19, no. 6, pp. 366–368, 2007.
- [46] D. Rife and R. Boorstyn, "Single tone parameter estimation from discrete-time observations," *IEEE Transactions on Information Theory*, vol. 20, no. 5, pp. 591–598, Sep 1974.
- [47] Y. Liu, Y. Peng, S. Wang, and Z. Chen, "Improved FFT-based frequency offset estimation algorithm for coherent optical systems," *IEEE Photon. Technol. Lett.*, vol. 26, no. 6, pp. 613–616, March 2014.
- [48] M. Selmi, Y. Jaouen, and P. Ciblat, "Accurate digital frequency offset estimator for coherent PolMux QAM transmission systems," in *Proc. 35th European Conf. Optical Communication (ECOC)*, paper P3.08, 2009.
- [49] X. Zhou, X. Chen, and K. Long, "Wide-range frequency offset estimation algorithm for optical coherent systems using training sequence," *IEEE Photonics Technology Letters*, vol. 24, no. 1, pp. 82–84, Jan 2012.
- [50] L. M. Pessoa, H. M. Salgado, and I. Darwazeh, "Performance evaluation of phase estimation algorithms in equalized coherent optical systems," *IEEE Photon. Technol. Lett.*, vol. 21, no. 17, pp. 1181–1183, 2009.
- [51] E. Ip and J. M. Kahn, "Feedforward carrier recovery for coherent optical communications," *J. Lightw. Technol.*, vol. 25, no. 9, pp. 2675–2692, 2007.
- [52] A. Viterbi, "Nonlinear estimation of PSK-modulated carrier phase with application to burst digital transmission," *IEEE Trans. Inf. Theory*, vol. 29, no. 4, pp. 543–551, 1983.
- [53] F. Chang, "Forward error correction for 100 G transport networks," *IEEE Commun. Mag.*, vol. 48, no. 3, pp. S48–S55, 2010.
- [54] Z. Wang, "Super-FEC codes for 40/100 Gbps networking," *IEEE Commun. Lett.*, vol. 16, no. 12, pp. 2056–2059, December 2012.
- [55] D. Chang, F. Yu, Z. Xiao, N. Stojanovic, F. Hauske, Y. Cai, C. Xie, L. Li, X. Xu, and Q. Xiong, "LDPC convolutional codes using layered decoding algorithm for high speed coherent optical transmission," in *Proc. Optical Fiber Communication Conf. and Exposition (OFC)*, paper OW1H.4, 2012.
- [56] D. J. Malyon, "Digital fibre transmission using optical homodyne detection," *Electron. Lett.*, vol. 20, no. 7, pp. 281–283, 1984.
- [57] F. Favre, L. Jeunhomme, I. Joindot, M. Monerie, and J. C. Simon, "Progress towards heterodyne-type single-mode fiber communication systems," *IEEE J. Quantum Electron.*, vol. 17, no. 6, pp. 897–906, 1981.

- 
- [58] T. Okoshi, "Recent advances in coherent optical fiber communication systems," *J. Lightw. Technol.*, vol. 5, no. 1, pp. 44–52, 1987.
- [59] Y. Frignac, G. Charlet, W. Idler, R. Dischler, P. Tran, S. Lanne, S. Borne, C. Martinelli, G. Veith, A. Jourdan, J.-P. Hamaide, and S. Bigo, "Transmission of 256 wavelength-division and polarization-division-multiplexed channels at 42.7Gb/s (10.2Tb/s capacity) over 3×100km of TeraLight™ fiber," in *Proc. Optical Fiber Communication Conf. and Exposition (OFC)*, paper FC5, 2002.
- [60] R. A. Griffin and A. C. Carter, "Optical differential quadrature phase-shift key (oDQPSK) for high capacity optical transmission," in *Proc. Optical Fiber Communication Conf. and Exposition (OFC)*, paper WX6, 2002, pp. 367–368.
- [61] J. M. Kahn and K.-P. Ho, "Spectral efficiency limits and modulation/detection techniques for DWDM systems," *IEEE J. Sel. Topics Quantum Electron.*, vol. 10, no. 2, pp. 259–272, 2004.
- [62] C. Wree, N. Hecker-Denschlag, E. Gottwald, P. Krummrich, J. Leibrich, E.-D. Schmidt, B. Lankl, and W. Rosenkranz, "High spectral efficiency 1.6-b/s/Hz transmission (8×40 Gb/s with a 25-GHz grid) over 200-km SSMF using RZ-DQPSK and polarization multiplexing," *IEEE Photon. Technol. Lett.*, vol. 15, no. 9, pp. 1303–1305, 2003.
- [63] A. H. Gnauck, G. Charlet, P. Tran, P. J. Winzer, C. R. Doerr, J. C. Centanni, E. C. Burrows, T. Kawanishi, T. Sakamoto, and K. Higuma, "25.6-Tb/s WDM transmission of polarization-multiplexed RZ-DQPSK signals," *J. Lightw. Technol.*, vol. 26, no. 1, pp. 79–84, 2008.
- [64] T. Kataoka, S. Matsuoka, T. Matsuda, H. Maeda, N. Sakaida, T. Kubo, T. Kotanigawa, and T. Kawasaki, "Field transmission by using a commercially-ready 43 Gbit/s DWDM system employing RZ-DQPSK transponders in high PMD installed fiber," in *Proc. Optical Fiber Communication Conf. and Exposition (OFC)*, paper JThA45, 2007.
- [65] S. Tsukamoto, D.-S. Ly-Gagnon, K. Katoh, and K. Kikuchi, "Coherent demodulation of 40-Gbit/s polarization-multiplexed QPSK signals with 16-GHz spacing after 200-km transmission," in *Proc. Optical Fiber Communication Conf. and Exposition (OFC)*, paper PDP29, 2005.
- [66] S. J. Savory, G. Gavioli, R. I. Killey, and P. Bayvel, "Electronic compensation of chromatic dispersion using a digital coherent receiver," *Opt. Express*, vol. 15, no. 5, pp. 2120–2126, Mar 2007.
- [67] X. Zhou, J. Yu, M.-F. Huang, Y. Shao, T. Wang, P. Magill, M. Cvijetic, L. Nelson, M. Birk, G. Zhang, S. Ten, H. B. Matthew, and S. K. Mishra, "32Tb/s (320×114Gb/s) PDM-RZ-8QAM transmission over 580km of SMF-28 ultra-low-loss fiber," in *Proc. Optical Fiber Communication Conf. and Exposition (OFC)*, paper PDPB4, 2009.

- [68] A. H. Gnauck, P. J. Winzer, C. R. Doerr, and L. L. Buhl, "10×112-Gb/s PDM 16-QAM transmission over 630 km of fiber with 6.2-b/s/Hz spectral efficiency," in *Proc. Optical Fiber Communication Conf. and Exposition (OFC)*, paper PDPB8, 2009.
- [69] C. R. S. Fludger, T. Duthel, D. van den Borne, C. Schulien, E.-D. Schmidt, T. Wuth, J. Geyer, E. De Man, K. Giok-Djan, and H. de Waardt, "Coherent equalization and POLMUX-RZ-DQPSK for robust 100-GE transmission," *J. Lightw. Technol.*, vol. 26, no. 1, pp. 64–72, 2008.
- [70] G. Gavioli, E. Torrenco, G. Bosco, A. Carena, S. Savory, F. Forghieri, and P. Poggiolini, "Ultra-narrow-spacing 10-channel 1.12 Tb/s D-WDM long-haul transmission over uncompensated SMF and NZDSF," *IEEE Photon. Technol. Lett.*, vol. 22, no. 19, pp. 1419–1421, Oct 2010.
- [71] J.-X. Cai, Y. Cai, Y. Sun, C. R. Davidson, D. G. Foursa, A. Lucero, O. Sinkin, W. Patterson, A. Pilipetskii, G. Mohs, and N. S. Bergano, "112×112 Gb/s transmission over 9,360 km with channel spacing set to the baud rate (360% spectral efficiency)," in *Proc. 36th European Conf. Optical Communication (ECOC)*, paper PD2.1, 2010.
- [72] G. Zhang, L. E. Nelson, Y. Pan, M. Birk, C. Skolnick, C. Rasmussen, M. Givehchi, B. Mikkelsen, T. Scherer, T. Downs, and W. Keil, "3760km, 100G SSMF transmission over commercial terrestrial DWDM ROADM systems using SD-FEC," in *Proc. Optical Fiber Communication Conf. and Exposition (OFC)*, paper PDP5D, 2012.
- [73] G. Raybon, A. Adamiecki, P. Winzer, C. Xie, A. Konczykowska, F. Jorge, J.-Y. Dupuy, L. Buhl, S. Chandrashekhara, S. Draving, M. Grove, and K. Rush, "Single-carrier 400G interface and 10-channel WDM transmission over 4,800 km using all-ETDM 107-Gbaud PDM-QPSK," in *Proc. Optical Fiber Communication Conf. and Exposition (OFC)*, paper PDP5A.5, 2013.
- [74] N. Fontaine, "Spectrally-sliced coherent receivers for THz bandwidth optical communications," in *Proc. 39th European Conf. Optical Communication (ECOC)*, paper Mo.3.C.1, Sept 2013.
- [75] C. E. Shannon, "A mathematical theory of communication," *The Bell System Technical Journal*, vol. 27, no. 3, pp. 379–423, July 1948.
- [76] A. Nespola, S. Straullu, G. Bosco, A. Carena, J. Yanchao, P. Poggiolini, F. Forghieri, Y. Yamamoto, M. Hirano, T. Sasaki, J. Bauwelinck, and K. Verheyen, "1306-km 20x124.8-Gb/s PM-64QAM transmission over PSCF with net SEDP 11,300 (b.km)/s/Hz using 1.15 samp/symb DAC," *Opt. Express*, vol. 22, no. 2, pp. 1796–1805, Jan 2014.

- 
- [77] O. Bertran-Pardo, J. Renaudier, H. Mardoyan, P. Tran, R. Rios-Muller, A. Konczykowska, J. Dupuy, F. Jorge, M. Riet, B. Duval, J. Godin, S. Randel, G. Charlet, and S. Bigo, "Transmission of 50-GHz-spaced single-carrier channels at 516Gb/s over 600km," in *Proc. Optical Fiber Communication Conf. and Exposition (OFC)*, paper OTh4E.2, 2013.
- [78] X. Zhou, L. E. Nelson, P. Magill, R. Isaac, B. Zhu, D. W. Peckham, P. I. Borel, and K. Carlson, "High spectral efficiency 400 Gb/s transmission using PDM time-domain hybrid 32–64 QAM and training-assisted carrier recovery," *J. Lightw. Technol.*, vol. 31, no. 7, pp. 999–1005, 2013.
- [79] G. Bosco, V. Curri, A. Carena, P. Poggiolini, and F. Forghieri, "On the performance of Nyquist-WDM Terabit superchannels based on PM-BPSK, PM-QPSK, PM-8QAM or PM-16QAM subcarriers," *J. Lightw. Technol.*, vol. 29, no. 1, pp. 53–61, Jan 2011.
- [80] X. Liu, S. Chandrasekhar, B. Zhu, P. J. Winzer, A. H. Gnauck, and D. W. Peckham, "448-Gb/s reduced-guard-interval CO-OFDM transmission over 2000 km of ultra-large-area fiber and five 80-GHz-grid ROADMs," *J. Lightw. Technol.*, vol. 29, no. 4, pp. 483–490, 2011.
- [81] S. Chandrasekhar, X. Liu, B. Zhu, and D. W. Peckham, "Transmission of a 1.2-Tb/s 24-carrier no-guard-interval coherent OFDM superchannel over 7200-km of ultra-large-area fiber," in *Proc. 35th European Conf. Optical Communication (ECOC)*, paper PD2.6, 2009.
- [82] R. Dischler and F. Buchali, "Transmission of 1.2 Tb/s continuous waveband PDM-OFDM-FDM signal with spectral efficiency of 3.3 bit/s/Hz over 400 km of SSMF," in *Proc. Optical Fiber Communication Conf. and Exposition (OFC)*, paper PDPC2, March 2009.
- [83] R. Schmogrow, M. Winter, M. Meyer, D. Hillerkuss, S. Wolf, B. Baeuerle, A. Ludwig, B. Nebendahl, S. Ben-Ezra, J. Meyer, M. Dreschmann, M. Huebner, J. Becker, C. Koos, W. Freude, and J. Leuthold, "Real-time Nyquist pulse generation beyond 100 Gbit/s and its relation to OFDM," *Opt. Express*, vol. 20, no. 1, pp. 317–337, Jan 2012.
- [84] R. Schmogrow, R. Bouziane, M. Meyer, P. A. Milder, P. C. Schindler, R. I. Killey, P. Bayvel, C. Koos, W. Freude, and J. Leuthold, "Real-time OFDM or Nyquist pulse generation – which performs better with limited resources?" *Opt. Express*, vol. 20, no. 26, pp. B543–B551, Dec 2012.
- [85] G. Bosco, A. Carena, V. Curri, P. Poggiolini, and F. Forghieri, "Performance limits of Nyquist-WDM and CO-OFDM in high-speed PM-QPSK systems," *IEEE Photon. Technol. Lett.*, vol. 22, no. 15, pp. 1129–1131, 2010.

- [86] H. Zhang, J.-X. Cai, H. G. Batshon, M. Mazurczyk, O. Sinkin, D. Foursa, A. Pilipetskii, G. Mohs, and N. Bergano, “200 Gb/s and dual wavelength 400 Gb/s transmission over transpacific distance at 6 b/s/Hz spectral efficiency,” in *Proc. Optical Fiber Communication Conf. and Exposition (OFC)*, paper PDP5A.6, 2013.
- [87] A. Carena, V. Curri, G. Bosco, P. Poggiolini, and F. Forghieri, “Modeling of the impact of nonlinear propagation effects in uncompensated optical coherent transmission links,” *J. Lightw. Technol.*, vol. 30, no. 10, pp. 1524–1539, 2012.
- [88] G. Bosco, R. Cigliutti, A. Nespola, A. Carena, V. Curri, F. Forghieri, Y. Yamamoto, T. Sasaki, Y. Jiang, and P. Poggiolini, “Experimental investigation of nonlinear interference accumulation in uncompensated links,” *IEEE Photon. Technol. Lett.*, vol. 24, no. 14, pp. 1230–1232, 2012.
- [89] G. Bosco, P. Poggiolini, A. Carena, V. Curri, and F. Forghieri, “Analytical results on channel capacity in uncompensated optical links with coherent detection,” *Opt. Express*, vol. 19, no. 26, pp. B440–B451, Dec 2011.
- [90] P. Poggiolini, A. Carena, V. Curri, G. Bosco, and F. Forghieri, “Analytical modeling of nonlinear propagation in uncompensated optical transmission links,” *IEEE Photon. Technol. Lett.*, vol. 23, no. 11, pp. 742–744, 2011.
- [91] A. Nespola, S. Straullu, A. Carena, G. Bosco, R. Cigliutti, V. Curri, P. Poggiolini, M. Hirano, Y. Yamamoto, T. Sasaki, J. Bauwelinck, K. Verheyen, and F. Forghieri, “GN-model validation over seven fiber types in uncompensated PM-16QAM Nyquist-WDM links,” *IEEE Photon. Technol. Lett.*, vol. 26, no. 2, pp. 206–209, Jan 2014.
- [92] K. V. Peddanarappagari and M. Brandt-Pearce, “Volterra series transfer function of single-mode fibers,” *J. Lightw. Technol.*, vol. 15, no. 12, pp. 2232–2241, 1997.
- [93] D. Rafique, M. Mussolin, M. Forzati, J. Mårtensson, M. N. Chughtai, and A. D. Ellis, “Compensation of intra-channel nonlinear fibre impairments using simplified digital back-propagation algorithm,” *Opt. Express*, vol. 19, no. 10, pp. 9453–9460, May 2011.
- [94] F. P. Guiomar, J. D. Reis, A. L. Teixeira, and A. N. Pinto, “Mitigation of intra-channel nonlinearities using a frequency-domain Volterra series equalizer,” *Opt. Express*, vol. 20, no. 2, pp. 1360–1369, Jan 2012.
- [95] F. P. Guiomar and A. N. Pinto, “Simplified Volterra series nonlinear equalizer for polarization-multiplexed coherent optical systems,” *J. Lightw. Technol.*, vol. 31, no. 23, pp. 3879–3891, 2013.
- [96] F. P. Guiomar, S. B. Amado, A. Carena, G. Bosco, A. Nespola, A. L. Teixeira, and A. N. Pinto, “Fully-blind linear and nonlinear equalization for 100G PM-64QAM optical systems,” *J. Lightw. Technol.*, vol. 33, no. 7, pp. 1265–1274, 2015.

- [97] F. P. Guiomar, S. B. Amado, C. S. Martins, and A. N. Pinto, “Parallel split-step method for digital backpropagation,” in *Proc. Optical Fiber Communication Conf. and Exposition (OFC)*, paper Th2A.28, 2015.
- [98] A. Bononi, P. Serena, and N. Rossi, “Nonlinear signal-noise interactions in dispersion-managed links with various modulation formats,” *Optical Fiber Technology*, vol. 16, no. 2, pp. 73 – 85, 2010.
- [99] A. Carena, G. Bosco, V. Curri, Y. Jiang, P. Poggiolini, and F. Forghieri, “EGN model of non-linear fiber propagation,” *Opt. Express*, vol. 22, no. 13, pp. 16 335–16 362, 2014.
- [100] T. Fehenberger and N. Hanik, “Digital back-propagation of a superchannel: Achievable rates and adaption of the GN model,” in *Proc. 40th European Conference on Optical Communication (ECOC)*, paper We.3.3.6, 2014.
- [101] L. Beygi, N. V. Irukulapati, E. Agrell, P. Johannisson, M. Karlsson, H. Wymeersch, P. Serena, and A. Bononi, “On nonlinearly-induced noise in single-channel optical links with digital backpropagation,” *Opt. Express*, vol. 21, no. 22, pp. 26 376–26 386, Nov 2013.
- [102] J. P. Gordon and L. F. Mollenauer, “Phase noise in photonic communications systems using linear amplifiers,” *Opt. Lett.*, vol. 15, no. 23, pp. 1351–1353, Dec 1990.
- [103] K.-P. Ho and J. M. Kahn, “Electronic compensation technique to mitigate nonlinear phase noise,” *J. Lightw. Technol.*, vol. 22, no. 3, pp. 779–783, 2004.
- [104] A. P. T. Lau and J. M. Kahn, “Signal design and detection in presence of nonlinear phase noise,” *J. Lightw. Technol.*, vol. 25, no. 10, pp. 3008–3016, 2007.
- [105] Y. Gao, J. C. Cartledge, J. D. Downie, J. E. Hurley, D. Pikula, and S. S.-H. Yam, “Nonlinearity compensation of 224 Gb/s dual-polarization 16-QAM transmission over 2700 km,” *IEEE Photon. Technol. Lett.*, vol. 25, no. 1, pp. 14 –17, 2013.

## Chapter 2

# Signal Propagation in Single-Mode Optical Fibers

Being an electromagnetic phenomena, the propagation of optical signals in single-mode fibers can be analytically modelled by the Maxwell's equations [1], a set of partial differential equations composed of the Gauss's laws for electricity and magnetism, Faraday's law of induction and Ampère's circuital law. In differential form, Maxwell's equations can be written as,

$$\nabla \cdot \mathbf{D} = \rho, \quad (2.1)$$

$$\nabla \cdot \mathbf{B} = 0, \quad (2.2)$$

$$\nabla \times \mathbf{E} = -\frac{\partial \mathbf{B}}{\partial \tau}, \quad (2.3)$$

$$\nabla \times \mathbf{H} = \mathbf{J} + \frac{\partial \mathbf{D}}{\partial \tau} \quad (2.4)$$

where  $\mathbf{E}$ ,  $\mathbf{H}$ ,  $\mathbf{D}$ ,  $\mathbf{B}$  and  $\mathbf{J}$  are vectors representing the electric field, magnetic field, electric flux density, magnetic flux density and current density, respectively, and  $\rho$  represents the charge density. Due to the absence of free charges in optical fibers, both the current density and charge density are null, yielding  $\mathbf{J} = 0$  and  $\rho = 0$ . Starting from the Maxwell's equations and employing a slowly varying optical field envelope approximation, the pulse propagation in nonlinear dispersive media can be modelled by the nonlinear Schrödinger equation (NLSE) [2–4]. The NLSE is of particular interest for the modelling and analysis of optical transmission systems, as it describes the spatial and temporal evolution of an incident optical field during its propagation in fiber. In the framework of this thesis, the NLSE acquires a particular relevance, since it provides the underlying physical model required for the design of the proposed nonlinear equalization techniques.

The organization of this chapter is as follows. The scalar NLSE, describing the propagation of single-polarization signals, is introduced in section 2.1, providing an independent treatment of linear and nonlinear phenomena due to group velocity dispersion and the Kerr-induced nonlinearities. The analytical formulation is then extended to dual-polarization transmission in section 2.2, considering the coupled NLSE, which accounts for the fiber birefringence and first-order PMD. The Manakov equation

is also introduced as a computationally efficient approximation for the coupled NLSE, which will be used throughout this thesis as the physical equalization model for dual-polarization optical systems. Building from the analytical models, a macroscopic overview of the most relevant signal propagation regimes is then briefly addressed in section 2.3. Finally, the numerical implementation of the scalar NLSE is addressed in section 2.4, using the well-known split-step Fourier method (SSFM) and the VSTF proposed in [5].

## 2.1 Scalar Nonlinear Schrödinger Equation

In the absence of polarization effects and neglecting the higher-order nonlinear terms such as self-steepening and Raman scattering, signal propagation in single-mode optical fibers can be analytically described by the following partial differential equation [3],

$$\frac{\partial A(\tau, z)}{\partial z} = -\frac{\alpha}{2}A(\tau, z) - \sum_{k=1} \frac{i^{k-1}}{k!} \beta_k \frac{\partial^k A(\tau, z)}{\partial \tau^k} + i\gamma |A(\tau, z)|^2 A(\tau, z), \quad (2.5)$$

where  $A(\tau, z)$  is the slowly varying complex field envelope at time  $\tau$  and position  $z$ . The fiber attenuation is represented by  $\alpha$ . The imaginary unit is represented by  $i$  and  $\gamma$  is the nonlinear coefficient. The  $\beta_k$  coefficients are derivatives of the linear propagation constant,  $\beta(\omega)$ ,

$$\beta_k = \left. \frac{d^k \beta(\Omega)}{d\Omega^k} \right|_{\Omega=\Omega_0}, \quad (2.6)$$

resulting from its Taylor series expansion around the central angular frequency,  $\omega_0$ , usually truncated to the third-order [6],

$$\beta(\Omega) = \beta_0 + \beta_1\omega + \frac{1}{2}\beta_2\omega^2 + \frac{1}{6}\beta_3\omega^3 + \dots \quad (2.7)$$

where  $\Omega$  is the angular frequency,  $\Omega_0 = \frac{2\pi c}{\lambda_0}$  is the central angular frequency and  $\omega = \Omega - \Omega_0$  is the baseband angular frequency associated with the complex field envelope,  $A(t, z)$ . The speed of light and the central wavelength in vacuum are represented by  $c$  and  $\lambda_0$ , respectively. The  $\beta_0$  coefficient represents the wave-number,  $\beta_1 = 1/v_g$  accounts for the pulse group velocity,  $v_g$ ,  $\beta_2$  is the group velocity dispersion (GVD) parameter and  $\beta_3$  is the third-order dispersion coefficient.

For the convenience of notation and numerical implementation, equation (2.5) can be rewritten in a reference time-frame moving at the pulse group velocity [3],

$$\frac{\partial A(t, z)}{\partial z} = -\frac{\alpha}{2}A(t, z) - \sum_{k=2} \frac{i^{k-1}}{k!} \beta_k \frac{\partial^k A(t, z)}{\partial t^k} + i\gamma |A(t, z)|^2 A(t, z), \quad (2.8)$$

where  $t = \tau - z/v_g$  is the so-called retarded time-frame. In addition, considering state-of-the-art optical transmission systems, where the typical pulse width is on the order of tens of picoseconds and the carrier wavelength is far away from the zero-dispersion

## 2.1. Scalar Nonlinear Schrödinger Equation

---

wavelength, the  $\beta_k$  terms in (2.8) with  $k > 2$  provide a negligible contribution and thus can be dropped,

$$\frac{\partial A(t, z)}{\partial z} = -\frac{\alpha}{2}A(t, z) - i\frac{\beta_2}{2}\frac{\partial^2 A(t, z)}{\partial t^2} + i\gamma |A(t, z)|^2 A(t, z), \quad (2.9)$$

yielding the scalar NLSE formulation that will be considered throughout this thesis. Alternatively, the NLSE can also be formulated in the frequency domain [7], yielding

$$\begin{aligned} \frac{\partial \tilde{A}(\omega, z)}{\partial z} = & -\frac{\alpha}{2}\tilde{A}(\omega, z) + i\frac{\beta_2}{2}\omega^2\tilde{A}(\omega, z) \\ & + \frac{i\gamma}{4\pi^2} \iint \tilde{A}(\omega_1, z)\tilde{A}^*(\omega_2, z)\tilde{A}(\omega - \omega_1 + \omega_2, z) d\omega_1 d\omega_2, \end{aligned} \quad (2.10)$$

where  $(\cdot)^*$  represents the complex conjugate operation and  $\tilde{A}(\omega, z)$  is the Fourier transform of  $A(t, z)$ , defined as<sup>1</sup>

$$\tilde{A}(\omega, z) = \mathcal{F}\{A(t, z)\} = \int_{-\infty}^{\infty} A(t, z) \exp(i\omega t) dt, \quad (2.11)$$

where  $\mathcal{F}\{\cdot\}$  represents the Fourier transform of  $(\cdot)$ . The corresponding inverse Fourier transform is then given by<sup>2</sup>

$$A(t, z) = \mathcal{F}^{-1}\{\tilde{A}(\omega, z)\} = \frac{1}{2\pi} \int_{-\infty}^{\infty} \tilde{A}(\omega, z) \exp(-i\omega t) d\omega, \quad (2.12)$$

where  $\mathcal{F}^{-1}\{\cdot\}$  represents the inverse Fourier transform of  $(\cdot)$ . A detailed derivation of expression (2.10) is presented in Appendix A.

### 2.1.1 Group velocity dispersion

Isolating the effect of GVD, by neglecting the attenuation and nonlinear terms in (2.10), yields the following first-order linear ordinary differential equation (ODE),

$$\frac{\partial \tilde{A}(\omega, z)}{\partial z} - i\frac{\beta_2}{2}\omega^2\tilde{A}(\omega, z) = 0, \quad (2.13)$$

which can be easily solved to obtain a simple frequency domain transfer function,

$$\frac{\tilde{A}(\omega, z)}{\tilde{A}(\omega, 0)} = \exp\left(i\frac{\beta_2}{2}\omega^2 z\right), \quad (2.14)$$

---

<sup>1</sup>The Fourier transform definition adopted in this thesis is in accordance with the *physicists* convention, as utilized in [3] to derive the scalar NLSE.

<sup>2</sup>Note the presence of  $1/(2\pi)$  factor in the inverse Fourier transform definition, which is responsible for the  $1/(4\pi^2)$  term in the frequency domain NLSE of expression (2.10). For the numerical implementation, care must be taken in order to match the utilized Fourier transform definition with the underlying analytical model.

evidencing that the GVD induces a pure phase rotation in the frequency domain, with no transference of energy between frequencies, i.e.  $|A(\omega, z)|^2 = |A(\omega, 0)|^2$ , confirming the linearity of the GVD effect. Taking the inverse Fourier transform of (2.14), one obtains

$$A(t, z) = \int_{-\infty}^{\infty} A(\tau, 0) h_{\text{GVD}}(t - \tau, z) d\tau, \quad (2.15)$$

where  $h_{\text{GVD}}(t, z)$  is the linear impulse response of the fiber up to coordinate  $z$ , given by

$$h_{\text{GVD}}(t, z) = \sqrt{\frac{i}{2\pi\beta_2 z}} \exp\left(-i\frac{t^2}{2\beta_2 z}\right). \quad (2.16)$$

Instead of using the  $\beta_2$  coefficient, it is common to describe the GVD characteristic of a fiber in terms of the dispersion parameter,  $D$ ,

$$D = -\frac{2\pi c}{\lambda^2} \beta_2, \quad (2.17)$$

which is usually expressed in [ps/(nm·km)]. In addition, the effect of GVD in optical transmission systems can also be quantified by the dispersion length,  $L_D$ , which indicates the length scale for which GVD plays an important role in signal propagation,

$$L_D = \frac{T_0^2}{|\beta_2|}, \quad (2.18)$$

where  $T_0$  is the symbol period. For an input Gaussian pulse,  $L_D$  corresponds to the propagation length after which the half-width of the pulse intensity is doubled [3].

### 2.1.2 Kerr nonlinearities

Neglecting the GVD effect in the time domain NLSE, equation (2.9), the following linear ODE is obtained,

$$\frac{\partial A(t, z)}{\partial z} + \frac{\alpha}{2} A(t, z) - i\gamma \exp(-\alpha z) |A(t, 0)|^2 A(t, z) = 0, \quad (2.19)$$

where  $|A(t, z)|^2 = \exp(-\alpha z) |A(t, 0)|^2$ . Note that the Kerr effect only induces a phase change on the signal. Analogously to (2.13), equation (2.19) can be easily solved in time domain, yielding

$$A(t, z) = A(t, 0) \exp\left(-\frac{\alpha}{2} z + i\gamma |A(t, 0)|^2 L_{\text{eff}}(z)\right) \quad (2.20)$$

where  $L_{\text{eff}}(z)$  is the effective fiber length up to coordinate  $z$ , given by

$$L_{\text{eff}}(z) = \frac{1 - \exp(-\alpha z)}{\alpha}, \quad (2.21)$$

which provides an indication of the propagation distance (measured from the transmission point, where the power is highest) over which the Kerr nonlinear effect is more relevant.

## 2.1. Scalar Nonlinear Schrödinger Equation

---

**Table 2.1:** Time/frequency comparative analysis of the GVD and SPM effects.

	GVD	SPM
No transference of energy in	<i>frequency domain</i>	<i>time domain</i>
Applies a phase rotation in	<i>frequency domain</i>	<i>time domain</i>
Causes pulse broadening in	<i>time domain</i>	<i>frequency domain</i>

---

It results from (2.21) that  $L_{\text{eff}} \simeq 1/\alpha$  for  $z \gg 1/\alpha$ , indicating that the nonlinear effect is negligible after  $z \gg 1/\alpha$ , due to the strongly attenuated optical power. The signal propagation solution of equation (2.20) is memoryless, i.e. the output signal at a given time  $t$  does not depend on the input signal at other past or future time instants, exposing the instantaneous characteristic of the Kerr nonlinearity. Additionally, equation (2.20) shows that the isolated effect of nonlinearity does not affect the shape of a propagating optical pulse. Instead, it causes a pure nonlinear phase rotation in time domain,  $\phi_{\text{NL}}(t, z) = \gamma |A(t, 0)|^2 L_{\text{eff}}(z)$ , which depends on the optical power profile of the pulse. Due to the imposed nonlinear phase rotation, this effect is known as SPM [3]. Neglecting the effect of attenuation and GVD in the NLSE of equation (2.10), the following equation enables to analyze the behavior of SPM in frequency domain,

$$\frac{\partial \tilde{A}(\omega, z)}{\partial z} = \frac{i\gamma}{4\pi^2} \iint \tilde{A}(\omega_1, z) \tilde{A}^*(\omega_2, z) \tilde{A}(\omega - \omega_1 + \omega_2, z) d\omega_1 d\omega_2, \quad (2.22)$$

where the double integral puts in evidence the effect of SPM-induced spectral broadening. This time and frequency domain analysis confirms the time/frequency duality of the GVD and SPM effects, which is summarized in Table 2.1. Nevertheless, due to the frequency beating inside the double integral of equation (2.22), SPM is actually a much more complex effect than GVD. Depending on the indexes of the mixing triplet  $\tilde{A}(\omega_1, z) \tilde{A}(\omega_2, z) \tilde{A}(\omega - \omega_1 + \omega_2, z)$ , the SPM effect can be sub-categorized into intra-channel self-phase modulation (iSPM), intra-channel cross-phase modulation (iXPM) and intra-channel four-wave mixing (iFWM) [8, 9]. A thorough analysis of these intra-channel nonlinear effects will be provided in chapter 4.

The nonlinear coefficient  $\gamma$  is obtained from the nonlinear refractive index,  $n_2$ , of the fiber,

$$\gamma = \frac{n_2 \Omega_0}{c A_{\text{eff}}}, \quad (2.23)$$

where  $A_{\text{eff}}$  is the effective core area, typically varying in the range of 20-200  $\mu\text{m}^2$ , depending on the fiber design [3]. Considering the 1550 nm region and for a typical value of  $n_2 \approx 2.6 \times 10^{-20} \text{ m}^2/\text{W}$ , the nonlinear parameter  $\gamma$  takes values on the range of 0.5-5  $\text{W}^{-1}\text{km}^{-1}$ .

Analogously to the dispersion length, a nonlinear length,  $L_{\text{NL}}$ , can be defined as

$$L_{\text{NL}} = \frac{1}{\gamma P_0}, \quad (2.24)$$

where  $P_0$  is the peak optical power of the propagated signal. Substituting  $L_{\text{eff}}(z)$  by  $L_{\text{NL}}$  in equation (2.20), it results that the nonlinear length corresponds to the effective length required to impose a nonlinear phase rotation of 1 rad at the pulse peak power.

## 2.2 Coupled Nonlinear Schrödinger Equation

The analytical formulation for the scalar NLSE of equation (2.9) makes the assumption that the optical field is polarized across a single polarization axis, which is maintained along propagation in fiber. However, even single-mode optical fibers actually support two orthogonally-polarized propagation modes with almost identical spatial distribution, to which we can associate two different propagation constants,  $\beta_s$  and  $\beta_f$ , corresponding to the slow and fast polarization axes, respectively. This difference,  $\Delta\beta(\omega) = \beta_s(\omega) - \beta_f(\omega)$ , is due to fiber birefringence and can fluctuate both in time (usually slowly compared to the symbol period) and along the fiber length, depending on intrinsic factors, such as fiber manufacturing, and external factors, such as mechanical stress and environment temperature. Birefringence is usually treated as a stochastic phenomenon and its variation along  $z$  causes random mode coupling between the two polarization components.

In order to account for the effect of fiber birefringence and associated polarization-dependent effects, the scalar NLSE can be rewritten in vectorial form [2],

$$\frac{\partial \mathbf{A}}{\partial z} = -\frac{\alpha}{2} \mathbf{A} - \Theta(z) \left[ \frac{\Delta\beta_0}{2} \mathbf{A} - \frac{\Delta\beta_1}{2} \frac{\partial \mathbf{A}}{\partial t} \right] - i \frac{\beta_2}{2} \frac{\partial^2 \mathbf{A}}{\partial t^2} + i\gamma \left[ |\mathbf{A}|^2 \mathbf{A} - \frac{1}{3} (\mathbf{A}^\dagger \sigma_3 \mathbf{A}) \sigma_3 \mathbf{A} \right], \quad (2.25)$$

where  $\mathbf{A} = [A_x(t, z) \ A_y(t, z)]^T$  is the Jones vector, whose components are the optical field envelopes polarized along the  $x$  and  $y$  states of polarization and  $(\cdot)^\dagger$  represents the transpose conjugate of  $(\cdot)$ . The  $\Delta\beta_k$  coefficients are derivatives of  $\Delta\beta(\omega)$ , expanded in a Taylor series expansion similarly to (2.7), here truncated to first-order for simplicity. The polarization mode-coupling is introduced by  $\Theta(z)$ ,

$$\Theta(z) = \sigma_1 \cos(\theta(z)) + \sigma_2 \sin(\theta(z)), \quad (2.26)$$

where  $\theta(z)$  introduces the random rotation of the birefringence axes in  $z$  and  $\sigma_1, \sigma_2$  and  $\sigma_3$  are the Pauli spin matrices,

$$\sigma_1 = \begin{bmatrix} 1 & 0 \\ 0 & -1 \end{bmatrix}, \quad \sigma_2 = \begin{bmatrix} 0 & 1 \\ 1 & 0 \end{bmatrix}, \quad \sigma_3 = \begin{bmatrix} 0 & -i \\ i & 0 \end{bmatrix}. \quad (2.27)$$

Since equation (2.25) can be written as a system of two coupled equations, corresponding to the principal states of polarization, it is commonly designated as coupled nonlinear Schrödinger equation (CNLSE). Relatively to the scalar NLSE of equation (2.9), the coupled NLSE introduces two additional linear terms associated with  $\Delta\beta_{0,1}$ . These terms account for the polarization-dependency of the propagation constant in birefringent fibers. The  $\Delta\beta_0$  term in (2.25) is responsible for the rotation of the signal state of polarization, whereas the  $\Delta\beta_1$  term is responsible for the first-order PMD effect [10]. In time domain, PMD manifests itself in the form of differential group delay (DGD), which represents a time delay,  $\Delta\tau$ , between the two polarization components. For long fiber distances,  $L$ , compared with the PMD correlation length, the root mean square value of  $\Delta\tau$  is given by [11],

$$\Delta\tau_{\text{rms}} = D_p \sqrt{L}, \quad (2.28)$$

## 2.2. Coupled Nonlinear Schrödinger Equation

---

where  $D_p$  is the PMD parameter, usually provided by the fiber manufacturer and whose value for modern fibers is typically  $D_p < 0.1$  ps/ $\sqrt{\text{km}}$ . The  $D_p$  is related with the  $\Delta\beta_1$  term as [11],

$$D_p = \Delta\beta_1 \sqrt{2L_C}, \quad (2.29)$$

where  $L_C$  is the correlation length of the fiber, which represents the length scale on which the orientation of birefringence axes changes randomly [2]. Alternatively, the effect of fiber birefringence can also be quantified by the beat length [12],  $L_B$ ,

$$L_B = \frac{2\pi}{\Delta\beta_0}, \quad (2.30)$$

which defines the fiber length that an initially linear-polarized signal must travel to return to the same linear state of polarization. In currently installed fibers this value is typically of the order of tens of meters [12].

### 2.2.1 Manakov equation

The CNLSE formulation of equation (2.25) poses significant challenges for the calculation of numerical solutions, namely by using the SSFM. As we are going to discuss in more detail in section 2.4.1, the application of the SSFM to equation (2.25) requires very small integration steps in order to capture the effects caused by randomly varying birefringence. This is due to the typically very small correlation length,  $L_C$ , when compared to the nonlinear length,  $L_{\text{NL}}$ , which causes very fast and random interactions between polarization and nonlinear effects [2]. Fortunately, it has been observed that the  $L_C \ll L_{\text{NL}}$  property can also be used to simplify the CNLSE formulation with negligible approximation error. The approach is to consider that the birefringence interaction with Kerr nonlinearities can be accurately approximated by an ensemble average of the nonlinear operator over the entire Poincaré sphere, leading to the Manakov-PMD equation [13],

$$\frac{\partial \mathbf{A}}{\partial z} = -\frac{\alpha}{2} \mathbf{A} - \Theta(z) \left[ \frac{\Delta\beta_0}{2} \mathbf{A} - \frac{\Delta\beta_1}{2} \frac{\partial \mathbf{A}}{\partial t} \right] - i \frac{\beta_2}{2} \frac{\partial^2 \mathbf{A}}{\partial t^2} + i \frac{8}{9} \gamma |\mathbf{A}|^2 \mathbf{A}, \quad (2.31)$$

in which the  $\frac{1}{3}(\mathbf{A}^\dagger \sigma_3 \mathbf{A}) \sigma_3 \mathbf{A}$  term of equation (2.25) is averaged out to  $\frac{1}{9} |\mathbf{A}|^2 \mathbf{A}$ , yielding the 8/9 factor affecting the  $\gamma$  parameter [14]. Equation (2.31) also neglects the effect of nonlinear PMD, which is only significant when  $L_C$  is comparable with  $L_{\text{NL}}$ , and therefore does not apply to commercial communication systems. Note that although the effect of birefringence is still present in the Manakov-PMD equation, the nonlinear operator now only depends on the optical intensity and not on the state of polarization, and therefore the numerical integration of equation (2.31) can be performed in steps larger than  $L_C$ .

Finally, when the effect of PMD can be neglected, equation (2.31) can be further simplified,

$$\frac{\partial \mathbf{A}}{\partial z} = -\frac{\alpha}{2} \mathbf{A} - i \frac{\beta_2}{2} \frac{\partial^2 \mathbf{A}}{\partial t^2} + i \frac{8}{9} \gamma |\mathbf{A}|^2 \mathbf{A}, \quad (2.32)$$

yielding the Manakov equation, which will be of particular interest for the design of digital nonlinear equalizers in chapters 3, 4 and 5.

## 2.3 Propagation Regimes

Neglecting the effect of PMD and using the dispersion and nonlinear lengths defined in expressions (2.18) and (2.24) the macroscopic behavior of signal propagation can be classified into different categories.

Firstly, consider that the propagation length,  $L$ , is such that  $L \ll L_D$  and  $L \ll L_{NL}$ . In this case, the effect of both GVD and SPM are very weak and do not play a significant role in signal propagation. In this regime, it can be considered that the signal is propagated in a distortion-free medium, being only affected by the fiber attenuation. Although this is the ideal regime for communication systems, in practical scenarios with typical fiber parameters this regime can only be considered for short-reach ( $< 100$  km) optical links associated with low symbol-rate ( $< 10$  Gbaud) signal transmission, such as for passive optical networks, where signal quality is therefore primarily assessed through the optical power budget.

In turn, when  $L_D \ll L_{NL}$  and  $L \sim L_D$ , the SPM contribution can be considered negligible and the NLSE becomes dominated by the attenuation and GVD terms, originating signal propagation in the linear regime. This propagation regime requires the product  $\gamma P_0$  to be low enough so that SPM can be neglected. In a practical scenario however, the  $\gamma$  coefficient is fixed to the installed fiber and the input optical power must be sufficiently high to ensure a given required OSNR. With the demand for increased spectral efficiency, higher-order modulation is currently being adopted, requiring enhanced OSNR and consequently increased optical power. In addition, it has been proved that the impact of nonlinearities accumulates super-linearly in optical links composed of multiple fiber spans [15]. Therefore, signal propagation in the linear regime may be difficult to achieve in long-haul and high-speed optical transmission systems.

On the opposite end, when  $L_{NL} \ll L_D$  and  $L \sim L_{NL}$  the GVD term in the NLSE becomes of negligible importance and the signal is propagated in the nonlinear regime, under the dominance of the SPM effect. Considering that both  $\beta_2$  and  $\gamma$  are fiber specific parameters, signal propagation in the nonlinear regime requires high transmitted input power,  $P_0$ , and/or large symbol period,  $T_0$ . However, in state-of-the-art high-speed optical transmission systems, where the symbol period is of the order of tens of picoseconds, an optical power of  $\sim 1$  W would be required for propagation in the nonlinear regime. Such a high optical power is not feasible in commercial multi-channel optical transmission systems as (among other engineering challenges) the fiber fuse effect would be very likely to happen.

Given the current commercially available optical fibers and network design requirements in terms of bit-rate and OSNR, signal propagation in long-haul and high-speed optical communication systems is most likely to occur in regime where  $L$ ,  $L_D$  and  $L_{NL}$  are comparable, implying that both linear and nonlinear effects play relevant roles in the NLSE. In such a regime, the separate treatment of linear and nonlinear NLSE operators as described in equations (2.14) and (2.20) does not hold anymore, and signal propagation must take into account the interplay between linear and nonlinear phenomena. In general terms, the effects of GVD and SPM act simultaneously, in such a way that the temporal broadening caused by GVD affects the spectral broadening caused

by SPM. Conversely, the newly SPM-generated frequency components instantaneously affect the GVD-induced temporal broadening.

## 2.4 Numerical Methods for Approximate Solutions

Except for the cases where either the linear or nonlinear operators can be neglected, the NLSE is a nonlinear partial differential equation, whose analytical solution is only possible under some specific circumstances, for which the inverse scattering method is applicable, as in the case of soliton propagation [6]. However, in most common cases of practical interest, solving the NLSE in its scalar or vectorial form requires the use of numerical methods for an approximate solution. In this section, we will analyze the SSFM and the VSTF methods for solving the scalar NLSE.

### 2.4.1 Split-step Fourier method

The SSFM has been widely utilized to solve nonlinear wave equations. Due to its enhanced stability and computational efficiency over most finite difference methods, the SSFM has been extensively used to solve the NLSE, with the purpose of analyzing the physics of signal propagation in fiber [16]. To initiate our analysis of the SSFM it is useful to firstly rewrite the scalar NLSE of equation (2.9) as,

$$\frac{\partial A(t, z)}{\partial z} = \left( \hat{\mathcal{D}}(t) + \hat{\mathcal{N}}(A(t, z)) \right) A(t, z), \quad (2.33)$$

where  $\hat{\mathcal{D}}$  is the linear operator given by,

$$\hat{\mathcal{D}}(t) = -\frac{\alpha}{2} - i\frac{\beta_2}{2} \frac{\partial^2}{\partial t^2}, \quad (2.34)$$

and  $\hat{\mathcal{N}}$  is the nonlinear operator given by,

$$\hat{\mathcal{N}}(A(t, z)) = i\gamma |A(t, z)|^2. \quad (2.35)$$

The SSFM is based on a pseudo-spectral approach where the linear and nonlinear operators in the NLSE are considered to act independently, being separately evaluated over a certain spatial-step,  $h$ . To better understand this procedure, notice that an exact solution for equation (2.33) (neglecting the  $z$  dependence of  $\hat{\mathcal{N}}$ ) can be written as,

$$A(t, z + h) = \exp \left( h \left( \hat{\mathcal{D}}(t) + \hat{\mathcal{N}}(A(t, z)) \right) \right) A(t, z), \quad (2.36)$$

where  $h$  represents a given increment on the spatial coordinate. However, the formal solution presented on (2.36) has no interest from a practical point of view, since the  $\hat{\mathcal{D}}$  and  $\hat{\mathcal{N}}$  operators cannot be applied at the same time within the exponential. This is underlying motivation for the SSFM, which ignores the noncommutative property of  $\hat{\mathcal{D}}$

and  $\hat{\mathcal{N}}$  and splits the exponential in equation (2.36) into two separate terms. The exact solution of equation (2.36) is then transformed into an approximate solution,

$$A(t, z + h) \approx \exp\left(h\hat{\mathcal{D}}(t)\right) \exp\left(h\hat{\mathcal{N}}(A(t, z))\right) A(t, z), \quad (2.37)$$

where the linear and nonlinear operators are considered to act independently, enabling to obtain an estimative of the optical field at a given point  $z + h$  at the expense of the optical field at point  $z$ . Nevertheless, this approximation has an associated error due to the commutation of the  $\hat{\mathcal{D}}$  and  $\hat{\mathcal{N}}$  operators. This numerical error can be quantified by the Baker-Campbell-Hausdorff formula [3],

$$\exp(\hat{a}) \exp(\hat{b}) = \exp\left(\hat{a} + \hat{b} + \frac{1}{2} [\hat{a}, \hat{b}] + \frac{1}{12} [\hat{a} - \hat{b}, [\hat{a}, \hat{b}]] + \dots\right), \quad (2.38)$$

where  $\hat{a}$  and  $\hat{b}$  are some noncommutative operators and  $[\hat{a}, \hat{b}] = \hat{a}\hat{b} - \hat{b}\hat{a}$ . Substituting the  $\hat{a}$  and  $\hat{b}$  operators by  $h\hat{\mathcal{D}}$  and  $h\hat{\mathcal{N}}$  into expression (2.38) yields

$$\exp\left(h\hat{\mathcal{D}}\right) \exp\left(h\hat{\mathcal{N}}\right) = \exp\left(h\hat{\mathcal{D}} + h\hat{\mathcal{N}} + \frac{1}{2}h^2 [\hat{\mathcal{D}}, \hat{\mathcal{N}}] + \frac{1}{12}h^3 [\hat{\mathcal{D}} - \hat{\mathcal{N}}, [\hat{\mathcal{D}}, \hat{\mathcal{N}}]] + \dots\right), \quad (2.39)$$

where the dominant error term is given by  $\frac{1}{2}h^2 [\hat{\mathcal{D}}, \hat{\mathcal{N}}]$ . From the above expression, it becomes apparent that, in the limit of an infinitesimal  $h$ , the approximation error vanishes and the estimative given by equation (2.37) converges to the exact solution of the NLSE. This observation clearly reveals the importance of the  $h$  parameter to control the error of the SSFM.

A key advantage of this method, which allows it to attain a fast solution convergence, lies on the application of the linear parameter in the Fourier domain. Following equation (2.10), the frequency domain  $\hat{\mathcal{D}}$  operator reads as,

$$\hat{\mathcal{D}}(\omega) = -\frac{\alpha}{2} + i\frac{\beta_2}{2}\omega^2. \quad (2.40)$$

The frequency domain linear SSFM step,  $\hat{\mathcal{D}}_{\text{SSFM}}$ , is then be defined as,

$$\begin{aligned} \hat{\mathcal{D}}_{\text{SSFM}}[A(t, z)] &= \mathcal{F}^{-1}\left\{\exp\left(h\hat{\mathcal{D}}(\omega)\right) \mathcal{F}\{A(t, z)\}\right\} \\ &= \mathcal{F}^{-1}\left\{\exp\left(-\frac{\alpha}{2}h + i\frac{\beta_2}{2}\omega^2h\right) \mathcal{F}\{A(t, z)\}\right\}. \end{aligned} \quad (2.41)$$

In turn, the nonlinear SSFM step,  $\hat{\mathcal{N}}_{\text{SSFM}}$ , can be directly evaluated in time domain as,

$$\begin{aligned} \hat{\mathcal{N}}_{\text{SSFM}}[A(t, z)] &= \exp\left(h\hat{\mathcal{N}}(A(t, z))\right)A(t, z) \\ &= \exp\left(i\gamma h |A(t, z)|^2\right)A(t, z). \end{aligned} \quad (2.42)$$

The input optical field at a given spatial coordinate,  $A(t, z)$ , is then propagated over the fiber in spatial steps of  $h$ , iteratively applying the linear and nonlinear steps as,

$$A(t, z + nh) = \hat{\mathcal{D}}_{\text{SSFM}} \left[ \hat{\mathcal{N}}_{\text{SSFM}} \left[ A(t, z + (n-1)h) \right] \right], \quad (2.43)$$

where  $n$  represents the  $n$ -th SSFM step. Note that the order by which the linear and nonlinear steps are applied is interchangeable. However, for the purpose of signal propagation in the forward direction, the nonlinear step is typically applied in the first place, based on the heuristic that the optical power is highest at the beginning of each fiber span. The algorithm described by expression (2.43) is designated as the asymmetric and non-iterative SSFM, due to the asymmetric evaluation of the  $\hat{\mathcal{D}}_{\text{SSFM}}$  and  $\hat{\mathcal{N}}_{\text{SSFM}}$  steps and the non-iterative implementation of the nonlinear step. Symmetric and iterative methods [17] as well as other higher-order solutions [18] and advanced step-size criteria [16] can also be adopted in order to minimize the overall numerical errors. However, the performance advantage of such approaches is often counterbalanced by additional numerical complexity. In order to avoid excessive memory consumption and aliasing phenomena due to fast Fourier transform (FFT) block processing, fully time domain implementations have also been developed, using digital FIR and infinite impulse response (IIR) filters to implement the  $\hat{\mathcal{D}}_{\text{SSFM}}$  step [19–21].

### 2.4.2 Volterra series transfer function

Alternatively to the SSFM algorithm, a frequency domain Volterra series approach has been originally proposed in [5], enabling to numerically solve the scalar NLSE without the need for sub-span iterations. In the following, we review the analytical foundations of the third-order VSTF, providing a detailed derivation of its single-span and multi-span analytical models and addressing the output modification proposed in [22] to extend its applicability for higher optical powers.

#### Single-Span Analytical Model

To initiate the analytical derivation of the single-span VSTF let us first rewrite the frequency domain NLSE of equation (2.10) in the following general form,

$$\frac{\partial \tilde{A}(\omega, z)}{\partial z} = \tilde{A}(\omega, z)G_1(\omega) + \iint G_3 \tilde{A}(\omega_1, z) \tilde{A}^*(\omega_2, z) \tilde{A}(\omega - \omega_1 + \omega_2, z) d\omega_1 d\omega_2, \quad (2.44)$$

where

$$G_1(\omega) = -\frac{\alpha}{2} + i\frac{\beta_2}{2}\omega^2, \quad (2.45)$$

and

$$G_3 = \frac{i\gamma}{4\pi^2}, \quad (2.46)$$

We now want to redescribe expression (2.44) by an input-output relationship in the form of a Volterra series expansion in the frequency domain, where the output field

spectrum,  $\tilde{Y}(\omega)$ , is obtained from the input field spectrum,  $\tilde{X}(\omega)$ , as

$$\begin{aligned} \tilde{Y}(\omega, z) = \sum_{n=1}^{\infty} \int \cdots \int H_n(\omega, \omega_1, \dots, \omega_{n-1}) \\ \times \tilde{X}(\omega_1) \dots \tilde{X}(\omega_{n-1}) \tilde{X}(\omega - \omega_1 - \dots - \omega_{n-1}) d\omega_1 \dots d\omega_{n-1}, \end{aligned} \quad (2.47)$$

In this thesis we will restrict our analysis to the VSTF truncated to third-order. Therefore, we are seeking for an approximated NLSE solution of the form,

$$\begin{aligned} \tilde{A}(\omega, z) = \tilde{A}(\omega, 0)H_1(\omega, z) \\ + \iint H_3(\omega, \omega_1, \omega_2, z)\tilde{A}(\omega_1, 0)\tilde{A}^*(\omega_2, 0)\tilde{A}(\omega - \omega_1 + \omega_2, 0) d\omega_1 d\omega_2, \end{aligned} \quad (2.48)$$

where  $H_1(\omega, z)$  is the first-order (linear) kernel and  $H_3(\omega, \omega_1, \omega_2, z)$  is the third-order (nonlinear) kernel. Note the absence of the second-order Volterra kernel in (2.48), which is due to the molecular symmetric of silica optical fibers [3]. A strategy to obtain closed form expressions for  $H_1$  and  $H_3$  is to substitute equation (2.48) into (2.44), as proposed in [5, 23], yielding

$$\begin{aligned} \frac{\partial \tilde{L}(\omega, z)}{\partial z} + \frac{\partial \tilde{N}(\omega, \omega_1, \omega_2, z)}{\partial z} = G_1(\omega)\tilde{L}(\omega, z) + G_1(\omega)\tilde{N}(\omega, \omega_1, \omega_2, z) \\ + \iint G_3 \left\{ \left[ \tilde{L}(\omega_1, z) + \tilde{N}(\omega_1, \omega'_1, \omega'_2, z) \right] \left[ \tilde{L}(\omega_2, z) + \tilde{N}(\omega_2, \omega'_1, \omega'_2, z) \right]^* \right. \\ \left. \times \left[ \tilde{L}(\omega + \omega_1 - \omega_2, z) + \tilde{N}(\omega - \omega_1 + \omega_2, \omega'_1, \omega'_2, z) \right] \right\} d\omega_1 d\omega_2, \end{aligned} \quad (2.49)$$

where  $\tilde{N}(\omega, \omega_1, \omega_2, z) = \iint H_3(\omega, \omega_1, \omega_2, z)\tilde{A}(\omega_1, 0)\tilde{A}^*(\omega_2, 0)\tilde{A}(\omega - \omega_1 + \omega_2, 0) d\omega_1 d\omega_2$  and  $\tilde{L}(\omega, z) = H_1(\omega, z)\tilde{A}(\omega, 0)$  represent the nonlinear and linear terms on the right-hand side (RHS) of (2.48), respectively. Equating the first-order terms in the RHS and left-hand side (LHS) of equation (2.49) yields

$$\frac{\partial \tilde{L}(\omega, z)}{\partial z} = G_1(\omega)\tilde{L}(\omega, z) \Leftrightarrow \frac{\partial H_1(\omega, z)}{\partial z} = G_1(\omega)H_1(\omega, z), \quad (2.50)$$

which is a first-order partial differential equation of the form  $\frac{\partial y}{\partial z} = ay \Rightarrow y = y(0) \exp(az)$ , with the initial condition  $y(0) = 1$ , thus enabling to determine  $H_1(\omega, z)$ ,

$$H_1(\omega, z) = \exp(G_1(\omega)z) = \exp\left(-\frac{\alpha}{2}z + i\frac{\beta_2}{2}\omega^2 z\right), \quad (2.51)$$

Conversely, equating the third-order terms in (2.49) yields the following partial differential

equation

$$\begin{aligned}
 \frac{\partial \tilde{N}(\omega, \omega_1, \omega_2, z)}{\partial z} &= G_1(\omega) \tilde{N}(\omega, \omega_1, \omega_2, z) \\
 &\quad + \iint G_3 \tilde{L}(\omega_1, z) \tilde{L}^*(\omega_2, z) \tilde{L}(\omega - \omega_1 + \omega_2, z) d\omega_1 d\omega_2 \Leftrightarrow \\
 \Leftrightarrow \frac{\partial H_3(\omega, \omega_1, \omega_2, z)}{\partial z} &= G_1(\omega) H_3(\omega, \omega_1, \omega_2, z) \\
 &\quad + G_3 H_1(\omega_1, z) H_1^*(\omega_2, z) H_1(\omega - \omega_1 + \omega_2, z), \tag{2.52}
 \end{aligned}$$

whose solution is of the form  $\frac{\partial y}{\partial z} = ay + b \exp(cz) \Rightarrow y = b \frac{\exp(cz) - \exp(az)}{c-a}$ , enabling to determine the third-order nonlinear kernel,  $H_3(\omega, \omega_1, \omega_2, z)$ , as

$$H_3(\omega, \omega_1, \omega_2, z) = G_3 \frac{\exp \left[ G_1(\omega_1)z + G_1^*(\omega_2)z + G_1(\omega - \omega_1 + \omega_2)z \right] - \exp \left[ G_1(\omega)z \right]}{G_1(\omega_1) + G_1^*(\omega_2) + G_1(\omega - \omega_1 + \omega_2) - G_1(\omega)}. \tag{2.53}$$

Substituting (2.45) and (2.46) in (2.53) finally yields

$$H_3(\omega, \omega_1, \omega_2, z) = i \frac{\gamma}{4\pi^2} H_1(\omega, z) \frac{1 - \exp \left( -\alpha z + i\beta_2(\omega_1 - \omega)(\omega_1 - \omega_2)z \right)}{\alpha - i\beta_2(\omega_1 - \omega)(\omega_1 - \omega_2)}. \tag{2.54}$$

The third-order truncated VSTF of a single-mode optical fiber section of length  $L_s$  is then given by

$$\begin{aligned}
 \tilde{A}(\omega, z + L_s) &= H_1(\omega, L_s) \tilde{A}(\omega, z) \\
 &\quad + i \frac{\gamma}{4\pi^2} H_1(\omega, L_s) \iint H_3'(\omega, \omega_1, \omega_2, L_s) \tilde{A}(\omega_1, z) \tilde{A}^*(\omega_2, z) \tilde{A}(\omega - \omega_1 + \omega_2, z) d\omega_1 d\omega_2, \tag{2.55}
 \end{aligned}$$

where  $H_3'(\omega, \omega_1, \omega_2, z)$  is defined as

$$H_3'(\omega, \omega_1, \omega_2, z) = \frac{1 - \exp \left( -\alpha z + i\Delta\beta_{1,2}(\omega)z \right)}{\alpha - i\Delta\beta_{1,2}(\omega)}. \tag{2.56}$$

in order to remove the  $i \frac{\gamma}{4\pi^2} H_1(\omega, z)$  term from the double integral. Also note the introduction of the  $\Delta\beta_{1,2}(\omega) = \beta_2(\omega_1 - \omega)(\omega_1 - \omega_2)$  factor to simplify the notation.

One of the major advantages of the VSTF method is to enable the separate evaluation of the linear and nonlinear operators in the NLSE. The output optical field of equation (2.55) can be written as

$$\tilde{A}(\omega, z) = \tilde{A}^{\text{LI}}(\omega, z) + \tilde{A}^{\text{NL}}(\omega, z), \tag{2.57}$$

where  $\tilde{A}^{\text{LI}}$  and  $\tilde{A}^{\text{NL}}$  are the Fourier transforms of the linear and nonlinear output optical fields, respectively given by the first and second terms on the RHS of equation (2.55).

## Multi-Span Analytical Model

The VSTF described by expression (2.55) is only valid for a single fiber span. In a typical optical transmission system composed of many individual fiber spans, the use of a VSTF model to obtain a numerical solution for the NLSE can be considered under two distinct approaches:

- a) apply the single-span VSTF of equation (2.55) recursively for each fiber span, i.e. obtain the output field of the VSTF for the  $n$ -th fiber span and utilize it as the input field for the following  $n + 1$ -th span. This approach requires an iterative process with a total of  $N_s$  consecutive steps, where  $N_s$  is the number of fiber spans in the optical link;
- b) account for the coherent accumulation of fiber nonlinearities from span to span, employing a phase-array factor, as proposed in [8, 24, 25]. This approach enables to implement the VSTF of the full optical link in a single step, or at least using step-sizes larger than the span length.

From the complexity point of view, option b) apparently provides the most efficient approach<sup>3</sup>, also enabling to more easily analyze the ensemble effect of nonlinear impairments after a cascade of fiber spans. Starting from the single-span formulation and assuming an optical link composed of  $N_s$  identical fiber spans, an approximated multi-span VSTF can be derived, yielding

$$\begin{aligned} \tilde{A}(\omega, z + L) &= H_1^{\text{MS}}(\omega, L)\tilde{A}(\omega, z) \\ &+ i\frac{\gamma}{4\pi^2}H_1^{\text{MS}}(\omega, L)\iint H_3^{\text{MS}}(\omega, \omega_1, \omega_2, L)\tilde{A}(\omega_1, z)\tilde{A}^*(\omega_2, z)\tilde{A}(\omega - \omega_1 + \omega_2, z) d\omega_1 d\omega_2, \end{aligned} \quad (2.58)$$

where  $L = N_s L_s$  is the total link length,  $H_1^{\text{MS}}(\omega, z)$  is the multi-span linear kernel,

$$H_1^{\text{MS}}(\omega, z) = \exp\left(-\frac{\alpha}{2}L_s + i\frac{\beta_2}{2}\omega^2 z\right), \quad (2.59)$$

and  $H_3^{\text{MS}}(\omega, \omega_1, \omega_2, z)$  is the multi-span third-order nonlinear kernel,

$$H_3^{\text{MS}}(\omega, \omega_1, \omega_2, z) = F(\omega, \omega_1, \omega_2, z/L_s)H_3'(\omega, \omega_1, \omega_2, L_s), \quad (2.60)$$

where  $F(\omega, \omega_1, \omega_2, N_s)$  is a phased-array factor [8, 24, 25],

$$\begin{aligned} F(\omega, \omega_1, \omega_2, N_s) &= \sum_{n=1}^{N_s} \exp(i\Delta\beta_{1,2}(\omega)(n-1)L_s) \\ &= \exp\left(i\frac{\Delta\beta_{1,2}(\omega)}{2}(N_s-1)L_s\right) \frac{\sin(\Delta\beta_{1,2}(\omega)N_s L_s/2)}{\sin(\Delta\beta_{1,2}(\omega)L_s/2)}. \end{aligned} \quad (2.61)$$

Note that the multi-span expressions of (2.59) and (2.60) coincide with single-span

---

<sup>3</sup>However, due the  $O(N^3)$  VSTF complexity, the reduction on number of steps may not be compensated by the increased FFT block-size,  $N$ , required by the multi-span approach. This issue will be more thoroughly assessed in Chapter 4.

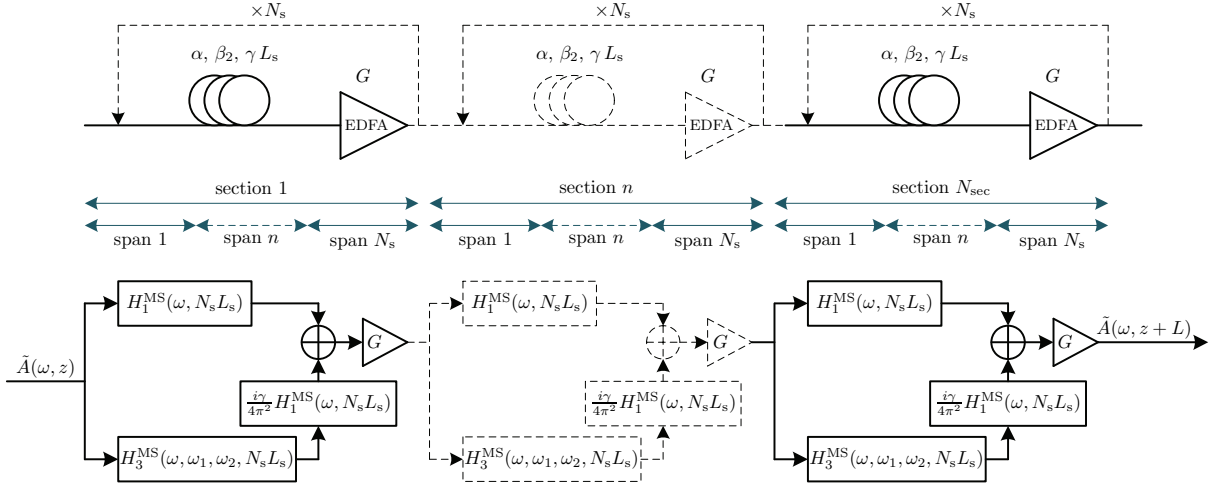


**Figure 2.1:** Implementation diagram of a cascaded multi-span VSTF for an optical link composed of  $N_{\text{sec}}N_s$  spans of fiber. All spans are assumed to have identical fiber parameters ( $\alpha$ ,  $\beta_2$ ,  $\gamma$  and  $L_s$ ) and all optical amplifiers provide the same gain,  $G$ , which exactly compensates for the fiber loss. In each VSTF step, the linear and nonlinear optical field contributions are calculated in parallel and added after each section.

expressions of (2.51) and (2.56) for  $z = L_s$ , and therefore provide a generalization of the VSTF kernels for all  $z$  multiple of  $L_s$ . The full analytical derivation of equation (2.58) is detailed in Appendix B, where it is shown that the multi-span VSTF neglects higher-order terms generated by the cascade of  $N_s$  fiber spans. Therefore, its performance is expected to progressively degrade for increasing  $N_s$  due to the third-order inter-span approximation. On the contrary, VSTF-based modelling of multi-span optical links employing option a) is only impacted by the intra-span approximation associated with the third-order truncation in (2.55). Joining the merits of approaches a) and b), the accuracy/efficiency tradeoff can be adjusted by a hybrid multi-span and single-span VSTF implementation. Consider a fiber link composed of  $N_{\text{sec}}$  sections, each of which is composed of  $N_s$  fiber spans, so that the total link length is  $L = N_{\text{sec}}N_sL_s$ , as illustrated in Fig. 2.1. A single-step multi-span VSTF can be applied for each section, while the cascade of  $N_{\text{sec}}$  sections can be solved iteratively applying  $N_{\text{sec}}$  consecutive steps. This kind of approach will be further explored in Chapters 4 and 5, within the context of VSTF-based nonlinear equalization.

### Modified VSTF

Through an extensive simulation analysis [5, 23, 24, 26–28], the accuracy of the VSTF has proven to be comparable to that of traditional split-step methods, when moderate power levels are considered (in the order of 1 mW). However, as opposed to split-step methods, the VSTF defined by equation (2.55) is not an energy conservative approach. For high input powers, energy divergence may limit the VSTF practical application. In order to partially solve this issue, a simple phase correction can be applied to the output

optical field, giving rise to the following modified VSTF [22],

$$A(t, z) = \begin{cases} A^{\text{LI}}(t, z) \exp\left(\frac{A^{\text{NL}}(t, z)}{A^{\text{LI}}(t, z)}\right), & \text{if } |A^{\text{NL}}(t, z)| < |A^{\text{LI}}(t, z)| \\ A^{\text{LI}}(t, z) + A^{\text{NL}}(t, z), & \text{otherwise,} \end{cases} \quad (2.62)$$

where  $A^{\text{LI}}(t, z)$  and  $A^{\text{NL}}(t, z)$  are obtained by the inverse Fourier transform of  $\tilde{A}^{\text{LI}}(\omega, z)$  and  $\tilde{A}^{\text{NL}}(\omega, z)$ , respectively.

### Physical meaning and comparison with other nonlinear modelling techniques

The double integral in the  $\tilde{A}^{\text{NL}}$  term originates a frequency sweeping over all spectrum, where the optical field interactions at all possible triplets of frequencies,  $[\omega_1, \omega_2, \omega + \omega_1 - \omega_2]$ , are weighted by the  $H'_3$  kernel, measuring its contribution to a fourth optical field component (on the LHS of (2.56)) at frequency  $\omega$ . Note that, through this frequency sweeping process, the third-order VSTF fully describes the FWM phenomenon. Analogously to the  $H_1$  linear transfer function, the  $H'_3$  kernel can be viewed as a nonlinear transfer function, which measures the efficiency of FWM originated by each frequency triplet. In fact, several closed-form analytical expressions analogous to (2.55) and (2.56) can also be found in other pioneer derivations of FWM-like models of signal propagation in single-mode fibers [8, 29–32]. Figure 2.2 illustrates the FWM efficiency, obtained as  $|H_3^{\text{MS}}(\omega, \omega_1, \omega_2, z)|^2$  [33], for an optical link composed of 1 span (Figures 2.2a and 2.2c) and 10 spans (Figure 2.2b and 2.2d) of non-zero dispersion-shifted fiber (NZDSF) (Figures 2.2a and 2.2b) and SSMF (Figures 2.2c and 2.2d) with 80 km each. Since  $H_3^{\text{MS}}$  is  $\omega$ -dependent, Figure 2.2 shows  $H_3^{\text{MS}}(\omega, \omega_1, \omega_2, z)$  defined over a grid of  $N \times N \times N$  angular frequency values, such that  $\omega_{-N/2} \leq \omega, \omega_1, \omega_2 \leq \omega_{N/2}$ . Note that, due to the diagonal dragging effect of  $H_3^{\text{MS}}$  with varying  $\omega$ , the 3-dimensional  $N \times N \times N$  kernel can be visualized without loss of information as a 2-dimensional  $2N \times 2N$  matrix. The matrices corresponding to the efficiency of FWM generation on the  $\omega_{-N/2}$ ,  $\omega_0$  and  $\omega_{N/2}$  frequencies, corresponding to the first, middle and last points of the considered frequency grid, are indicated by dashed lines.

As widely reported in the literature [30, 31, 34, 35], the FWM effect is shown to be more efficient for lower-dispersion fibers such as NZDSF, since chromatic dispersion increases the phase mismatch between the FWM triplets through the  $\Delta\beta_{1,2}(\omega)$  factor in (2.56). In addition, a direct comparison between the 1 span and 10 spans cases for both the SSMF and NZDSF link reveals that the frequency regions of high FWM efficiency tend to become narrower for longer transmission distance. This observation is in agreement with the phased-array cancellation of FWM reported in [8] for dispersive multi-span links. Note that, in other works employing FWM-like models it is common to find a similar representation of the FWM efficiency with a slightly different geometrical arrangement<sup>4</sup>, which is due to a different frequency index management in the definition of the FWM

<sup>4</sup>See, for instance, Figure 1 in [8], where the FWM interference pattern is dominated by symmetric star-shaped contributions along the matrix columns and rows, instead of the diagonal symmetry evidenced in Figure 2.2.

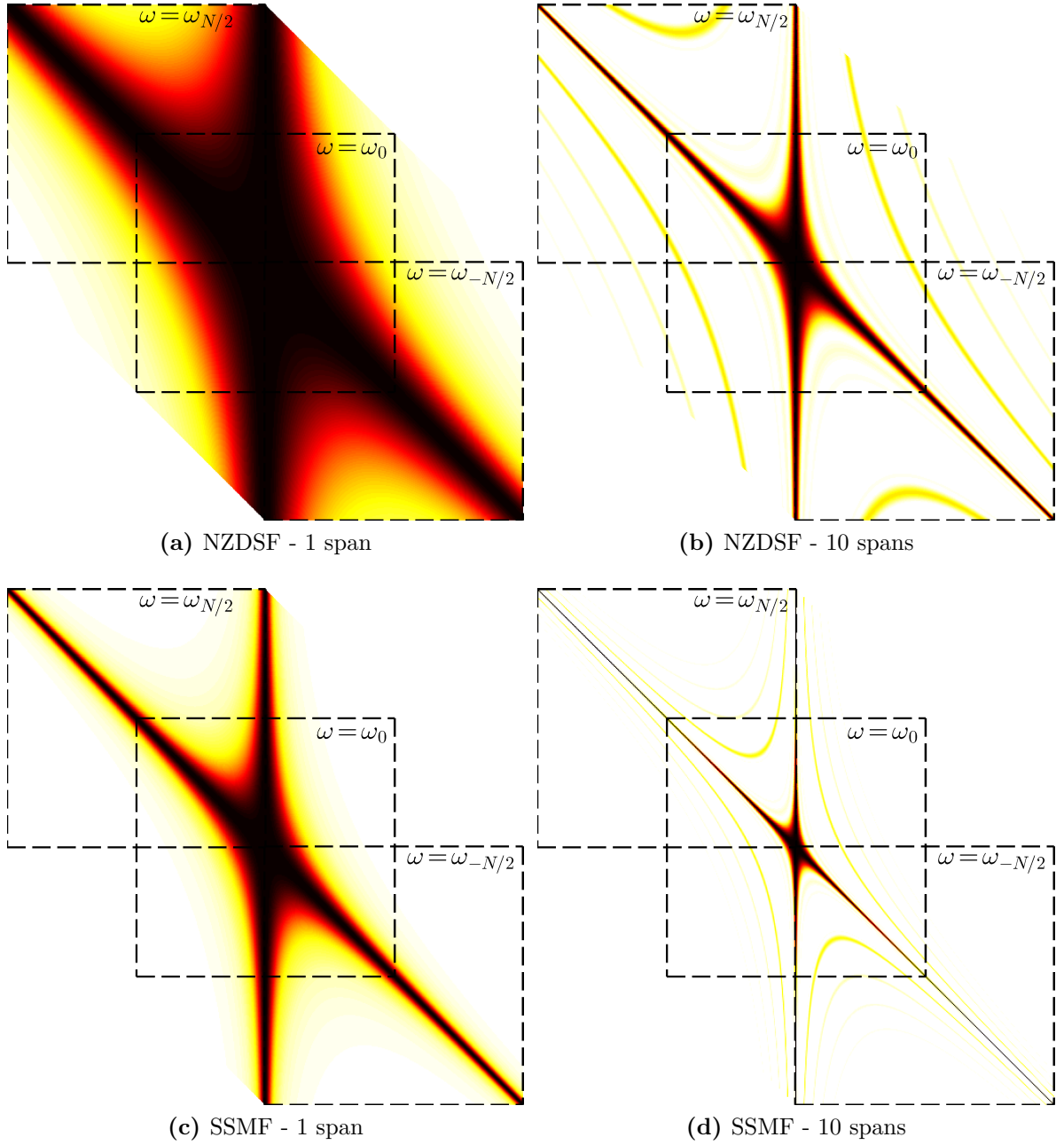


**Figure 2.2:** FWM efficiency indicated by the third-order VSTF kernel for single-span and multi-span SSMF and NZDSF optical links. a) 1 span of NZDSF; b) 10 spans of NZDSF; c) 1 span of SSMF; d) 10 spans of SSMF. SSMF parameters:  $\alpha = 0.2$  dB/km,  $D = 16$  ps/(nm·km) and  $\gamma = 1.3$  W<sup>-1</sup>km<sup>-1</sup>; NZDSF parameters:  $\alpha = 0.22$  dB/km,  $D = 2.5$  ps/(nm·km) and  $\gamma = 2$  W<sup>-1</sup>km<sup>-1</sup>.

---

triplets. Equivalence between these different representations can be obtained by a simple change of variables in the  $\Delta\beta_{1,2}(\omega)$  factor.

Another alternative approach is proposed in [36], where the authors apply the regular

---

perturbation (RP) theory to the NLSE, seeking for an approximate solution in the form of power series expansion over  $\gamma$ . Despite the different analytical foundations of the VSTF and RP theory, the  $[2n + 1]$ -th truncated VSTF is shown to be equivalent to the  $n$ -th order RP solution. This equivalency is not surprising given that the VSTF can also be seen as a perturbative approach, as evidenced by (2.57), where the initial trivial solution for the linear propagation regime,  $\tilde{A}^{\text{LI}}(\omega, z)$ , is perturbed by a *small* nonlinear contribution,  $\tilde{A}^{\text{NL}}(\omega, z)$ .

More recently, a prominent novel approach to the modelling of nonlinear phenomena in dispersion unmanaged fiber links – the well-known GN model – has also been derived from a FWM-like model, slicing the signal spectrum into individual components and thereby assessing the power spectral density (PSD) of nonlinear interference. As consequence, the similarities between the third-order kernel of (2.56) and the single-span PSD of [25, Eq. (15)] are noteworthy. The similitude between all the aforementioned approaches reinforces the scientific relevance and the enormous potential of the VSTF described by 2.55. Within the framework of this thesis, the third-order VSTF will be utilized as the underlying analytical model for development and optimization of digital nonlinear equalization techniques, formulated both in frequency (see Chapter 4) and time domain (see Chapter 5).

## 2.5 Summary

This chapter provided an overview of analytical and numerical methods to model signal propagation in single-mode optical fibers, including a macroscopic analysis of time and frequency domain properties. Neglecting the effect of PMD and its interaction with nonlinear phenomena, the Manakov equation of (2.32) will be used in the remaining of this thesis as the underlying analytical model for simplified signal propagation in fiber. Anchored by its non-iterative structure, the VSTF of (2.58) will be of special interest for the development of the nonlinear compensation techniques proposed in Chapters 3, 4 and 5.

## References

- [1] J. C. Maxwell, “A dynamical theory of the electromagnetic field,” *Philosophical Transactions of the Royal Society of London*, vol. 155, p. 459512, 1865.
- [2] C. R. Menyuk, “Application of multiple-length-scale methods to the study of optical fiber transmission,” *Journal of Engineering Mathematics*, vol. 36, pp. 113–136, 1999.
- [3] G. P. Agrawal, *Nonlinear Fiber Optics*, 3rd ed. University of Rochester, New York: Academic Press, 2001.
- [4] C. Menyuk and B. Marks, “Interaction of polarization mode dispersion and nonlinearity in optical fiber transmission systems,” *J. Lightw. Technol.*, vol. 24, no. 7, pp. 2806 – 2826, 2006.

- [5] K. V. Peddanarappagari and M. Brandt-Pearce, “Volterra series transfer function of single-mode fibers,” *J. Lightw. Technol.*, vol. 15, no. 12, pp. 2232–2241, 1997.
- [6] A. N. Pinto, “Análise e optimização de sistemas de comunicação ópticos baseados em solitões,” Ph.D. dissertation, University of Aveiro, 1999.
- [7] C. Pask and A. Vatarescu, “Spectral approach to pulse propagation in a dispersive nonlinear medium,” *J. Opt. Soc. Am.*, vol. 3, no. 7, pp. 1018–1024, 1986.
- [8] M. Nazarathy, J. Khurgin, R. Weidenfeld, Y. Meiman, P. Cho, R. Noe, I. Shpantzer, and V. Karagodsky, “Phased-array cancellation of nonlinear FWM in coherent OFDM dispersive multi-span links,” *Opt. Express*, vol. 16, no. 20, pp. 15 777–15 810, Sep 2008.
- [9] F. P. Guiomar, J. D. Reis, A. Carena, G. Bosco, A. L. Teixeira, and A. N. Pinto, “Experimental demonstration of a frequency-domain Volterra series nonlinear equalizer in polarization-multiplexed transmission,” *Opt. Express*, vol. 21, no. 1, pp. 276–288, 2013.
- [10] P. K. A. Wai and C. R. Menyuk, “Polarization mode dispersion, decorrelation, and diffusion in optical fibers with randomly varying birefringence,” *J. Lightw. Technol.*, vol. 14, no. 2, pp. 148–157, 1996.
- [11] N. J. Muga, “Polarization effects in fiber-optic communication systems,” Ph.D. dissertation, Universidade de Aveiro, 2011.
- [12] A. Galtarossa, L. Palmieri, A. Pizzinat, M. Schiano, and T. Tambosso, “Measurement of local beat length and differential group delay in installed single-mode fibers,” *J. Lightw. Technol.*, vol. 18, no. 10, pp. 1389–1394, 2000.
- [13] D. Marcuse, C. R. Menyuk, and P. K. A. Wai, “Application of the Manakov-PMD equation to studies of signal propagation in optical fibers with randomly varying birefringence,” *J. Lightw. Technol.*, vol. 15, no. 9, pp. 1735–1746, 1997.
- [14] N. Silva, N. Muga, and A. Pinto, “Effective nonlinear parameter measurement using FWM in optical fibers in a low power regime,” *IEEE J. Quantum Electron.*, vol. 46, no. 3, pp. 285–291, March 2010.
- [15] G. Bosco, R. Cigliutti, A. Nespola, A. Carena, V. Curri, F. Forghieri, Y. Yamamoto, T. Sasaki, Y. Jiang, and P. Poggiolini, “Experimental investigation of nonlinear interference accumulation in uncompensated links,” *IEEE Photon. Technol. Lett.*, vol. 24, no. 14, pp. 1230–1232, 2012.
- [16] O. V. Sinkin, R. Holzlohner, J. Zweck, and C. R. Menyuk, “Optimization of the split-step Fourier method in modeling optical-fiber communications systems,” *J. Lightw. Technol.*, vol. 21, no. 1, pp. 61–68, 2003.

- 
- [17] Q. Zhang and M. I. Hayee, “Symmetrized split-step fourier scheme to control global simulation accuracy in fiber-optic communication systems,” *J. Lightw. Technol.*, vol. 26, no. 2, pp. 302–316, 2008.
- [18] G. Muslu and H. Erbay, “Higher-order split-step Fourier schemes for the generalized nonlinear Schrödinger equation,” *Mathematics and Computers in Simulation*, vol. 67, no. 6, pp. 581 – 595, 2005.
- [19] A. Carena, V. Curri, R. Gaudino, P. Poggiolini, and S. Benedetto, “A time-domain optical transmission system simulation package accounting for nonlinear and polarization-related effects in fiber,” *IEEE J. Sel. Areas Commun.*, vol. 15, no. 4, pp. 751–765, 1997.
- [20] K. He and X. Li, “An efficient approach for time-domain simulation of pulse propagation in optical fiber,” *J. Lightw. Technol.*, vol. 28, no. 20, pp. 2912–2918, 2010.
- [21] Y. Zhu and D. V. Plant, “Optimal design of dispersion filter for time-domain split-step simulation of pulse propagation in optical fiber,” *J. Lightw. Technol.*, vol. 30, no. 10, pp. 1405–1421, 2012.
- [22] B. Xu and M. Brandt-Pearce, “Modified Volterra series transfer function method,” *IEEE Photon. Technol. Lett.*, vol. 14, no. 1, pp. 47–49, 2002.
- [23] J. D. Reis, “Design and optimization next generation passive all-optical networks,” Ph.D. dissertation, Universidade de Aveiro, 2012.
- [24] B. Xu and M. Brandt-Pearce, “Comparison of FWM- and XPM-induced crosstalk using the Volterra series transfer function method,” *J. Lightw. Technol.*, vol. 21, no. 1, pp. 40–53, 2003.
- [25] A. Carena, V. Curri, G. Bosco, P. Poggiolini, and F. Forghieri, “Modeling of the impact of nonlinear propagation effects in uncompensated optical coherent transmission links,” *J. Lightw. Technol.*, vol. 30, no. 10, pp. 1524–1539, 2012.
- [26] K. V. Peddanarappagari and M. Brandt-Pearce, “Volterra series approach for optimizing fiber-optic communications system designs,” *J. Lightw. Technol.*, vol. 16, no. 11, pp. 2046–2055, 1998.
- [27] J. D. Reis and A. L. Teixeira, “Unveiling nonlinear effects in dense coherent optical WDM systems with Volterra series,” *Opt. Express*, vol. 18, no. 8, pp. 8660–8670, Apr 2010.
- [28] J. D. Reis, D. M. Neves, and A. L. Teixeira, “Analysis of nonlinearities on coherent ultradense WDM-PONs using Volterra series,” *J. Lightw. Technol.*, vol. 30, no. 2, pp. 234–241, 2012.
- [29] K. Inoue, “Phase-mismatching characteristic of four-wave mixing in fiber lines with multistage optical amplifiers,” *Opt. Lett.*, vol. 17, no. 11, pp. 801–803, Jun 1992.

- [30] K. Inoue and H. Toba, "Fiber four-wave mixing in multi-amplifier systems with nonuniform chromatic dispersion," *J. Lightw. Technol.*, vol. 13, no. 1, pp. 88–93, Jan 1995.
- [31] M. Eiselt, "Limits on WDM systems due to four-wave mixing: a statistical approach," *J. Lightw. Technol.*, vol. 17, no. 11, pp. 2261–2267, Nov 1999.
- [32] S. Turitsyn, M. Fedoruk, E. Shapiro, V. Mezenrsev, and E. Turitsyna, "Novel approaches to numerical modeling of periodic dispersion-managed fiber communication systems," *IEEE J. Sel. Topics Quantum Electron.*, vol. 6, no. 2, pp. 263–275, March 2000.
- [33] J. K. Fischer, C.-A. Bunge, and K. Petermann, "Equivalent single-span model for dispersion-managed fiber-optic transmission systems," *J. Lightw. Technol.*, vol. 27, no. 16, pp. 3425–3432, 2009.
- [34] M. Maeda, W. Sessa, W. Way, A. Yi-Yan, L. Curtis, R. Spicer, and R. Laming, "The effect of four-wave mixing in fibers on optical frequency-division multiplexed systems," *J. Lightw. Technol.*, vol. 8, no. 9, pp. 1402–1408, Sep 1990.
- [35] W. Zeiler, F. Di Pasquale, P. Bayvel, and J. E. Midwinter, "Modeling of four-wave mixing and gain peaking in amplified WDM optical communication systems and networks," *J. Lightw. Technol.*, vol. 14, no. 9, pp. 1933–1942, Sep 1996.
- [36] A. Vannucci, P. Serena, and A. Bononi, "The RP method: a new tool for the iterative solution of the nonlinear Schrödinger equation," *J. Lightw. Technol.*, vol. 20, no. 7, pp. 1102–1112, 2002.



## Chapter 3

# Nonlinear Equalization via Digital Backpropagation

The capacity limits of single-mode optical transmission systems is ultimately limited by the impact of nonlinear fiber impairments [1–3]. The use of digital backpropagation (DBP) has been recently proposed as an effective way of compensating nonlinear distortions in coherent optical systems. In this chapter, we propose a novel algorithm for the numerical implementation of DBP, which is based on an inverse Volterra series transfer function (VSTF) formulated in the frequency domain and truncated to the third-order. The DBP-VSTF is analytically derived for single- and dual-polarization transmission systems and its performance and complexity are numerically assessed for 40 Gb/s and 112 Gb/s optical channels, followed by experimental demonstration in several 100G propagation scenarios. The obtained simulation and experimental results demonstrate the high performance of the DBP-VSTF technique, associated with a highly parallel equalizer structure, which may potentially benefit real-time implementation.

The organization of this chapter is as follows. The concept of DBP is introduced in section 3.1, supported by the analytical background on the scalar and coupled NLSE addressed in chapter 2. Taking into account the large number of scientific publications and the considerable attention drawn by the use of the split-step Fourier method (SSFM) as a DBP algorithm, in section 3.2 we provide a detailed description of the DBP-SSFM approach in single- and dual-polarization optical systems. The DBP-VSTF method is then introduced in section 3.3 and numerically assessed in section 3.4. The experimental validation work in 100G optical transmission systems, performed in collaboration with Politecnico di Torino, is described in section 3.5. Finally, the major conclusions drawn from this chapter are summarized in section 3.6.

### 3.1 The Concept of Digital Backpropagation

As evidenced by both the scalar and vectorial NLSE that governs signal propagation in fiber, linear and nonlinear effects occur simultaneously, causing a distributed interplay between different fiber impairments. As previously highlighted in chapter 2, linear and

nonlinear effects cause complementary distortions in time and frequency domain, acting together throughout propagation. This distributed nature of nonlinear effects drastically differs from other common problems of nonlinear distortion and equalization in telecom applications, such as the compensation of nonlinearities in radio-frequency amplifiers, where the nonlinear distortion can be considered as being concentrated [4]. Consequently, the problem of nonlinear compensation in optical fiber systems requires new research efforts for a dedicated treatment. From a theoretical point of view, the optimum strategy for impairment compensation in optical fiber systems is by spatially reversing the NLSE, enabling to exactly recover the transmitted signal from the received one, which leads to the concept of backpropagation. Taking advantage of the fact that the NLSE is an invertible equation, an inverse scalar NLSE can be obtained from (2.9) as,

$$\frac{\partial A(t, z)}{\partial(-z)} = \frac{\alpha}{2} A(t, z) + i \frac{\beta_2}{2} \frac{\partial^2 A(t, z)}{\partial t^2} - i \gamma |A(t, z)|^2 A(t, z), \quad (3.1)$$

which in practice corresponds to re-propagate the received optical field over a virtual fiber with symmetric parameters  $(-\alpha, -\beta_2$  and  $-\gamma)$ , as depicted in Figure 3.1. Under the theoretical assumption of a noiseless transmission system, the backpropagation technique enables to fully remove all fiber impairments and exactly recover the transmitted signal. However, the existence of non-ideal characteristics in practical transmission systems, such as the presence of optical and electrical noise, uncertainty on the fiber parameters, and transceiver-induced distortions, sets the maximum achievable accuracy for backpropagation.

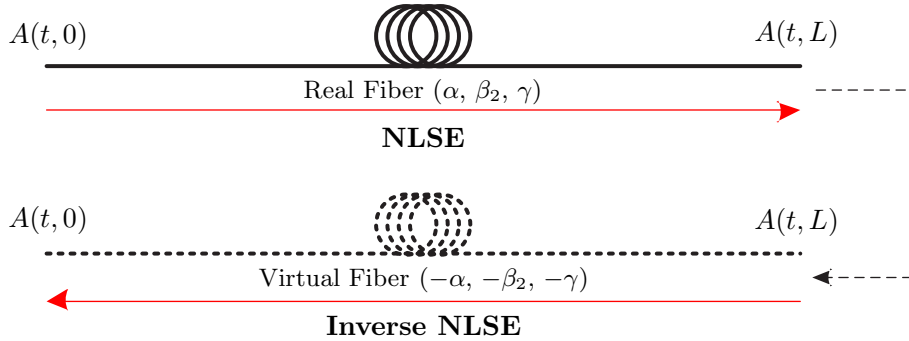


**Figure 3.1:** Schematic representation of the concept of optical backpropagation. Within a given fiber span with parameters  $\alpha$ ,  $\beta_2$  and  $\gamma$ , the input optical field,  $A(t, 0)$ , can be reobtained from the output optical field at position  $z = L$ ,  $A(t, L)$ , by applying it as the input of a virtual fiber with opposite sign parameters,  $-\alpha$ ,  $-\beta_2$  and  $-\gamma$ . In mathematical terms, the virtual fiber can be described by the inverse NLSE of equation (3.1).

Since the analytical description of the inverse NLSE implies a continuous-time analysis in the optical domain, the resulting compensation technique can be classified as optical backpropagation (OBP). Physical implementation of OBP requires to introduce additional active optical components in the transmission system, in order to emulate the virtual backward fiber, such as optical phase conjugators [5], highly nonlinear and highly dispersive fibers [6, 7]. Note that the use of DCFs modules in legacy fiber systems can

be considered as a specific case of linear OBP, in which only the accumulated CD is optically reversed.

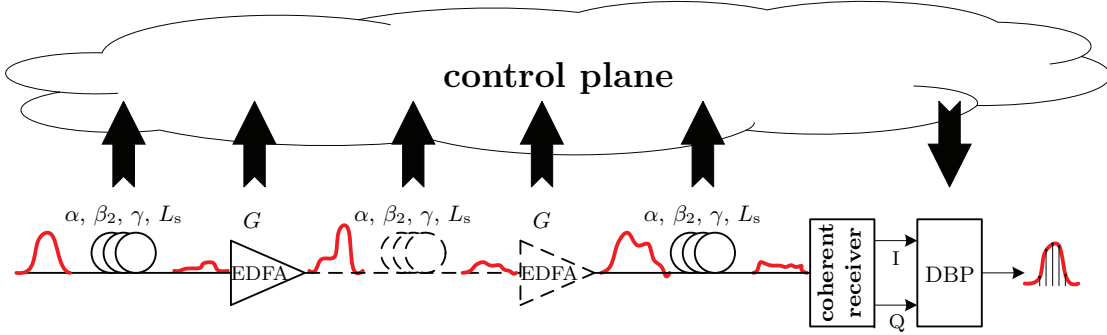
With the advent of coherent optical transmission systems, it became possible to apply the backpropagation concept digitally in the electrical domain, either before transmission or after signal detection, giving rise to the DBP technique [8]. The first works employing DBP in optical communication systems were based on transmitter-side electronic pre-compensation, in order to improve the performance of direct detection systems [9]. With the advent of coherent detection, DBP has become feasible as a receiver-side compensation method [10]. In 2008, DBP was proposed for the first time as a post-compensation method for single-polarization optical transmission systems, in the context of both single-channel [8] and WDM systems [11]. From a theoretical point of view, considering a noiseless transmission system, pre- and post-compensation DBP are equivalent. However, DBP-based pre-compensation poses additional challenges in terms of high precision and high resolution DAC technology. In addition, the use of DBP as a post-compensation technique shows the advantage of enabling adaptive equalization of linear and nonlinear impairments, without full knowledge of the transmission system. For these reasons, in this thesis we will focus our attention on the application of DBP as a post-detection compensation technique.

Figure 3.2 illustrates the application of post-detection DBP to a standard dispersion-unmanaged multi-span optical transmission system with inline EDFAs. During propagation, the optical signal becomes highly distorted due to linear and nonlinear fiber impairments. At the receiver, coherent detection is employed to enable a linear optical-to-electrical downconversion, thus preserving the full<sup>1</sup> signal information in the electrical domain. The I and Q electrical signal components are then sampled and quantized by dedicated ADC devices, producing a complex-valued digital waveform that represents the received optical signal. Assuming that the receiver has full knowledge of the transmission link, including the fiber parameters  $\alpha$ ,  $\beta_2$  and  $\gamma$ , the span length,  $L_s$ , and the EDFA gains,  $G$ , the DBP technique can be applied to compensate for the propagation impairments, enabling to approximately recover the transmitted signal. In the framework of this thesis we will assume that the information about the link parameters can be obtained from the control plane, as shown in Figure 3.2.

The accuracy of the DBP technique depends upon many system parameters, such as the EDFAs noise figure, the uncertainty on the fiber parameters, the electrical noise generated by the transceiver and the digital noise due to the sampling and quantization processes. Since these noise sources are by definition random processes that cannot be physically pre-determined, their contribution cannot be removed through backpropagation. Furthermore, because the noise generated by different concentrated noise sources becomes indistinct at the receiver, the DBP technique will virtually backpropagate the full amount of received noise through the optical link. Therefore, not only added noise cannot be removed via DBP, as it also generates artificial signal-noise interactions during backpropagation. This limitation is currently being addressed by several authors [12, 13], aiming to extend the fundamental performance limits of DBP.

---

<sup>1</sup>Note that, in practice, the optical signal information is not fully preserved after coherent detection due to the non-ideal behavior of the receiver front-end, which inevitably introduces added noise.



**Figure 3.2:** Schematic representation of the concept of digital backpropagation in a dispersion-unmanaged multi-span optical transmission system. A transmitted pulse is propagated over a fiber link composed of  $N_s$  fiber spans with inline EDFA-based optical amplification. The key parameters describing the optical link are communicated to the control plane, which provides the required information to apply DBP at the receiver-side. Through DBP, the distorted received signal is compensated for linear and nonlinear fiber impairments, yielding an approximate copy of the transmitted signal.

Using the maximum a posteriori principle, a stochastic DBP algorithm is proposed in [12] in which the optical noise introduced in each fiber span is taken into account. However, this technique requires very high computational power and is only shown to provide significant gains over standard DBP in dispersion-managed links. An alternative and more practical approach is proposed in [13], where it is shown that the DBP performance in dispersion-unmanaged links can be improved by applying a post-DBP Viterbi detector. In order to minimize the impact of added noise in the DBP performance, the analytical equation describing DBP is obtained by modifying equation (3.1) as,

$$\frac{\partial A(t, z)}{\partial(-z)} = \frac{\alpha}{2}A(t, z) + i\frac{\beta_2}{2}\frac{\partial^2 A(t, z)}{\partial t^2} - i\xi\gamma|A(t, z)|^2 A(t, z), \quad (3.2)$$

where  $0 \leq \xi \leq 1$  is a free optimization parameter that controls optimum fraction of nonlinearities to be digitally backpropagated. The optimum  $\xi$ ,  $\xi_{\text{opt}}$ , strongly depends on the received signal SNR and corresponds to the  $\xi$  value that minimizes the mean square error (MSE) between the transmitted and compensated signals. In the absence of noise and considering infinite temporal resolution for DBP,  $\xi$  converges to unity and the transmitted signal is exactly recovered. In practical applications, typical values of  $0.6 \leq \xi \leq 0.9$  have been experimentally demonstrated in numerous works. Note that, because it works as a tuning parameter for the nonlinear operator in (3.2), the  $\xi$  parameter can also be used to correct for small errors on the estimation of the received optical power and span length.

The analytical DBP equation (3.2) is valid for a single-polarization optical system modeled by the scalar NLSE of expression (2.9). In polarization-multiplexed optical systems, backpropagation can be analytical described by the reverse spatial evolution of the CNLSE of expression (2.25). However, from a practical point of view, backpropagation based on the CNLSE may be unfeasible, since it would require to continuously track the state of polarization of the transmitted signal during propagation.

In [14] it has been shown that the polarization-dependent effects can be safely neglected in DBP, provided that DGD is a small fraction of the symbol period, which is a valid assumption for typical long-haul fiber links. Enabled by this critical simplification, DBP in polarization-multiplexed transmission systems can be obtained by spatially reversing the Manakov equation of (2.32), yielding [15]

$$\frac{\partial A_{x/y}(t, z)}{\partial(-z)} = \frac{\alpha}{2} A_{x/y}(t, z) + i \frac{\beta_2}{2} \frac{\partial^2 A_{x/y}(t, z)}{\partial t^2} - i \xi \frac{8}{9} \gamma \left( |A_x(t, z)|^2 + |A_y(t, z)|^2 \right) A_{x/y}(t, z), \quad (3.3)$$

where  $A_{x/y}$  represents the optical field envelope in the  $x/y$  states of polarization. Expression (3.3) thus corresponds to a system of coupled equations simultaneously describing backpropagation in the  $x$  and  $y$  polarization axes.

Since DBP only requires an electric field representation of the received signal, its applicability is completely independent of the signal properties, such as the modulation format and baud-rate. In order to be implemented in practice, the single- and dual-polarization DBP equations (3.2) and (3.3) must be numerically solved in real-time, which poses a critical challenge in terms of algorithm development and complexity minimization. This has driven the emergence of a novel research topic in the optical communications scientific community. Originated in 2008 by a couple of pioneer research works [8, 11], the study of efficient and low-complexity DBP algorithms [16–23] has been attracting an increasing attention both from academic and industrial players. In the following sections we address two state-of-the-art numerical implementation algorithms for DBP: i) SSFM-based DBP, which is the most popular algorithm, supported by a vast number of publications and experimental demonstrations, and ii) Volterra-based DBP, which is an emerging research topic and the core contribution of this thesis, targeting a more computationally efficient DBP implementation.

## 3.2 DBP Using the Split-Step Fourier Method

Following its widespread use for the modelling of signal propagation in fiber, the pioneer works on DBP have relied on the use of the SSFM to solve the inverse NLSE. The motivations behind the popularity of the SSFM are mainly two-fold: i) a simple and easy to implement algorithm architecture based on an independent treatment of linear and nonlinear phenomena in fiber, and ii) high accuracy when applied with sufficient temporal and spatial resolution. However, the SSFM also presents some important limitations, namely in terms of its highly iterative structure and hybrid time/frequency implementation, which can pose serious challenges for the practical implementation of DBP. In the following, we review the fundamentals of SSFM-based DBP for single- and dual-polarization optical systems, detailing the algorithm architecture and its associated computational effort.

### 3.2.1 Single-polarization optical systems

The SSFM described in section 2.4.1 can be straightforwardly extended to numerically solve DBP, as analytically described by equation (3.2). By taking the inverse linear and

nonlinear operators,  $\hat{\mathcal{D}}^{-1} = -\hat{\mathcal{D}}$  and  $\hat{\mathcal{N}}^{-1} = -\hat{\mathcal{N}}$ , the corresponding linear and nonlinear DBP-SSFM steps for single-polarization systems can be defined as,

$$\begin{aligned}\hat{\mathcal{D}}_{\text{SSFM}}^{\text{DBP}}[A(t, z)] &= \mathcal{F}^{-1}\left\{\exp\left(-h\hat{\mathcal{D}}(\omega)\right)\mathcal{F}\{A(t, z)\}\right\} \\ &= \mathcal{F}^{-1}\left\{\exp\left(\frac{\alpha}{2}h - i\frac{\beta_2}{2}\omega^2h\right)\mathcal{F}\{A(t, z)\}\right\}.\end{aligned}\quad (3.4)$$

and

$$\begin{aligned}\hat{\mathcal{N}}_{\text{SSFM}}^{\text{DBP}}[A(t, z)] &= \exp\left(-\xi h_{\text{eff,DBP}}\hat{\mathcal{N}}(A(t, z))\right)A(t, z) \\ &= \exp\left(-i\xi\gamma h_{\text{eff,DBP}}|A(t, z)|^2\right)A(t, z),\end{aligned}\quad (3.5)$$

respectively. The optical field envelope at the input of a given fiber span,  $A(t, 0)$ , is then obtained from the optical field envelope at the output of the same fiber span,  $A(t, L_s)$ , by recursively applying the linear and nonlinear DBP-SSFM steps of (3.4) and (3.5) as,

$$A(t, L_s - nh) = \hat{\mathcal{N}}_{\text{SSFM}}^{\text{DBP}}\left[\hat{\mathcal{D}}_{\text{SSFM}}^{\text{DBP}}[A(t, L_s - (n-1)h)]\right],\quad (3.6)$$

where the input optical field,  $A(t, 0)$ , is obtained after  $n = L_s/h = N_{\text{steps/span}}$  steps. Relatively to equation (2.43) describing the SSFM implementation for conventional (forward) signal propagation modeling, note the introduction of the  $\xi$  optimization parameter in the nonlinear step, resulting from equation (3.2). In addition to its SNR dependence, the  $\xi$  parameter in (3.6) also becomes dependent on the number of SSFM steps per span,  $N_{\text{steps/span}}$ , as it controls the accuracy of optical field estimation in each step. Lower  $N_{\text{steps/span}}$  values generally lead to coarser field estimation and consequently lower  $\xi_{\text{opt}}$ . Also note the use of  $h_{\text{eff,DBP}}$  in the nonlinear step, representing the effective step-size for SSFM-based DBP, given by

$$h_{\text{eff,DBP}} = \frac{\exp(\alpha h) - 1}{\alpha},\quad (3.7)$$

which plays a similar role as  $L_{\text{eff}}$  in (2.20), but for the virtual backward fiber. It is worth mentioning that, for short step-sizes,  $h$ , the corresponding effective step-size for DBP,  $h_{\text{eff,DBP}}$ , given by (3.7) tends to converge to the value of  $h$ . This is the reason why the use of an effective step-size in the nonlinear step is typically omitted when the SSFM is applied to the simulation of signal propagation in the forward direction, as previously described in equation (2.43), since its application in that context is intrinsically associated with the use of a very short step-size.

A block diagram representing the numerical implementation of the DBP-SSFM technique for single-polarization optical signals is shown in Figure 3.3. The depicted implementation corresponds to the asymmetric version of the SSFM, as described by equation (3.6). Since the optical power during backward propagation increases exponentially within each fiber span, the linear step is preferably placed before the nonlinear step, when the SSFM is applied with a sub-span step-size [24]. The frequency

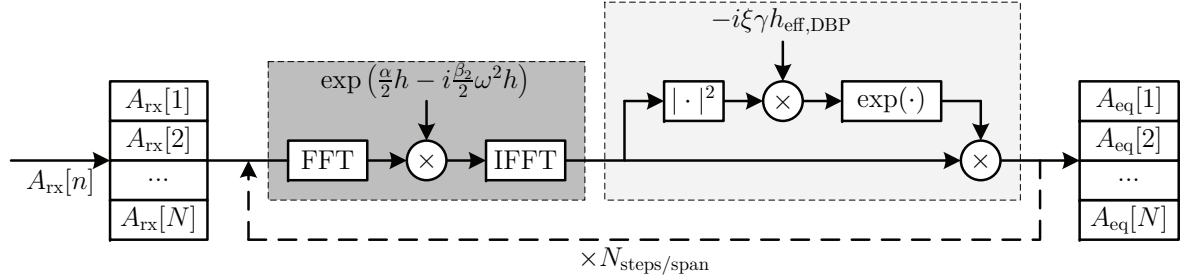


**Figure 3.3:** Numerical implementation of the asymmetric scalar DBP-SSFM for a single fiber span and a single FFT block. The received optical field,  $A_{\text{rx}}$ , is initially stored in an  $N$ -length buffer in order to enable  $N$ -point FFT computation. The nonlinear step is implemented as a pure phase rotation in time domain, proportional to the received optical power and the effective step-size  $h_{\text{eff,DBP}}$ . The linear step is then solved in the frequency domain, resorting to an FFT/IFFT pair. The equalized signal,  $A_{\text{eq}}$ , is obtained by repeating this procedure  $N_{\text{steps}}$  times, such that the fiber span length,  $L_s$ , is given by  $L_s = N_{\text{steps}/\text{span}} \times h$ . For an optical link composed of  $N_s$  fiber spans, the algorithm is then iteratively applied  $N_s \times N_{\text{steps}/\text{span}}$  times.

domain implementation of the linear step requires block processing of the digital signal, which must be grouped in blocks of  $N$  samples for the FFT and inverse fast Fourier transform (IFFT) computing. Alternatively, fully time domain DBP split-step implementations can also be adopted, using FIR or IIR filtering to implement the linear step, thus avoiding block processing at the cost of increased complexity. Offline experimental demonstrations of DBP post-compensation using split-step FIR [25] and split-step IIR [26] approaches have proved its feasibility and equivalent performance to frequency domain DBP-SSFM.

If enough spatial and temporal resolutions are considered, the DBP-SSFM is able to fully compensate all deterministic linear and nonlinear impairments in fiber [8]. However, practical application of the DBP-SSFM for digital post-compensation purposes faces new challenges due to non-ideal conditions. Reduced temporal resolution due to low sampling rates (near to the Nyquist limit) and large amounts of noise in the received signal may have a strong impact on the equalization performance. On the other hand, the limited computational resources at the receiver-side strongly limit the implementable spatial resolution. Nevertheless, extensive experimental implementation of the DBP-SSFM technique for intra-channel nonlinear mitigation has demonstrated significant gains in signal reach and nonlinear tolerance using a temporal resolution of 2 samples per symbol (SpS) and a spatial resolution of 1 step per span. Several computationally-optimized DBP-SSFM variants have been proposed in the literature, with the aim to enable longer step-sizes to reduce the overall computational load. Most of these optimized DBP-SSFM techniques employ simple modification in the nonlinear step. In [24], a low-pass filter is introduced within the nonlinear step to limit the aliasing effect of time-frequency transformations at low sampling rate. In [18], the original instantaneous nonlinear step is modified to include finite-time memory, by the use of a weighting time window to account for the dispersion-induced power spilling between neighboring samples that occurs for long step-sizes.

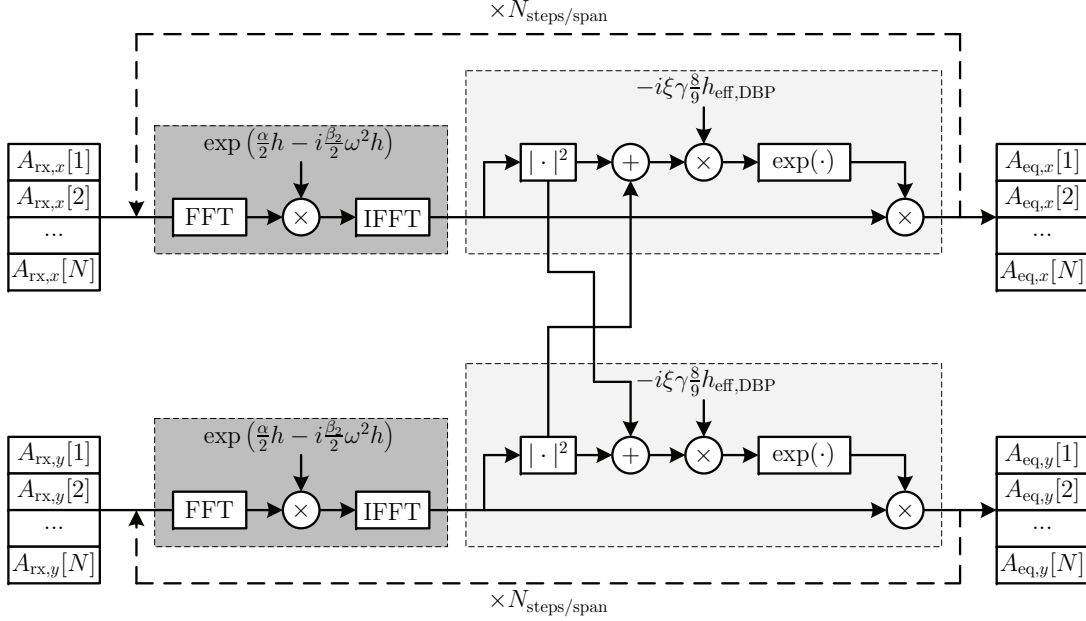


**Figure 3.4:** Numerical implementation of the asymmetric dual-polarization DBP-SSFM for a single fiber span and a single FFT block. Within each polarization component, the implementation is similar to the scalar DBP-SSFM depicted in Figure 3.3, with the addition of inter-polarization nonlinear crosstalk paths to compensate for the cross-polarization nonlinearities.

### 3.2.2 Dual-polarization optical systems

It must be emphasized that the scalar DBP-SSFM, as defined by equation (3.6) and proposed in [8, 11], does not take into account the polarization-dependent effects, being only valid for single-polarization optical systems. However, due to the possibility of doubling the spectral efficiency, polarization-multiplexing is nowadays widely employed in long-haul optical fiber systems. In theory, a vectorial digital DBP-SSFM approach taking into account the Jones matrix to model arbitrary rotations in the principle states of polarization can be employed [14]. However, estimating the  $2 \times 2$  Jones matrix for each fiber span is unfeasible in a practical scenario. To overcome this complexity issue, the vectorial model can be replaced by the inverse Manakov equation of (3.3), allowing to iteratively implement the dual-polarization DBP-SSFM as [15],

$$A_{x/y}(t, L_s - nh) = \hat{\mathcal{N}}_{\text{SSFM}}^{\text{DBP}} \left[ \hat{\mathcal{D}}_{\text{SSFM}}^{\text{DBP}} \left[ A_{x/y}(t, L_s - (n-1)h) \right] \right], \quad (3.8)$$

where  $A_{x/y}$  represents the optical field envelope in the  $x/y$  polarization components and the dual-polarization nonlinear step,  $\hat{\mathcal{N}}_{\text{SSFM}}^{\text{DBP}}$ , is redefined as

$$\hat{\mathcal{N}}_{\text{SSFM}}^{\text{DBP}} \left[ A_{x/y}(t, z) \right] = \exp \left( -i \xi \frac{8}{9} \gamma h_{\text{eff,DBP}} (|A_x(t, z)|^2 + |A_y(t, z)|^2) \right) A_{x/y}(t, z), \quad (3.9)$$

in order to account for the inter-polarization nonlinear crosstalk.

The numerical implementation of the dual-polarization DBP-SSFM is schematically depicted in Figure 3.4. The algorithm architecture is similar to its scalar counterpart depicted in Figure 3.3, except that new inter-polarization nonlinear coupling terms are introduced to account for the average polarization rotations along the fiber. Offline experimental demonstration of the dual-polarization DBP-SSFM concept has proved the applicability of this compensation method for PM transmission [27, 28].

### 3.2.3 Implementation complexity

This section provides a thorough analysis of the complexity in terms of number of real multiplications (RMs) and latency associated with the implementation of the asymmetric DBP-SSFM in its single- and dual-polarization variants. A standard complex multiplication (CM) implementation will be considered throughout this thesis, requiring 4 RMs and 2 real additions, although other configurations are also possible [29]. To initiate the analysis, consider the linear step for CD compensation, which is implemented in the frequency domain, resorting to FFT processing. For this purpose, the overlap between FFT blocks required by the overlap-add/overlap-save algorithms will be neglected. Let us first define the complexity and latency required by each FFT/IFFT, as

$$M_{\text{FFT}}(N) = 2 \log_2(N), \quad (3.10)$$

and

$$\tau_{\text{FFT}}(N) = 2 \log_2(N), \quad (3.11)$$

where  $M_{\text{FFT}}$  is the number of RMs per processed sample and  $\tau_{\text{FFT}}$  is the latency in number of serial RMs, required by a standard Cooley-Tukey radix-2 implementation [30].

The complexity of the linear SSFM step, as depicted in Figures 3.3 and 3.4, and in expression (3.4), is equivalent to the complexity of frequency domain CD compensation, being given by

$$M_{\mathcal{D}}(N) = N_{\text{pol}} [4 + 2M_{\text{FFT}}(N)], \quad (3.12)$$

where  $N_{\text{pol}}$  represents the number of polarization components ( $N_{\text{pol}} = 1$  for single-polarization and  $N_{\text{pol}} = 2$  for dual-polarization optical systems). The CD transfer function is considered to be calculated *a priori* from equation (2.40) and stored in memory, so that the computational effort required for its calculation can be neglected. The  $M_{\mathcal{D}}$  complexity in each polarization is then given by the FFT/IFFT pair plus 1 CM per sample to multiply the input signal by the CD transfer function in frequency domain. In turn, the latency associated with the implementation of the linear SSFM step is

$$\tau_{\mathcal{D}}(N) = 2\tau_{\text{FFT}}(N) + 1, \quad (3.13)$$

where the  $2\tau_{\text{FFT}}(N)$  component corresponds to the FFT/IFFT pair required in each step, and the additional RM is due to the frequency domain multiplication by the CD transfer function.

Regarding the implementation of the DBP-SSFM nonlinear step, as depicted in Figures 3.3 and 3.4, and analytically described by expressions (3.5) and (3.9), the

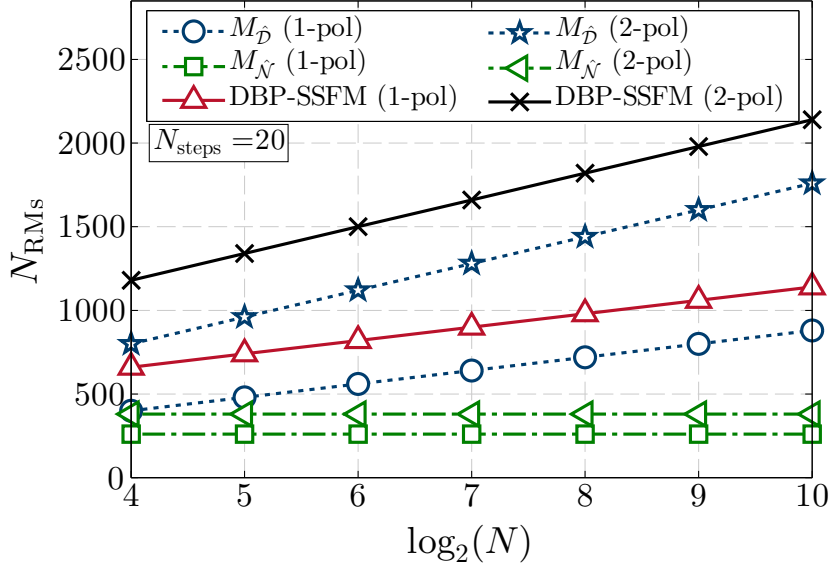


**Figure 3.5:** Implementation complexity, in number of RMs, of the DBP-SSFM algorithm, considering a total of 20 DBP steps.

associated implementation complexity in number of RMs per sample can be written as

$$M_{\hat{N}} = N_{\text{pol}} (M_{|\cdot|^2} + M_{A \times \exp}) + M_{\text{cte}} + M_{\text{exp}}, \quad (3.14)$$

where  $M_{|\cdot|^2} = 2$  is the complexity of the  $|\cdot|^2$  operations in (3.5) and (3.9),  $M_{\text{cte}} = 1$  is the complexity associated with the multiplication by the real-valued constant  $\left(\frac{8}{9}\right) \gamma \xi h_{\text{eff, DBP}}$ ,  $M_{A \times \exp} = 4$  is the number of RMs required for the  $A_{x/y} \times \exp(\cdot)$  complex multiplication and  $M_{\text{exp}}$  is the complexity required to evaluate the exponential function. Note that the factor of  $N_{\text{pol}}$  accounting for the number of polarization tributaries only affects the  $M_{|\cdot|^2}$  and  $A_{x/y} \exp(\cdot)$  terms, since the remaining operations are shared by the two polarizations. A 4th order Taylor expansion has been suggested in [17] for a reliable implementation of the nonlinear phase rotation, implying  $M_{\text{exp}} = 6$ . The complexity of the nonlinear step in DBP-SSFM is then given by

$$M_{\hat{N}} = 6N_{\text{pol}} + 7, \quad (3.15)$$

RMs per processed sample. In terms of latency, from Figure 3.4 it can be readily seen that the nonlinear step involves 4 serial multiplications, so that  $\tau_{\hat{N}} = 4$ .

The overall DBP-SSFM complexity and latency is then given by

$$M_{\text{SSFM}}^{\text{DBP}}(N) = N_{\text{steps}} (M_{\hat{D}}(N) + M_{\hat{N}}), \quad (3.16)$$

and

$$\tau_{\text{SSFM}}^{\text{DBP}}(N) = N_{\text{steps}} (\tau_{\hat{D}}(N) + \tau_{\hat{N}}), \quad (3.17)$$

where  $N_{\text{steps}}$  accounts for the total number of DBP-SSFM steps required for backpropagation. Note that, since the two polarization branches in Figure 3.4 are applied

synchronously, the DBP-SSFM latency does not depend on the number of polarization tributaries,  $N_{\text{pol}}$ . The number of RMs,  $N_{\text{RMs}}$ , required by the single- and dual-polarization DBP-SSFM is depicted in Figure 3.5, detailing the complexity associated with the linear and nonlinear steps separately, for an exemplary case of  $N_{\text{steps}} = 20$ . It can be seen that, even for relatively small FFT block-sizes,  $M_{\mathcal{D}}$  always tends to largely surpass the nonlinear step complexity, evidencing that the linear step is in fact the most significant source of computational effort in the DBP-SSFM algorithm. For a typical value of  $N = 256$ , the linear step consumes approximately 80% of the overall dual-polarization DBP-SSFM computational effort.

### 3.3 DBP Using the Inverse Volterra Series Transfer Function

The single- and dual-polarization DBP-SSFM has been extensively validated by several independent authors using both simulation and experimental data [8, 14, 15, 18, 25, 28, 31, 32]. Indeed, it has been the most widely reported DBP approach for long-haul coherent optical systems, mostly due to its ease of implementation associated with a high equalization performance. However, the heavily iterative procedure required by the DBP-SSFM is a major drawback that has been hindering its real-time implementation and commercial deployment. Taking advantage of the VSTF potentialities identified in Chapter 2, namely in terms of the availability of closed-form expressions for single-span and multi-span modelling of nonlinear interactions, in the following we explore a novel DBP approach based on an inverse VSTF. The derivation of the analytical models for single- and dual-polarization optical systems is accompanied by a comprehensive complexity analysis and performance assessment using simulation and experimental data.

#### 3.3.1 Single-polarization optical systems

##### Single-span DBP-VSTF

Starting from inverse scalar NLSE of (3.2) and following a similar procedure to the one described in section 2.4.2, it is possible to obtain an inverse VSTF, describing backpropagation through a third-order Volterra series approximation. Using such an approach, the equalized field spectrum  $\tilde{A}_{\text{eq}}(\omega, z - L_s)$  can be determined from the output field spectrum  $\tilde{A}(\omega, z)$ , as

$$\begin{aligned} \tilde{A}_{\text{eq}}(\omega, z - L_s) &= K_1(\omega, L_s)\tilde{A}(\omega, z) \\ &+ \Gamma(\omega, L_s) \iint K_3(\omega, \omega_1, \omega_2)\tilde{A}(\omega_1, z)\tilde{A}^*(\omega_2, z)\tilde{A}(\omega - \omega_1 + \omega_2, z) d\omega_1 d\omega_2, \end{aligned} \quad (3.18)$$

where  $K_1(\omega, z)$  is the inverse linear kernel,

$$K_1(\omega, z) = \exp\left(\frac{\alpha}{2}L_s - i\frac{\beta_2}{2}\omega^2 z\right), \quad (3.19)$$

and  $K_3(\omega, \omega_1, \omega_2)$  is the inverse third-order nonlinear kernel<sup>2</sup>,

$$K_3(\omega, \omega_1, \omega_2) = \frac{1 - \exp\left(\alpha L_s - i\beta_2(\omega_1 - \omega)(\omega_1 - \omega_2)L_s\right)}{-\alpha + i\beta_2(\omega_1 - \omega)(\omega_1 - \omega_2)}. \quad (3.20)$$

Finally,  $\Gamma(\omega, z)$  is a frequency-dependent nonlinear term that accounts for the Kerr coefficient and the interaction between the linear and third-order nonlinear kernels<sup>3</sup>,

$$\Gamma(\omega, z) = -i\xi\gamma K_1(\omega, z). \quad (3.21)$$

Given the perturbative nature of equation (3.18), the equalized optical field,  $\tilde{A}_{\text{eq}}(\omega, z)$ , is obtained by the addition of independent linear and nonlinear contributions,

$$\tilde{A}_{\text{eq}}(\omega, z) = \tilde{A}^{\text{LI}}(\omega, z) + \tilde{A}^{\text{NL}}(\omega, z), \quad (3.22)$$

where  $\tilde{A}^{\text{LI}}(\omega, z)$  and  $\tilde{A}^{\text{NL}}(\omega, z)$  are the linear and nonlinear contributions to the equalized optical field, given by the first and second right-hand terms in equation (3.18), respectively.

Note that the formulation of inverse VSTF described by equations (3.18) to (3.20) is analogous to the forward VSTF of equation (2.55), but with symmetric fiber parameters  $(-\alpha, -\beta_2$  and  $-\gamma)$ . Similarly to the forward VSTF method, a modified inverse VSTF can also be considered in order to extend its applicability for larger input powers [33], yielding the inverse modified VSTF (MVSTF),

$$A_{\text{eq}}(t, z) = \begin{cases} A^{\text{LI}}(t, z) \exp\left(\frac{A^{\text{NL}}(t, z)}{A^{\text{LI}}(t, z)}\right), & \text{if } |A^{\text{NL}}(t, z)| < |A^{\text{LI}}(t, z)| \\ A^{\text{LI}}(t, z) + A^{\text{NL}}(t, z), & \text{otherwise,} \end{cases} \quad (3.23)$$

where  $A^{\text{LI}}$  and  $A^{\text{NL}}$  are the time domain equivalents of  $\tilde{A}^{\text{LI}}$  and  $\tilde{A}^{\text{NL}}$ , respectively. Using expressions (3.18) to (3.23) we are able to describe the reverse propagation of signal in fiber, in a similar way as the DBP-SSFM algorithm. Therefore, henceforward we will denominate this technique as DBP-VSTF. On the contrary of the DBP-SSFM, which is an iterative method, the DBP-VSTF of equation (3.18) shows the advantage of being an approximated closed-form solution of the inverse NLSE within each fiber span.

## Numerical implementation

Being entirely applied in frequency domain, the inverse VSTF requires block processing of the incoming samples. Therefore, the input signal is initially divided into blocks of  $N$  samples which are transformed into frequency domain by an FFT. In order

---

<sup>2</sup>Note that in context of single-span equalization the spatial variable in  $K_3$  is always  $z = L_s$ . Therefore, in order to simplify the notation, we have dropped the  $z$ -dependency in  $K_3$ .

<sup>3</sup>In order to simplify the notation, and to match the adopted discrete Fourier transform for numerical implementation (see equation (3.25)), in this Chapter we will drop the  $1/(4\pi^2)$  factor in the double integral of the inverse VSTF.

### 3.3. DBP Using the Inverse Volterra Series Transfer Function

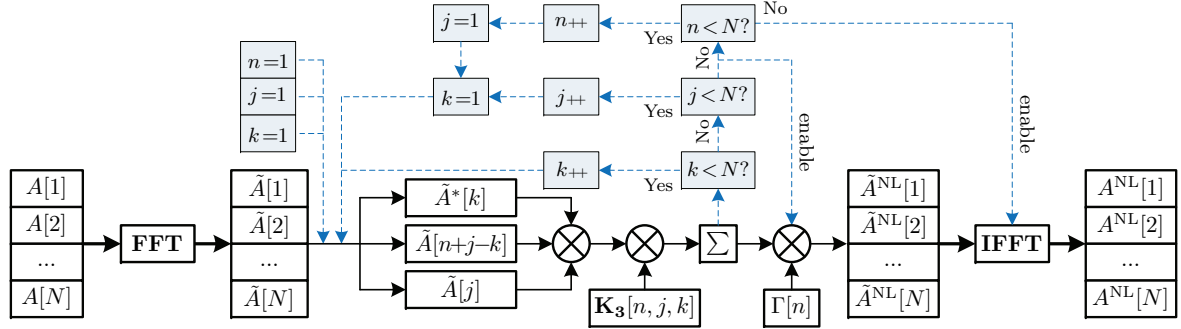


**Figure 3.6:** Serial implementation of the single-polarization VSNE algorithm for a single fiber span and a single FFT block. Blue line paths correspond to the control plane of the algorithm, whereas the black line paths represent actual computations. The received samples are stored in a  $N$ -length buffer and transformed into frequency domain using an FFT. Then, the operations within the double summation in equation (3.26) are performed and the obtained value is sent to the accumulation block. Each time equation (3.26) is completed, a sample is released to the output frequency buffer. Finally, when the output buffer is full, the time domain nonlinearly equalized signal is obtained by applying an IFFT.

to break the cyclic convolution imposed by the FFT, methods such as the overlap-add or overlap-save must be applied. Assuming uniform sampling, the angular frequencies,  $\omega_n$ , are obtained as,

$$\omega_n = (n - 1)\Delta\omega - \pi f_s, \quad 1 \leq n \leq N, \quad n \in \mathbb{N}, \quad (3.24)$$

where  $f_s$  is the sampling rate in Hz and  $\Delta\omega = 2\pi f_s/N$  defines the angular frequency grid. To implement the frequency domain transformation, the following discrete Fourier transform (DFT) definition is adopted,

$$\tilde{A}(\omega_n) = \frac{1}{N} \sum_{k=1}^N A(t_k) \exp\left(i \frac{2\pi(n-1)(k-1)}{N}\right), \quad (3.25)$$

consistently with the previously defined NLSE formulation [34]. Since the DFT definition is based on a discretization of the continuous Fourier transform using a left Riemann sum, we may directly substitute the double integral in Eq. (3.18) by two algebraic sums over the entire integration range. In a span-by-span basis, each sample of the nonlinearly equalized input field spectrum,  $\tilde{A}^{\text{NL}}(\omega_n)$ , is then obtained at the expense of an  $N$ -length FFT of the output field, by applying the transfer function

$$\tilde{A}^{\text{NL}}(\omega_n, z - L_s) = \Gamma(\omega_n, L_s) \sum_{j=1}^N \sum_{k=1}^N K_3(\omega_n, \omega_k, \omega_j) \tilde{A}(\omega_k, z) \tilde{A}^*(\omega_j, z) \tilde{A}(\omega_{n+j-k}, z), \quad (3.26)$$

where  $j$  and  $k$  are auxiliary indices used to evaluate the double sum for each block of frequency samples. Each sample of the nonlinearly equalized optical field,  $\tilde{A}^{\text{NL}}$ , at position  $z - L_s$  is then obtained by a two-dimensional weighting function,  $K_3(\omega_n, \omega_k, \omega_j)$ , of the input optical field,  $\tilde{A}$ , at position  $z$ . Because equation (3.26) enables to equalize

only the third-order nonlinear impairments, independently of the linear equalization subsystem, henceforward it will be designated as a Volterra series nonlinear equalizer (VSNE). The single-span VSNE of equation (3.26) is then sequentially applied to each sample of the current FFT block. The numerical implementation of the VSNE described by equation (3.26) is schematically depicted in Figure 3.6, considering a serial processing paradigm.

### Multi-span DBP-VSTF

Analogously to the forward VSTF described in Chapter 2, the DBP-VSTF of the full optical link composed of  $N_s$  fiber spans, such that  $L = N_s L_s$ , can be obtained either by i) concatenating equation (3.18)  $N_s$  times, or ii) coherently add the nonlinear field contributions of each fiber span, applying a phased-array factor [35–37],

$$F(\omega_n, \omega_k, \omega_j) = \exp\left(-i \frac{\Delta\beta_{j,k}(\omega_n)}{2} (N_s - 1)L_s\right) \frac{\sin(\Delta\beta_{j,k}(\omega_n)N_s L_s/2)}{\sin(\Delta\beta_{j,k}(\omega_n)L_s/2)}, \quad (3.27)$$

where  $\Delta\beta_{j,k}(\omega) = \beta_2(\omega_k - \omega)(\omega_k - \omega_j)$ . Using the phased-array factor,  $F(\omega_n, \omega_k, \omega_j)$ , a multi-span third-order Volterra kernel can be obtained as,

$$K_3^{\text{MS}}(\omega_n, \omega_k, \omega_j) = F(\omega_n, \omega_k, \omega_j)K_3(\omega_n, \omega_k, \omega_j). \quad (3.28)$$

The multi-span VSNE is then obtained by replacing the single-span  $K_3$  kernel by its multi-span equivalent of (3.28), enabling to implement DBP over  $N_s$  fiber spans in a single step,

$$\tilde{A}^{\text{NL}}(\omega_n, z-L) = \Gamma(\omega_n, L) \sum_{j=1}^N \sum_{k=1}^N K_3^{\text{MS}}(\omega_n, \omega_k, \omega_j) \tilde{A}(\omega_k, z) \tilde{A}^*(\omega_j, z) \tilde{A}(\omega_{n+j-k}, z). \quad (3.29)$$

Note however, that the concatenation of multiple third-order DBP-VSTF spans originates higher-order nonlinearities that cannot be captured by the phased-array factor. Therefore, the performance of the multi-span DBP-VSTF is expected to gradually degrade with increasing  $N_s$ . This effect will be thoroughly assessed both by numerical simulation and experimental validation in chapter 4.

### 3.3.2 Dual-polarization optical systems

The DBP-VSTF technique of equation (3.18) and the corresponding VSNE algorithm described by equations (3.26) and (3.29) and by Figure 3.6, has been derived from the scalar inverse NLSE and therefore is only valid for single-polarization optical systems. Extending this technique to dual-polarization optical systems requires to perform a similar derivation for the inverse Manakov equation of (3.3), yielding

$$\tilde{A}_{x/y}^{\text{NL}}(\omega_n, z - L_s) = \frac{8}{9} \Gamma(\omega_n, L_s) \sum_{j=1}^N \sum_{k=1}^N K_3(\omega_n, \omega_k, \omega_j) \tilde{P}(\omega_j, \omega_k, z) \tilde{A}_{x/y}(\omega_{n+j-k}, z), \quad (3.30)$$

### 3.3. DBP Using the Inverse Volterra Series Transfer Function

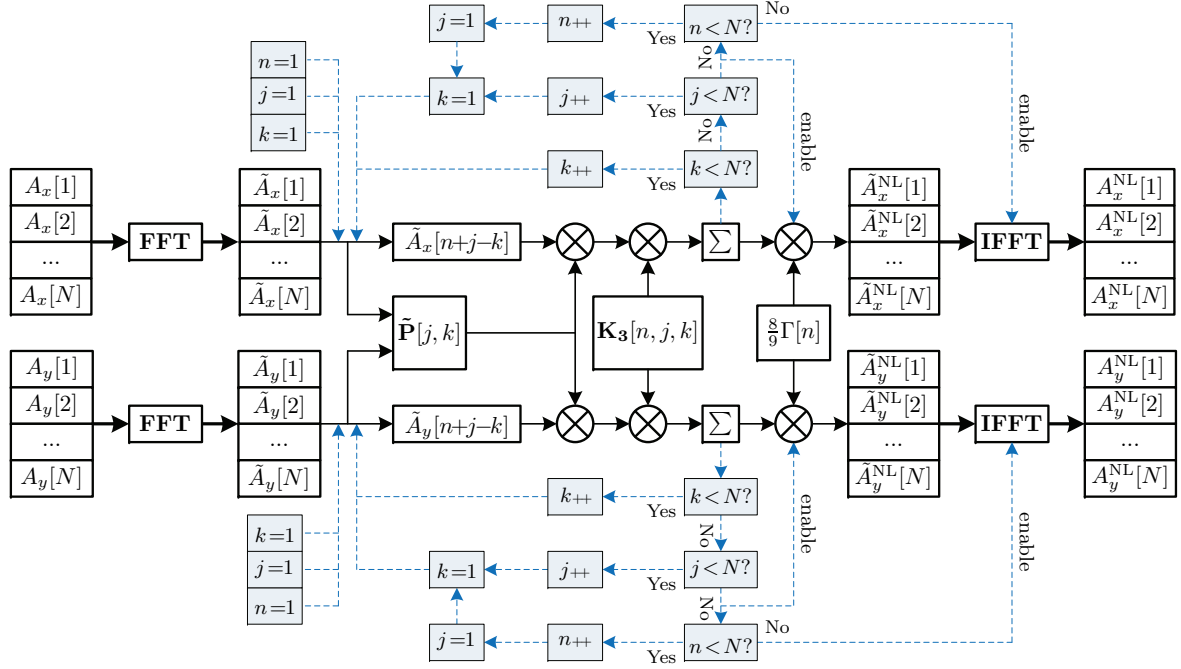


**Figure 3.7:** Serial implementation of the dual-polarization VSNE algorithm for a single fiber span and a single FFT block. Blue line paths correspond to the control plane of the algorithm, whereas the black line paths represent actual computations.

where  $\tilde{A}_{x/y}$  represents the optical field envelope in the  $x/y$  polarization components and  $\tilde{P}(\omega_j, \omega_k, z)$  accounts for the overall frequency domain beating due to intra- and inter-polarization crosstalk,

$$\tilde{P}(\omega_j, \omega_k, z) = \tilde{P}_{xx}(\omega_j, \omega_k, z) + \tilde{P}_{yy}(\omega_j, \omega_k, z), \quad (3.31)$$

where  $\tilde{P}_{xx/yy}(\omega_j, \omega_k, z) = \tilde{A}_{x/y}(\omega_k, z)\tilde{A}_{x/y}^*(\omega_j, z)$ . Note that the linear and third-order nonlinear Volterra kernels maintain their original definition of equations (3.19) and (3.20). A factor of  $\frac{8}{9}$  stemming from the Manakov approximation affects the overall nonlinearly equalized optical field in each polarization component.

The numerical implementation of the dual-polarization VSNE is schematically presented in Figure 3.7. Note that, similarly to the DBP-SSFM, the architecture of the dual-polarization DBP-VSTF naturally expands from its single-polarization implementation by introducing nonlinear polarization crosstalk paths and the averaging factor of  $8/9$ .

In order to simplify the mathematical description and facilitate the visual interpretation of the VSNE technique, a matrix-based notation can be adopted. The VSNE numerical implementation can be redefined as a Hadamard (entrywise) product of  $N$ -by- $N$  matrices. The double summation in (3.30) can then be rewritten as

$$\tilde{\mathbf{N}}_{\mathbf{x}/\mathbf{y}}(\omega_n, z) = \mathbf{K}_3(\omega_n) \circ \tilde{\mathbf{P}}(z) \circ \tilde{\mathbf{A}}_{\mathbf{x}/\mathbf{y}}(\omega_n, z), \quad (3.32)$$

where  $\mathbf{K}_3$  is the two-dimensional third-order Volterra kernel, whose matrix elements<sup>4</sup> are

<sup>4</sup>Note that  $(\cdot)^{(j,k)}$  represents the element lying in the  $j$ -th row and  $k$ -th column of the  $(\cdot)$  matrix.

$$\mathbf{K}_3^{(j,k)}(\omega_n) = K_3(\omega_n, \omega_k, \omega_j),$$

$$\mathbf{K}_3(\omega_n) = \begin{matrix} & & & & k \\ & & & & \overbrace{\left[ \begin{array}{cccc} K_3(\omega_n, \omega_1, \omega_1) & K_3(\omega_n, \omega_2, \omega_1) & \dots & K_3(\omega_n, \omega_N, \omega_1) \\ K_3(\omega_n, \omega_1, \omega_2) & K_3(\omega_n, \omega_2, \omega_2) & \dots & K_3(\omega_n, \omega_N, \omega_2) \\ \vdots & \vdots & \ddots & \vdots \\ K_3(\omega_n, \omega_1, \omega_N) & K_3(\omega_n, \omega_2, \omega_N) & \dots & K_3(\omega_n, \omega_N, \omega_N) \end{array} \right]}^j \\ & & & & \end{matrix}, \quad (3.33)$$

The  $\tilde{\mathbf{P}}$  matrix is defined as  $\tilde{\mathbf{P}}^{(j,k)}(z) = \tilde{P}(\omega_j, \omega_k, z)$ . Alternatively,  $\tilde{\mathbf{P}}$  can be decomposed into  $\tilde{\mathbf{P}}(z) = \tilde{\mathbf{P}}_{\mathbf{xx}}(z) + \tilde{\mathbf{P}}_{\mathbf{yy}}(z)$ , with  $\tilde{\mathbf{P}}_{\mathbf{xx}/\mathbf{yy}}$  defined as

$$\tilde{\mathbf{P}}_{\mathbf{xx}/\mathbf{yy}}(z) = \begin{bmatrix} |\tilde{A}_{x/y}(\omega_1, z)|^2 & \tilde{A}_{x/y}(\omega_2, z)\tilde{A}_{x/y}^*(\omega_1, z) & \dots & \tilde{A}_{x/y}(\omega_N, z)\tilde{A}_{x/y}^*(\omega_1, z) \\ \tilde{A}_{x/y}(\omega_1, z)\tilde{A}_{x/y}^*(\omega_2, z) & |\tilde{A}_{x/y}(\omega_2, z)|^2 & \dots & \tilde{A}_{x/y}(\omega_N, z)\tilde{A}_{x/y}^*(\omega_2, z) \\ \vdots & \vdots & \ddots & \vdots \\ \tilde{A}_{x/y}(\omega_1, z)\tilde{A}_{x/y}^*(\omega_N, z) & \tilde{A}_{x/y}(\omega_2, z)\tilde{A}_{x/y}^*(\omega_N, z) & \dots & |\tilde{A}_{x/y}(\omega_N, z)|^2 \end{bmatrix}, \quad (3.34)$$

Finally,  $\tilde{\mathbf{A}}_{\mathbf{x}/\mathbf{y}}$  is a signal matrix defined as  $\tilde{\mathbf{A}}_{\mathbf{x}/\mathbf{y}}^{(j,k)}(\omega_n, z) = \tilde{A}_{x/y}(\omega_{n+j-k}, z)$ ,

$$\tilde{\mathbf{A}}_{\mathbf{x}/\mathbf{y}}(\omega_n, z) = \begin{bmatrix} \tilde{A}_{x/y}(\omega_n, z) & \tilde{A}_{x/y}(\omega_{n-1}, z) & \dots & \tilde{A}_{x/y}(\omega_{n-N+1}, z) \\ \tilde{A}_{x/y}(\omega_{n+1}, z) & \tilde{A}_{x/y}(\omega_n, z) & \dots & \tilde{A}_{x/y}(\omega_{n-N+2}, z) \\ \vdots & \vdots & \ddots & \vdots \\ \tilde{A}_{x/y}(\omega_{n+N-1}, z) & \tilde{A}_{x/y}(\omega_{n+N-2}, z) & \dots & \tilde{A}_{x/y}(\omega_n, z) \end{bmatrix}. \quad (3.35)$$

The matrix form of expressions (3.32) to (3.35) facilitates the analysis of the fundamental characteristics of the VSNE technique. It can be easily observed that the  $\tilde{\mathbf{P}}$  matrix is frequency-independent, i.e. it is independent of  $\omega_n$ , thus being constant within each FFT block. In turn,  $\mathbf{K}_3$  is frequency-dependent but  $z$ -independent, thus remaining constant between different FFT blocks. Finally,  $\tilde{\mathbf{A}}_{\mathbf{x}/\mathbf{y}}$  is a function of  $\omega_n$  and  $z$ , requiring continuous updating. The resulting product,  $\tilde{\mathbf{N}}_{\mathbf{x}/\mathbf{y}}$ , is a  $N$ -by- $N$  matrix from which the nonlinearly equalized field can be obtained,

$$\tilde{A}_{x/y}^{\text{NL}}(\omega_n, z - L_s) = \frac{8}{9}\Gamma(\omega_n, L_s) \sum_{j=1}^N \sum_{k=1}^N \tilde{\mathbf{N}}_{\mathbf{x}/\mathbf{y}}^{(j,k)}(\omega_n, z). \quad (3.36)$$

Finally, the dual-polarization DBP-VSTF output signal is obtained by summing up the linear and nonlinear equalized signals in both polarization components,

$$\tilde{A}_{\text{eq}}(\omega_n, z) = \tilde{A}_{x/y}^{\text{LI}}(\omega_n, z) + \tilde{A}_{x/y}^{\text{NL}}(\omega_n, z). \quad (3.37)$$

Alternatively, the output signal modification of equation (3.23) can be also be applied to reduce energy divergence for high optical powers.

Note that expressions (3.32) and (3.36) can be readily extended to single-polarization optical systems simply by setting  $\tilde{\mathbf{P}} = \tilde{\mathbf{P}}_{\mathbf{xx}/\mathbf{yy}}$  in (3.32) and removing the  $\frac{8}{9}$  term in (3.36).

**Figure 3.8:** Parallel implementation of the dual-polarization VSNE algorithm for a single fiber span and a single FFT block. An exemplary case of  $N = 8$  is depicted to ease visual interpretation. The input frequency domain signals in both polarization tributaries,  $\tilde{A}_{x/y}$ , are expanded into  $N$ -by- $N$  matrices,  $\tilde{\mathbf{A}}_{x/y}$ , and multiplied element-wise by the resulting matrix obtained from  $\mathbf{K}_3(\omega_n) \circ \tilde{\mathbf{P}}(z)$ , yielding the output  $\tilde{\mathbf{N}}_{x/y}(\omega_n, z)$  matrices. Each sample of the equalized output signal,  $\tilde{A}_{x/y}^{\text{NL}}(\omega_n)$ , is then obtained by summing all the  $\tilde{\mathbf{N}}_{x/y}$  elements. Animated figure is available in the digital document.

---

In addition, note that the multi-span VSNE can be obtained from (3.32), replacing the single-span third-order Volterra kernel,  $\mathbf{K}_3$ , by

$$\mathbf{K}_3^{\text{MS}}(\omega_n) = \mathbf{F}(\omega_n) \circ \mathbf{K}_3(\omega_n), \quad (3.38)$$

where  $\mathbf{F}^{(j,k)}(\omega_n) = F(\omega_n, \omega_k, \omega_j)$  and  $\mathbf{K}_3^{\text{MS}}$  is the multi-span third-order Volterra kernel.

### 3.3.3 Implementation complexity

Given the  $N$ -by- $N$  matrix multiplication of (3.32), it becomes apparent that the number of RMs required by the VSNE is proportional to  $N^2$  per sample, or  $N^3$  per FFT block. A more insightful analysis of the VSNE complexity can be performed by inspecting the specificities of its numerical implementation.

Taking advantage of the matrix formulation of equation (3.32), a two-dimensional VSNE architecture is depicted in Figure 3.8, which enables to clearly expose its highly parallel implementation. Each nonlinearly equalized sample in the two polarization tributaries,  $\tilde{A}_{x/y}^{\text{NL}}(\omega_n)$ , is obtained at the expense of 3 matrix multiplications. As depicted in Figure 3.8 and evidenced by expression (3.35), the signal matrices,  $\tilde{\mathbf{A}}_{x/y}$ , are characterized by constant main diagonals. In addition, due to the  $N$ -samples FFT, not all matrix entries are valid. Indeed, the  $\tilde{A}_{x/y}(\omega_{n+j-k}, z)$  values are only valid for  $1 \leq n + j - k \leq N$ . Other index values correspond to out-of-band components that must be rejected during numerical implementation. As a result,  $\tilde{\mathbf{A}}_{x/y}$  can be seen as a sparse matrix, that evolves from lower triangular ( $n = 1$ ) to upper triangular ( $n = N$ ),

---

being a banded matrix ( $1 < n < N$ ) in between. Consequently, only a fraction of the  $N^2$  elements in  $\tilde{\mathbf{A}}_{\mathbf{x}/\mathbf{y}}$  are in fact used to evaluate the VSNE. The effective number RMs required by (3.32) is then proportional to the number of non-zero  $\tilde{\mathbf{A}}_{\mathbf{x}/\mathbf{y}}$  elements per equalized sample,  $N_{\text{el/sp}}$ , which depends on the sample index,  $n$ , as

$$N_{\text{el/sp}}(n) = \frac{N}{2}(N+1) + (n-1)(N-n). \quad (3.39)$$

The total number of non-zero elements in  $\tilde{\mathbf{A}}_{\mathbf{x}/\mathbf{y}}$  per FFT block,  $N_{\text{el/FFT}}$ , is then given by

$$N_{\text{el/FFT}} = \sum_{n=1}^N N_{\text{el/sp}}(n) = \frac{2}{3}N^3 + \frac{1}{3}N. \quad (3.40)$$

Given that the  $\mathbf{K}_3(\omega_n) \circ \tilde{\mathbf{P}}(z)$  operation is polarization-independent, only 1 matrix multiplication is required. In turn,  $(\mathbf{K}_3(\omega_n) \circ \tilde{\mathbf{P}}(z)) \circ \tilde{\mathbf{A}}_{\mathbf{x}/\mathbf{y}}(\omega_n, z)$  requires 2 extra matrix multiplications (1 per polarization). Hence the total number of RMs per sample associated with the evaluation of expression (3.8) is given by,

$$M_{\mathbf{K}_3 \circ \tilde{\mathbf{P}} \circ \tilde{\mathbf{A}}} (N) = \frac{4(N_{\text{pol}} + 1)}{N} \left( \frac{2}{3}N^3 + \frac{1}{3}N \right) = 4(N_{\text{pol}} + 1) \left( \frac{2}{3}N^2 + \frac{1}{3} \right). \quad (3.41)$$

Since the  $\mathbf{K}_3$  matrix does not depend on the input signal, it has to be calculated only once and stored in memory. Therefore, the computational effort required for its calculation can be neglected. In addition, the  $\tilde{\mathbf{P}}$  matrix does not depend on the current sample, and thus it has to be evaluated only once per FFT block. Given that  $\tilde{\mathbf{P}}$  is an Hermitian matrix, its upper (lower) triangular elements can be directly obtained from the lower (upper) triangular ones by simple changing the sign of the imaginary part. Thus, the number of distinct elements in  $\tilde{\mathbf{P}}$  is reduced to  $N^2/2 + N/2$ , and the associated number of RMs per sample is given by

$$M_{\tilde{\mathbf{P}}} (N) = \frac{4N_{\text{pol}} \left( \frac{N^2}{2} + \frac{N}{2} \right)}{N} = 2N_{\text{pol}}(N+1). \quad (3.42)$$

Finally, the multiplication by the  $\Gamma(\omega_n, L_s)$  term in (3.36) requires an additional CM per polarization, so that the overall VSNE complexity in number of RMs per sample can be analytically described as,

$$\begin{aligned} M_{\text{VSNE}}(N) &= M_{\mathbf{K}_3 \circ \tilde{\mathbf{P}} \circ \tilde{\mathbf{A}}} (N) + M_{\tilde{\mathbf{P}}} (N) + 4N_{\text{pol}} \\ &= \frac{8}{3} (N_{\text{pol}} + 1) N^2 + 2N_{\text{pol}}N + \frac{22}{3}N_{\text{pol}} + \frac{4}{3}. \end{aligned} \quad (3.43)$$

The total number of RMs per sample required by the DBP-VSTF,  $M_{\text{DBP-VSTF}}$ , is then given by

$$M_{\text{VSTF}}(N) = N_{\text{steps}} [M_{\text{VSNE}}(N) + M_{K_1}] + 2N_{\text{pol}}M_{\text{FFT}}(N), \quad (3.44)$$

where  $2N_{\text{pol}}M_{\text{FFT}}(N)$  is the complexity associated with the FFT/IFFT pair required for the time-frequency transformation. Note that, on the contrary of the DBP-SSFM, the

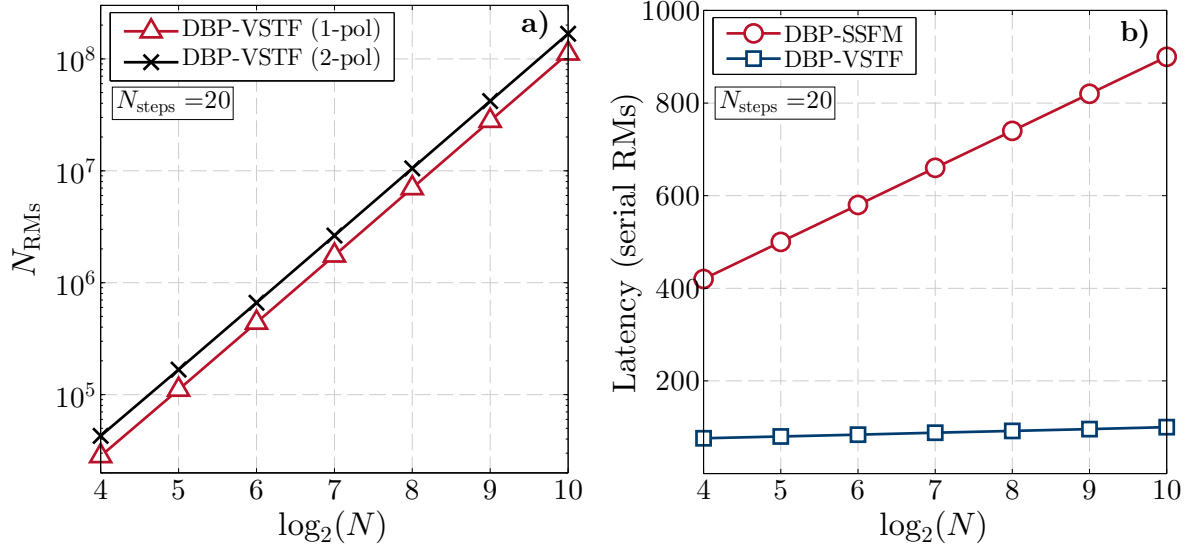


**Figure 3.9:** Implementation complexity, in terms of latency and overall number of RMs, of the DBP-VSTF algorithm, considering a total of 20 DBP steps. a) Number of RMs,  $N_{\text{RMs}}$ , as a function of the FFT block-size,  $N$ ; b) Latency in terms of serial RMs as a function of  $N$ , required by the DBP-VSTF and DBP-SSFM algorithms.

entire algorithm is implemented in frequency domain, so that FFT only needs to be applied in the first step and the corresponding IFFT is applied in the last step. The  $M_{K_1}(N)$  term represents the number of RMs required for the computation of  $\tilde{A}_{x/y}^{\text{LI}}$  in frequency domain using the linear kernel,  $K_1$ , in equation (3.18). Hence, its complexity in number of RMs per sample is

$$M_{K_1} = 4N_{\text{pol}}. \quad (3.45)$$

The analysis of the DBP-VSTF latency is much simpler, as it can be straightforwardly observed from expressions (3.32) and (3.36) that only 4 serial multiplications are involved for the determination of  $\tilde{A}_{x/y}^{\text{NL}}$ . In addition, the latency associated with the FFT/IFFT must also be taken into account, yielding

$$\tau_{\text{VSTF}} = 4N_{\text{steps}} + 2\tau_{\text{FFT}}. \quad (3.46)$$

Note that both the complexity and latency described by expressions (3.44) and (3.46) assume that the output modification of expression (3.23) is not adopted, enabling fully frequency domain processing. Alternatively, if DBP-MVSTF is to be used instead of the DBP-VSTF, the complexity and latency expressions must be redefined as

$$M_{\text{MVSTF}}(N) = N_{\text{steps}} [M_{\text{VSNE}}(N) + N_{\text{pol}}M_{K_1} + 2N_{\text{pol}}M_{\text{FFT}}(N)], \quad (3.47)$$

and

$$\tau_{\text{MVSTF}} = N_{\text{steps}} (4 + 2\tau_{\text{FFT}}), \quad (3.48)$$

where an FFT/IFFT pair is now required in each step.

The complexity of the single- and dual-polarization DBP-VSTF algorithms as given by expression (3.44) is illustrated in Figure 3.9, for a set of FFT values,  $N$ . As evidenced by expression (3.43), the DBP-VSTF complexity is dominated by a  $O(N^2)$  term, causing a quadratic dependence of  $N_{\text{RMs}}$  on  $N$ . Also note that due to the  $O(N^2)$  term in (3.43), the single-polarization DBP-VSTF implies approximately  $\frac{2}{3}$  of the corresponding dual-polarization algorithm. A quick comparison between Figures 3.5 and 3.9a reveals that the overall number of RMs required by the DBP-VSTF largely surpasses that of the DBP-SSFM for FFT block-sizes of practical interest. However, the highly parallel implementation of the DBP-VSTF can be very advantageous for a real-time implementation. This advantage is well captured by the latency expressions of (3.17) and (3.46) plotted in Figure 3.9b, which expose the superior efficiency of the DBP-VSTF algorithm for increasing  $N$ , making it a potential attractive candidate for real-time implementation. In addition, although 20 DBP have been considered in Figure 3.9b for both algorithms, the DBP-VSTF technique can potentially be applied with much coarser step-sizes, given its non-iterative analytical definition. This potential advantage will be comprehensively assessed in section 3.4 through numerical simulations. In addition, a thorough analysis of the VSNE computational effort is carried out in chapter 4, employing a kernel reconstruction technique and critical simplifications to reduce the overall number of computations.

## 3.4 Numerical Assessment

In this section, a comprehensive numerical assessment of the previously described DBP techniques is performed, considering both single-polarization and dual-polarization optical transmission systems. Considering that the DBP-SSFM has been the most widely used nonlinear compensation method in optical fiber links, the simulation analysis described in this section will be supported by comprehensive performance comparisons between the DBP-VSTF and DBP-SSFM techniques. The following analysis includes the impact of critical receiver-side and digital equalization aspects, such as the temporal and spatial resolution used for DBP and the electrical analog bandwidth of the receiver, together with the impact of optical signal propagation for varying input powers, transmission distances and fiber parameters. A computational effort comparison between DBP techniques is also presented, taking into account the considered simulation scenarios.

### 3.4.1 Single-polarization optical systems

Following the organization of sections 3.2 and 3.3, this numerical analysis section will be initiated by a dedicated treatment of single-polarization optical transmission systems, with the aim to assess the performance and complexity of the corresponding single-polarization DBP algorithms introduced in sections 3.2 and 3.3. For this purpose, a 40 Gb/s QPSK optical transmission system will be considered. Extension to dual-polarization transmission will be addressed in section 3.4.2.

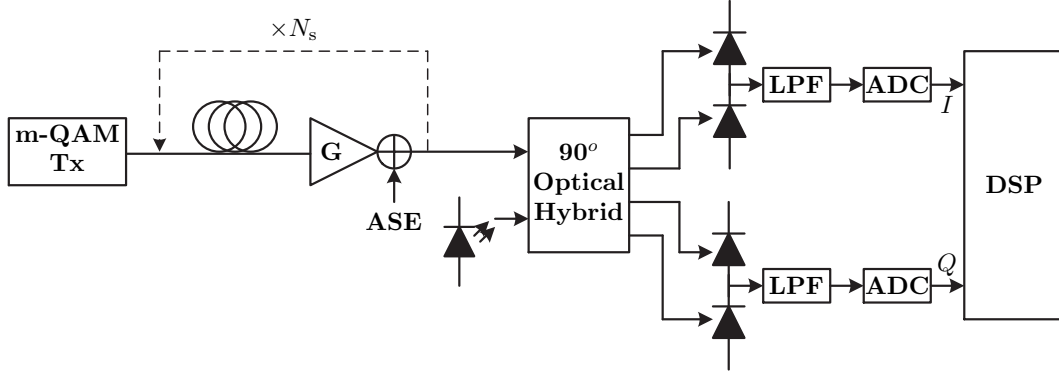


**Figure 3.10:** Coherent single-polarization m-QAM optical system model adopted for simulation purposes. The QPSK optical signal is modulated in a m-QAM transmitter and injected in a recirculating loop composed of a fiber span and an amplification stage with ideal gain,  $G$ , and added ASE noise.

### Simulation model

The simulation model adopted for numerical assessment of the DBP-SSFM and DBP-VSTF techniques is shown in Figure 3.10, consisting of a single-channel coherent QPSK optical transmission system with post-detection DSP for the mitigation of fiber impairments. A 40 Gb/s QPSK signal is modulated at the transmitter and propagated over  $20 \times 80$  km of both SSMF and NZDSF. The emulation of forward signal propagation in fiber has been performed by the symmetric SSFM with a step-size of 10 m and a sampling rate of 640 GHz to solve the scalar NLSE. The simulation model does not include any in-line dispersion compensation modules. This option is based on the results obtained in [8], where it was shown that the use of in-line dispersion compensation degrades the system performance when using DBP for impairment compensation. Optical amplification with ideal gain coefficient and 5 dB noise figure is applied at the end of each fiber span. For simplicity, laser phase noise and frequency mismatch between the received and LO laser have been neglected. The 90 degree optical hybrid and the pair of balanced photodiodes are assumed to perform optical-to-electrical down-conversion without distorting the received signal. The most relevant simulation and transmission system parameters are summarized in Table 3.1.

The error vector magnitude (EVM) percentage relatively to the optimal constellation

**Table 3.1:** Set of numerical parameters corresponding to the simulation model of Fig. 3.10.

Input Signal	SSMF	NZDSF	Optical Amplifier
Format: NRZ-QPSK	$\alpha = 0.2$ dB/km	$\alpha = 0.2$ dB/km	$G = 16$ dB
$R_b = 40$ Gb/s	$\beta_2 = -20.4$ ps <sup>2</sup> /km	$\beta_2 = -6.0$ ps <sup>2</sup> /km	$F_n = 5$ dB
$N_{\text{bits}} = 32768$	$\gamma = 1.3$ W <sup>-1</sup> km <sup>-1</sup>	$\gamma = 1.5$ W <sup>-1</sup> km <sup>-1</sup>	
	$L_s = 80$ km	$L_s = 80$ km	

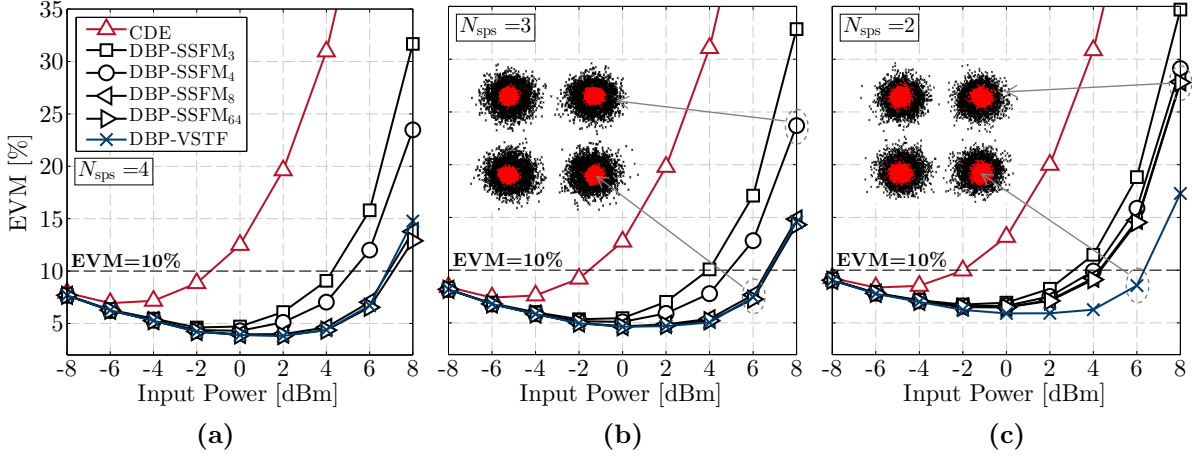


**Figure 3.11:** EVM after digital equalization of a 40 Gb/s QPSK signal propagated over  $20 \times 80$  km of SSMF. The oversampling factors are a) 4; b) 3; c) 2. The insets in b) and c) represent the QPSK constellation after compensation with the DBP-VSTF and DBP-SSFM<sub>4</sub> at 6 dBm and 8 dBm input power, respectively, clearly illustrating the SNR enhancement provided by high performance DBP.

is used as a figure of merit for compensation performance, defined as

$$\text{EVM}[\%] = \sqrt{\frac{\sum |A_{\text{eq}} - A_{\text{tx}}|^2}{\sum |A_{\text{tx}}|^2}} \times 100\%, \quad (3.49)$$

where  $A_{\text{tx}}$  and  $A_{\text{eq}}$  are the transmitted and equalized optical fields, respectively. The EVM is calculated over 16384 symbols, corresponding to 32768 bits, as indicated in Table 3.1.

After coherent detection, the baseband signal is passed through a third-order Butterworth low-pass filter (LPF) with cutoff frequency at 80% of the symbol rate, in order to filter the out-of-band ASE noise and reduce the aliasing effect due to downsampling. Finally, the digital equalization stage follows. Linear equalization (linear DBP) is performed with a frequency domain chromatic dispersion equalizer (CDE). Full compensation of linear and nonlinear impairments is achieved by the single-polarization DBP-SSFM and DBP-VSTF algorithms. The DBP-SSFM with  $N_{\text{steps}}$  steps per fiber span is denoted as DBP-SSFM <sub>$N_{\text{steps}}$</sub> .

### Impact of the sampling rate and propagation length in an SSMF link

To initiate the numerical assessment let us consider the impact of the ADC sampling rate, i.e. the temporal resolution, on the equalization performance of the previously addressed DBP techniques. A set of numerical results obtained for the simulation model of Figure 3.10 is shown in Figures 3.11 and 3.12, considering variable input powers and propagation length, respectively.

The results presented in Figures 3.11a and 3.11b, corresponding to the application of DBP with 4 and 3 samples per symbol, show that the three best performance curves

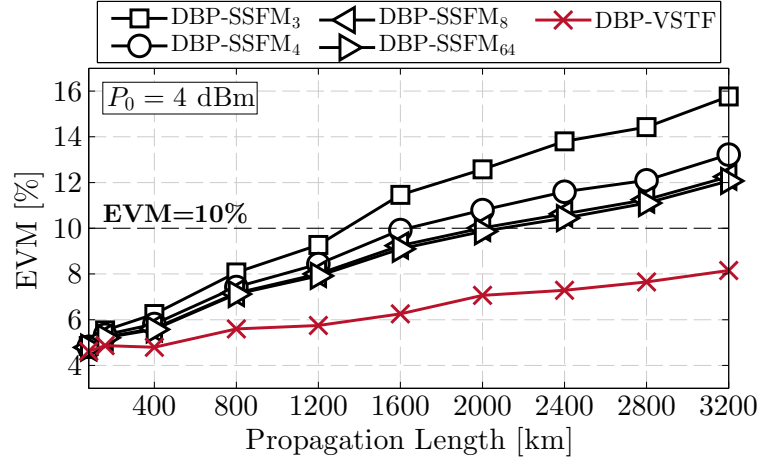


**Figure 3.12:** EVM after digital equalization of a 40 Gb/s QPSK signal, as a function of propagation length, for a fixed input power of 4 dBm and  $2\times$  oversampling.

corresponding to DBP-SSFM<sub>8</sub>, DBP-SSFM<sub>64</sub> and DBP-VSTF are almost completely overlaid, which enables to draw two main conclusions. First, it becomes clear that DBP-SSFM algorithms reaches its performance limit at approximately 8 steps per span for the considered simulation scenario. This spatial resolution limitation is caused by two main factors: i) the considered  $low^5$  temporal resolution of only 4 and 3 samples per symbol, and ii) the accumulated ASE during signal propagation, that prevents more accurate optical field estimation at each DBP-SSFM step. These constraints set the upper limit for DBP-SSFM compensation performance, above which it becomes useless to increase the spatial resolution. Secondly, it is also shown that the third-order approximation used to derive the DBP-VSTF is sufficient to approximately reach the best DBP performance at the considered sampling rates. In fact, Figure 3.11a shows a marginal advantage of the DBP-SSFM with 8 and 64 steps per span for very high input powers ( $>6$  dBm), which exposes the performance limit of the DBP-VSTF third-order approximation. However, at 3 samples per symbol, this small gap between highest performance curves is not visible anymore, denoting a slightly higher degradation of performance of the DBP-SSFM with the sampling rate reduction from  $N_{\text{sps}} = 4$  to  $N_{\text{sps}} = 3$ . Indeed, when the temporal resolution is further reduced to the Nyquist limit of 2 samples per symbol,  $N_{\text{sps}} = 2$ , as shown in Figure 3.11c, the DBP-SSFM shows a significative degradation of performance, with the maximum spatial resolution now being reduced to approximately 4 steps per span. In contrast, the DBP-VSTF performance is only marginally affected by this loss of temporal resolution, enabling to achieve a superior performance, which translates into a  $\sim 2$  dB improvement in nonlinear tolerance relatively to the DBP-SSFM, considering the 10% limit in EVM values for which the system BER is kept bellow  $10^{-9}$ . The degradation of performance experienced by the DBP-SSFM at 2 samples per symbol is attributed to the aliasing components generated by the time domain implementation of the nonlinear

<sup>5</sup>Note that, albeit 4 samples per symbol can be considered as a low temporal resolution for DBP compared with the sampling rates used for signal propagation modelling, commercial optical transmission systems typically operate at 2 samples per symbol.

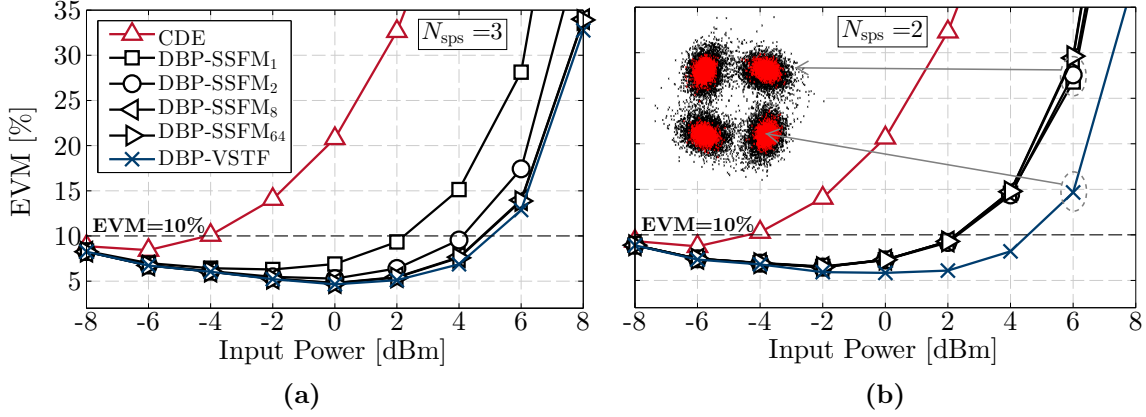


**Figure 3.13:** EVM after digital equalization of a 40 Gb/s QPSK signal transmitted over  $20 \times 80$  km of NZDSF. The oversampling factors are a) 3 and b) 2. The insets represent the QPSK constellation after compensation with the DBP-VSTF and DBP-SSFM<sub>2</sub> at 6 dBm input power.

operator, which is subsequently transposed to frequency domain in order to apply the linear step. In fact, the DBP-SSFM has been reported to require at least 3 samples per symbol in order to produce reliable results [24]. In order to partially overcome this issue, a modified DBP-SSFM version has been proposed in [38], using a low-pass filtering stage within the nonlinear operator to filter out the high frequency components generated in the intensity waveform in each nonlinear step. On its turn, the DBP-VSTF inherently avoids this aliasing enhancement phenomenon since it is entirely implemented in frequency domain. It is important to clarify, however, that aliasing still occurs at the sampling stage, and that the DBP-VSTF only avoids extra aliasing generation within the equalization stage.

Considering the Nyquist sampling rate of 2 samples per symbol, which is of particular interest for practical applications, the impact of propagation distance is analyzed in Figure 3.12, showing an increasing performance gain of the DBP-VSTF over DBP-SSFM with increasing reach. In fact, after 3200 km, the DBP-VSTF performance becomes comparable to the maximum DBP-SSFM performance at 1200 km, representing an improvement of approximately 2.6 fold in propagation distance.

### Performance comparison between SSMF and NZDSF links

The previous simulation scenario has been restricted to a non-dispersion-managed SSMF link. In the following, the DBP numerical assessment is extended to an NZDSF link, where the effect of nonlinearities is much stronger, both due to a higher Kerr coefficient and lower accumulated dispersion per unit length. This scenario serves the purpose of testing the robustness of the DBP-based algorithms in a highly nonlinear regime [39]. Complementarily to the results of Figure 3.11, the performance of DBP-SSFM and DBP-VSTF are evaluated in Figure 3.13 for a  $20 \times 80$  km NZDSF link. The remaining simulation parameters are in accordance with Table 3.1.

Similarly to the previous analysis performed in an SSMF link with  $3\times$  oversampling (see Figure 3.11b), the EVM results presented in Figure 3.13a show that the equalization performance of the DBP-VSTF technique approximately matches that of the best DBP-SSFM. However, the stronger effect of intra-channel nonlinearities causes a significant degradation of performance relatively to the SSMF link, which is well visible in the figure insets depicting signal constellations at 6 dBm input power. Note that, mostly due to the lower accumulated dispersion, the Gaussian-like shape of the QPSK constellations in Figure 3.11 is not observed anymore. Instead, the compensated constellations tend to acquire a phase-stretched shape, which is caused by the predominance of nonlinear phase noise, thus testifying the highly nonlinear regime. At  $2\times$  oversampling (see Figure 3.13b), it is shown that the DBP-SSFM performance becomes now limited to only 1 step per span, representing a significant loss of spatial resolution relatively to the SSMF link. This behavior exposes an increasing degradation of the DBP-SSFM performance with stronger nonlinear phenomena. Kerr effects, such as SPM, are known to generate high frequency components, which take increasing power spectral density as we move further into the nonlinear regime. When operating at low enough sampling rates such as 2 samples per symbol, these high frequencies are folded into the signal bandwidth during the transition between time and frequency domains, causing the aforementioned internal aliasing generation. It thus becomes apparent that this harmful aliasing effect will take increasing importance as nonlinearities become stronger, hindering the application of a hybrid time- and frequency domain equalization technique, such as the DBP-SSFM. In contrast, the DBP-VSTF technique applied with 2 samples per symbol only suffers from a slight performance degradation relatively to the  $3\times$  oversampling case, which is naturally caused by the loss of temporal resolution. As a result, we may observe a large accuracy gain over DBP-SSFM equalization at high input powers ( $>10\%$  EVM gain at 6 dBm). This simulation analysis thus enables to prove the robustness and high performance of the DBP-VSTF technique for digital equalization under highly nonlinear propagation regimes.

#### Required bandwidth for nonlinear equalization

One of the most important conclusions stemming from the numerical assessment performed so far is that the DBP-VSTF algorithm is able to operate with only 2 samples per symbol maintaining high performance. In terms of bandwidth this corresponds to use the information contained in 40 GHz to equalize a 20 Gbaud signal. In this section we aim to perform a more thorough assessment of the effective required bandwidth to apply the DBP-VSTF method.

The evolution of EVM after nonlinear equalization as a function of the 3 dB cutoff frequency in the 3rd order Butterworth LPF is shown in Figure 3.14. The results obtained at  $3\times$  oversampling (see Figure 3.14a) show similar accuracies between the DBP-VSTF and DBP-SSFM<sub>8</sub> methods and also a similar evolution with respect to the LPF cutoff frequency. The maximum accuracy is attained when the LPF cutoff frequency is around 18 GHz, corresponding to 90% of the symbol rate. For higher cutoff frequencies the equalization performance tends to degrade due to aliasing enhancement in the sampling stage. On the other hand, narrower filtering degrades performance

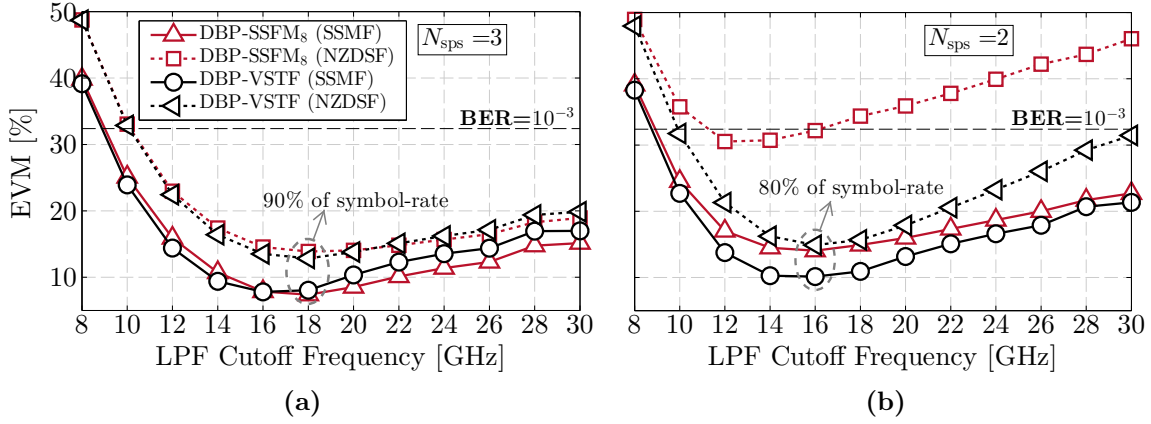


**Figure 3.14:** EVM after digital equalization of a 40 Gb/s QPSK signal, as a function of the LPF cutoff frequency. a)  $N_{\text{sps}} = 3$ ; b)  $N_{\text{sps}} = 2$ . Input optical power is 6 dBm. The  $10^{-3}$  BER limit corresponding to an EVM of 32.4% [40] is indicated by a horizontal dashed line.

due to the attenuation of relevant spectral components. The optical spectra of the propagated signal at different filtering and sampling stages is shown in Figure 3.15a. A similar analysis for  $2\times$  oversampling is shown in Figure 3.14b. As expected, since the aliasing effect tends to become stronger for lower sampling rates, the optimum cutoff frequency is now reduced to  $\sim 16$  GHz, corresponding to 80% of the symbol rate. The only exception is the DBP-SSFM<sub>8</sub> curve for an NZDSF transmission link, where the optimum LPF cutoff frequency is found at approximately 60% of the symbol rate. The strong effect of nonlinearities in the NZDSF link exposes the DBP-SSFM limitation in terms of internal aliasing generation. Although a narrower LPF before equalization can residually counteract this effect, it does not avoid a severe performance degradation relatively to the DBP-VSTF algorithm. Overall, this analysis in terms of LPF bandwidth provides a clearer picture of how nonlinear equalization performance may be impacted by tight electrical filtering in the receiver.

Let us now consider now that 3 samples per symbol are available for digital equalization. The DBP-VSTF algorithm can then be applied over a total bandwidth of 60 GHz, as shown in Figure 3.15a. However, the double summation indices of the VSNE filter in Equation (3.26) can be redefined in order to apply the method over a narrower bandwidth, thereby avoiding excessive computational effort. The performance impact of the spectral support extent used in the DBP-VSTF evaluation is shown in Figure 3.15b, where the spectral region used for nonlinear equalization has been gradually reduced from 60 GHz (full spectrum at 3 samples per symbol) down to 25 GHz by adjusting the double summation range of the VSNE filter in DBP-VSTF.

Although the effect of the LPF cutoff frequency is minor, it can be observed that a wider LPF tends to benefit equalization accuracy when the VSNE is evaluated over a broader spectral support, but it prejudices performance when a narrower spectral support is used. The EVM degradation between 60 GHz and 40 GHz is barely visible, confirming the DBP-VSTF capability to operate at 2 samples per symbol with negligible loss of performance. However, as expected, a severe penalty quickly arises when the spectral

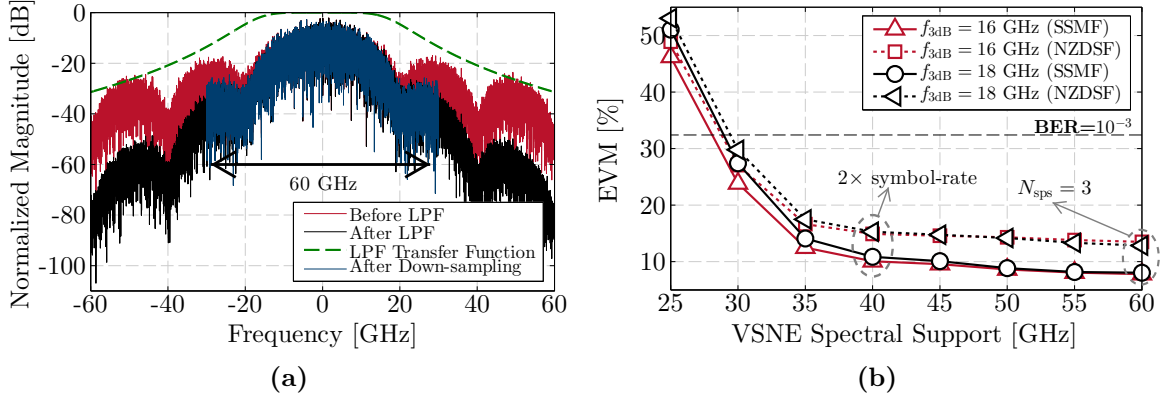


**Figure 3.15:** a) Optical spectra of the propagated signal before and after the LPF and after down-sampling at 3 samples per symbol. The LPF cutoff frequency is placed at 18 GHz. b) EVM after digital equalization of a 40 Gb/s QPSK signal, as a function of the VSNE spectral support and the LPF cutoff frequency ( $f_{3dB}$ ). The signal fed to the equalization block is sampled at 3 samples per symbol and the input power is 6 dBm.

support is further reduced, cutting higher power spectral components. In fact, it is shown that at least 80-90% of two times the symbol rate is required for an accurate nonlinear equalization.

### Computational Effort Assessment

Computational effort is a key measure for digital equalization of fiber impairments since real-time implementation is limited by currently available processing speeds and associated power consumption. The computational effort, in number of RMs per sample, required by the DBP-SSFM and DBP-VSTF algorithms, as given by expressions (3.16) and (3.44), is shown in Figure 3.16a, as a function of the FFT block-size,  $N$ . It becomes clear that reduced FFT block-sizes must be considered in order to keep the DBP-VSTF in a tolerable region of complexity. Indeed, the DBP-VSTF only provides lower overall complexity than the DBP-SSFM for FFT blocks of length up to 16 samples. However, it is well known that FFT block-size cannot be arbitrarily reduced without incurring inter-block interference. In order to break the circular convolution implemented by FFT/IFFT algorithms, the data must be partitioned into small blocks arranged with partial overlapping, using algorithms such as the overlap-and-add or overlap-and-save (OS). A schematic representation of the OS algorithm adopted in this work is shown in Figure 3.17. In order to guarantee the minimum FFT length, each  $N$ -sample block overlaps with  $N/2$  samples of the adjacent blocks, thereby assuming that the first and last  $N/4$  samples in each block are corrupted by the wrap around effect of circular convolution. Using this configuration, the minimum penalty-free FFT block-size depends on the duration of the impulse response associated with the fiber link, which is mainly set by the amount of accumulated chromatic dispersion. Longer fiber impulse response requires higher frequency resolution and hence larger FFT block-size. In order to assess the limits for the minimum FFT block-size, its adjustment has been carried out

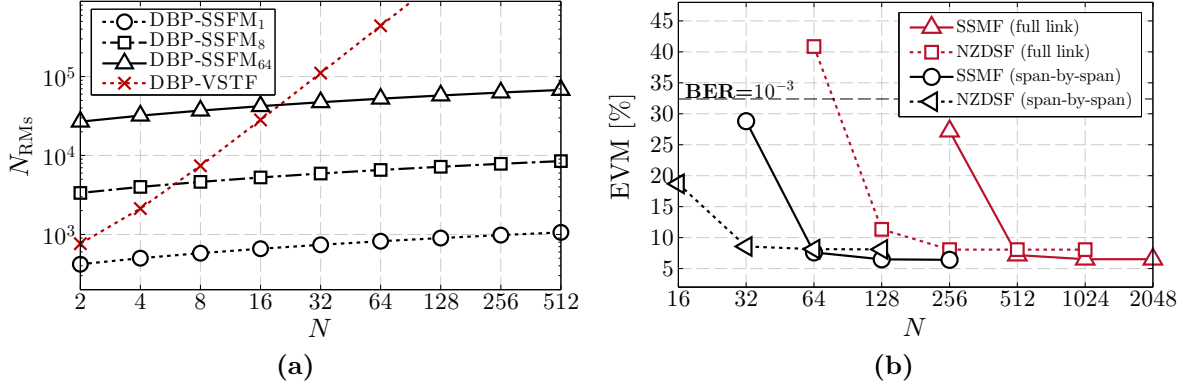


**Figure 3.16:** Analysis of the computational requirements associated with DBP-based impairment compensation. a) Number of RMs required by DBP-SSFM and DBP-VSTF as a function of the FFT block-size; b) Inter-block interference as a function of the FFT block-size. Red lines refer to the implementation of OS only in the first and last DBP steps. Black lines correspond to the span-by-span implementation of OS. Input power is 4 dBm and  $N_{sps} = 2$ .

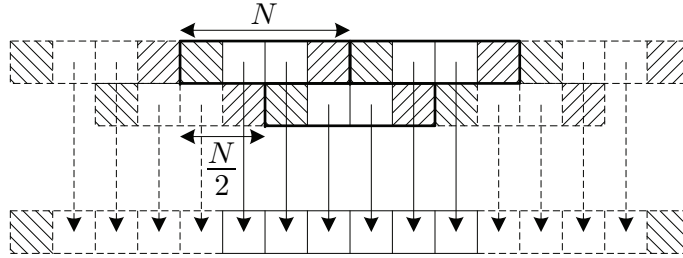


**Figure 3.17:** Overlap-and-save algorithm configuration adopted for frequency domain simulations. Each  $N$ -sample block overlaps with  $N/2$  samples of the previous and following blocks. Filled squares indicate corrupted data, in the first and last  $N/4$  samples of each block, due to the circular convolution. Empty squares indicate valid data.

numerically by assessing the EVM performance with varying block-sizes. In an initial approach, the OS method has been applied only at the link ends, i.e., the received samples are split into blocks and then rejoined when fully compensated (after  $N_s$  fiber spans). However, as shown in Figure 3.16b, the accumulated dispersion along the entire link requires large FFT blocks (128/256 for the NZDSF link and 512 for the SSMF link). In addition, the FFT block-size required by this approach would actually depend on the system under test, resulting in increasing  $N$  with increasing  $N_s$ . Alternatively, the OS method can also be applied in a span-by-span basis, reducing the accumulated dispersion that needs to be inverted in each step. This way, the penalty-free minimum FFT block-size can be reduced to 32 and 64, for the NZDSF and SSMF links, respectively. In fact, these values can be further reduced to 16 and 32 at the expense of some inter-block interference, maintaining the system below the  $10^{-3}$  BER floor.

This analysis suggests that a span-by-span implementation of the DBP-VSTF can be preferable in terms of computational requirements. A sub-span approach can also be considered if a further reduction of FFT block-size is worth the required additional

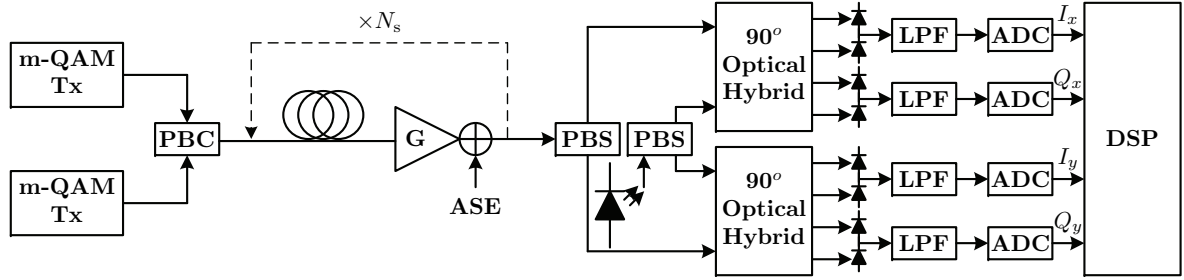


**Figure 3.18:** Coherent PM-QPSK optical system model adopted for simulation purposes. The simulation setup is similar to that of Figure 3.10 with duplicated transmitter and receiver structures. Additionally, the signal propagation in fiber must be now emulated using the coupled NLSE of equation (2.25), accounting for polarization-dependent effects.

iterations. Also note that the high performance of the DBP-VSTF algorithm, as demonstrated by the previously analyzed numerical results of Figures 3.11 to 3.15b, gives margin for further computational savings by neglecting less significant elements in the third-order Volterra kernel. This possibility will be thoroughly explored in chapter 4, using a kernel reconstruction approach and applying reduced complexity approximations.

As previously highlighted in section 3.3, a key advantage of the DBP-VSTF approach over DBP-SSFM, which is not depicted in Figure 3.16a, lies in its highly parallel structure, which eases the application of parallel processing strategies in order to enable real-time implementation. Besides, the DBP-VSTF provides independent compensation of linear and nonlinear impairments, using parallel CDE and VSNE equalizers, which enables to apply nonlinear compensation as an optional add-on for the equalization subsystem, thus bringing more flexibility and ease of implementation.

### 3.4.2 Dual-polarization optical systems

In order to numerically validate the dual-polarization DBP algorithms introduced in sections 3.2 and 3.3, in this section the previous simulation analysis will be extended to dual-polarization optical transmission systems. The importance of considering Manakov-based DBP is demonstrated through direct performance comparisons between the single- and dual-polarization DBP methods. A more detailed analysis of DBP performance in dual-polarization optical transmission systems is then continued in section 3.5, resorting to experimental results.

#### Simulation model

The simulation setup adopted in this section is based on the dual-polarization transmission system model presented in Figure 3.18. As opposed to the single-polarization simulation setup, which has been fully developed in MATLAB, the dual-polarization scenario depicted in Figure 3.18 has been partially implemented in VPItransmissionMaker8.6, taking advantage of its built-in functions and optical components, namely in terms of signal propagation in dual-polarization transmission systems. The down-sampling and post-detection DSP stages are then implemented in

MATLAB. Being the most realistic option in terms of practical implementation, a fixed sampling rate of twice the symbol-rate ( $N_{\text{sps}} = 2$ ) has been adopted for all simulation in this scenario. The considered 112 Gb/s PM-QPSK optical transmission link is composed of 20 spans of NZDSF, each with 80 km length. A linewidth of 100 kHz has been defined for both the transmitter and LO lasers. After coherent detection, the I and Q electrical currents are low-pass filtered by a third-order Butterworth filter with 22.4 GHz cutoff frequency and downsampled to 2 samples per symbol. Static equalization of chromatic dispersion is performed by a frequency domain CDE. Nonlinear equalization is implemented through DBP using the dual-polarization DBP-SSFM and DBP-VSTF techniques. The FFT block-length has been minimized to 64 samples without incurring inter-block interference. After the equalization subsystem, polarization demultiplexing and PMD compensation are performed by an adaptive  $2 \times 2$  multiple-input multiple-output (MIMO) filter with 25 taps, controlled by the CMA criterion [41]. Then, the carrier phase is estimated using a Viterbi-Viterbi algorithm [42]. The most relevant simulation parameters are shown in Table 3.2. The mean EVM between both states of polarization has been used as a figure of merit to quantify the performance of digital equalization, defined as

$$\text{EVM} = \frac{1}{2} \sqrt{\frac{\sum |A_{x,\text{eq}} - A_{x,\text{tx}}|^2}{\sum |A_{x,\text{tx}}|^2}} + \frac{1}{2} \sqrt{\frac{\sum |A_{y,\text{eq}} - A_{y,\text{tx}}|^2}{\sum |A_{y,\text{tx}}|^2}}. \quad (3.50)$$

where  $A_{x/y,\text{tx}}$  and  $A_{x/y,\text{eq}}$  represent the transmitted and equalized optical field envelopes in the  $x/y$  polarization tributaries, respectively.

### Simulation results

The input signal power has been varied between -2 dBm and 8 dBm with steps of 1 dB, in order to assess the impact of nonlinearities with increasing optical power. The obtained EVM results, as a function of input power and digital equalization method, are shown in Figure 3.19a [43, 44]. It can be readily observed that the system performance employing only CD equalization is severely limited by nonlinearities, yielding an optimum input optical power of approximately -1 dBm. In addition, it is also shown that only a small performance improvement is obtained by the use of single-polarization DBP. In fact, considering the 32.4% EVM limit which roughly corresponds to a BER of  $10^{-3}$  [40], the nonlinear tolerance improvement relatively to CDE is limited to approximately 1 dB. In fact, Figure 3.19a shows that the single-polarization DBP-SSFM<sub>1</sub> and DBP-VSTF curves are almost overlaid, since both methods share the performance limitation caused by

**Table 3.2:** Set of simulation parameters for the system model of Figure 3.18.

Signal	NZDSF	EDFA
Format: PM-QPSK	$\alpha = 0.22$ dB/km	$F_n = 5$ dB
$R_b = 112$ Gb/s	$\beta_2 = -3.2$ ps <sup>2</sup> /km	$G = 17.6$ dB
$f_s = 640$ GHz	$\gamma = 2$ W <sup>-1</sup> km <sup>-1</sup>	
$N_{\text{bits}} = 131072$	$L_s = 80$ km	

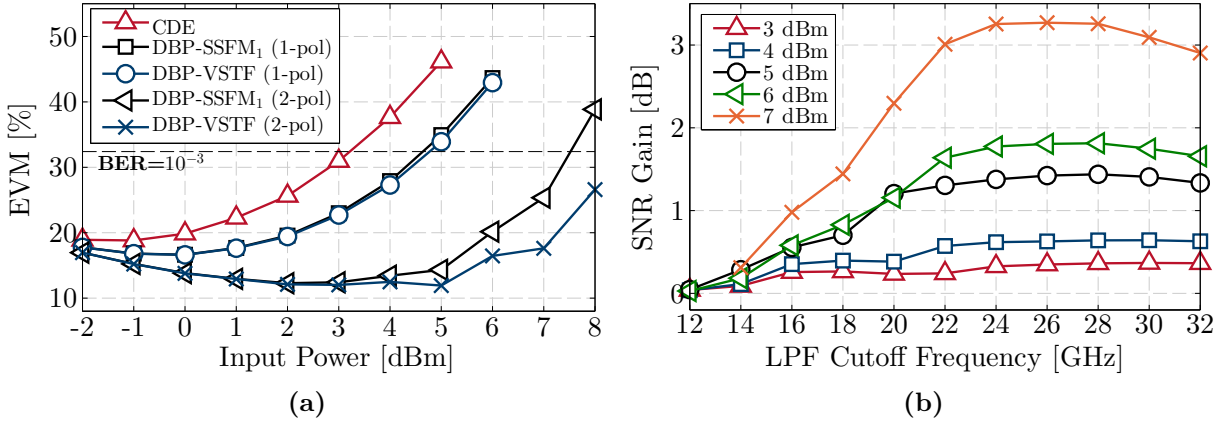


**Figure 3.19:** Performance of dual-polarization nonlinear equalization in a 112 Gb/s PM-QPSK optical transmission system composed of  $20 \times 80$  km of NZDSF. a) EVM after static digital equalization, as a function of input power and equalization method. b) SNR gain of the DBP-VSTF over DBP-SSFM<sub>1</sub> as a function of the LPF cutoff frequency.

neglecting the nonlinear interaction between the polarization tributaries. This limitation is imposed by the fast polarization rotations that cause the nonlinear effects to be distributed over the Poincaré sphere. Therefore, as depicted in Figure 3.19a, the Manakov versions of DBP-SSFM and DBP-VSTF are able to provide a much more effective mitigation of nonlinearities in transmission fibers with randomly varying birefringence. As a result, the optimum power levels are increased from about 0 dBm (single-polarization DBP) to around 3-5 dBm. The obtained results at the maximum considered input power of 8 dBm show that the DBP-VSTF algorithm roughly provides a 12% lower EVM than the corresponding DBP-SSFM<sub>1</sub>. This confirms the enhanced performance of the DBP-VSTF due to its aliasing robust frequency domain implementation, being in accordance with previous results obtained under a simplified single-polarization approach. Also note that, similarly to the obtained results in the single-polarization scenario for an NZDSF link (see Figure 3.13), the maximum DBP-SSFM spatial resolution at  $2 \times$  oversampling has been found to be limited to 1 step per span. In order to thoroughly assess the dependence of the DBP-VSTF performance gain over DBP-SSFM, the previous simulations have been repeated for a range of LPF cutoff frequencies varying from 12 to 32 GHz. The obtained results are shown in Figure 3.19b, are in good agreement with the ones obtained for the single-polarization scenario (see Figure 3.14), from which two main conclusions can be highlighted:

- i) the SNR gain provided by the DBP-VSTF over DBP-SSFM tends to increase with increasing power, proving the DBP-VSTF robustness to highly nonlinear propagation scenarios. Given the third-order approximation of the algorithm, this is a very relevant observation, since it proves that the DBP-VSTF does not suffer from catastrophic degradation within a practical range of optical powers. The output signal modification applied after each fiber span, as proposed in [33], plays a key role on extending the nonlinear robustness;

- ii) the LPF cutoff frequency dependence of the SNR gain provided by the DBP-SSFM is generally described by a parabolic function whose maximum peak is located around the signal baud-rate (24-30 GHz). The SNR gain provided by the DBP-VSTF method tends to vanish for a very narrow receiver bandwidth. Then, the SNR gain tends to increase with a wider LPF, up to a cutoff frequency of about 80% of the symbol-rate. An approximately stable performance is achieved with a cutoff frequency framing between 80% to 110% of the symbol-rate. As the LPF cutoff frequency is further increased, the SNR gain tends to decrease once again due to the effect of aliasing from downsampling.

### 3.5 Experimental Validation

The numerical assessment performed in section 3.4 has enabled to test and optimize the single- and dual-polarization DBP-based algorithms described in sections 3.2 and 3.3. Although numerical simulation is indeed a powerful tool to aid during the algorithm development and preliminary testing stages, experimental demonstration is the ultimate validation tool, as it effectively tests the applicability to practical scenarios involving many non-ideal characteristics. In this section, the DBP-VSTF technique is thoroughly assessed through offline processing of experimentally generated data obtained from state-of-the-art 100G long-haul optical transmission links in laboratorial environment. This laboratorial validation has been carried out in close collaboration with Politecnico di Torino (POLITO), Italy, within the framework of the EURO-FOS project, an FP7 network of excellence funded by the European Commission. The experimental measurements were obtained during a short-term (1 week) scientific mission and recorded in data files for subsequent offline processing. A detailed analysis of the laboratorial setup and obtained results is provided in the following subsections.

#### 3.5.1 Laboratorial setup and DSP subsystems

Two major distinct experimental setups will be considered for the experimental validation of DBP-VSTF, which are summarized in Table 3.3. A simplified schematic

**Table 3.3:** Experimental setup parameters for the considered long-haul 100G PM-QPSK transmission systems.  $\Delta f$  - inter-channel spacing;  $R_s$  - symbol rate.

	A			B
	A.1	A.2	A.2	
WDM	1-channel -	10-channel $\Delta f = 66$ GHz	10-channel $\Delta f = 33$ GHz	1-channel -
Tx	$R_s = 30$ Gbaud			$R_s = 25$ Gbaud
Fiber	NZDSF: $\alpha = 0.22$ dB/km $\beta_2 = -3.29$ ps <sup>2</sup> /km $\gamma = 2.01$ W <sup>-1</sup> km <sup>-1</sup> $L_s = 100$ km			SSMF: $\alpha = 0.20$ dB/km $\beta_2 = -21.37$ ps <sup>2</sup> /km $\gamma = 1.35$ W <sup>-1</sup> km <sup>-1</sup> $L_s = 63.6$ km
Rx	$N_{\text{sps}} = 5/3$			$N_{\text{sps}} = 2$

### 3.5. Experimental Validation

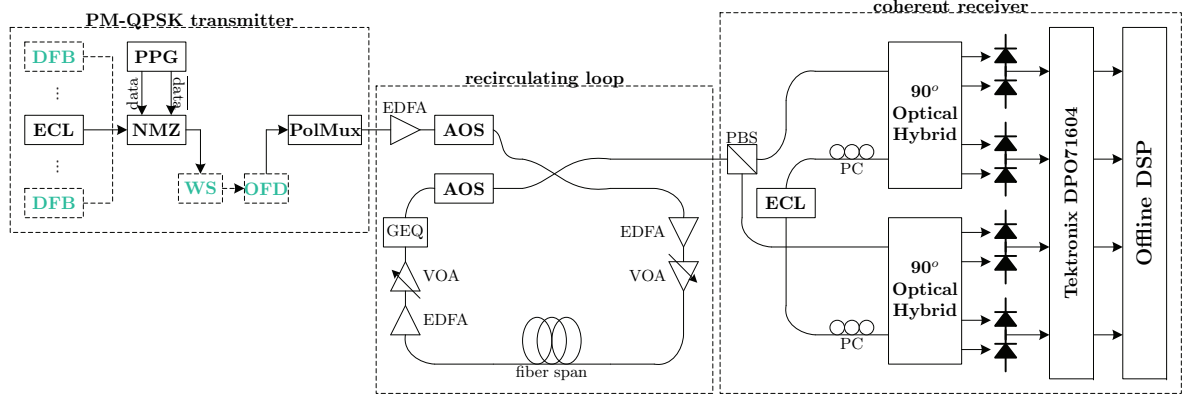


**Figure 3.20:** Experimental setup of the long-haul 100G PM-QPSK transmission system. OFD - optical frequency doubler; VOA - variable optical attenuator. The dashed blocks indicate optional equipment: the WS filter is only used in setup **A**; the DFB lasers are employed in the WDM scenarios **A.2** and **A.3**; the OFD is only required in scenario **A.3**, in order to halve the inter-channel spacing from 66 GHz down to 33 GHz.

representation of all experimental scenarios is presented in Figure 3.20. The differences between scenarios **A** and **B** are on the transmitter side and on the propagation fiber. In experimental setup **A**, the transmitted signal is a Nyquist-shaped 30 Gbaud PM-QPSK, which is propagated in a recirculating loop consisting of a single 100 km NZDSF spooled span. In turn, setup **B** is based on a 25 Gbaud PM-QPSK signal recirculated over 63.6 km of installed SSMF (FASTWEB’s Turin Metro Plant). Additionally, within experimental setup **A** we will consider three different sub-scenarios: **A.1**, which is a single-channel experiment; **A.2**, which is based on a 66 GHz-spaced 10-channel WDM experiment; and **A.3**, which is a 10-channel ultra-dense WDM experiment (33 GHz inter-channel spacing). In all scenarios, the central channel is optically generated by an external cavity laser (ECL) with 100 kHz linewidth. In scenarios **A.2** and **A.3**, additional distributed feedback (DFB) lasers are used to generate the WDM signal. A pulse pattern generator (PPG) outputs the digital data, which is modulated onto the optical field by a nested Mach-Zehnder (NMZ) modulator. A bandwidth-adjustable Finisar’s waveshaper (WS) filter is employed in setup **A**, providing a Nyquist pulse shaping to the transmitted optical signal [45]. The -3 dB bandwidth of the WS filter has been set to 32 GHz, and a  $\sim 2$  dB pre-emphasis towards the filter sides has been applied to enhance high frequencies, partially compensating for the receiver bandwidth limitation. In setup **A.3**, an optical frequency doubler (OFD) is used to halve the inter-channel frequency spacing from 66 GHz down to 33 GHz [46]. Finally, polarization-multiplexing is emulated by applying an optical delay line. The delay between the two polarization tributaries is of 882 symbols (29.4 ns) for scenario **A** and 916 symbols (36.64 ns) for scenario **B**, thus ensuring polarization de-correlation. The transmitted signal is then propagated in a recirculating fiber loop controlled by acousto-optical switches (AOSs). Optical power at the fiber input and output is controlled by two pairs of EDFAs cascaded with variable optical attenuators (VOAs). A gain equalizer (GEQ) filter is employed to equalize the power level in all channels, compensating for the EDFA unbalancing. After coherent

detection, the four resulting electrical signals are finally sampled at 50 Gsample/s in a Tektronix DPO71604 and stored for subsequent offline processing. Given the different symbol rates, the temporal resolution provided for the DSP subsystem is of 1.67 and 2 samples per symbol, for scenarios **A** and **B**, respectively.

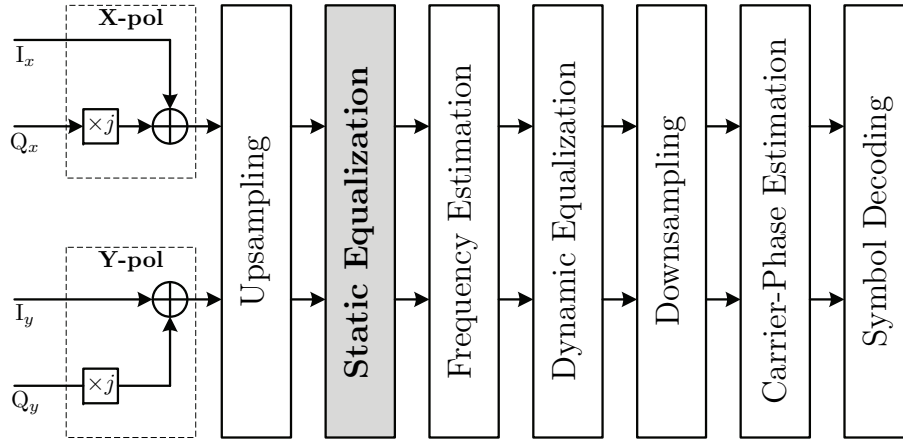


**Figure 3.21:** Sequential application of DSP subsystems for offline processing of the received signal samples stored by the Tektronix DPO71604 oscilloscope.

A block diagram representing the required DSP subsystems for processing of the received data is presented in Figure 3.21. Offline processing for BER evaluation has been carried out on  $2^{17}$  bits. A digital upsampling stage is applied for scenario **A**, in order to provide 2 SpS for the remaining DSP subsystems. Both chromatic dispersion and intra-channel nonlinearities are equalized within the static equalization block. Frequency domain equalization is enabled by the OS method, using the minimum FFT block length that captures the long-term memory effects of the signal, thus avoiding inter-block interference ( $N = 32$  for scenario **A** and  $N = 128$  for scenario **B**). Linear equalization is performed by a frequency domain CDE. Digital backpropagation is performed using both the single- and dual-polarization versions of the DBP-SSFM and DBP-VSTF methods. Subsequently, frequency estimation is achieved by a common feedforward spectral method [47]. In the dynamic equalization block, polarization demultiplexing and residual dispersion compensation are performed by a 25 taps adaptive filter driven by the CMA. After downsampling to 1 SpS, phase estimation is implemented by the Viterbi-Viterbi algorithm (no differential coding) with an optimized block-length. Finally, BER calculation is carried out after symbol decoding.

### 3.5.2 Experimental results

As aforementioned, the obtained experimental results can be divided into two main categories: single-channel and WDM. Following the adopted numerical simulation strategy, two different fiber types (NZDSF and SSMF) are also considered in order to assess the DBP performance under different propagation regimes. In this section, these results will be separately analyzed, taking into account the receiver bandwidth constraints that limit the application of DBP to intra-channel equalization.

### 3.5. Experimental Validation

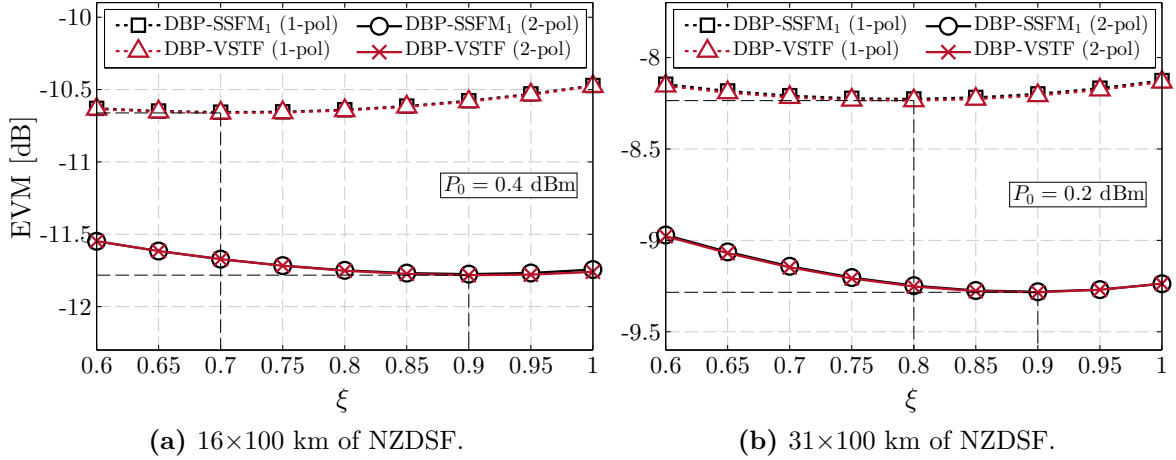


**Figure 3.22:** Optimization of the DBP-SSFM and DBP-VSTF methods at the optimum power level, as a function of the  $\xi$  parameter, for experimental scenario **A.1**. The  $\xi$  parameter has been varied between 0.6 and 1, with a step-size of 0.05.

#### Single-channel NZDSF optical link (scenario A.1)

In order to find the best nonlinear compensation provided by the DBP-SSFM and DBP-VSTF methods, a simple optimization procedure has been carried out for each input power, measuring the nonlinear equalization performance for a set of predefined trial values of the  $\xi$  factor. The EVM of the equalized signal is used as a figure of merit for this optimization procedure, defined in logarithmic scale as

$$\text{EVM [dB]} = 20 \log_{10} \left[ \frac{1}{2} \sqrt{\frac{\sum |A_{x,\text{eq}} - A_{x,\text{tx}}|^2}{\sum |A_{x,\text{tx}}|^2}} + \frac{1}{2} \sqrt{\frac{\sum |A_{y,\text{eq}} - A_{y,\text{tx}}|^2}{\sum |A_{y,\text{tx}}|^2}} \right]. \quad (3.51)$$

The  $\xi$  parameter optimization for scenario **A.1** is illustrated in Figure 3.22, considering both single- and dual-polarization DBP at the optimum launched power (0.4 dBm for the 16 spans experiment and 0.2 dBm for the 31 spans experiment, as shown in Figure 3.23) for scenario **A.1**, composed of 16 and 31 spans. The best DBP-SSFM performance, for both the single- and dual-polarization models, has been found by applying only 1 step per span, which is in accordance with the previous simulation results for NZDSF links (see Figure 3.19). Note that the experimental receiver-side constraints are even more stringent than the ones previously tested in simulation. Indeed, the low ADC sampling rate ( $\sim 1.67$  SpS) and analog bandwidth ( $\sim 13$  GHz, corresponding to  $\sim 43\%$  of the symbol rate), significantly reduce the available spectrum (before digital interpolation) for nonlinear equalization. In addition, at the transmitter side, the employed Nyquist pulse shaping imposes an aggressive optical filtering to the signal spectrum, causing some inter-symbol interference that cannot be removed by DBP. Being limited by the same external factors, the DBP-VSTF optimization curves are also overlapped with those obtained by DBP-SSFM. It is also worth mentioning that the dual-polarization DBP methods enable to significantly increase the optimum fraction

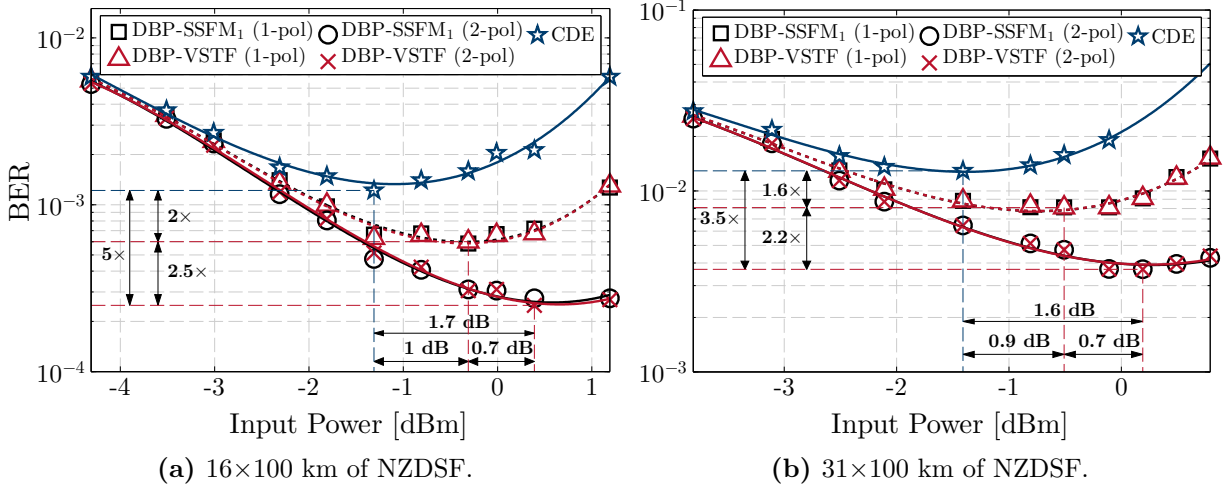


**Figure 3.23:** Experimental BER results obtained for a single-channel 120 Gb/s PM-QPSK signal, corresponding to scenario **A.1** composed of 16 spans (a)) and 31 spans (b)) of NZDSF. Solid/dashed lines are obtained by quadratic polynomial fittings of data.

of nonlinear compensation, which is a consequence of taking into account the cross-polarization effects. The same  $\xi$  optimization procedure has been carried out for each input power, with similar conclusions.

The evolution of BER as a function of input power for the experimental setup **A.1** is shown in Figure 3.23, considering a total propagation distance of 1600 km (Figure 3.23a) and 3100 km (Figure 3.23b). The obtained results reemphasize the idea that the above mentioned experimental limitations are ceiling the maximum performance of the single- and dual-polarization DBP-VSTF, causing an overlap with the DBP-SSFM curves and thus preventing to achieve the performance advantage that has been previously demonstrated by means of simulation [39]. Despite of these challenging experimental conditions, the results in Figure 3.23 reveal that nonlinear equalization can still bring a significant improvement both in terms of BER and optimum power. For the  $16 \times 100$  km scenario, the dual-polarization nonlinear equalizers provide a BER reduction by a factor of  $\sim 5$  ( $\sim 80\%$  improvement), relatively to the use of CDE, leading to an increase in optimum power of about 1.7 dB. In addition, a BER gain of about  $2.5 \times$  ( $\sim 60\%$  reduction) is obtained over the single-polarization nonlinear equalizers, representing an increase in optimum power of  $\sim 0.7$  dB. Regarding the  $31 \times 100$  km loop, we may observe that the BER curves are roughly shifted up by one order of magnitude due to the accumulated noise and under-compensated nonlinearities. Although the BER gain is slightly decreased, the optimum powers for each curve remain almost unchanged.

### Single-channel SSMF optical link (scenario B)

In order to assess the DBP performance with less stringent filtering conditions, we will now analyze the alternative experimental setup **B**, which presents the following advantages: i) absence of tight optical filtering (no WS is used) at the transmitter side;

### 3.5. Experimental Validation

ii) higher sampling rate (2 SpS) and higher ratio between analog ADC bandwidth and signal symbol rate, at the receiver side.

The optimization of the  $\xi$  parameter is illustrated in Figure 3.24a, where it is shown that due to the higher sampling rate (2 SpS) and higher accumulated dispersion per SSMF span, the best DBP-SSFM performance in this scenario is now attained with 4 steps per span. As previously observed for scenario **A.1**, the optimum fraction of nonlinear compensation is significantly increased by the dual-polarization equalizers. However, the optimum  $\xi$  values have slightly decreased relatively to the previous scenario. This can be justified by the larger chromatic dispersion per span associated with accumulated noise, which tends to degrade the inversion of the nonlinear phase-shift. The BER results provided in Figure 3.24b show that the dual-polarization nonlinear equalizers provide a  $\sim 3$  dB increase in the optimum power over CDE, with a corresponding BER gain of approximately  $6.6\times$  ( $\sim 85\%$  reduction). Relatively to the single-polarization counterparts, the dual-polarization equalizers provide around 1 dB improvement in terms of optimal input power and a BER reduction of  $\sim 2.7\times$ , which corresponds to a  $\sim 63\%$  improvement. On the contrary of scenario **A.1**, where the DBP-VSTF and DBP-SSFM performances were almost perfectly matched, in Figure 3.24b a slight DBP-VSTF advantage can be seen at the optimum input power. However, this negligible improvement denotes that the DBP performance remains strongly limited by the available electrical bandwidth, which is still only about 52% of the symbol rate. Indeed, besides limiting the performance of nonlinear equalization in general, a low ADC bandwidth also works as an analog low-pass anti-aliasing filter, reducing the DBP-VSTF performance gain over DBP-SSFM, as numerically analyzed in Figure 3.19 and reported in [39]. Simulation results obtained for less stringent optical and electrical filtering conditions have confirmed that the assessed experimental equalization performance can be substantially optimized when considering near-optimum optical/electrical filtering [48].

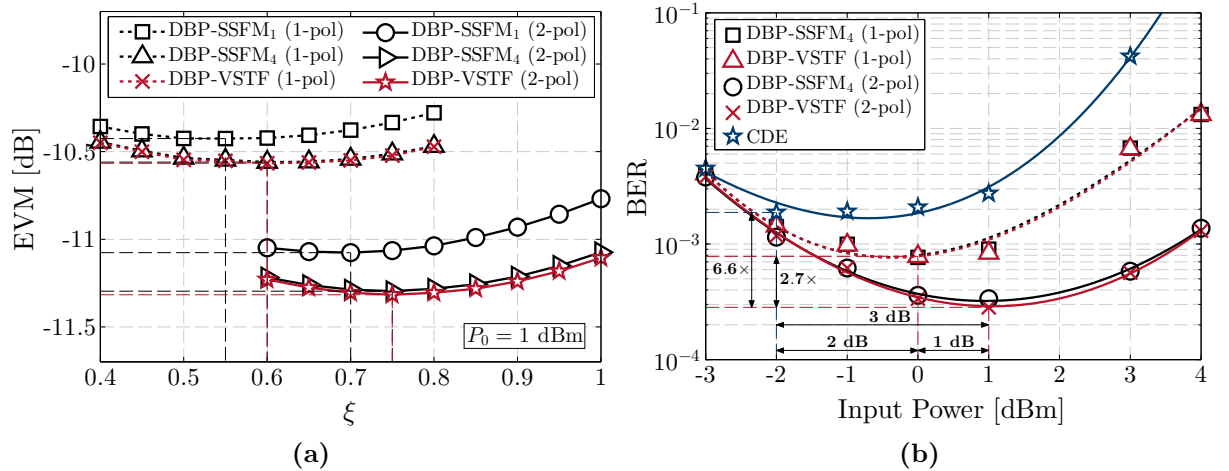


**Figure 3.24:** Experimental results obtained for a single-channel 100 Gb/s PM-QPSK signal, corresponding to scenario **B**, composed of 50 spans of SSMF. a)  $\xi$  optimization at the optimum power (1 dBm); b) BER as a function of input power.

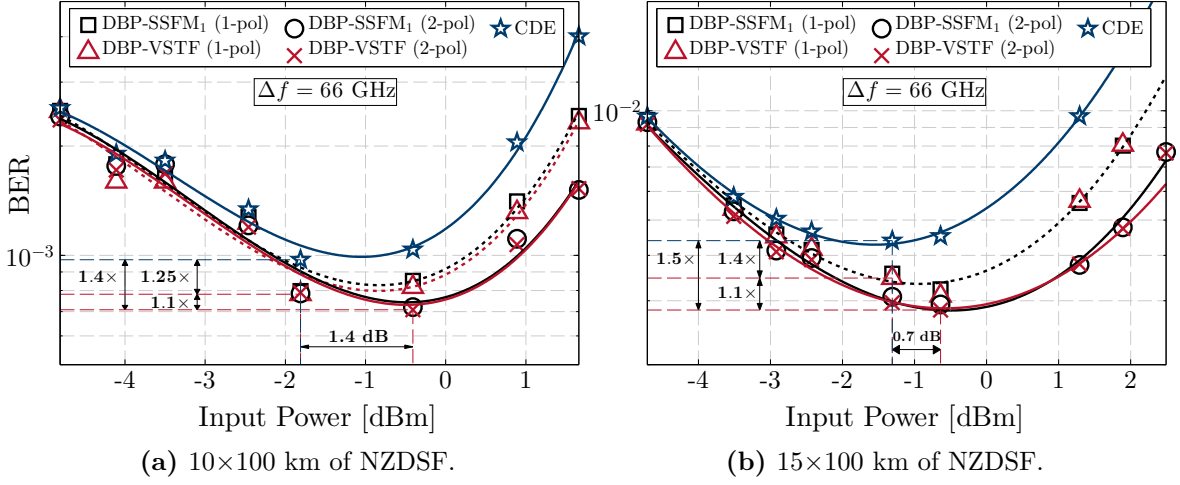


**Figure 3.25:** Experimental BER results obtained for a 10-channel 120 Gb/s PM-QPSK signal with 66 GHz channel spacing, corresponding to scenario **A.2**, composed of 10 spans (a)) and 15 spans (b)) of NZDSF.

### WDM NZDSF optical link (scenarios **A.2** and **A.3**)

With the aim to study the effectiveness of intra-channel nonlinear equalization in multi-channel signal propagation, two additional 10-channel WDM scenarios have also been analyzed, considering an inter-channel spacing of 66 GHz and 33 GHz, which correspond to experimental setups **A.2** and **A.3**, respectively. The performance of linear and nonlinear equalization in scenario **A.2** is presented in Figure 3.25. As expected, due to the effect of inter-channel nonlinearities, the nonlinear tolerance enhancement and BER improvement provided by DBP are now significantly reduced, relatively to the single-channel scenarios. A direct comparison between Figures 3.25b and 3.23a, which roughly correspond to the same propagation distance (1500/1600 km), reveals a BER degradation of approximately half an order of magnitude in terms of CDE performance. However, when the same comparison is performed in terms of nonlinear equalization, this BER degradation is now increased to approximately one order of magnitude, revealing the strong impact of uncompensated inter-channel nonlinearities. Nevertheless, despite of the impact of inter-channel nonlinearities, a nonlinear tolerance improvement of 1.4 dB and 0.7 dB is demonstrated for a propagation distance of 1000 km and 1500 km, respectively, together with a BER reduction of approximately 30%.

To conclude the WDM analysis, the performance of DBP-based intra-channel nonlinear compensation is tested in scenario **A.3**, which is based on a WDM transmission system with ultra-narrow spacing of  $1.1\times$  the symbol rate. The experimental results presented in Figure 3.26 clearly show that the effectiveness of intra-channel DBP becomes severely limited by the impact of intra-channel nonlinearities in ultra-dense WDM scenarios. A direct comparison between Figures 3.25a and 3.26b, both corresponding to a propagation distance of 1000 km, reveals that the nonlinear tolerance enhancement due to dual-polarization DBP is reduced from 1.4 dB to approximately 0.5 dB when the inter-

### 3.6. Summary

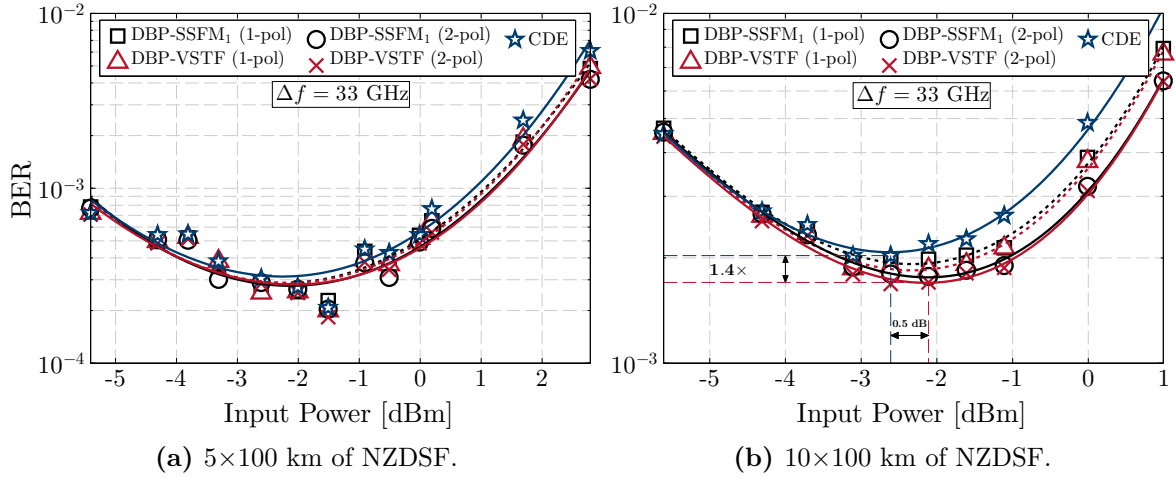


**Figure 3.26:** Experimental BER results obtained for a 10-channel 120 Gb/s PM-QPSK signal with 33 GHz channel spacing, corresponding to scenario **A.3**, composed of 5 spans (a)) and 10 spans (b)) of NZDSF.

channel spacing is halved. Nevertheless, the BER reduction is kept at approximately 30%, demonstrating that, although limited by the linear and nonlinear inter-channel crosstalk, intra-channel DBP is still able to boost the signal quality. A more effective nonlinear compensation in the considered WDM scenarios (especially in scenario **A.3**) would require a multi-channel DBP approach [49, 50]. Note however, that multi-channel DBP compensation implies the use of either i) a very wideband receiver, capable of capturing the spectrum of several WDM channels or ii) synchronized cooperating receivers, with common DSP subsystems. Although state-of-the-art laboratorial facilities were used during this experimental validation work, both of the aforementioned options could not be experimentally tested due to equipment limitations. For multi-channel DBP experimental evaluation, the reader is referred to chapter 6, where a wideband receiver with 35 GHz analog bandwidth is used to test several 400G super-channel configurations.

## 3.6 Summary

This chapter addressed the performance and complexity of DBP-based linear and nonlinear compensation in long-haul and high-speed optical transmission systems. Inverting the third-order VSTF of single-mode optical fibers derived in [51] and described in chapter 2, we have proposed a closed-form algorithm for the numerical implementation of DBP, which we have denominated as the DBP-VSTF method. Sectioning the transmission system into a cascade of  $N_s$  fiber spans, the DBP-VSTF method can be implemented through an  $N_{\text{steps}}$  iterative approach, with  $N_{\text{steps}} = N_s$ , on the contrary of the DBP-SSFM, which typically requires  $N_{\text{steps}} \gg N_s$  to achieve its best performance. In addition, the DBP-VSTF provides the important advantage of performing parallel equalization of linear and nonlinear impairments, thus enabling to apply nonlinear compensation as an optional add-on for the equalization system. The performance of

the DBP-VSTF has been initially assessed through numerical simulation and considering both single-polarization [39, 52, 53] and dual-polarization transmission systems [43, 44], providing direct comparison with the well-known DBP-SSFM. The DBP-VSTF was then experimentally validated in a joint research effort with the optical communications group of Politecnico di Torino, considering several 100G channel configurations for both single-channel and WDM transmission [48, 54].

The simulation results obtained for a 40 Gb/s QPSK signal propagated over  $20 \times 80$  km of SSMF and NZDSF links and considering a temporal resolution of only 2 samples per symbol have shown a nonlinear tolerance improvement of approximately 2 dB, relatively to a highly iterative DBP-SSFM implementation, thus enabling to extend the quasi-linear propagation regime in fiber. The key factor for the DBP-VSTF performance advantage at low temporal resolution lies on its fully frequency domain implementation, which avoids the generation of aliasing phenomena in the equalization stage. Considering the Manakov equation, the DBP-VSTF technique has been extended for dual-polarization transmission systems, and the obtained numerical results were shown to corroborate the analysis performed for single-polarization transmission.

Considering PM-QPSK single-channel and WDM propagation scenarios, we have then experimentally demonstrated the dual-polarization DBP-VSTF. Due to the tight optical filtering and the ADC bandwidth limitations, the dual-polarization DBP-VSTF and DBP-SSFM methods were found to be approximately equivalent in performance. In single-channel transmission, we have demonstrated a BER improvement at the optimum power of about 60%, relatively to the previous single-polarization approach, and over 80%, relatively to linear equalization. The obtained WDM results reveal that intra-channel nonlinear equalization is still able to provide a moderate nonlinear tolerance improvement over linear equalization of approximately 1.4 dB for a channel spacing of  $2.2 \times$  the symbol rate. Employing an ultra-dense WDM packaging with a channel spacing of  $1.1 \times$  the symbol rate, this improvement is then further reduced to  $\sim 0.5$  dB, due to the limiting effect of uncompensated inter-channel nonlinearities.

In terms of computational load, it has been demonstrated that the DBP-VSTF complexity is proportional to  $N^2$  per sample, thus requiring the use of reduced FFT block-sizes. Although typical block processing strategies such as the overlap-and-save can be used to partition the received samples into small blocks, the limits for the minimum FFT block-size are ultimately set by the amount of CD to be inverted in each DBP step. Nevertheless, being based on a matrix multiplication approach, the DBP-VSTF structure is highly parallel, favouring a low latency real-time implementation. The reduction of computational effort and other practical implementation issues will be explored in more detail in the following chapters 4 and 5, using a symmetric kernel reconstruction technique and applying several critical time and frequency domain simplifications.

## References

- [1] A. D. Ellis, J. Zhao, and D. Cotter, "Approaching the non-linear Shannon limit," *J. Lightw. Technol.*, vol. 28, no. 4, pp. 423–433, Feb 2010.

- [2] A. Mecozzi and R. Essiambre, “Nonlinear Shannon limit in pseudolinear coherent systems,” *J. Lightw. Technol.*, vol. 30, no. 12, pp. 2011–2024, 2012.
- [3] E. Agrell, A. Alvarado, G. Durisi, and M. Karlsson, “Capacity of a nonlinear optical channel with finite memory,” *J. Lightw. Technol.*, vol. 32, no. 16, pp. 2862–2876, Aug 2014.
- [4] A. Zhu, J. C. Pedro, and T. R. Cunha, “Pruning the Volterra series for behavioral modeling of power amplifiers using physical knowledge,” *IEEE Trans. Microw. Theory Tech.*, vol. 55, no. 5, pp. 813–821, 2007.
- [5] S. Kumar and L. Liu, “Reduction of nonlinear phase noise using optical phase conjugation in quasi-linear optical transmission systems,” *Opt. Express*, vol. 15, no. 5, pp. 2166–2177, Mar 2007.
- [6] S. Kumar and D. Yang, “Optical backpropagation for fiber-optic communications using highly nonlinear fibers,” *Opt. Lett.*, vol. 36, no. 7, pp. 1038–1040, Apr 2011.
- [7] J. Shao and S. Kumar, “Optical backpropagation for fiber-optic communications using optical phase conjugation at the receiver,” *Opt. Lett.*, vol. 37, no. 15, pp. 3012–3014, Aug 2012.
- [8] E. Ip and J. M. Kahn, “Compensation of dispersion and nonlinear impairments using digital backpropagation,” *J. Lightw. Technol.*, vol. 26, no. 20, pp. 3416–3425, 2008.
- [9] K. Roberts, C. Li, L. Strawczynski, M. O’Sullivan, and I. Hardcastle, “Electronic precompensation of optical nonlinearity,” *IEEE Photon. Technol. Lett.*, vol. 18, no. 2, pp. 403–405, 2006.
- [10] E. M. Ip and J. M. Kahn, “Fiber impairment compensation using coherent detection and digital signal processing,” *J. Lightw. Technol.*, vol. 28, no. 4, pp. 502–519, 2010.
- [11] X. Li, X. Chen, G. Goldfarb, E. Mateo, I. Kim, F. Yaman, and G. Li, “Electronic post-compensation of WDM transmission impairments using coherent detection and digital signal processing,” *Opt. Express*, vol. 16, no. 2, pp. 880–888, Jan 2008.
- [12] N. Irukulapati, H. Wymeersch, P. Johannisson, and E. Agrell, “Stochastic digital backpropagation,” *IEEE Trans. Commun.*, vol. 62, no. 11, pp. 3956–3968, Nov 2014.
- [13] D. Marsella, M. Secondini, and E. Forestieri, “Maximum likelihood sequence detection for mitigating nonlinear effects,” *J. Lightw. Technol.*, vol. 32, no. 5, pp. 908–916, March 2014.
- [14] E. Ip, “Nonlinear compensation using backpropagation for polarization-multiplexed transmission,” *J. Lightw. Technol.*, vol. 28, no. 6, pp. 939–951, 2010.
- [15] F. Yaman and G. Li, “Nonlinear impairment compensation for polarization-division multiplexed WDM transmission using digital backward propagation,” *IEEE Photonics Journal*, vol. 2, no. 5, pp. 816–832, 2010.

- 
- [16] G. Goldfarb and G. Li, “Efficient backward-propagation using wavelet-based filtering for fiber backward-propagation,” *Opt. Express*, vol. 17, no. 11, pp. 8815–8821, May 2009.
- [17] E. F. Mateo, F. Yaman, and G. Li, “Efficient compensation of inter-channel nonlinear effects via digital backward propagation in WDM optical transmission,” *Opt. Express*, vol. 18, no. 14, pp. 15 144–15 154, Jul 2010.
- [18] D. Rafique, M. Mussolin, M. Forzati, J. Mårtensson, M. N. Chugtai, and A. D. Ellis, “Compensation of intra-channel nonlinear fibre impairments using simplified digital back-propagation algorithm,” *Opt. Express*, vol. 19, no. 10, pp. 9453–9460, May 2011.
- [19] L. Zhu and G. Li, “Folded digital backward propagation for dispersion-managed fiber-optic transmission,” *Opt. Express*, vol. 19, no. 7, pp. 5953–5959, 2011.
- [20] Z. Tao, L. Dou, W. Yan, L. Li, T. Hoshida, and J. Rasmussen, “Multiplier-free intrachannel nonlinearity compensating algorithm operating at symbol rate,” *J. Lightw. Technol.*, vol. 29, no. 17, pp. 2570–2576, 2011.
- [21] A. Napoli, Z. Maalej, V. Sleiffer, M. Kuschnerov, D. Rafique, E. Timmers, B. Spinnler, T. Rahman, L. Coelho, and N. Hanik, “Reduced complexity digital back-propagation methods for optical communication systems,” *J. Lightw. Technol.*, vol. 32, no. 7, pp. 1351–1362, April 2014.
- [22] F. P. Guiomar and A. N. Pinto, “Simplified Volterra series nonlinear equalizer for polarization-multiplexed coherent optical systems,” *J. Lightw. Technol.*, vol. 31, no. 23, pp. 3879–3891, 2013.
- [23] G. Shulkind and M. Nazarathy, “Nonlinear digital back propagation compensator for coherent optical OFDM based on factorizing the Volterra series transfer function,” *Opt. Express*, vol. 21, no. 11, pp. 13 145–13 161, Jun 2013.
- [24] L. B. Du and A. J. Lowery, “Improved single channel backpropagation for intra-channel fiber nonlinearity compensation in long-haul optical communication systems,” *Opt. Express*, vol. 18, no. 16, pp. 17 075–17 088, Aug 2010.
- [25] G. Goldfarb, M. G. Taylor, and G. Li, “Experimental demonstration of fiber impairment compensation using the split-step finite-impulse-response filtering method,” *IEEE Photon. Technol. Lett.*, vol. 20, no. 22, pp. 1887–1889, 2008.
- [26] G. Goldfarb and G. Li, “Demonstration of fibre impairment compensation using split-step infinite-impulse-response filtering method,” *Electron. Lett.*, vol. 44, no. 13, pp. 814–816, 2008.
- [27] L. Zhu, F. Yaman, and G. Li, “Experimental demonstration of XPM compensation for WDM fibre transmission,” *Electron. Lett.*, vol. 46, no. 16, pp. 1140–1141, 2010.

- [28] S. J. Savory, G. Gavioli, E. Torrenco, and P. Poggiolini, "Impact of interchannel nonlinearities on a split-step intrachannel nonlinear equalizer," *IEEE Photon. Technol. Lett.*, vol. 22, no. 10, pp. 673–675, 2010.
- [29] Y. Mahdy, S. Ali, and K. Shaaban, "Algorithm and two efficient implementations for complex multiplier," in *IEEE International Conference on Electronics, Circuits and Systems (ICECS)*, vol. 2, Sep 1999, pp. 949–952.
- [30] J. W. Cooley and J. W. Tukey, "An algorithm for the machine computation of the complex Fourier series," *Math. Computation*, vol. 19, pp. 297–301, 1965.
- [31] D. S. Millar, S. Makovejs, C. Behrens, S. Hellerbrand, R. I. Killey, P. Bayvel, and S. J. Savory, "Mitigation of fiber nonlinearity using a digital coherent receiver," *IEEE J. Sel. Topics Quantum Electron.*, vol. 16, no. 5, pp. 1217–1226, 2010.
- [32] D. Rafique, M. Mussolin, J. Mårtensson, M. Forzati, J. K. Fischer, L. Molle, M. Nölle, C. Schubert, and A. D. Ellis, "Polarization multiplexed 16QAM transmission employing modified digital back-propagation," *Opt. Express*, vol. 19, no. 26, pp. B805–B810, Dec 2011.
- [33] B. Xu and M. Brandt-Pearce, "Modified Volterra series transfer function method," *IEEE Photon. Technol. Lett.*, vol. 14, no. 1, pp. 47–49, 2002.
- [34] G. P. Agrawal, *Nonlinear Fiber Optics*, 3rd ed. University of Rochester, New York: Academic Press, 2001.
- [35] B. Xu and M. Brandt-Pearce, "Comparison of FWM- and XPM-induced crosstalk using the Volterra series transfer function method," *J. Lightw. Technol.*, vol. 21, no. 1, pp. 40–53, 2003.
- [36] M. Nazarathy, J. Khurgin, R. Weidenfeld, Y. Meiman, P. Cho, R. Noe, I. Shpantzer, and V. Karagodsky, "Phased-array cancellation of nonlinear FWM in coherent OFDM dispersive multi-span links," *Opt. Express*, vol. 16, no. 20, pp. 15 777–15 810, Sep 2008.
- [37] A. Carena, V. Curri, G. Bosco, P. Poggiolini, and F. Forghieri, "Modeling of the impact of nonlinear propagation effects in uncompensated optical coherent transmission links," *J. Lightw. Technol.*, vol. 30, no. 10, pp. 1524–1539, 2012.
- [38] L. Du, B. Schmidt, and A. Lowery, "Efficient digital backpropagation for PDM-CO-OFDM optical transmission systems," in *Proc. Optical Fiber Communication Conf. and Exposition (OFC)*, paper OTuE2, 2010.
- [39] F. P. Guiomar, J. D. Reis, A. L. Teixeira, and A. N. Pinto, "Mitigation of intra-channel nonlinearities using a frequency-domain Volterra series equalizer," *Opt. Express*, vol. 20, no. 2, pp. 1360–1369, Jan 2012.
- [40] J. D. Reis, "Design and optimization next generation passive all-optical networks," Ph.D. dissertation, Universidade de Aveiro, 2012.

- 
- [41] D. Godard, "Self-recovering equalization and carrier tracking in two-dimensional data communication systems," *IEEE Trans. Commun.*, vol. 28, no. 11, pp. 1867–1875, 1980.
- [42] A. Viterbi, "Nonlinear estimation of PSK-modulated carrier phase with application to burst digital transmission," *IEEE Trans. Inf. Theory*, vol. 29, no. 4, pp. 543–551, 1983.
- [43] F. P. Guiomar and A. N. Pinto, "Receiver-side digital signal processing for 100-GE coherent optical transmission systems," in *17th European Conference on Networks and Optical Communications (NOC)*, 2012.
- [44] A. N. Pinto and F. P. Guiomar, "Flexible optical receivers," in *14th International Conference on Transparent Optical Networks (ICTON)*, paper Tu.C1.3, 2012.
- [45] G. Gavioli, E. Torrenco, G. Bosco, A. Carena, S. Savory, F. Forghieri, and P. Poggiolini, "Ultra-narrow-spacing 10-channel 1.12 Tb/s D-WDM long-haul transmission over uncompensated SMF and NZDSF," *IEEE Photon. Technol. Lett.*, vol. 22, no. 19, pp. 1419–1421, Oct 2010.
- [46] E. Torrenco, R. Cigliutti, G. Bosco, A. Carena, V. Curri, P. Poggiolini, A. Nespola, D. Zeolla, and F. Forghieri, "Experimental validation of an analytical model for nonlinear propagation in uncompensated optical links," in *Proc. 37th European Conf. Optical Communication (ECOC)*, paper We.7.B.2, 2011.
- [47] S. J. Savory, "Digital coherent optical receivers: Algorithms and subsystems," *IEEE J. Sel. Topics Quantum Electron.*, vol. 16, no. 5, pp. 1164–1179, 2010.
- [48] F. P. Guiomar, J. D. Reis, A. Carena, G. Bosco, A. L. Teixeira, and A. N. Pinto, "Experimental demonstration of a frequency-domain Volterra series nonlinear equalizer in polarization-multiplexed transmission," *Opt. Express*, vol. 21, no. 1, pp. 276–288, 2013.
- [49] E. Mateo, L. Zhu, and G. Li, "Impact of XPM and FWM on the digital implementation of impairment compensation for WDM transmission using backward propagation," *Opt. Express*, vol. 16, no. 20, pp. 16 124–16 137, Sep 2008.
- [50] E. F. Mateo and G. Li, "Compensation of interchannel nonlinearities using enhanced coupled equations for digital backward propagation," *Appl. Opt.*, vol. 48, no. 25, pp. F6–F10, Sep 2009.
- [51] K. V. Peddanarappagari and M. Brandt-Pearce, "Volterra series transfer function of single-mode fibers," *J. Lightw. Technol.*, vol. 15, no. 12, pp. 2232–2241, 1997.
- [52] F. P. Guiomar, J. D. Reis, A. L. Teixeira, and A. N. Pinto, "Digital postcompensation using Volterra series transfer function," *IEEE Photonics Technology Letters*, vol. 23, no. 19, pp. 1412–1414, 2011.
-

- [53] —, “Mitigation of intra-channel nonlinearities using a frequency-domain Volterra series equalizer,” in *Proc. 37th European Conf. Optical Communication (ECOC)*, paper Tu.6.B.1, 2011.
- [54] F. P. Guiomar, J. D. Reis, A. Carena, G. Bosco, A. L. Teixeira, and A. N. Pinto, “Experimental demonstration of a frequency-domain Volterra series nonlinear equalizer in polarization-multiplexed transmission,” in *Proc. 38th European Conf. Optical Communication (ECOC)*, paper Th.1.D.1, 2012.



## Chapter 4

# Frequency Domain Volterra Series Nonlinear Equalizer

The frequency domain VSNE proposed in Chapter 3, obtained from an inverse VSTF for single-mode fibers, was shown to provide high equalization performance associated with a highly parallel algorithm structure, which favors real-time processing. However, the total number of real multiplications per sample evolves as  $O(N^2)$ , with  $N$  being the FFT block length, thus limiting the applicability of the algorithm in scenarios with large accumulated CD that creates long memory effects. The complexity reduction of the VSTF for nonlinear compensation purposes has been recently addressed by several authors [1–3]. In [1], the equivalence between the third-order VSTF and the first-order regular perturbation method [4] is exploited to design a nonlinear compensation technique where each fiber span can be backpropagated in parallel. A factorized approximation for the single-polarization VSTF with overall  $O(N \log(N))$  complexity has been proposed in [2, 3], employing decision-feedback [2] and feed-forward [3] equalizer structures. All these reduced complexity nonlinear equalization algorithms [1–3] make use of time-frequency transformations, similarly to the SSFM, exploiting the convolution theorem to speed up the calculations. In order to enable real-time estimation of the VSTF coefficients, an efficient nonlinear system identification strategy for single-polarization transmission systems has been proposed in [5], using a compressed VSTF notation that significantly reduces the number of required probing tones.

In this chapter, we carry out a comprehensive study on the minimization of the VSNE computational effort. Exploiting the symmetries shared by the third-order VSNE kernel and the signal triplet matrices, we derive a lossless compressed VSNE formulation for polarization-multiplexed transmission, whose filter array structure benefits the tradeoff between performance and complexity. Employing a frequency-flat approximation, we then derive a simplified VSNE algorithm with  $O(N_k N)$  complexity per FFT block, where  $N_k$  is the number of parallel frequency domain filters. A comprehensive numerical analysis is carried out for a long-haul 224 Gb/s PM-16-ary quadrature amplitude modulation (QAM) transmission system, demonstrating the efficiency of the proposed nonlinear equalization techniques. The numerical analysis is complemented by experimental demonstration in a 100G PM-64QAM transmission system, considering a 50 GHz WDM

grid.

The organization of this chapter is as follows. The symmetric VSNE formulation is analytically derived in section 4.1, including an in-depth analysis of the algorithm complexity in terms of real multiplications per sample. The analytical formulation and complexity analysis of the frequency-flat simplified VSNE is introduced in section 4.2. The numerical assessment of the performance versus complexity tradeoff of both the symmetric and simplified VSNE algorithms is addressed in section 4.3. Section 4.4 shows the experimental validation of the proposed VSNE-based techniques for intra-channel nonlinear compensation in a 50 GHz WDM grid 100G PM-64QAM transmission system. Finally, the main conclusions are summarized in section 4.5.

## 4.1 Symmetric VSNE

To contextualize the analytical formulation of the symmetric VSNE, let us first recall the matrix form of the matrix-based VSNE algorithm as described in (3.32),

$$\tilde{\mathbf{N}}_{\mathbf{x}/\mathbf{y}}(\omega_n, z) = \mathbf{K}_3(\omega_n) \circ \tilde{\mathbf{P}}(z) \circ \tilde{\mathbf{A}}_{\mathbf{x}/\mathbf{y}}(\omega_n, z), \quad (4.1)$$

where the third-order Volterra kernel,  $\mathbf{K}_3(\omega_n)$ , is written as a  $n$ -dependent  $N$ -by- $N$  matrix. Denoting the triple optical field spectrum multiplication in (4.1) as  $\tilde{\mathcal{A}}_{\mathbf{x}/\mathbf{y}}(\omega_n, z) = \tilde{\mathbf{P}}(z) \circ \tilde{\mathbf{A}}_{\mathbf{x}/\mathbf{y}}(\omega_n, z)$ , we can explicitly write

$$\tilde{\mathcal{A}}_{\mathbf{x}/\mathbf{y}}^{(j,k)}(\omega_n, z) = \left( \tilde{A}_x(\omega_k, z) \tilde{A}_x^*(\omega_j, z) + \tilde{A}_y(\omega_k, z) \tilde{A}_y^*(\omega_j, z) \right) \tilde{A}_{x/y}(\omega_{n+j-k}, z), \quad (4.2)$$

exposing the so-called optical field triplets. Based on the frequency matching between each of the  $\tilde{A}_{x/y}$  terms, the originated nonlinearity can be classified as:

- iSPM – when the three optical field components coincide in frequency, i.e. for  $j = k = n$ ;
- iXPM – when the conjugated optical field component coincides in frequency with only one other component, i.e. for  $j = k \neq n$  or  $j = n + j - k \neq k \Leftrightarrow n = k \neq j$ ;
- degenerated iFWM (DG-iFWM) – when the two non-conjugated optical field components coincide in frequency, i.e. for  $k = n + j - k \Leftrightarrow j = 2k - n$ ;
- iFWM – for all other possible combinations of  $j$ ,  $k$  and  $n$ .

Note that this frequency domain intra-channel nonlinear analysis differs from classical time domain analysis, where iXPM manifests itself as a timing jitter caused by two-pulse nonlinear interactions and iFWM is associated with the generation of echo pulses caused by the interaction of adjacent pulses in time [6–8]. Instead, these definitions resemble the traditional analysis performed for **OFDM!** (**OFDM!**) optical systems, where each spectral component corresponds to an independent subcarrier [9]. This is also the case of other FWM-like nonlinear models that split the signal into individual spectral components and analyze the interactions between them [10, 11]. In our formulation, the

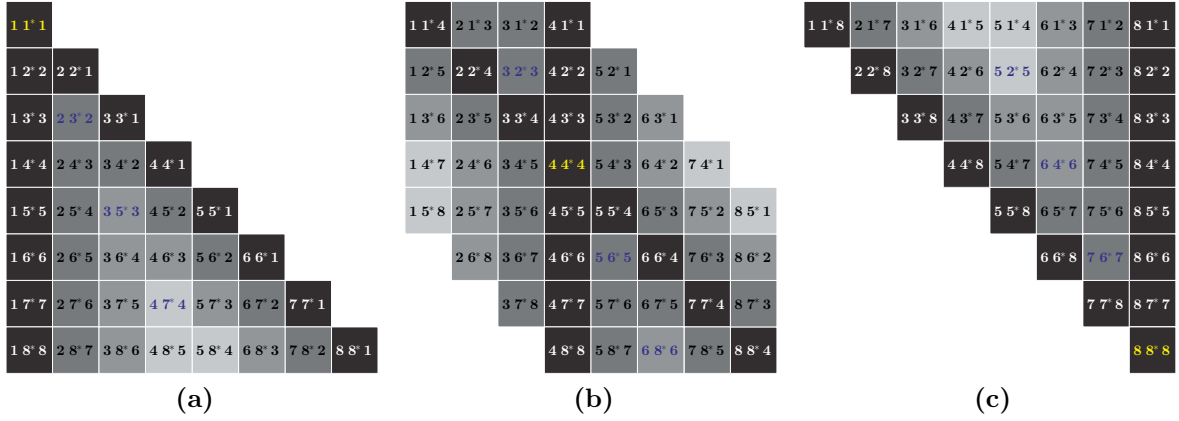


**Figure 4.1:** Matrix representation of the optical field triplets,  $\tilde{\mathcal{A}}_{x/y}$ , as a function of  $n$ , for an illustrative  $8 \times 8$  VSNE. a)  $n = 1$ ; b)  $n = 4$ ; c)  $n = 8$ . iSPM occurs when  $j = k = n$ ; iXPM occurs when  $k = n \neq j$  or  $j = k \neq n$ ; DG-iFWM occurs when  $j = 2k - n$ ; iFWM occurs otherwise. The different colors for each matrix element identify the symmetric column/diagonal pairs.

width of each spectral component,  $\Delta\omega$ , is determined by the sampling rate at the receiver,  $f_s$ , defining the angular frequencies,  $\omega_n$ , as (rewriting equation (3.24) for convenience),

$$\omega_n = (n - 1)\Delta\omega - \pi f_s. \quad (4.3)$$

The distribution of the optical field triplets in the  $\tilde{\mathcal{A}}_{x/y}$  matrix is illustrated in Figure 4.1, for an exemplary  $8 \times 8$  VSNE, where each triplet is presented in the form  $[k, j^*, n - k + j]$ . Through the observation of Figure 4.1 it is possible to identify a symmetry between the columns and diagonals of  $\tilde{\mathcal{A}}_{x/y}$ , which is a function of the  $n$ -th sample index, such that

$$\tilde{\mathcal{A}}_{x/y}^{(j,k)} = \tilde{\mathcal{A}}_{x/y}^{(j,n-k+j)}. \quad (4.4)$$

This is an important observation since it enables to approximately halve the total number of distinct elements in the signal triplet,  $\tilde{\mathcal{A}}_{x/y}$ . Figure 4.1 also allows to geometrically identify the distribution of intra-channel nonlinearities over the defined frequency grid. The iSPM contribution is only originated by a single element in each  $\tilde{\mathcal{A}}_{x/y}(\omega_n, z)$  matrix, where  $j = k = n$ . In turn, the iXPM contributions are located on the  $\tilde{\mathcal{A}}_{x/y}$  main diagonal and  $n$ -th column (excluding the interception of both), where  $k = n \neq j$  or  $j = k \neq n$ . The remaining terms are iFWM contributions, including DG-iFWM which occurs when  $j = 2k - n$ . Note that, due to the out-of-band  $\tilde{\mathcal{A}}_{x/y}(\omega_{n+j-k}, z)$  spectral components, the  $\tilde{\mathcal{A}}_{x/y}$  matrix is populated with an  $n$ -dependent pattern of non-valid entries, which are set to zero values. Therefore, as previously discussed in section 3.3.3, the  $\tilde{\mathcal{A}}_{x/y}(\omega_n, z)$  matrix evolves from lower triangular ( $n = 1$ ) to upper triangular ( $n = N$ ). This is also an important observation, since the computation of null  $\tilde{\mathcal{A}}_{x/y}$  entries can be avoided.

A crucial question at this point is whether the  $\mathbf{K}_3$  matrix also shows identical symmetric properties. If so, it becomes apparent that the total number of VSNE multiplications can be reduced.

### 4.1.1 Analytical formulation

#### Frequency domain iXPM equalizer

Let us start by considering the main  $\mathbf{K}_3$  diagonal, where  $j = k$ . Given that  $\Delta\beta_{j,j}(\omega_n) = 0$ , the elements in  $\mathbf{K}_3$ 's main diagonal can be described by a real-valued constant,

$$K_3^{\text{iXPM}} = \mathbf{K}_3^{(j,j)} = \frac{1 - \exp(\alpha L_s)}{-\alpha}, \quad (4.5)$$

that mitigates both the iSPM and iXPM distortions. This enables to move  $K_3(\omega_j, \omega_j, \omega_n)$  out of the double summation in (3.30). Considering now the  $n$ -th column in  $\mathbf{K}_3$ , where  $k = n$ , it becomes straightforward to observe that  $\mathbf{K}_3^{(j,n)} = \mathbf{K}_3^{(j,j)}$ , which is a particular case of (4.4). Following (4.1), the aggregate contribution of iSPM and iXPM,  $\tilde{N}_{x/y}^{\text{iXPM}}$ , can then be written as

$$\tilde{N}_{x/y}^{\text{iXPM}}(\omega_n) = \sum_{j=1}^N \tilde{\mathbf{N}}_{\mathbf{x}/\mathbf{y}}^{(j,n)}(\omega_n) + \sum_{j=1}^N \tilde{\mathbf{N}}_{\mathbf{x}/\mathbf{y}}^{(j,j)}(\omega_n) - \tilde{\mathbf{N}}_{\mathbf{x}/\mathbf{y}}^{(n,n)}(\omega_n), \quad (4.6)$$

where, for simplicity, we have dropped the  $z$ -dependency in both  $\tilde{\mathbf{N}}_{\mathbf{x}/\mathbf{y}}$  and  $\tilde{N}_{x/y}^{\text{iXPM}}$ . The two first RHS terms account for iSPM and iXPM distortions, while the third RHS term removes the excess iSPM generated by the overlap between the main diagonal and its symmetric  $n$ -th column. Taking advantage of this symmetry, a joint iSPM+iXPM nonlinear equalizer can be derived as

$$\begin{aligned} \tilde{N}_{x/y}^{\text{iXPM}}(\omega_n) = K_3^{\text{iXPM}} \left[ \tilde{A}_{x/y}(\omega_n) \left( 2 \sum_{j=1}^N \tilde{\mathbf{P}}_{\mathbf{xx}/\mathbf{yy}}^{(j,j)} + \sum_{j=1}^N \tilde{\mathbf{P}}_{\mathbf{yy}/\mathbf{xx}}^{(j,j)} - \tilde{\mathbf{P}}^{(n,n)} \right) \right. \\ \left. + \tilde{A}_{y/x}(\omega_n) \sum_{j=1}^N \tilde{\mathbf{P}}_{\mathbf{xy}/\mathbf{yx}}^{(j,j)} \right], \end{aligned} \quad (4.7)$$

where,

$$\tilde{\mathbf{P}}_{\mathbf{xx}/\mathbf{yy}}^{(j,k)} = \tilde{A}_{x/y}(\omega_k) \tilde{A}_{x/y}^*(\omega_j), \quad (4.8a)$$

$$\tilde{\mathbf{P}}_{\mathbf{xy}/\mathbf{yx}}^{(j,k)} = \tilde{A}_{x/y}(\omega_k) \tilde{A}_{y/x}^*(\omega_j). \quad (4.8b)$$

Note that  $\tilde{\mathbf{P}}_{\mathbf{xx}/\mathbf{yy}}^{(j,j)} = \left| \tilde{A}_{x/y}(\omega_j) \right|^2$  is a phase-insensitive intra-polarization term and that  $\tilde{\mathbf{P}}_{\mathbf{xy}/\mathbf{yx}}^{(j,j)}$  is a phase-coherent polarization-mixing term. Once again,  $z$ -dependency in all variables has been omitted to favor readability.

Consider now the  $K$ -diagonals of  $\mathbf{K}_3$ , such that  $k = j - K$ . If  $K > 0$ , the  $K$ -diagonal is located above the main diagonal, whereas if  $K < 0$ , it lies below the main diagonal. Conversely, consider the  $K$ -columns on the left- and right-sides of the  $n$ -th column, such that  $k = n + K$ . Given the distribution of the non-null elements in  $\mathbf{K}_3$ , it becomes apparent that  $K$  must fulfill the condition  $-n + 1 \leq K \leq N - n$ . Taking into account

#### 4.1. Symmetric VSNE

---

that  $\Delta\beta_{j,n+K}(\omega_n) = \Delta\beta_{j,j-K}(\omega_n) = \beta_2 K(n + K - j)\Delta\omega^2$ , the  $\mathbf{K}_3$  elements in the  $K$ -diagonal/column can then be written as

$$\mathbf{K}_3^{(j,n+K)}(\omega_n) = \mathbf{K}_3^{(j,j-K)}(\omega_n) = \frac{1 - \exp\left(\alpha L_s - i\beta_2 K(n + K - j)\Delta\omega^2 L_s\right)}{-\alpha + i\beta_2 K(n + K - j)\Delta\omega^2}, \quad (4.9)$$

evidencing that, besides being  $n$ -dependent,  $\mathbf{K}_3$  is no longer constant outside of its iSPM+iXPM region. Applying the substitution  $K = k - n$ , we obtain a symmetry of the form  $\mathbf{K}_3^{(j,k)} = \mathbf{K}_3^{(j,n-k+j)}$ , compatible with the one identified in (4.4).

#### Frequency domain iFWM equalizer

Let us now consider  $K > 0$ . In accordance with (4.1), the aggregate contribution of each  $K$ -column/diagonal pair can be written as

$$\tilde{N}_{x/y}^{[J](K)}(\omega_n) = \sum_{j \in J} \tilde{N}_{x/y}^{(j,n+K)}(\omega_n) + \sum_{j \in J} \tilde{N}_{x/y}^{(j,j-K)}(\omega_n) - \tilde{N}_{x/y}^{(n+2K,n+K)}(\omega_n), \quad (4.10)$$

where the resulting output,  $\tilde{N}_{x/y}^{[J](K)}(\omega_n)$ , represents the nonlinear equalization contribution generated by the symmetric  $K$ -column/diagonal pair, evaluated over every row  $j \in J$ , where  $J = \{j : K + 1 \leq j \leq N\}$ . The two first RHS terms in (4.10) include the iFWM contribution generated by the  $K$ -column/diagonal pair, whereas the third RHS term accounts for the DG-iFWM occurring at the column/diagonal interception. Note that (4.10) can be seen as a generalization of the iSPM+iXPM distortion given by (4.6), with  $\tilde{N}_{x/y}^{\text{iXPM}}(\omega_n) = \tilde{N}_{x/y}^{[J](0)}(\omega_n)$ . Taking advantage of the identified symmetric properties, (4.10) can be rewritten as

$$\tilde{N}_{x/y}^{[J](K)}(\omega_n) = \tilde{A}_{x/y}(\omega_{n+K}) \left[ 2\tilde{A}_{xx/yy}^{[J](K)}(n) + \tilde{A}_{yy/xx}^{[J](K)}(n) - \text{DG}^{(K)}(n) \right] + \tilde{A}_{y/x}(\omega_{n+K}) \tilde{A}_{xy/yx}^{[J](K)}(n), \quad (4.11)$$

with  $1 \leq n \leq N - K$ .  $\tilde{A}_{xx/yy}^{[J](K)}(n)$  and  $\tilde{A}_{xy/yx}^{[J](K)}(n)$  are scalar values obtained from a  $j$ -index summation over the pre-defined  $J$  interval, being respectively given by

$$\tilde{A}_{xx/yy}^{[J](K)}(n) = \sum_{j \in J} \mathbf{K}_3^{(j,n+K)}(\omega_n) \tilde{\mathbf{P}}_{xx/yy}^{(j,j-K)}, \quad (4.12a)$$

$$\tilde{A}_{xy/yx}^{[J](K)}(n) = \sum_{j \in J} \mathbf{K}_3^{(j,n+K)}(\omega_n) \tilde{\mathbf{P}}_{xy/yx}^{(j,j-K)}. \quad (4.12b)$$

The DG-iFWM at the overlapping index  $j = n + 2K$  is corrected by the  $\text{DG}^{(K)}(n)$  term in (4.11), which is given by

$$\text{DG}^{(K)}(n) = \mathbf{K}_3^{(n+2K,n+K)}(\omega_n) \tilde{\mathbf{P}}^{(n+2K,n+K)}. \quad (4.13)$$

Conversely, the  $K$ -column/diagonal pairs for  $K < 0$  can be obtained in the same form of (4.11), by simply adjusting the summation interval,  $J$ , in order to avoid

invalid indexes. However, a more efficient implementation is possible by noticing that  $\tilde{A}_{xx/yy}^{[J](-K)}(n) = \tilde{A}_{xx/yy}^{*[J](K)}(n - K)$  and  $\tilde{A}_{xy/yx}^{[J](-K)}(n) = \tilde{A}_{yx/xy}^{*[J](K)}(n - K)$ . This inserts a new  $K$ -delayed symmetry between the  $K$ -diagonals above/below the main diagonal and the  $K$ -columns on the right/left-side of the  $n$ -th column, thus enabling to write

$$\begin{aligned} \tilde{N}_{x/y}^{[J](-K)}(\omega_n) = \tilde{A}_{x/y}(\omega_{n-K}) & \left[ 2\tilde{A}_{xx/yy}^{*[J](K)}(n - K) + \tilde{A}_{yy/xx}^{*[J](K)}(n - K) - \text{DG}^{(-K)}(n) \right] \\ & + \tilde{A}_{y/x}(\omega_{n-K})\tilde{A}_{yx/xy}^{*[J](K)}(n - K), \end{aligned} \quad (4.14)$$

with  $K + 1 \leq n \leq N$ . The resulting  $\tilde{N}_{x/y}^{[J](-K)}(\omega_n)$  term undoes the  $\omega_n$  nonlinear distortion generated by the  $K$ -column on the left-side of the  $n$ -th column and by its symmetric  $K$ -diagonal below the main diagonal. This delayed symmetry between  $\pm K$ -column/diagonal pairs avoids duplicate block processing to determine  $\tilde{A}_{xx/yy}^{[J](-K)}(n)$  and  $\tilde{A}_{xy/yx}^{[J](-K)}(n)$ , therefore leading to a more efficient computation of the aggregate  $\pm K$ -column/diagonal nonlinear distortion. Note that  $\text{DG}^{(-K)}(n)$  cannot be directly obtained from  $\text{DG}^{(K)}(n - K)$  since  $\tilde{\mathbf{P}}^{(n-2K, n-K)}$  and  $\tilde{\mathbf{P}}^{(n+K, n)}$  are uncorrelated.

### The symVSNE filter array

By considering  $1 \leq |K| \leq N_k$ , with  $N_k \leq N/2 - 1$ , an array of  $N_k$  parallel equalizers of the form of (4.11) and (4.14) can be obtained. However, care must be taken to avoid partial overlapping between different  $K$ -column/diagonal pairs. One possible efficient strategy to aggregate increasing  $K$ -columns/diagonals is to apply an iXPM-oriented reconstruction of the  $\mathbf{K}_3$  matrix, starting by the lower  $|K|$  symmetric pairs. Then, in order to avoid interference between columns and diagonals, priority must be granted to the lower (upper)  $K$ -diagonals over the right-sided (left-sided)  $K$ -columns. In practice, this aggregating strategy of increasing order  $K$ -column/diagonal pairs corresponds to a reconstruction process of the matrix VSNE, which is conducted from its inner main diagonal to its outer  $K$ -diagonals, while taking advantage of the symmetric relation with the corresponding  $K$ -columns. Following this methodology, the nonlinearly equalized optical field resulting from the overlap-free aggregate of  $2N_k$   $K$ -column/diagonal pairs, plus the iSPM+iXPM contribution, can be obtained as

$$\begin{aligned} \tilde{A}_{x/y}^{\text{NL},(N_k)}(\omega_n, z - L_s) = \Gamma(\omega_n, L_s) & \left[ \tilde{N}_{x/y}^{\text{iXPM}}(\omega_n, z) + \sum_{K=1}^{N_k} \tilde{N}_{x/y}^{[J_U](K)}(\omega_n, z) \right. \\ & \left. + \sum_{K=1}^{N_k} \tilde{N}_{x/y}^{[J_L](-K)}(\omega_n, z) \right], \end{aligned} \quad (4.15)$$

where

$$J_U = \{j : K + 1 \leq j \leq n - 1 \vee n + 2K \leq j \leq N\}, \quad (4.16)$$

and

$$J_L = \{j : K + 1 \leq j \leq n \vee n + 2K \leq j \leq N\}, \quad (4.17)$$

are subsets of the  $J$  interval which control the  $j$ -index for the upper and lower  $K$ -diagonals, respectively.

The filter structure defined by (4.15) will onwards be referred to as the symVSNE, which is an  $N_k$  filter array (symVSNE[ $N_k$ ]). Conversely, we shall from now on refer to the  $K$ -th branch of the symVSNE[ $N_k$ ] filter array as symVSNE{ $K$ }. The full VSNE matrix output optical field,  $\tilde{A}_{x/y}^{\text{NL}}(\omega_n, z - L_s)$ , corresponding to the application of (3.36), can then be obtained by simply setting  $N_k = N/2 - 1$  in (4.15), being therefore equivalent to the symVSNE[ $N/2 - 1$ ]. Finally, since the phased array factor,  $\mathbf{F}^{(j,k)}$ , shares the same symmetric properties as the  $\mathbf{K}_3$  matrix, the multi-span symVSNE[ $N_k$ ] can be straightforwardly obtained by including  $\mathbf{F}^{(j,k)}$  directly into the VSNE kernel as  $\mathbf{K}_3^{\text{MS}}(\omega_n) = \mathbf{K}_3(\omega_n) \circ \mathbf{F}(\omega_n)$ .

The symmetric reconstruction process of the  $\mathbf{K}_3$  kernel with the symVSNE[ $N_k$ ] filter array is shown in Figure 4.2, for an exemplary NZDSF span and an FFT block-size of  $N = 32$ . Figures 4.2a to 4.2d illustrate the progressive population of  $\mathbf{K}_3$  coefficients for increasing values of  $N_k$ , where it can be seen that reconstruction process is faster for lower  $N_k$  and it slows down as  $N_k$  approaches its maximum value of  $N/2 - 1$ , i.e. the symVSNE{ $K$ } filters utilize fewer coefficients with increasing  $K$ . The exact number of coefficients per  $K$ -filter is given by the cardinality of the  $J_L$  interval. Also note that each symVSNE{ $K$ } filter includes the contribution of two symmetric column/diagonal pairs<sup>1</sup>, thus speeding up the reconstruction process.

The numerical implementation of symVSNE-based DBP is schematically illustrated in Figure 4.3, where VSNE-based nonlinear equalization is applied in parallel with frequency domain CDE. Alternatively to the full matrix VSNE, each symVSNE{ $K$ } filter branch is applied in parallel, building a symVSNE[ $N_k$ ] filter array, whose maximum dimension is  $N/2 - 1$ . The number of steps,  $N_{\text{steps}}$ , is obtained from the total number of fiber spans,  $N_s$ , and the number of spans per each VSNE step,  $N_{\text{spans/step}}$ , as  $N_{\text{steps}} = N_s / N_{\text{spans/step}}$ . Note that all DBP steps are applied exclusively in the frequency domain, since the FFT/IFFT pairs are only required to transform the signal into frequency domain for DBP and to transform it back to time domain for the subsequent DSP stages.

### 4.1.2 Implementation complexity

Since it is a special case of the derived symVSNE, let us start by evaluating the total computational effort required by the iXPM+iSPM equalizer defined by (4.7). Although it is easy to conclude that the iXPM+iSPM equalizer is obtained at the expense of  $N^2$  elements per FFT, the direct evaluation of (4.7) reveals that only  $3N$  CMs and  $12N + 2$  RMs are in fact required per FFT block:

- the first RHS term requires  $8N + 2$  RMs;
  - $4N$  RMs to compute  $\sum_{j=1}^N \tilde{\mathbf{P}}_{\mathbf{xx}/\mathbf{yy}}^{(j,j)}$ ;
  - 1 RM per polarization to compute the  $2 \times$  factor;

---

<sup>1</sup>At the exception of the symVSNE{0} filter, whose coefficients correspond to the  $\mathbf{K}_3$  main diagonal and  $n$ -th column.

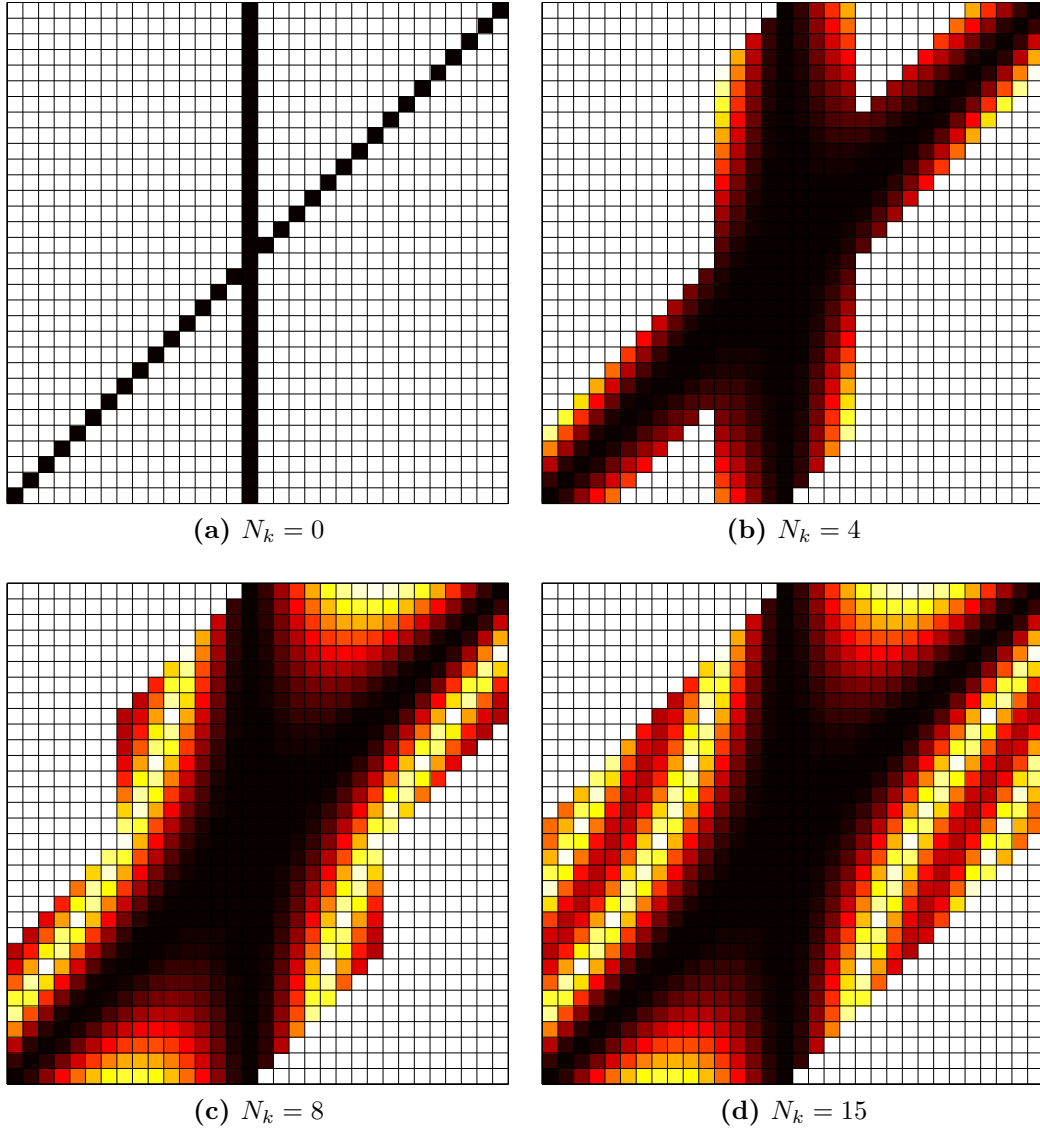


**Figure 4.2:** Illustration of the symmetric  $\mathbf{K}_3$  kernel reconstruction technique for an exemplary NZDSF transfer function with  $N = 32$ . The colormap qualitatively represents the values of  $|\Re\{\mathbf{K}_3^{(j,k)}(\omega_{16})\}|$  (darker elements correspond to larger absolute values). Each subfigure corresponds to the partial/full  $\mathbf{K}_3$  reconstruction with a)  $N_k = 0$ , b)  $N_k = 4$ , c)  $N_k = 8$  and d)  $N_k = 15$ .

- $2N$  RMs per polarization to multiply by  $\tilde{A}_{x/y}(\omega_n)$ .
- the second RHS term requires  $3N$  CMs;
  - $N$  CMs to compute  $\sum_{j=1}^N \tilde{\mathbf{P}}_{xy/yx}^{(j,j)}$ , since  $\tilde{\mathbf{P}}_{yx}^{(j,j)} = \tilde{\mathbf{P}}_{xy}^{*(j,j)}$ ;
  - $N$  CMs per polarization to multiply by  $\tilde{A}_{y/x}(\omega_n)$ .
- the multiplication by  $K_3^{\text{iXPM}}$  requires  $2N$  RMs per polarization.

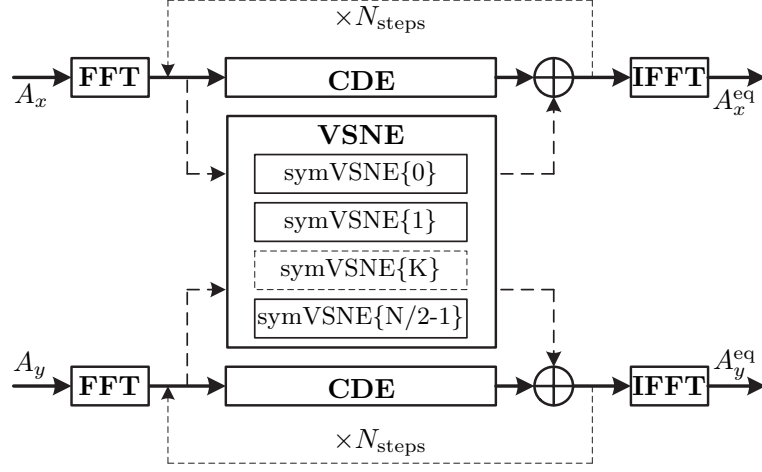


**Figure 4.3:** Numerical implementation diagram of the VSNE and symVSNE algorithms in parallel with a frequency domain CDE. The time domain input signal,  $A_{x/y}$ , is transformed into frequency domain by an FFT and then iteratively compensated in linear and nonlinear parallel branches, yielding the equalized signal,  $A_{x/y}^{\text{eq}}$ , after the IFFT.

Considering that 1 CM requires 4 RMs, the total number of RMs per sample required by the iSPM+iXPM equalizer is given by

$$M_{\text{symVSNE}}^{(1)}(N) = 24 + \frac{2}{N}. \quad (4.18)$$

In turn, for  $N_k > 0$ , the  $n$ -dependence of  $\mathbf{K}_3$  imposes to recalculate all the  $j$ -summation terms for every sample,  $n$ . From (4.11), (4.14) and (4.15) it becomes apparent that the main source of computations is due to the calculation of the  $\tilde{A}_{xx/yy}^{[J](K)}(n)$  and  $\tilde{A}_{xy/yx}^{[J](K)}(n)$  coefficients, which require block processing to evaluate the multiply-accumulate operations as a function of the  $j$ -index within the  $J_U$  and  $J_L$  intervals. By noticing that  $J_U \subset J_L$  in (4.15), and that 4 CMs per  $j$ -index are required (1 CM per  $j$ -index for each  $\tilde{A}_{xx/yy}^{[J](K)}(n)$  and  $\tilde{A}_{xy/yx}^{[J](K)}(n)$  coefficient), the total number of RMs per sample, as a function of  $N_k$ , can be written as

$$M_{\text{symVSNE}}^{(2)}(N, N_k) = \frac{16}{N} \sum_{K=1}^{N_k} \left[ \sum_{n=K+1}^{N-K} (n-K) + \sum_{n=1}^{N-2K} (N-n-2K+1) \right], \quad (4.19)$$

where the first RHS summation term includes all RMs for  $K+1 \leq j \leq n$ , while the second RHS summation includes all RMs for  $n+2K \leq j \leq N$ . Note that the  $\tilde{A}_{xx/yy}^{[J](-K)}(n)$  and  $\tilde{A}_{xy/yx}^{[J](-K)}(n)$  coefficients can be obtained by employing a simple complex conjugate operation.

Additionally, 4 CMs are required to calculate the  $\tilde{\mathbf{P}}_{xx/yy}^{(j,j-K)}$  and  $\tilde{\mathbf{P}}_{xy/yx}^{(j,j-K)}$  terms in (4.12a) and (4.12b). Considering the  $N-K$  valid  $j$ -indexes, the total number of RMs per sample, as a function of  $N_k$ , is given by

$$M_{\text{symVSNE}}^{(3)}(N, N_k) = \frac{16}{N} \sum_{K=1}^{N_k} (N-K). \quad (4.20)$$

The above computation counting encloses all block processing operations required to obtain the  $\tilde{A}_{xx/yy}$ ,  $\tilde{A}_{xy/yx}$  and DG coefficients. Finally, we must account for the *per-sample* processing required to evaluate (4.11) and (4.14), which are applied  $N - K$  times for  $1 \leq K \leq N_k$  and involves a total of 8 CMs per sample (4 CMs per polarization). The total number of RMs required for per-sample processing, as a function of  $N_k$ , is then

$$M_{\text{symVSNE}}^{(4)}(N, N_k) = \frac{32}{N} \sum_{K=1}^{N_k} (N - K). \quad (4.21)$$

Finally, the multiplication by  $\Gamma(\omega_n, z)$  in (4.15) requires an additional  $M_{\text{symVSNE}}^{(5)} = 4$  RMs. The total number of RMs per sample required by the symVSNE, as a function of  $N_k$ , is then given by

$$\begin{aligned} M_{\text{symVSNE}}(N, N_k) &= \sum_{j=1}^5 M_{\text{symVSNE}}^{(j)}(N, N_k) \\ &= 16N_k N - 32 \left( N_k^2 - N_k - \frac{7}{8} \right) + \left( \frac{64}{3} N_k^3 - 8N_k^2 - \frac{88}{3} N_k + 2 \right) \frac{1}{N}, \end{aligned} \quad (4.22)$$

from where the number of CMs for a full VSNE reconstruction can be obtained as

$$M_{\text{symVSNE}}(N, N/2 - 1) = \frac{8}{3} N^2 + 14N - \frac{32}{3} + \frac{2}{N}. \quad (4.23)$$

Finally, the overall complexity of symVSNE-based DBP as depicted in Figure 4.3 is given by

$$M_{\text{symVSNE}}^{\text{DBP}}(N, N_k) = N_{\text{steps}}(M_{\text{symVSNE}}(N, N_k) + 2M_{\text{CDE}}) + 4M_{\text{FFT}}(N), \quad (4.24)$$

where  $M_{\text{CDE}} = 4$  represents the complexity of frequency domain CD equalization and  $M_{\text{FFT}}$  is the number of RMs per sample required by each FFT, as given by expression (3.10). The factor of 2 in the  $M_{\text{CDE}}$  term accounts for the two polarization tributaries and the factor of 4 in the  $M_{\text{FFT}}$  term accounts for the FFT/IFFT pair in each polarization. Also note that the  $M_{\text{FFT}}$  term is not affected by  $N_{\text{steps}}$ , since all steps are entirely applied in frequency domain. In terms of processing latency, the symVSNE-based DBP is equivalent to the matrix-based VSNE, thus yielding

$$\tau_{\text{symVSNE}}^{\text{DBP}} = 4N_{\text{steps}} + 2\tau_{\text{FFT}}. \quad (4.25)$$

where  $\tau_{\text{FFT}}$  represents the latency of FFT processing, as given by (3.11).

To facilitate the direct comparison with the original VSNE formulation, let us rewrite the complexity of the matrix-based VSNE given by expression (3.43) for the case of a dual-polarization system,

$$M_{\text{VSNE}}(N) = 8N^2 + 4N + 16. \quad (4.26)$$

By comparing the  $O(N^2)$  terms in (4.26) and (4.23), it can be straightforwardly concluded that the full matrix VSNE reconstruction via the symVSNE filter array is obtained with a reduction on the computational effort that asymptotically converges to a factor of 3. More detailed insights on this computational efficiency comparison will be discussed in the following section.

## 4.2 Simplified VSNE

The previous symVSNE computational effort analysis reveals that the largest source of complexity arises from the multiplication of the  $\mathbf{K}_3$  kernel by the  $\tilde{\mathbf{P}}_{\mathbf{xx}/\mathbf{yy}}/\tilde{\mathbf{P}}_{\mathbf{xy}/\mathbf{yx}}$  vectors in (4.12a) and (4.12b), which is caused by the  $n$ -index dependence of  $\mathbf{K}_3$ . Indeed, the  $O(N)$  term in (4.22) and the  $O(N^2)$  term in (4.23) are exclusively caused by these operations. Stemming from this observation, in this section we introduce a simVSNE based on ignoring the  $n$ -dependence of  $\mathbf{K}_3$  for  $N_k > 0$ . By doing so we seek for an optimized tradeoff between complexity and performance, tackling the most critical part of the symVSNE algorithm in terms of computational effort.

### 4.2.1 Analytical formulation

Using the heuristic that the  $j$  and  $n$  dependencies in  $\mathbf{K}_3$  are weaker in its lower  $|K|$ -column/diagonal pairs, we will assume that these columns/diagonals are populated by constant real-valued scalars,  $K_3^{\text{iXPM}}$ , as in the iSPM+iXPM equalizer (symVSNE[0]). This allows to remove  $\mathbf{K}_3$  from (4.12a) and (4.12b), by simply including it in the  $\Gamma(\omega_n, z)$  term, as

$$\Gamma'(\omega, z) = \frac{1 - \exp(\alpha L_s)}{-\alpha} \Gamma(\omega, z). \quad (4.27)$$

Then, (4.11), (4.14) and (4.15) can be rewritten as,

$$\begin{aligned} \tilde{N}'_{x/y}^{[J](K)}(\omega_n) &= \tilde{A}_{x/y}(\omega_{n+K}) \left[ 2 \sum_{j \in J} \tilde{\mathbf{P}}_{\mathbf{xx}/\mathbf{yy}}^{(j,j-K)} + \sum_{j \in J} \tilde{\mathbf{P}}_{\mathbf{yy}/\mathbf{xx}}^{(j,j-K)} - \tilde{\mathbf{P}}^{(n+2K, n+K)} \right] \\ &\quad + \tilde{A}_{y/x}(\omega_{n+K}) \sum_{j \in J} \tilde{\mathbf{P}}_{\mathbf{xy}/\mathbf{yx}}^{(j,j-K)}, \end{aligned} \quad (4.28)$$

$$\begin{aligned} \tilde{N}'_{x/y}^{[J](-K)}(\omega_n) &= \tilde{A}_{x/y}(\omega_{n-K}) \left[ 2 \sum_{j \in J} \tilde{\mathbf{P}}_{\mathbf{xx}/\mathbf{yy}}^{*(j,j-K)} + \sum_{j \in J} \tilde{\mathbf{P}}_{\mathbf{yy}/\mathbf{xx}}^{*(j,j-K)} - \tilde{\mathbf{P}}^{(n-2K, n-K)} \right] \\ &\quad + \tilde{A}_{y/x}(\omega_{n-K}) \sum_{j \in J} \tilde{\mathbf{P}}_{\mathbf{xy}/\mathbf{yx}}^{*(j,j-K)}, \end{aligned} \quad (4.29)$$

and

$$\begin{aligned} \tilde{A}'_{x/y}{}^{\text{NL},(N_k)}(\omega_n, z - L_s) &= \Gamma'(\omega_n, L_s) \left[ \frac{\tilde{N}'_{x/y}{}^{\text{iXPM}}(\omega_n, z)}{K_3^{\text{iXPM}}} + \sum_{K=1}^{N_k} \tilde{N}'_{x/y}{}^{[Jv](K)}(\omega_n, z) \right. \\ &\quad \left. + \sum_{K=1}^{N_k} \tilde{N}'_{x/y}{}^{[Jl](-K)}(\omega_n, z) \right], \end{aligned} \quad (4.30)$$

where  $\tilde{A}'_{x/y}{}^{\text{NL},(N_k)}$  is the nonlinearly equalized field obtained by the application of a simVSNE[ $N_k$ ] filter. Finally, for multi-span equalization with the simVSNE, the phased-array factor is simplified into a non-coherent term, given by

$$F^{\text{iXPM}} = \frac{N_s}{N_{\text{steps}}}, \quad (4.31)$$

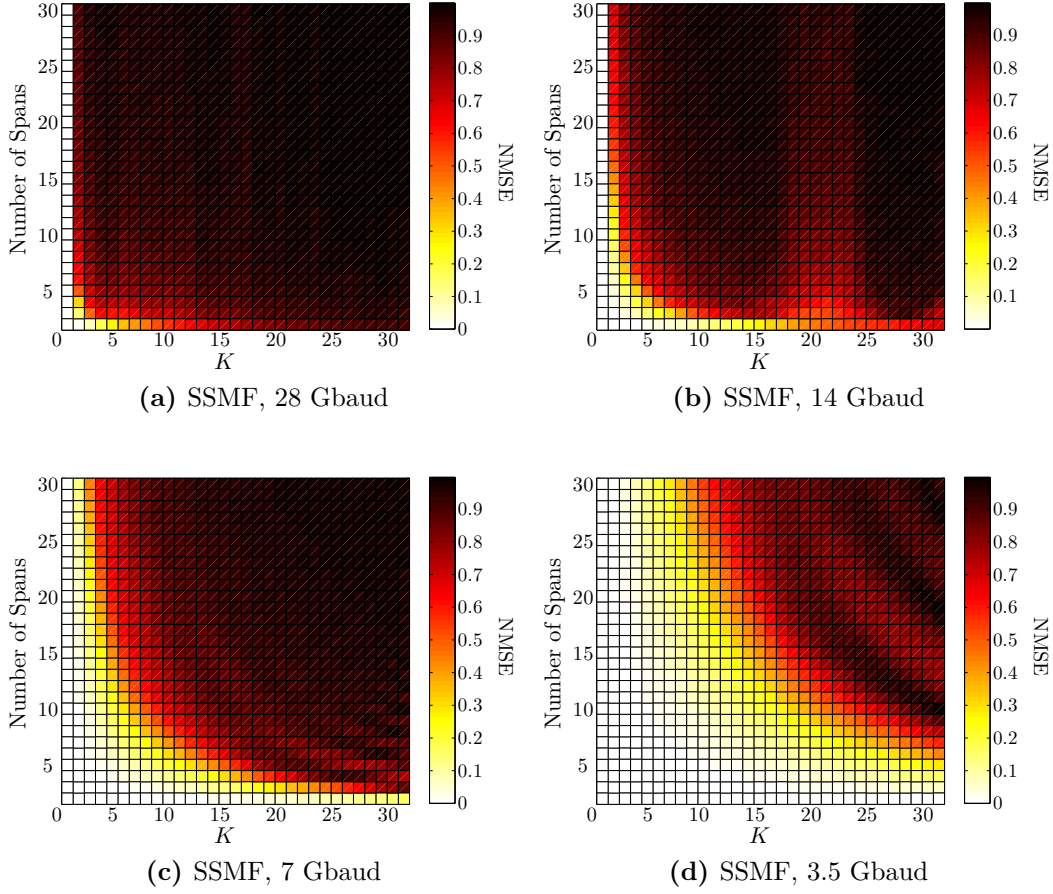


**Figure 4.4:** Normalized mean squared error between the simVSNE and symVSNE coefficients as a function of the filter dimension,  $N_k$ , and number of fiber spans per transfer function for an SSF optical link. The FFT block-size is  $N = 64$  and the analyzed sample index is  $n = 32$ .

where  $N_s/N_{\text{steps}} = N_{\text{spans/step}}$  represents the number of spans per each simVSNE step. This factor is then integrated in the  $\Gamma'(\omega, z)$  term as

$$\Gamma^{\text{MS}'}(\omega, z) = \Gamma'(\omega, z)F^{\text{iXPM}}, \quad (4.32)$$

and the multi-span simVSNE is obtained by simply substituting  $\Gamma'(\omega_n, L_s)$  by  $\Gamma^{\text{MS}'}(\omega, L_s)$  in 4.30.

Note that, in practical terms, the constant coefficient assumption utilized to derive the simVSNE algorithm corresponds to a frequency-flat approximation of the third-order nonlinear transfer function of the fiber. Although this seems to be a rough approximation when performed over a wide frequency range, its association with the iXPM-oriented symmetric kernel reconstruction proposed for the symVSNE filter array enables to delimitate a region of operation where the frequency-flat approximation is actually quite accurate. Figures 4.4 and 4.5 illustrate the normalized MSE between the

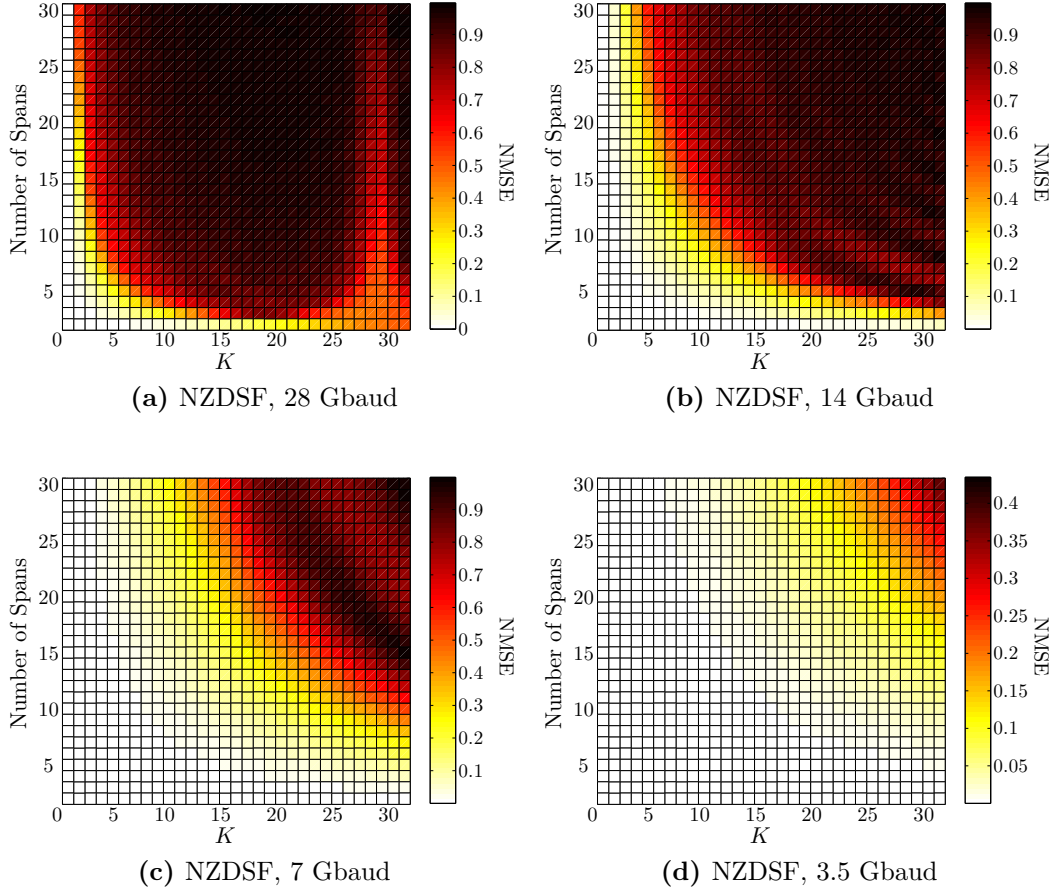


**Figure 4.5:** Normalized mean squared error between the simVSNE and symVSNE coefficients as a function of the filter dimension,  $N_k$ , and number of fiber spans per transfer function for an NZDSF optical link. The FFT block-size is  $N = 64$  and the analyzed sample index is  $n = 32$ .

symVSNE and simVSNE coefficients for SSMF and NZDSF optical links, defined as

$$\text{NMSE}(n, K) = \frac{\sqrt{\left( \sum_{j \in \mathcal{J}_U} \mathbf{K}_3^{(j, n+K)}(\omega_n) - K_3^{\text{iXPM}} \right)^2}}{K_3^{\text{iXPM}}}. \quad (4.33)$$

The obtained results for the SSMF and NZDSF optical links allow to draw several key conclusions:

- i) the error incurred by the simVSNE is minimum for  $K = 0$ , with the simVSNE[0] being exactly equivalent to the symVSNE[0], and it tends to progressively increase for  $K > 0$ . This shows that the frequency-flat approximation can be applied with reasonable accuracy for low simVSNE filter dimension,  $N_k$ , whose coefficients originate from iXPM-like column/diagonal pairs in  $\mathbf{K}_3$ . The maximum simVSNE performance can then be found by optimizing  $N_k$  for a given optical fiber link;

- ii) due to the phased-array accumulation of nonlinearities dictated by expression (3.38), the iXPM-like regions in  $\mathbf{K}_3$  become narrower with increasing number of spans, and consequently the validity of the frequency-flat approximation becomes restricted to lower  $K$  values. This effect will set the maximum number of fiber spans per simVSNE transfer function, or conversely, the minimum number of simVSNE steps required for a given fiber link;
- iii) similarly to the phased-array accumulation of nonlinearities between multiple fiber spans, higher local dispersion also leads to narrower iXPM-like regions in  $\mathbf{K}_3$ , as previously illustrated in Figure 2.2. Consequently, in low-dispersion fibers, such as NZDSF, the frequency-flat approximation maintains high accuracy for larger values of  $K$ , and therefore the maximum simVSNE performance is expected to be achieved for higher  $N_k$ ;
- iv) due to the quadratic dependence of the accumulated dispersion on the transmission symbol-rate, and due to the same reasoning of ii) and iii), the  $K$ -region of high simVSNE accuracy tends to increase for decreasing symbol-rate. This an important conclusion in terms of strategic evolution of next-generation long-haul optical transmission systems, corroborating the recent trend on subcarrier multiplexing, with per-subcarrier symbol-rates in the order of 2 to 10 Gbaud [12]. In particular, these results show that in addition to the benefits on uncompensated signal propagation demonstrated in [12], the reduction of per-subcarrier symbol-rates can also contribute to decrease the complexity of nonlinear compensation.

In summary, the lossy simVSNE kernel reconstruction provides a low-complexity alternative for the lossless symVSNE algorithm, using a frequency-flat approximation whose region of validity depends on key parameters such as the filter dimension ( $N_k$ ), the number of simVSNE steps ( $N_{\text{steps}}$ ), the local dispersion and dispersion map and the transmission symbol-rate. A comprehensive analysis of the performance versus complexity tradeoff is provided in the following sections.

### 4.2.2 Implementation complexity

Equations (4.28) and (4.29) explicitly show that, on the contrary of the symVSNE filter, the simVSNE algorithm does not use  $n$ -dependent coefficients. The number of RMs involved in the simVSNE filtering can then be obtained from (4.22), by shutting down the  $M_{\text{symVSNE}}^{(2)}$  term and by removing 4 RMs per sample from  $M_{\text{symVSNE}}^{(1)}$ , since the multiplication by  $K_3^{\text{iXPM}}$  is already included in  $M_{\text{symVSNE}}^{(5)}$ ,

$$\begin{aligned} M_{\text{simVSNE}}(N, N_k) &= M_{\text{symVSNE}}(N, N_k) - M_{\text{symVSNE}}^{(2)}(N, N_k) - 4 \\ &= 48 \left( N_k + \frac{1}{2} \right) - (24N_k^2 + 24N_k + 2) \frac{1}{N}. \end{aligned} \quad (4.34)$$

The complexity associated with a hypothetical full reconstruction of the matrix-based VSNE using the simVSNE algorithm is then described by

$$M_{\text{simVSNE}}(N, N/2 - 1) = 18N - 12 + \frac{2}{N}, \quad (4.35)$$

## 4.2. Simplified VSNE

---

exposing that the computational effort is now dominated by a  $O(N)$  term. However, as previously discussed, a full reconstruction of the VSNE kernel using the simVSNE algorithm is likely to generate an accumulation of numerical errors due to the constant coefficient simplification, causing divergence issues. The simVSNE algorithm is then specially designed for reduced dimension filter arrays. Analogously to the symVSNE, the overall complexity of simVSNE-based DBP for dual-polarization optical systems is given by

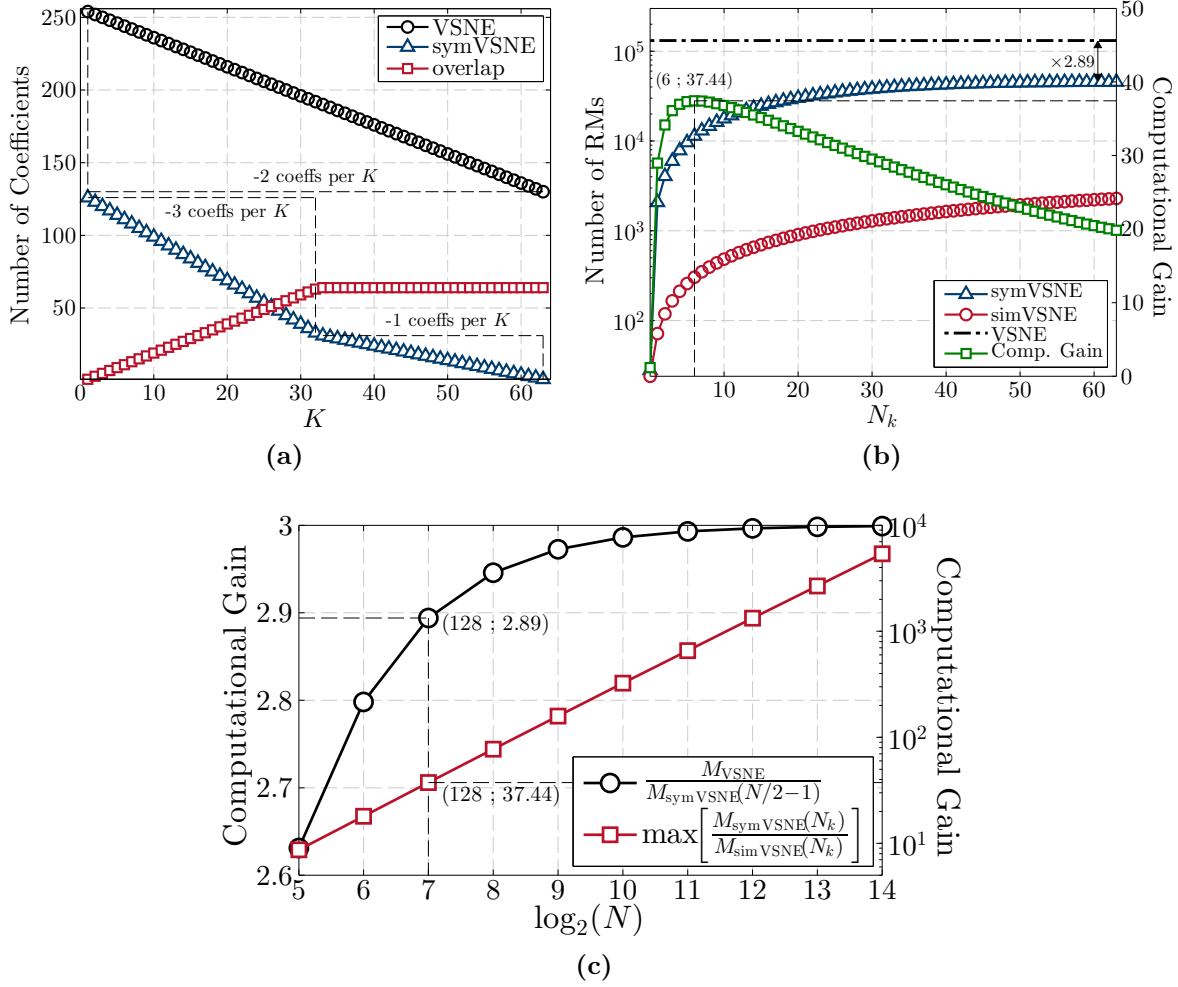
$$M_{\text{simVSNE}}^{\text{DBP}}(N, N_k) = N_{\text{steps}}(M_{\text{simVSNE}}(N_k) + 2M_{\text{CDE}}) + 4M_{\text{FFT}}(N). \quad (4.36)$$

In turn, the processing latency associated with the simVSNE-based DBP is given by

$$\tau_{\text{simVSNE}}^{\text{DBP}} = 3N_{\text{steps}} + 2\tau_{\text{FFT}}, \quad (4.37)$$

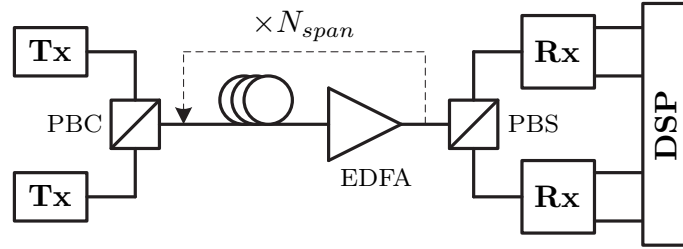
where the  $N_{\text{steps}}$  fewer serial RMs are due to the frequency-flat approximation, enabling to include the  $K_3^{\text{iXPM}}$  factor in the  $\Gamma'(\omega, z)$  terms, as given by equation (4.27).

Figure 4.6 shows some computational effort indicators for the symVSNE and simVSNE algorithms. The number of coefficients in the  $K$ -th branch of the symVSNE filter (for  $N = 128$  and  $n = 64$ ) is shown in Figure 4.6a, which basically corresponds to the cardinality of the  $J_L$  interval. We observe a steady decrease on the number of coefficients (-3 coefficients per  $K$ ) in each  $K$ -branch of the symVSNE filter array, matched with steady increase on the number of overlapping indexes, caused by the intersection between different  $K$ -column/diagonal pairs. At  $K = N/4 + 1$ , the number of overlapping indexes stabilizes at  $N/2$  and the number of coefficients per  $K$ -filter starts decreasing at 1 coefficient per  $K$ , until it reaches zero at  $K = N/2$ . As a figure of comparison, we also show the evolution on the number of coefficients of the matrix-based VSNE algorithm, considering a similar reconstruction of its kernel, but disregarding the identified symmetries. For  $K = 1$  a factor of  $\sim 2$  is found between the number of coefficients of the symVSNE and VSNE algorithms, due to the symmetry between  $K$  and  $-K$  column/diagonal pairs. Then, the number of coefficients on the VSNE algorithm decreases at a constant rate of 2 coefficients per  $K$ , thus increasing this ratio. The accumulation of all coefficients for a full kernel reconstruction yields 12160 coefficients for the VSNE algorithm and 3040 coefficients for the symVSNE algorithm, corresponding to a ratio of 4. Note that this analysis is only valid for  $n = N/2$ . A more general analysis is presented in Figure 4.6b, which shows the total number of RMs per sample, as a function of  $N_k$ , for the VSNE, symVSNE and simVSNE algorithms, as given by expressions (4.26), (4.22), and (4.34). On the contrary of the matrix VSNE, the computational effort of the symVSNE and simVSNE algorithms can be freely adjusted by controlling the filter array dimension through the  $N_k$  parameter. The computational benefit of the proposed symmetric kernel reconstruction is evidenced by the shape of the symVSNE and simVSNE curves. Due to the distribution of coefficients per  $K$ -filter, the associated computational effort of the symmetric-VSNE algorithms suffers from a rapid increase for low  $N_k$ , then leveling off for  $N_k > N/8$ . This behavior is more pronounced for the symVSNE filter array, as can be seen by the computational gain curve associated with the right-sided y-axis of Figure 4.6b, which shows that the simVSNE gain over symVSNE reaches a peak of 37.44 for  $N_k = 6$  and then gradually decreases down to a factor of  $\sim 20$  (for  $N = 128$ ), thus



**Figure 4.6:** Figures of merit for the computational effort required by frequency domain VSNE-based algorithms. a) Number of elements in the  $K$ -th branch of the symVSNE and matrix VSNE filters for  $N = 128$  and  $n = 64$ ; b) Number of RMs per FFT block of the matrix VSNE, symVSNE and simVSNE algorithms for  $N = 128$ , as a function of  $N_k$  (left y-axis) and computational gain of the simVSNE $[N_k]$  over the symVSNE $[N_k]$  algorithm (right y-axis); c) Computational gain of the symVSNE $[N/2 - 1]$  filter array over the matrix VSNE and peak computational gain of the simVSNE over the symVSNE algorithm, as a function of  $N$ .

evidencing the advantages of using a low- $N_k$  simVSNE filter array. Besides, a hypothetical full kernel reconstruction with the symVSNE algorithm provides a computational gain of  $\sim 2.89$  for  $N = 128$ , while a gain of approximately 2 orders of magnitude is obtained with the simVSNE. The dependence of these computational gains on the FFT block-size,  $N$ , is presented in Figure 4.6c, where it is shown that the symVSNE $[N/2 - 1]$  gain over the matrix VSNE asymptotically converges to a factor of 3, as  $N$  grows to infinity. In turn, the simVSNE peak computational gain over the symVSNE algorithm (right-side y-axis of Figure 4.6c) grows linearly with  $N$  (with a slope of  $\sim 2$ ), thus exposing a prominent computational advantage of the simVSNE algorithm for large FFT blocks.



**Figure 4.7:** Schematic representation of the simulated 224 Gb/s PM-16QAM transmission system for the numerical assessment of frequency domain VSNE-based equalization. Tx - transmitter; Rx - Receiver; PBC - Polarization Beam Combiner; PBS - Polarization Beam Splitter.

In the following section, we will thoroughly evaluate the equalization performance of the proposed VSNE-based algorithms, in order to identify optimized complexity/performance tradeoffs.

## 4.3 Numerical Assessment

Using VPItransmissionMaker9.0 we have simulated a single-channel 224 Gb/s PM-16QAM transmission system composed of 24 spans of SSMF with  $\alpha = 0.2$  dB/km,  $\beta_2 = -20.4$  s<sup>2</sup>/km and  $\gamma = 1.3$  W<sup>-1</sup>km<sup>-1</sup>. A simplified schematic representation of the simulated transmission system is depicted in Figure 4.7. Fiber loss is perfectly compensated at the end of each fiber span by an EDFA with 5 dB noise figure. The received electrical fields are then fully post-processed in MATLAB. A third-order Butterworth low-pass filter with cutoff-frequency at 80% of the symbol rate precedes the downsampling stage, where only 2 samples per symbol are considered for the subsequent DSP algorithms. Static linear equalization is performed by a frequency domain CDE. Nonlinear equalization is performed by the DBP-SSFM and VSNE-based algorithms in parallel with CDE, as depicted in Figure 4.3. Polarization-dependent effects are mitigated by a butterfly FIR filter driven by the radius-directed CMA [13]. Since both frequency mismatch and phase noise in the LO have been neglected for simplicity, carrier recovery is implemented by a constant phase rotation. Finally, symbol decoding is performed over  $2^{17}$  bits and the system performance is measured via the direct BER counting between the transmitted and decoded information.

### 4.3.1 Span-by-span equalization

In order to assess the maximum equalization performance that can be achieved for the considered transmission system, we will begin our analysis with a span-by-span DBP strategy, where the number of steps is equal to the number of fiber spans,  $N_{\text{steps}} \leq N_s$ . The BER evolution with increasing launched power in each fiber span is shown in Figure 4.8, employing different static equalization methods. A large performance gap between linear and nonlinear compensation algorithms is well visible for the selected range of input powers. Indeed, assuming a BER limit of  $3.8 \times 10^{-3}$  for hard-decision FEC with 7%

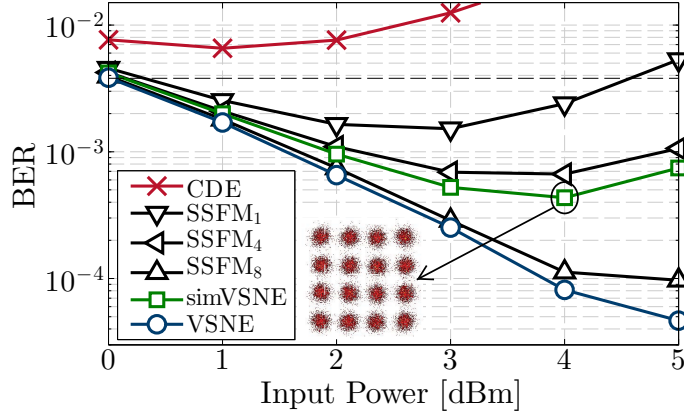


**Figure 4.8:** BER as a function of the launched power in each fiber span. Each curve corresponds to a different static equalization algorithm.

overhead [14], signal decoding employing only CDE remains unfeasible, even at the optimal input power. For universal impairment compensation (linear + nonlinear) we have then applied the asymmetric DBP-SSFM with different number of steps per span,  $N_{\text{steps}/\text{span}}$ , per span (DBP-SSFM $_{N_{\text{steps}}}$ ). In this particular case, the total number of steps is given by  $N_{\text{steps}} = N_{\text{steps}/\text{span}} N_s$ . Although DBP-SSFM $_1$  enables to increase the optimal power by 2 dB relatively to CDE and achieve a BER below the FEC limit, significant performance gains can be obtained by further reducing each iteration step-size. We found that the DBP-SSFM performance approximately saturates for 8 steps per span. As previously discussed in Chapter 3, due to the numerous time-frequency transitions during the equalization process, the DBP-SSFM technique tends to suffer from internal aliasing generation that limits its performance [15]. On the contrary, the bulk frequency domain operation of the VSNE avoids extra aliasing phenomena, justifying the marginal performance gain over DBP-SSFM $_8$  obtained in Figure 4.8 [16–18]. For this span-by-span implementation, the minimum penalty-free FFT block-size has been determined to be 128. Finally, we have applied a variable dimension simVSNE filter array, whose maximum performance is also plotted in Figure 4.8. It can be seen that the maximum simVSNE performance, when applied span-by-span, slightly surpasses that of DBP-SSFM $_4$  for the transmission system under study. The inset in Figure 4.8 shows the final PM-16QAM constellation ( $x$ -pol only) obtained after static equalization with the simVSNE+CDE algorithms at 4 dBm. Note that for both the DBP-SSFM and VSNE methods, the  $\xi$  parameter has been optimized a priori with a resolution of 0.05. The simVSNE method has then been applied with the same  $\xi$  as the one found for the matrix VSNE.

The impact of  $N_k$  on the symVSNE and simVSNE filters is evaluated in Figure 4.9. The results obtained for the symVSNE $[N_k]$  filter array allows to draw two main conclusions: (i) independently of the input power, a steep performance gain is obtained for  $N_k \leq 3$ , revealing the importance of the low  $|K|$  column/diagonal contributions; (ii) as we move further into the nonlinear regime, by increasing the input power, a slower performance optimization takes place for  $N_k > 3$ , thus requiring a larger filter array to

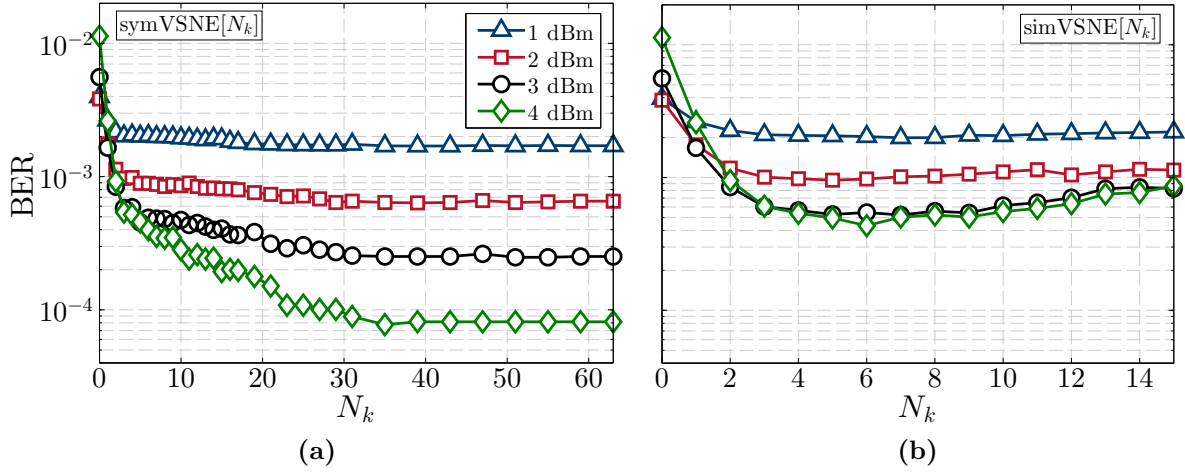


**Figure 4.9:** BER as a function of the  $N_k$  parameter in the symVSNE and simVSNE filters for a set of input powers ranging from 1 dBm to 5 dBm.

approximate the matrix VSNE performance. Besides, Figure 4.9a also demonstrates that the symVSNE[ $N/2 - 1$ ] filter array is effectively equivalent to the full matrix VSNE, as can be seen by directly comparing the BER results in Figures 4.8 and 4.9a. In turn, the simVSNE[ $N_k$ ] performance is shown in Figure 4.9b. For low  $N_k$  values, only a small performance penalty is incurred relatively to its symVSNE counterpart, enabling to achieve a significant performance gain with a reduced filter dimension. This is possible due to the iXPM-like properties of the column/diagonal pairs nearby the iXPM+iSPM contribution, where the constant coefficient assumption is an accurate approximation. Further increasing  $N_k$  leads to a rapid saturation of the simVSNE performance gain, after which a divergence process begins, signaling that the added filter branches are only contributing with noise. Note that this divergence process can be easily avoided by individually optimizing the  $\xi$  parameter for each filter branch. As the divergence process initiates,  $\xi$  will tend to zero, attenuating the noise generation. A small performance improvement for large  $N_k$  can also be obtained by using this strategy. We will further discuss this issue in following subsection, in the context of multi-span compensation.

### 4.3.2 Multi-span equalization

Although span-by-span equalization delivers the highest equalization performance, a multi-span implementation can be far more computationally efficient. Figure 4.10 shows the evolution of BER as a function of the total number of DBP steps: 24 steps refer to a span-by-span implementation, while 1 step refers to a full-link equalization in a single step. Optimizing the number of steps depends upon many variables including the fiber link, signal and equalizer parameters. In this work, this optimization is carried out numerically by assessing the BER performance with varying number of steps. In a practical scenario, a decision-feedback structure can be implemented to control  $N_{\text{steps}}$  based on a given BER target (the same applies to  $N_k$ ). The obtained results show that the multi-span DBP-SSFM quickly starts diverging as we increase its associated step-size.

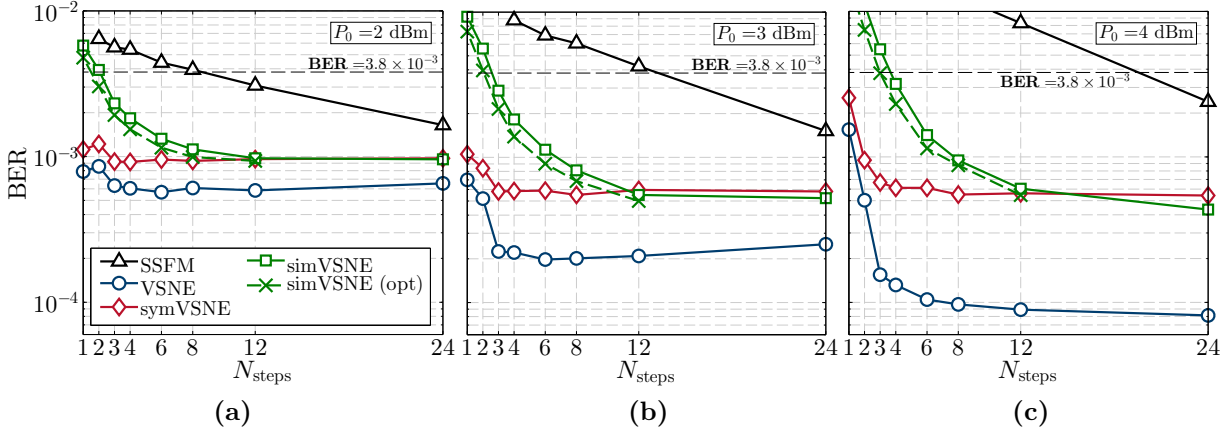


**Figure 4.10:** BER as a function of the total number of DBP steps for an input power of a) 2 dBm, b) 3 dBm and c) 4 dBm. The simVSNE curves refer to its maximum achievable performance. The symVSNE curves have been obtained for a fixed filter dimension of  $\lceil N/40 \rceil$ .

Indeed, for the transmission system under study with an input power higher than 2 dBm, SSFM-based DBP is only feasible with a span-by-span implementation. In contrast, the multi-span VSNE performance is kept approximately constant up to a maximum of 8 fiber spans per transfer function (3 steps). Then, a gradual performance loss starts taking place, due to the inability of capturing the higher-order nonlinearities generated by the multi-span accumulation of nonlinearities<sup>2</sup>. Nevertheless, a full-link VSNE is still able to surpass the performance of a span-by-span DBP-SSFM implementation. However, the overall computational effort is severely affected by the quadrativ dependence on the FFT block-size required for a multi-span compensation. Note that, for the full-link equalization, a minimum FFT block-size of 2048 has been determined, in contrast with the span-by-span equalization, where  $N = 128$ . The symVSNE curves have been obtained for a fixed filter array dimension, relatively to the correspondent FFT block-size, of  $\lceil N/40 \rceil$ . Similarly to the full VSNE implementation, the symVSNE performance remains stable up to 3 steps, then beginning to suffer from the same divergence issues. Depending on the BER target, the symVSNE filter dimension can be readjusted, thus enabling to minimize the computational effort.

For the simVSNE algorithm, the phased-array factor is modified into a non-coherent parameter, such that  $\mathbf{F}^{(j,k)} = N_{\text{spans/step}}$ , where  $N_{\text{spans/step}}$  is the number of fiber spans per step. The simVSNE results described by the solid lines with square markers correspond to the maximum simVSNE performance, regardless of the filter dimension,  $N_k$ , and considering a constant  $\xi = 0.8$  parameter, obtained from the VSNE optimization. The obtained results show that, for a high number of steps, the maximum simVSNE performance is nearly matched with that of a symVSNE $[\lceil N/40 \rceil]$  filter. However, with an increasing number of fiber spans per step the simVSNE performance tends to diverge at a faster pace. This is caused by an inaccurate addition of each step contribution, due

<sup>2</sup>Note this penalty is intrinsically bounded with the simplifications made to derive the phased-array factor for the multi-span modelling of nonlinearities, as detailed in Appendix B.

### 4.3. Numerical Assessment

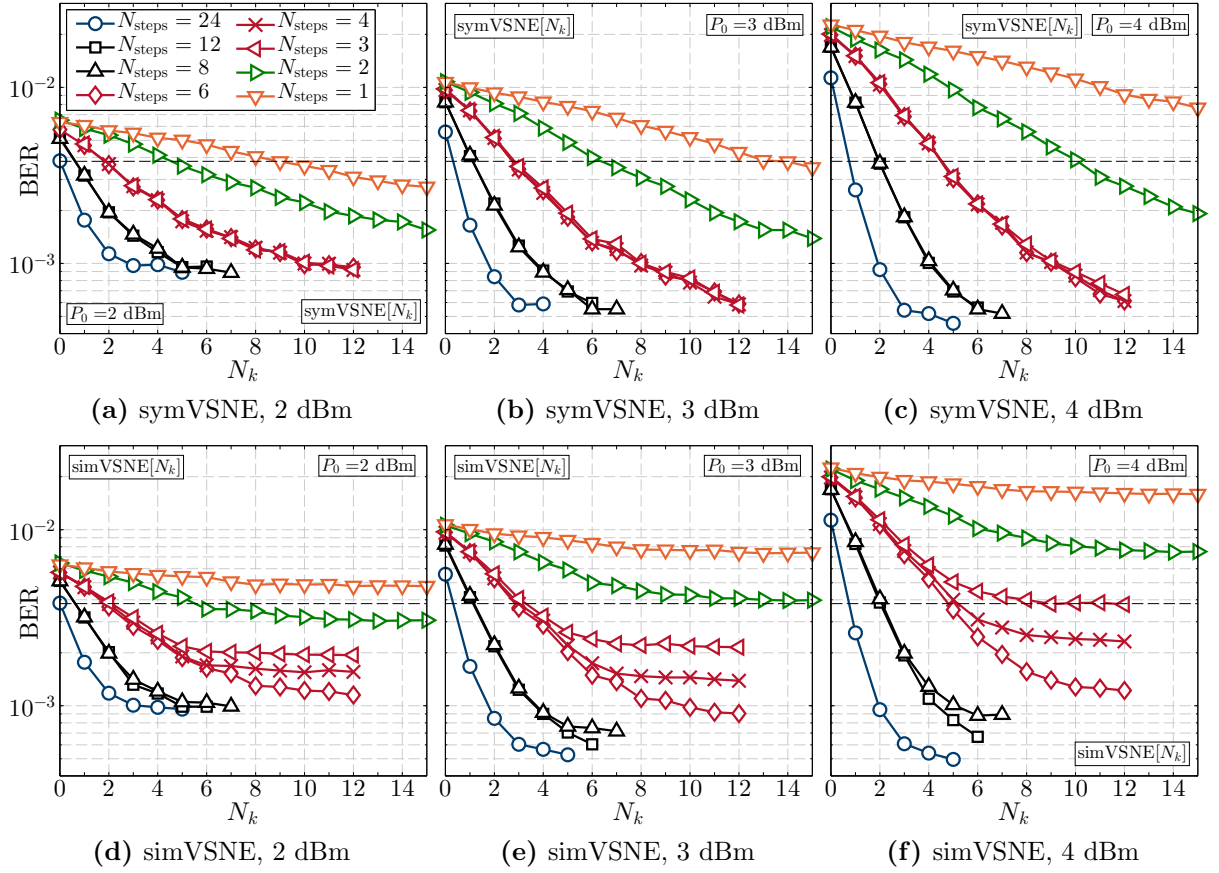


**Figure 4.11:** Performance of the symVSNE and simVSNE filter arrays as a function of  $N_k$  and  $N_{\text{steps}}$ .

to the non-coherent simplification on the phased-array factor. As previously discussed in section 4.2, as more fiber spans are considered in the phased-array parameter, the iXPM-like regions in the  $\mathbf{F} \circ \mathbf{K}_3$  product tend to become narrower, thus affecting the constant coefficient assumption. A minimum number of 3 simVSNE steps has then been determined to guarantee a FEC-compatible BER for an input power of 2 dBm and 3 dBm. Notwithstanding, it can be seen that the simVSNE always supersedes the multi-span SSFM performance, thus being an attractive alternative. The dashed lines with cross markers also refer to the maximum achievable simVSNE performance, but now considering an individual optimization of the  $\xi$  parameter for each simVSNE $\{K\}$  filter branch. A small performance improvement has been obtained for all input powers with this optimized simVSNE, enabling to reduce the minimum number of steps down to 2 for the 2 dBm case. However, it becomes apparent that the simVSNE divergence with equalization distance is mainly due to the frequency-flat assumption itself.

The impact of the  $N_k$  parameter on the simVSNE and symVSNE performance for multi-span equalization is shown in Figure 4.11, considering a varying number of steps and input powers ranging from 2 dBm to 4 dBm. Similarly to the previous span-by-span analysis, it is clearly shown that the performance of both algorithms is approximately

matched for small  $N_k$ , in which case the simVSNE filter takes advantage due to its reduced computational effort. This enables to achieve the FEC target using a reduced complexity DBP algorithm. However, since small  $N_{\text{steps}}$  requires large  $N_k$ , the simVSNE algorithm may not enable fully non-iterative compensation of very long links. The input power also plays an important role here, enhancing the simVSNE divergence, even for small  $N_{\text{steps}}$ . At 2 dBm, the simVSNE equalization is possible with only 2 steps and  $N_k = 6$ , whereas for input powers larger than 2 dBm the simVSNE equalization requires  $N_{\text{steps}} \geq 3$ . Moreover, even for a larger number of steps, the minimum  $N_k$  required to achieve the FEC limit tends to increase with increasing power. Considering 3 steps, the minimum  $N_k$  increases from 2 to 4 and 9 for an input power of 2 dBm, 3 dBm and 4 dBm, respectively. This indicates that there is a power-dependent compromise between  $N_{\text{steps}}$  and  $N_k$  that leads to the minimum computational effort. If a small number of steps is mandatory, e.g. due to latency restrictions, the symVSNE ensures the lower  $N_{\text{steps}}$  at the expense of additional computations.

### 4.3.3 Computational effort and latency

A summary of the VSNE-based DBP computational effort and latency required to achieve the  $3.8 \times 10^{-3}$  BER target at 3 dBm (see Figures 4.11b and 4.11e) is presented in Table 4.1. The computational effort and latency associated with the DBP-symVSNE is calculated in accordance to expressions (4.24) and (4.25). Conversely, the DBP-simVSNE computational effort and latency is calculated from expressions (4.36) and (4.37).

The computational effort results shown in Table 4.1 reveal that the computational gain obtained with the simVSNE is over two orders of magnitude, relatively to the symVSNE algorithm. Moreover, it is shown that reducing the number of steps does not necessarily lead to a lower computational effort. In fact, by increasing the propagation distance per simVSNE/symVSNE transfer function, the frequency resolution must be accordingly increased in order to accommodate the long-term memory effects caused by chromatic dispersion, requiring the use of larger FFT blocks. Consequently, the filter dimension must also be increased through the  $N_k$  parameter. Since the symVSNE computational

**Table 4.1:** Minimum computational effort and latency incurred by static equalization with the symVSNE and simVSNE filters at 3 dBm.

$N_{\text{steps}}$	symVSNE			simVSNE			$N$
	$N_k$	$M_{\text{symVSNE}}^{\text{DBP}}$	$\tau_{\text{symVSNE}}^{\text{DBP}}$	$N_k$	$M_{\text{simVSNE}}^{\text{DBP}}$	$\tau_{\text{simVSNE}}^{\text{DBP}}$	
24	1	50070	110	1	1968	86	128
12	2	98036	64	2	1594	52	256
8	2	65379	48	2	1084	40	256
6	3	146597	42	3	1125	36	512
4	3	97756	34	3	774	30	512
3	3	73335	30	4	742	27	512
2	7	226854	28	–	–	–	1024
1	14	453080	26	–	–	–	2048

effort per sample is dominated by a  $O(N_k N)$  term, a two-fold increase in both  $N_k$  and  $N$  leads to a four-fold increase in computational effort, which may not be compensated by the reduction of  $N_{\text{steps}}$ . In turn, since the simVSNE computational effort per sample is dominated by a  $O(N_k)$  term, it remains insensitive to the FFT block-size, narrowing down the computational effort optimization problem to the minimization of  $N_{\text{steps}} N_k$ . In terms of equalization latency, the difference between the symVSNE and simVSNE filters is residual, being only caused by the  $\mathbf{K}_3$  multiplication in (4.12a) and (4.12b), which is avoided in the simVSNE.

As a comparison benchmark, it is important to assess the computational effort and latency required by the widely-used DBP-SSFM for the system under study. Using expressions (3.16) and (3.17), and considering the minimum number of DBP-SSFM steps,  $N_{\text{steps}} = 24$ , to achieve the established BER target at 3 dBm, for which case an FFT block-size  $N = 128$  is required, we obtain  $M_{\text{SSFM}}^{\text{DBP}} = 1992$  and  $\tau_{\text{SSFM}}^{\text{DBP}} = 456$ . Relatively to the minimum computational effort obtained with the simVSNE algorithm,  $M_{\text{simVSNE}}^{\text{DBP}} = 742$ , obtained with 3 steps, a gain of approximately 63% is achieved by the simVSNE. In terms of latency, a reduction of roughly 94% is obtained with the same direct comparison. Performing a similar analysis for the 2 dBm and 4 dBm cases, a computational effort gain of approximately 60% is obtained, whereas the latency reduction is approximately of 84% and 93%, respectively.

The above computational effort analysis has been carried out neglecting the required overlapping between adjacent blocks. Following the overlap-save configuration of Figure 3.17 and since each FFT block is independently processed, the overall computational effort per sample is affected by a factor of 2, both for the VSNE-based and SSFM algorithms. In a general implementation, this factor will depend upon the overlap fraction between adjacent FFT blocks, which determines the average number of times each sample is processed. Nonetheless, the complexity ratio between the VSNE and SSFM remains constant. Finally, it must be referred that further computational savings can be obtained by reducing the simVSNE/symVSNE filter bandwidth, at the expense of controlled performance loss.

## 4.4 Experimental Validation

The numerical assessment of the symVSNE and simVSNE algorithms presented in section 4.3 has enabled to demonstrate the enhanced modularity provided by the symmetric kernel reconstruction and the validity of the frequency-flat approximation in delimited regions of  $N_k$  and  $N_{\text{steps}}$ , while preserving a high equalization performance. However, the practical application of these techniques requires a comprehensive experimental validation in state-of-the-art optical transmission systems. In this section, the frequency domain VSNE-based techniques proposed in sections 4.1 and 4.2 are experimentally validated in a long-haul 100G transmission system composed of 10 PM-64QAM individual channels placed in a 50 GHz frequency grid.

The use of PM-64QAM modulation has been recently attracting significant attention for high spectral efficient transmission of 100G and 400G channels. Although the vast majority of PM-64QAM experimental demonstrations rely on data-aided processing using

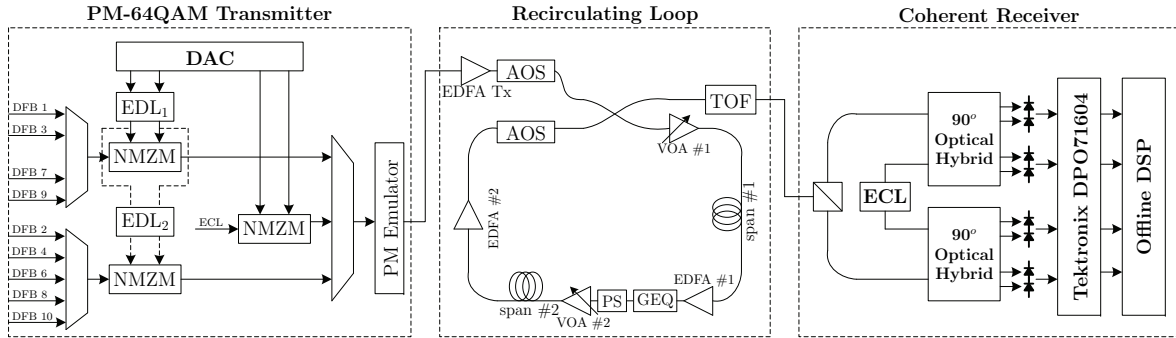


**Figure 4.12:** Laboratorial setup for the transmission, propagation and detection of 10.4 Gbaud PM-64QAM data.

training symbols [19, 20] and/or pilot tones [21], some works using blind equalization can also be found in the literature [22–24]. The most prominent PM-64QAM results reported in recent literature are reviewed in the following. In [21], 5.6 Gbaud Nyquist-shaped PM-64QAM subcarriers are utilized to transmit  $7 \times 538$  Gb/s superchannels over 1200 km of pure silica core fiber (PSCF), using digital pilot tones for phase noise compensation. The transmission of  $10 \times 494.85$  Gb/s over 3200 km of ultra large area fiber (ULAF) is demonstrated in [19], employing a hybrid PM-(32-64)QAM modulation technique and data-aided linear adaptive equalization and carrier recovery. Fully-blind equalization of 120.4 Gb/s PM-64QAM is reported in [22], achieving a maximum reach of 160 km over PSCF and employing all-Raman amplification and 7% FEC overhead. In [23], 516 Gb/s PM-64QAM is propagated over 600 km of alternating  $150 \mu\text{m}^2$  and  $112 \mu\text{m}^2$  fiber spans with 25 km each, considering a pre-FEC BER threshold of  $2 \times 10^{-2}$ . In [24], a simple CMA-based blind adaptive equalization and 4<sup>th</sup> power phase estimation is employed at the cost of extra performance penalty, requiring a pre-FEC BER of  $4.5 \times 10^{-2}$  and achieving a maximum signal reach of 300 km over ULAF ( $135 \mu\text{m}^2$ ) at 42.66 Gbaud.

Building upon a recent 12 GHz-spaced 124.8 Gb/s PM-64QAM experiment employing only CD equalization and data-aided processing [20], in this section we demonstrate fully-blind equalization yielding an extended reach of 1524 km at a 50 GHz channel spacing, enabled by nonlinear equalization with the symVSNE and simVSNE algorithms. The DBP complexity/performance tradeoff is thoroughly analyzed, taking advantage of the signal spectral properties imposed by Nyquist pulse shaping. Fully-blind equalization is supported by a multi-radii training strategy [25, 26] for the adaptive equalization subsystem, based on a radius-directed CMA filter [27].

The following experimental validation work has been carried out in collaboration with Politecnico di Torino (POLITO) and Istituto Superiore Mario Boella (ISMB), both located in Turin, Italy, within the framework of the national project DiNEq (Digital Nonlinear Equalization in Very-High Speed Coherent Optical Transmission Systems), funded by Fundação para a Ciência e a Tecnologia (FCT).

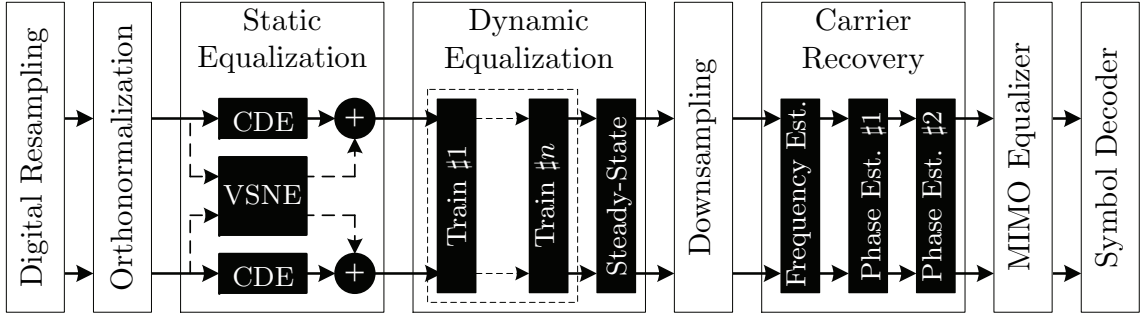


**Figure 4.13:** Sequence of post-detection DSP subsystems employed in this work for the processing of 100G PM-64QAM.

#### 4.4.1 Laboratorial setup and DSP subsystems

The experimental setup of the 100G PM-64QAM transmission system implemented in this work is shown in Figure 4.12. At the transmitter, 6 independent ( $2^{15} - 1$ ) pseudo-random bit sequences (PRBSs) are mapped into the I and Q components of the 10.4 Gbaud 64QAM. Transmitter-side digital processing includes Nyquist filtering with a roll-off factor of 0.05 and a 4 dB high-frequency pre-emphasis to partially compensate for analog bandwidth limitations. The analog I and Q components are then generated by a 10-bit Tektronix 7122B DAC with 9.6 GHz analog bandwidth and operating at 11.96 Gs/s (1.15 SpS), electrically driving three NMZ modulators. The first NMZ modulator is optically fed by an ECL with 100 kHz linewidth and is used to modulate the central channel under test. The remaining two NMZ modulators are fed by DFBs and are employed to modulate 9 additional odd and even optical channels with 50 GHz separation. Two electrical delay lines (EDLs) with 4.8 ns (EDL 1) and 4.4 ns (EDL 2) are applied to generate decorrelation with the test channel. Note that, at the DAC output, an analog anti-aliasing filter is applied to partially reject the alias signal replica centered at 11.96 GHz. The single-polarization outputs of the NMZ modulators are then sent to a PM emulator with 10 ns delay to generate the PM-64QAM signal. The recirculating loop, controlled by two AOSs, is composed of two identical PSCF spans with 54.44 km each, average attenuation of 0.161 dB/km, CD parameter of 20.7 ps/nm/km and effective core area of  $150 \mu\text{m}^2$  [28]. Fiber and splicing loss is compensated by EDFAs with a noise figure of 4.5 dB at the end of each span. In between the two fiber spans, a spectrally-resolved GEQ and a polarization scrambler (PS) are applied to respectively flatten the EDFA gain and average the impact of polarization effects. Before being fed to the coherent receiver, the signal is filtered by a tunable optical filter (TOF) with 30 GHz bandwidth in order to limit the optical power arriving at the photo-detectors. The local oscillator is an ECL with 100 kHz linewidth. Finally the signal is digitized by a 50 Gs/s real-time oscilloscope (Tektronix DPO71604) and is ready for the offline processing.

The sequence of DSP subsystems employed in this work is depicted in Figure 4.13. The 10.4 Gbaud PM-64QAM signal is sampled at 50 Gsample/s, yielding  $\sim 4.8$  SpS. The first DSP subsystem consists of a downsampling stage to 2 SpS, which is followed by a Gram-Schmidt orthonormalization procedure [27] to normalize the signal and compensate for quadrature imbalance. The equalization of static fiber impairments is

implemented by independent CD equalizers for each polarization tributary, optionally applied in parallel with VSNE-based filters. As a benchmark for DBP performance, joint compensation of linear and nonlinear impairments using the DBP-SSFM is also applied. Adaptive equalization of polarization-dependent effects, as well as residual CD, is blindly implemented using a 31-taps radius-directed CMA with a multi-radii training stage [25, 26]. The equalized signal is then downsampled to 1 SpS and fed to the carrier recovery block, where frequency estimation is performed by a 4<sup>th</sup> power spectral method. Phase estimation is sectioned into two stages. The first coarse stage is based on a simple 4<sup>th</sup> power Viterbi-Viterbi algorithm performed over the outer 64QAM symbols. In the second stage, decision-directed (DD) maximum likelihood phase estimation with 40 taps [29] provides a more accurate phase recovery. A final 75-taps  $2 \times 2$  DD FIR filter is applied to reduce long-term linear memory effects and narrow-band distortions [19]. Finally, we proceed to symbol decoding and BER counting over approximately  $2^{17}$  symbols.

#### 4.4.2 Performance of nonlinear equalization

The BER performance and maximum signal reach after full processing, including CDE and DBP, is shown in Figure 4.14, for a wide set of input powers and propagation distances. We consider an FEC BER threshold of  $2.7 \times 10^{-2}$ . The results in Figure 4.14a show that the maximum signal reach with CDE only is limited to 1198 km (22 spans) for an optimum channel power of -7 dBm. It can also be seen that the BER performance quickly degrades for channel input powers higher than -6 dBm due to the impact of nonlinearities. Considering DBP with the full matrix-based VSNE, the maximum signal reach is extended to 1524 km (28 spans) at a channel input power of -5 dBm, corresponding to a  $\sim 27\%$  reach extension and a 2 dB improvement in nonlinear tolerance. The obtained  $Q^2$  improvement due to DBP at -5 dBm and 28 spans is  $\sim 0.9$  dB. Although not achieving the established FEC threshold, a higher  $Q^2$  improvement of  $\sim 2.5$  dB has been obtained for a channel input power of -2 dBm, demonstrating the efficiency of VSNE-based DBP in the nonlinear regime. Not shown for simplicity in Figure 4.14a, the performance of the DBP-SSFM was found to be almost perfectly matched with that of VSNE-based DBP [25], corroborating the experimental results presented in Chapter 3, where the performance equivalency between DBP-SSFM and DBP-VSTF has been demonstrated for 100G PM-QPSK transmission systems [18]. The results in Figure 4.14b show the dependence of maximum signal reach on the channel input power, for both CDE and VSNE-based DBP. It can be observed that the added signal reach provided by the VSNE keeps increasing up to an input power of -5 dBm, after which it stabilizes to a value of approximately 500 km of additional reach.

Our analysis will now focus on the optimization of DBP for the maximum reach of 1524 km at the optimum power of -5 dBm. Figure 4.15 shows the dependence of the DBP-SSFM performance on the FFT length and on the total number of steps used to separately apply the linear and nonlinear operators. It is shown that a minimum of 14 steps are required to achieve the FEC threshold of  $2.7 \times 10^{-2}$  with  $N = 128$ . As  $N_{\text{steps}}$  is further reduced, the BER quickly increases as a result of the lower spatial resolution. In accordance with the previous analyzed simulation and experimental results, the FFT

#### 4.4. Experimental Validation

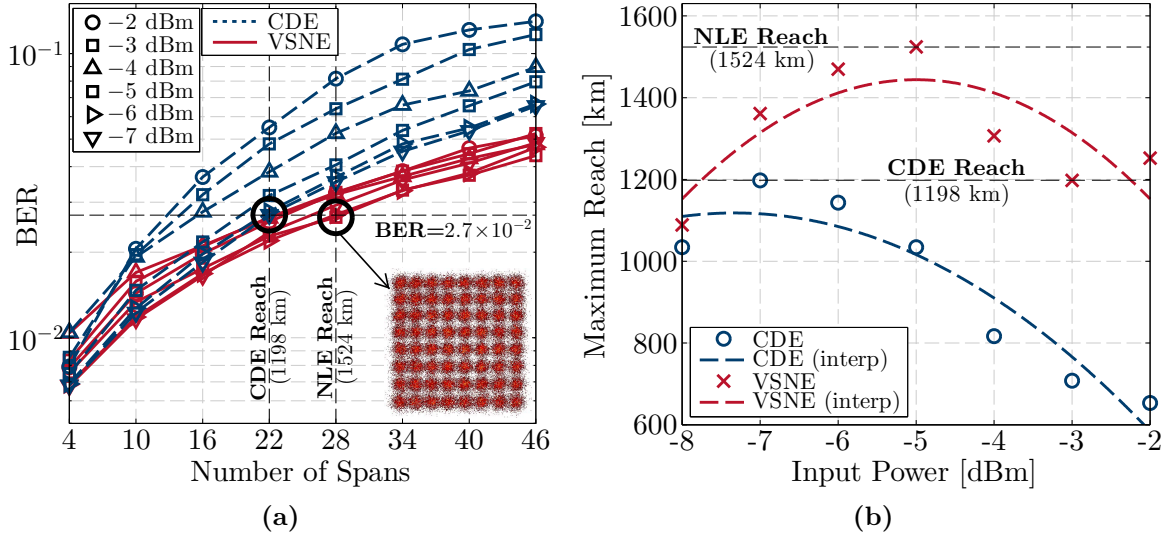


**Figure 4.14:** BER performance and maximum signal reach of 100G PM-64QAM enabled by CDE and VSNE-based DBP. a) Evolution of BER performance with propagation reach for several channel input powers; b) Maximum attainable reach as a function of input power. Dashed lines in b) are obtained from a quadratic interpolation of the data points.

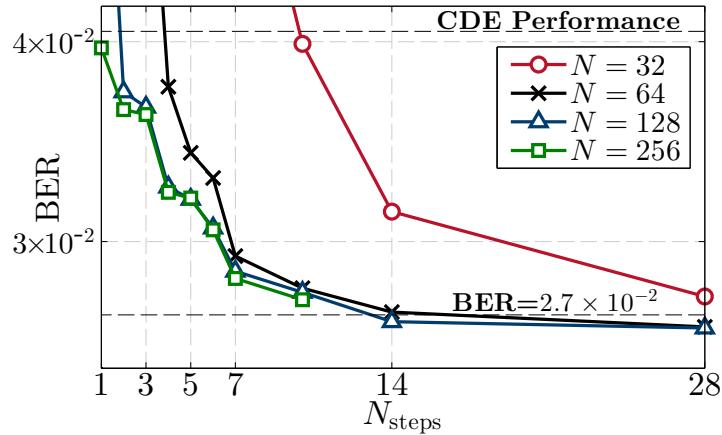


**Figure 4.15:** Optimization of the DBP-SSFM method in terms of  $N_{\text{steps}}$  and  $N$  for a fixed input power of -5 dBm and recirculation over 28 fiber spans.

length tends to increase for lower  $N_{\text{steps}}$ , due to the higher accumulated CD to be inverted, thus increasing the memory effects to be accommodated in each step. Finally, it is shown that in the limit of a single step, the performance improvement of DBP-SSFM over CDE is limited to approximately 0.05 dB. Note that the  $\xi$  parameter in DBP-SSFM has been individually optimized for each data point in Figure 4.15.

The optimization of the symVSNE and simVSNE algorithms for the maximum reach of 1524 km is shown in Figure 4.16. The dependence of BER performance on the number of symVSNE parallel filters,  $N_k + 1$ , is shown in Figure 4.16a, including individual curves

for different number of steps (multiples of the total number of fiber spans). This evidences the inter-dependence between  $N_k$  and  $N_{\text{steps}}$ . In general, lower  $N_{\text{steps}}$  requires larger  $N_k$ . The reason for this dependence is two-fold:

- i) lower  $N_{\text{steps}}$  is associated with higher  $N$ , resulting in higher frequency domain resolution and in a larger kernel matrix. Therefore the number of column/diagonal pairs required to capture the equivalent nonlinear distortion contributions is also proportionally increased. The correspondence between  $N_{\text{steps}}$  and  $N$  used in this work is indicated in Table 4.2;
- ii) lower  $N_{\text{steps}}$  corresponds to a higher number of fiber spans per transfer function,  $N_{\text{spans/step}}$ , in the phased-array factor of equation (3.27). This will strengthen the iFWM contributions located in matrix diagonals farther away from the central iXPM diagonal, thus requiring higher  $N_k$  for the same equalization performance.

The results in Figure 4.16a also show that the symVSNE enables to reach the FEC threshold with a single iteration and  $N_k = 19$ . This however may not correspond to the lowest complexity implementation, since the number of RMs per sample required by the symVSNE algorithm evolves as  $O(N_{\text{steps}}N_kN)$ . In turn, the analysis of the simVSNE performance illustrated in Figure 4.16b shows that the FEC limit cannot be achieved anymore with a single step. In fact, a minimum of  $N_{\text{steps}} = 4$  and  $N_k = 8$  is required to obtain a BER lower than  $2.7 \times 10^{-2}$ . This simVSNE performance penalty with decreasing  $N_{\text{steps}}$  is due to the non-coherent array factor simplification of (4.31). The non-coherent aggregation of simVSNE transfer functions for each fiber span generates an error that is proportional to  $N_s$ . Nevertheless, the maximum performance results shown in Figure 4.16c, which correspond to the optimum  $N_k$  in Figures 4.16a and 4.16b (indicated by open circles), clearly show that for  $N_s \leq 7$  ( $N_{\text{steps}} \geq 4$ ) the simVSNE and symVSNE algorithms are well matched in terms of performance, demonstrating the validity of the frequency-flat assumption when the accumulated CD to be inverted per step is moderately low (the  $\Delta\beta_{j,k}(\omega_n)N_sL_s$  term in (3.27) is weak).

So far, all static equalization processing has been performed with 2 SpS, with a 20.8 GHz spectral support,  $W$ , for a symbol-rate of  $R_s = 10.4$  Gbaud. However, due to the Nyquist pulse shaping, the magnitude of baseband frequencies higher than half of the symbol-rate is strongly attenuated, as shown in the inset of Figure 4.17. Therefore, in Figure 4.17 we numerically analyze the effective spectral support required to apply the simVSNE and symVSNE algorithms, by gradually truncating the signal in frequency domain (only in the VSNE branch). Consequently, the effective FFT length,  $N$ , used to evaluate the summation intervals,  $J_U$  and  $J_L$ , in (4.16) and (4.17), is redefined as  $N_W = N \frac{W}{2R_s}$ . The obtained results show that no significant performance penalty is obtained up to the limit of  $W = R_s$ , corresponding to the minimum bandwidth of a root-raised-cosine pulse. Further spectral support truncation leads to a quick degradation of performance due to the loss of nonlinear information in high magnitude spectral components.

#### 4.4. Experimental Validation

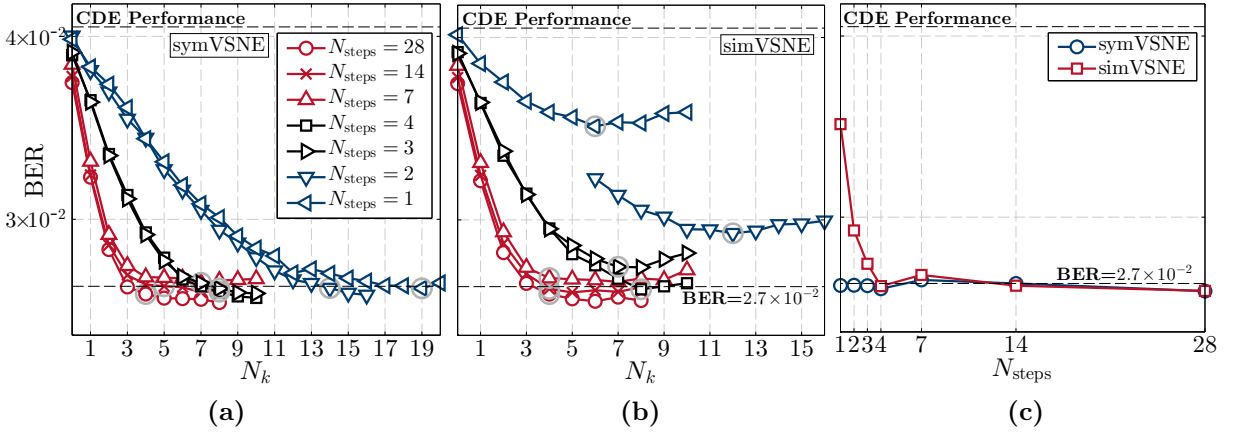


**Figure 4.16:** Optimization of the a) symVSNE and b) simVSNE filter arrays in terms of  $N_k$  and  $N_{\text{steps}}$  and c) maximum performance obtained for the optimum  $N_k$ , for a fixed input power of -5 dBm and recirculation over 28 fiber spans. Line colors in a) and b) indicate the associated FFT length, as blue:  $N = 256$ ; black:  $N = 128$  and red:  $N = 64$ .

#### 4.4.3 Implementation complexity

The total number of RMs per equalized sample,  $N_{\text{RMs}}$ , required by DBP with the SSFM, symVSNE and simVSNE algorithms, is indicated in Table 4.2. The  $N_{\text{RMs}}$  values are obtained according to the analytical expressions derived in sections 3.2.3 (for DBP-SSFM), 4.2.2 (for simVSNE) and 4.1.2 (for symVSNE). The minimum DBP-SSFM complexity is obtained with 14 steps, corresponding to 1050 RMs per sample. For the symVSNE, it is confirmed that the single-step case does not correspond to the minimum complexity, due to the increased  $N$  and  $N_k$ . Indeed, the minimum symVSNE complexity is obtained for  $N_{\text{steps}} = 7$ . It can also be observed that the 50% reduction on the spectral support,  $W$ , yields a reduction by a factor of  $\sim 4$  on the symVSNE complexity, given the  $O(N_{\text{steps}} N_k N_W^2 / N)$  dependence of  $N_{\text{RMs}}$ .

For the simVSNE, the implementation complexity per sample evolves with  $O(N_{\text{steps}} N_k N_W / N) = O(N_{\text{steps}} N_k \frac{W}{2R_s})$ , thus being independent of the FFT length.

**Table 4.2:** Computational effort of DBP using the SSFM, simVSNE and symVSNE algorithms, for the considered 100G PM-64QAM transmission system.

$N_{\text{steps}}$	$N$	SSFM	symVSNE				simVSNE			
		$N_{\text{RMs}}$	$N_k$		$N_{\text{RMs}}$		$N_k$		$N_{\text{RMs}}$	
			$W=2R_s$	$W=R_s$	$W=2R_s$	$W=R_s$	$W=2R_s$	$W=R_s$	$W=2R_s$	$W=R_s$
28	64	2100	4	4	105483	24451	4	4	6111	3087
14	64	<b>1050</b>	5	4	63780	12250	4	4	3080	1568
7	64	–	<b>7</b>	<b>5</b>	<b>41804</b>	<b>7176</b>	4	5	1564	950
4	128	–	8	8	58887	13263	<b>8</b>	<b>8</b>	<b>1667</b>	<b>851</b>
3	128	–	8	9	44179	10834	–	–	–	–
2	256	–	14	15	103618	24654	–	–	–	–
1	256	–	19	19	67539	14629	–	–	–	–

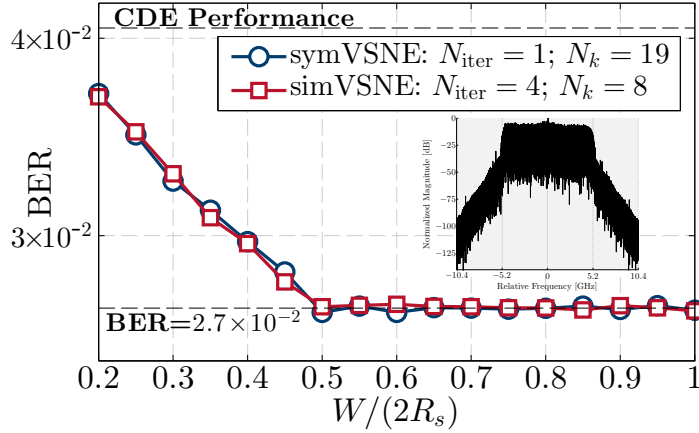


**Figure 4.17:** Optimization of symVSNE and simVSNE in terms of effective spectral support, for an input power of -5 dBm and recirculation over 28 fiber spans. The inset represents the normalized magnitude of the received electrical spectrum for  $W = 2R_s$ .

Therefore, for the same  $N_k$  and  $N_{\text{steps}}$ , it can be observed that the 50% spectral support reduction approximately halves the complexity. In addition, since the optimum  $N_k$  tends to decrease for low  $N_{\text{steps}}$  due to the associated performance degradation, the minimum simVSNE complexity is mainly driven by the  $N_{\text{steps}}$  parameter. For the current case study, a minimum  $N_{\text{steps}} = 4$  is required to achieve the FEC limit, thus setting the minimum attainable complexity of 851 RMs per sample, for  $W = R_s$ . Comparing with the 1050 RMs required by DBP-SSFM, the complexity reduction yielded by the simVSNE is of approximately 20%. Additionally, comparing the 14 steps required by the DBP-SSFM with the 4 steps required by simVSNE roughly translates into a latency reduction of 70%.

## 4.5 Summary

Starting from the matrix-based VSNE technique proposed in Chapter 3, which suffered from  $O(N^2)$  complexity per processed sample, in this chapter we have focused our efforts on the optimization of the complexity/performance tradeoff, resorting to an in-depth analysis of the properties of the third-order  $\mathbf{K}_3$  kernel. By identifying the key symmetries on  $\mathbf{K}_3$ , we have proposed an iXPM-oriented symmetric reconstruction of the matrix VSNE, yielding an array of  $N_k$  one-dimensional filters. We have then analytically demonstrated that the full VSNE reconstruction with the symVSNE algorithm is exact, and enables to reduce the total computational effort by a factor that asymptotically converges to 3. It has also been demonstrated that the reconstruction process yields a fast performance improvement for small  $N_k$ , thus enabling to use a reduced dimension symVSNE filter array with small performance penalty and  $O(N_k N)$  complexity. In order to further reduce the computational effort associated with the symVSNE algorithm, we have established an iXPM-based constant coefficient assumption, which has led to a  $O(N_k)$  computational effort per processed sample, thus avoiding the  $N$  dependence. In addition, the proposed VSNE-based algorithms show the advantage of being applied

in parallel with any CDE of choice, and thus can be used as an optional add-on for the equalization subsystem. Moreover, the proposed filter array structure gives more flexibility for the performance/complexity tradeoff, which can be freely adjusted to match the available DSP resources and required BER target. Being based on a numerical model of the propagation channel, the proposed VSNE-based equalizers are modulation-transparent, enabling seamless equalization of different optical signals.

The numerical results obtained for a 224 Gb/s PM-16QAM long-haul transmission system have revealed that the computational gain of the simVSNE over the DBP-SSFM can be over 60%, with more than 90% reduction in terms of latency. The symVSNE and simVSNE algorithms were experimentally demonstrated in a 100G PM-64QAM transmission system, enabling a 27% increase in maximum reach and a 2 dB nonlinear tolerance enhancement, relatively to CDE only. The obtained results experimentally demonstrate the validity of the frequency-flat simVSNE, when applied with sufficient spatial resolution. Direct comparison with the DBP-SSFM has revealed significant savings in terms of computational effort (up to 28%) and latency ( $\sim 70\%$ ). We recall that all experimental results have been obtained with a 50 GHz WDM grid. This has been a design choice, with the aim to reduce the impact of inter-channel nonlinearities on the performance of intra-channel DBP. If the channel spacing is further reduced to increase SE, and if DBP is still applied only on an intra-channel basis, it is expected that the overall system performance will be impaired due to increasing uncompensated inter-channel nonlinearities. In such a scenario, DBP-based inter-channel compensation requires considering a wideband receiver or the cooperation between several independent receivers [30]. However, besides the implied hardware complexity, this approach may be unrealistic in optical networks with reconfigurable routing of WDM channels, in which the inter-channel interaction during propagation may be unknown at the receiver side. Nevertheless, the equalization of inter-channel nonlinear fiber impairments may find practical application within the recently proposed concept of superchannels, which guarantees that all subcarriers are jointly routed through the network as a single entity. The available inter-channel information in the digital domain will then depend on the receiver hardware constraints, such as analog bandwidth and sampling rate. This scenario will be the central topic of discussion of Chapter 6.

Building upon the proposed VSNE algorithms, other modified approaches and simplifications can be explored. Using a maximum absolute value selection criteria, we have also implemented a pruning strategy for the matrix VSNE based on removing the lowest absolute value coefficients to increase the sparsity of the third-order kernel [31]. A performance/complexity comparison between this pruning strategy and the iXPM-oriented symmetric kernel reconstruction has demonstrated that the symVSNE algorithm provides a near-optimum blind criteria for selecting the kernel coefficients. In addition, the exploitation of kernel symmetries in the symVSNE algorithm avoids the replication of operations, enabling a lower implementation complexity than a simple coefficient pruning strategy. An intermediate approach between the symVSNE and simVSNE algorithms has also been demonstrated in [32], employing a quantization process to the  $\mathbf{K}_3$  coefficients to reduce complexity without sacrificing performance. Alternatively to the massively revisited DBP-SSFM, the VSNE algorithms proposed in this chapter, along with other

Volterra-based equalization approaches that have recently been proposed in the literature [1–3, 33, 34], open new research directions on digital nonlinear equalization for long-haul coherent optical transmission systems. The demonstrated advantages of VSNE-based DBP may contribute to increase the awareness of the optical communications scientific community on the use of Volterra models for nonlinear compensation, generating novel contributions and advances on this emerging research area.

## References

- [1] L. Liu, L. Li, Y. Huang, K. Cui, Q. Xiong, F. N. Hauske, C. Xie, and Y. Cai, “Intrachannel nonlinearity compensation by inverse Volterra series transfer function,” *J. Lightw. Technol.*, vol. 30, no. 3, pp. 310–316, 2012.
- [2] R. Weidenfeld, M. Nazarathy, R. Noe, and I. Shpantzer, “Volterra nonlinear compensation of 100G coherent OFDM with baud-rate ADC, tolerable complexity and low intra-channel FWM/XPM error propagation,” in *Proc. Optical Fiber Communication Conf. and Exposition (OFC)*, paper OTuE3, 2010.
- [3] G. Shulkind and M. Nazarathy, “Nonlinear digital back propagation compensator for coherent optical OFDM based on factorizing the Volterra series transfer function,” *Opt. Express*, vol. 21, no. 11, pp. 13 145–13 161, Jun 2013.
- [4] A. Vannucci, P. Serena, and A. Bononi, “The RP method: a new tool for the iterative solution of the nonlinear Schrödinger equation,” *J. Lightw. Technol.*, vol. 20, no. 7, pp. 1102–1112, 2002.
- [5] G. Shulkind and M. Nazarathy, “Estimating the Volterra series transfer function over coherent optical OFDM for efficient monitoring of the fiber channel nonlinearity,” *Opt. Express*, vol. 20, no. 27, pp. 29 035–29 062, 2012.
- [6] I. Shake, H. Takara, K. Mori, S. Kawanishi, and Y. Yamabayashi, “Influence of inter-bit four-wave mixing in optical TDM transmission,” *Electronics Letters*, vol. 34, no. 16, pp. 1600–1601, Aug 1998.
- [7] R. Essiambre, B. Mikkelsen, and G. Raybon, “Intra-channel cross-phase modulation and four-wave mixing in high-speed TDM systems,” *Electronics Letters*, vol. 35, no. 18, pp. 1576–1578, Sep 1999.
- [8] A. Mecozzi, C. Clausen, and M. Shtaif, “Analysis of intrachannel nonlinear effects in highly dispersed optical pulse transmission,” *IEEE Photon. Technol. Lett.*, vol. 12, no. 4, pp. 392–394, April 2000.
- [9] M. Nazarathy, J. Khurgin, R. Weidenfeld, Y. Meiman, P. Cho, R. Noe, I. Shpantzer, and V. Karagodsky, “Phased-array cancellation of nonlinear FWM in coherent OFDM dispersive multi-span links,” *Opt. Express*, vol. 16, no. 20, pp. 15 777–15 810, Sep 2008.

- [10] K. Inoue and H. Toba, "Fiber four-wave mixing in multi-amplifier systems with nonuniform chromatic dispersion," *J. Lightw. Technol.*, vol. 13, no. 1, pp. 88–93, Jan 1995.
- [11] A. Carena, V. Curri, G. Bosco, P. Poggiolini, and F. Forghieri, "Modeling of the impact of nonlinear propagation effects in uncompensated optical coherent transmission links," *J. Lightw. Technol.*, vol. 30, no. 10, pp. 1524–1539, 2012.
- [12] P. Poggiolini, Y. Jiang, A. Carena, G. Bosco, and F. Forghieri, "Analytical results on system maximum reach increase through symbol rate optimization," in *Proc. Optical Fiber Communication Conf. and Exposition (OFC)*, paper Th3D.6, 2015.
- [13] I. Fatadin, D. Ives, and S. Savory, "Blind equalization and carrier phase recovery in a 16-QAM optical coherent system," *J. Lightw. Technol.*, vol. 27, no. 15, pp. 3042–3049, 2009.
- [14] *ITU-T Recommendation G.975.1*, ITU-T Std. Appendix I.9., 2004.
- [15] L. B. Du and A. J. Lowery, "Improved single channel backpropagation for intra-channel fiber nonlinearity compensation in long-haul optical communication systems," *Opt. Express*, vol. 18, no. 16, pp. 17 075–17 088, Aug 2010.
- [16] F. P. Guiomar, J. D. Reis, A. L. Teixeira, and A. N. Pinto, "Digital postcompensation using Volterra series transfer function," *IEEE Photonics Technology Letters*, vol. 23, no. 19, pp. 1412–1414, 2011.
- [17] —, "Mitigation of intra-channel nonlinearities using a frequency-domain Volterra series equalizer," *Opt. Express*, vol. 20, no. 2, pp. 1360–1369, Jan 2012.
- [18] F. P. Guiomar, J. D. Reis, A. Carena, G. Bosco, A. L. Teixeira, and A. N. Pinto, "Experimental demonstration of a frequency-domain Volterra series nonlinear equalizer in polarization-multiplexed transmission," *Opt. Express*, vol. 21, no. 1, pp. 276–288, 2013.
- [19] X. Zhou, L. E. Nelson, P. Magill, R. Isaac, B. Zhu, D. W. Peckham, P. I. Borel, and K. Carlson, "High spectral efficiency 400 Gb/s transmission using PDM time-domain hybrid 32–64 QAM and training-assisted carrier recovery," *J. Lightw. Technol.*, vol. 31, no. 7, pp. 999–1005, 2013.
- [20] A. Nespola, S. Straullu, G. Bosco, A. Carena, J. Yanchao, P. Poggiolini, F. Forghieri, Y. Yamamoto, M. Hirano, T. Sasaki, J. Bauwelinck, and K. Verheyen, "1306-km 20x124.8-Gb/s PM-64QAM transmission over PSCF with net SEDP 11,300 (b.km)/s/Hz using 1.15 samp/symb DAC," *Opt. Express*, vol. 22, no. 2, pp. 1796–1805, Jan 2014.
- [21] T. Kobayashi, A. Sano, A. Matsuura, Y. Miyamoto, and K. Ishihara, "Nonlinear tolerant spectrally-efficient transmission using PDM 64-QAM single carrier FDM with digital pilot-tone," *J. Lightw. Technol.*, vol. 30, no. 24, pp. 3805–3815, 2012.

- 
- [22] A. Sano, T. Kobayashi, A. Matsuura, S. Yamamoto, S. Yamanaka, E. Yoshida, Y. Miyamoto, M. Matsui, M. Mizoguchi, and T. Mizuno, "100×120-Gb/s PDM 64-QAM transmission over 160 km using linewidth-tolerant pilotless digital coherent detection," in *Proc. Eur. Conf. Opt. Commun. (ECOC)*, paper PD2.2, 2010.
- [23] O. Bertran-Pardo, J. Renaudier, H. Mardoyan, P. Tran, R. Rios-Muller, A. Konczykowska, J. Dupuy, F. Jorge, M. Riet, B. Duval, J. Godin, S. Randel, G. Charlet, and S. Bigo, "Transmission of 50-GHz-spaced single-carrier channels at 516Gb/s over 600km," in *Proc. Optical Fiber Communication Conf. and Exposition (OFC)*, paper OTh4E.2, 2013.
- [24] F. Buchali, A. Klekamp, L. Schmalen, and D. Tomislav, "Implementation of 64QAM at 42.66 GBaud using 1.5 samples per symbol DAC and demonstration of up to 300 km fiber transmission," in *Proc. Opt. Fiber Commun. Conf. (OFC)*, paper M2A.1, 2014.
- [25] F. P. Guiomar, S. B. Amado, A. Carena, G. Bosco, A. Nespola, and A. N. Pinto, "Transmission of PM-64QAM over 1524 km of PSCF using fully-blind equalization and Volterra-based nonlinear mitigation," in *Proc. 40th European Conf. Optical Communication (ECOC)*, paper We.3.3.3, 2014.
- [26] F. P. Guiomar, S. B. Amado, A. Carena, G. Bosco, A. Nespola, A. L. Teixeira, and A. N. Pinto, "Fully-blind linear and nonlinear equalization for 100G PM-64QAM optical systems," *J. Lightw. Technol.*, vol. 33, no. 7, pp. 1265–1274, 2015.
- [27] I. Fatadin, S. J. Savory, and D. Ives, "Compensation of quadrature imbalance in an optical QPSK coherent receiver," *IEEE Photon. Technol. Lett.*, vol. 20, no. 20, pp. 1733–1735, 2008.
- [28] A. Nespola, S. Straullu, A. Carena, G. Bosco, R. Cigliutti, V. Curri, P. Poggiolini, M. Hirano, Y. Yamamoto, T. Sasaki, J. Bauwelinck, K. Verheyen, and F. Forghieri, "GN-model validation over seven fiber types in uncompensated PM-16QAM Nyquist-WDM links," *IEEE Photon. Technol. Lett.*, vol. 26, no. 2, pp. 206–209, Jan 2014.
- [29] X. Zhou, "An improved feed-forward carrier recovery algorithm for coherent receivers with M-QAM modulation format," *IEEE Photon. Technol. Lett.*, vol. 22, no. 14, pp. 1051–1053, 2010.
- [30] E. F. Mateo, X. Zhou, and G. Li, "Selective post-compensation of nonlinear impairments in polarization-division multiplexed WDM systems with different channel granularities," *IEEE J. Quantum Electron.*, vol. 47, no. 1, pp. 109–116, 2011.
- [31] F. P. Guiomar, S. B. Amado, and A. N. Pinto, "Reducing the complexity of digital nonlinear compensation for high-speed coherent optical communication systems," in *Proc. SPIE, Second International Conference on Applications of Optics and Photonics*, vol. 9286, 2014, pp. 92 864L–92 864L–9.

- [32] F. P. Guiomar, S. B. Amado, C. S. Martins, and A. N. Pinto, “Parallel split-step method for digital backpropagation,” in *Proc. Optical Fiber Communication Conf. and Exposition (OFC)*, paper Th2A.28, 2015.
- [33] R. Weidenfeld, M. Nazarathy, R. Noe, and I. Shpantzer, “Volterra nonlinear compensation of 112 Gb/s ultra-long-haul coherent optical OFDM based on frequency-shaped decision feedback,” in *Proc. 35th European Conf. Optical Communication (ECOC)*, paper 2.3.3, 2009.
- [34] E. Giacoumidis, I. Aldaya, M. Jarajreh, A. Tsokanos, S. T. Le, F. Farjady, Y. Jaouen, A. Ellis, and N. Doran, “Volterra-based reconfigurable nonlinear equalizer for coherent OFDM,” *IEEE Photon. Technol. Lett.*, vol. 26, no. 14, pp. 1383–1386, July 2014.



## Chapter 5

# Time Domain Volterra Series Nonlinear Equalizer

The VSNE-based algorithms proposed in Chapters 3 and 4 are entirely formulated and implemented in frequency domain, making use of several simplifications and identification of symmetries that stem from an in-depth frequency domain analysis of the third-order VSTF kernel. Despite of the demonstrated merits of bulk frequency domain processing, namely by avoiding recurrent time-frequency transformations on each DBP step, it becomes apparent that a complementary time domain analysis can be very useful to identify novel potential simplifications that may lead to further computational savings. In the context of coherent optical communication systems, time domain (TD) Volterra series equalization has been proposed for the adaptive compensation of nonlinear distortions [1–3]. On the contrary of the frequency domain (FD) VSNE approach, the time domain Volterra-based nonlinear filters available in the literature do not include an analytical formulation for the Volterra kernels. Instead, the kernel coefficients must be adaptively estimated resorting to training sequences or decision-feedback strategies. Besides the increased computational effort required for the kernel estimation, these techniques do not ensure convergence to a global minimum, thus yielding a significant performance penalty over DBP-based compensation.

In this chapter, we derive a time domain formulation for the simVSNE, enabling to implement fully time domain Volterra-based DBP using closed-form analytical expressions [4]. A set of novel time domain approximations are employed to reduce the computational effort, with emphasis on the insertion of a power weighting time window, inspired in the weighted SSFM (W-SSFM) concept [5]. Through numerical simulations we demonstrate that the W-VSNE enables to significantly reduce the DBP spatial resolution, while achieving the same performance as the W-SSFM [6]. Anchored by this advantage and employing implementation-oriented approximations, we demonstrate a reduction on computational effort and latency of approximately 45% and 70%, respectively. The W-VSNE technique is experimentally demonstrated in an ULH 400G transmission system composed of two PM-16QAM subcarriers modulated at 31.5 Gbaud, proving its applicability for low-complexity DBP-based nonlinear compensation in high capacity WDM optical systems [7].

The organization of this chapter is as follows. The analytical formulation of the TD-VSNE and W-VSNE algorithms is presented in section 5.1, resorting to an inverse Fourier analysis of the simVSNE filters derived in Chapter 4. Section 5.2 provides a detailed analysis of the implementation complexity in terms of number of RMs per sample and processing latency. The tradeoff between performance and complexity is thoroughly analyzed by means of numerical simulations and experimental validation in sections 5.3 and 5.4, respectively. Finally, this chapter is concluded in section 5.5 with a summary of the most important conclusions.

## 5.1 Analytical Formulation

The following analytical formulation is based on an inverse Fourier analysis of the frequency domain simVSNE algorithm derived in section 4.2. The reader is therefore referred to Chapter 4 for further details on simVSNE underlying concepts, such as the symmetric kernel reconstruction and the frequency-flat approximation.

### 5.1.1 Time domain iXPM equalizer

To initiate the analytical derivation of the TD-simVSNE algorithm, let us first recall the FD-simVSNE[0] equalizer of expression (4.7) accounting for the iSPM and iXPM distortions, which is rewritten here in the following equivalent form,

$$\tilde{A}_{x/y}^{\text{iXPM}}(\omega_n) = \kappa \left[ \tilde{A}_{x/y}^{\text{CD}}(\omega_n) \left( 2\tilde{\mathcal{P}}_{xx/yy} + \tilde{\mathcal{P}}_{yy/xx} - \tilde{\chi}(\omega_n) \right) + \tilde{A}_{y/x}^{\text{CD}}(\omega_n) \tilde{\mathcal{P}}_{xy/yx} \right], \quad (5.1)$$

where  $\tilde{A}_{x/y}^{\text{iXPM}}(\omega_n)$  represents the iXPM-equalized optical field and

$$\tilde{A}_{x/y}^{\text{CD}}(\omega_n) = \tilde{A}_{x/y}(\omega_n) H_{\text{CD}}(\omega_n), \quad (5.2)$$

is the CD-equalized optical field.  $H_{\text{CD}}$  is the frequency domain transfer function for CD compensation,

$$H_{\text{CD}}(\omega_n) = \exp \left( -i \frac{\beta_2}{2} \omega^2 h \right), \quad (5.3)$$

where  $h = N_{\text{spans/step}} L_s$  is the total fiber length to be considered in each step<sup>1</sup>. Note that, similarly to the notation of Chapter 4, the  $z$ -dependency of the optical field is omitted for simplicity. The  $\tilde{\mathcal{P}}_{xx/yy}$  coefficients account for the overall intra-polarization power in each FFT block,

$$\tilde{\mathcal{P}}_{xx/yy} = \sum_{k=1}^N \tilde{\mathbf{P}}_{\mathbf{xx/yy}}^{(k,k)} = \sum_{k=1}^N |\tilde{A}_{x/y}(\omega_k)|^2. \quad (5.4)$$

---

<sup>1</sup>In this work we assume that the step-size for VSNE-based equalization is always a multiple of the span length,  $h \geq kL_s$ , with  $k \in \mathbb{N}$ .

## 5.1. Analytical Formulation

---

In turn, the  $\tilde{\mathcal{P}}_{xy/yx}$  coefficients include the effect of coherent polarization mixing,

$$\tilde{\mathcal{P}}_{xy/yx} = \sum_{k=1}^N \tilde{\mathbf{P}}_{\mathbf{xy/yx}}^{(k,k)} = \sum_{k=1}^N \tilde{A}_{x/y}(\omega_k) \tilde{A}_{y/x}^*(\omega_k). \quad (5.5)$$

The  $\tilde{\chi}(\omega_n)$  term in (5.1) accounts for the removal of the extra iSPM contribution at  $\omega_n$  [8], which is caused by the overlapping symmetry employed to derive the iSPM+iXPM equalizer, and is given by

$$\tilde{\chi}(\omega_n) = \tilde{\mathbf{P}}^{(n,n)} = |\tilde{A}_x(\omega_n)|^2 + |\tilde{A}_y(\omega_n)|^2. \quad (5.6)$$

Finally,  $\kappa$  is an imaginary constant,

$$\kappa = \frac{\Gamma(\omega, z)}{K_1(\omega, z)} K_3^{\text{iXPM}} F^{\text{iXPM}} = -i \frac{8}{9} \xi \gamma K_3^{\text{iXPM}} \frac{N_s}{N_{\text{steps}}}, \quad (5.7)$$

which accounts for the non-coherent aggregation of multiple fiber spans. Applying an inverse discrete Fourier transform to equation (5.1), the following time domain iXPM equalizer is obtained,

$$A_{x/y}^{\text{iXPM}}(t_n) = \kappa \left[ A_{x/y}^{\text{CD}}(t_n) \left( 2\mathcal{P}_{xx/yy} + \mathcal{P}_{yy/xx} \right) + A_{y/x}^{\text{CD}}(t_n) \mathcal{P}_{xy/yx} - A_{x/y}^{\text{CD}}(t_n) \textcircled{\mathbb{N}} \chi(t_n) \right], \quad (5.8)$$

where  $A_{x/y}^{\text{CD}}$  is the time domain equivalent of  $\tilde{A}_{x/y}^{\text{CD}}$  defined at the discrete time instant,  $t_n$ , and the  $\mathcal{P}_{xx/yy}$ ,  $\mathcal{P}_{xy/yx}$  terms are obtained from the Parserval's theorem of Fourier transform,

$$\mathcal{P}_{xx/yy} = \frac{1}{N} \sum_{j \in J_0} |A_{x/y}(t_j)|^2, \quad (5.9a)$$

$$\mathcal{P}_{xy/yx} = \frac{1}{N} \sum_{j \in J_0} A_{x/y}(t_j) A_{y/x}^*(t_j), \quad (5.9b)$$

where  $J_0 = \{j : 1 \leq j \leq N\}$ . The TD-iSPM overlap term,  $\chi(t_n)$ , is given by

$$\chi(t_n) = A_x(t_n) \textcircled{\mathbb{N}} A_x^*(t_{N-n+2}) + A_y(t_n) \textcircled{\mathbb{N}} A_y^*(t_{N-n+2}), \quad (5.10)$$

with  $\textcircled{\mathbb{N}}$  representing the modulo  $N$  circular convolution,

$$f(t_n) \textcircled{\mathbb{N}} g(t_n) = \frac{1}{N} \sum_{k=1}^N \sum_{m=-\infty}^{\infty} f(t_k) g(t_{n-k-mN}), \quad (5.11)$$

where  $f(t_n)$  and  $g(t_n)$  can be any aperiodic functions of  $t_n$ .

Due to the high computational effort required for its calculation (a double circular convolution), associated with the low weight of the  $\tilde{\chi}(\omega_n)$  term in (5.1) ( $\sim N$  times lower than the remaining  $\tilde{\mathcal{P}}$  terms), in the following we will neglect the contribution of the  $A_{x/y}^{\text{CD}}(t_n) \textcircled{\mathbb{N}} \chi(t_n)$  term to the TD-iXPM equalizer.

Given the usage of the circular convolution theorem, the TD-iXPM equalizer of expression (5.8) is exactly equivalent to the FD-iXPM equalizer of (5.1), also requiring block-wise treatment of data. Neglecting the  $\chi(t_n)$  term and breaking the circular convolution into a more convenient linear convolution, equation (5.8) can be rewritten as

$$A_{x/y}^{\text{iXPM}}(t_n) \simeq \kappa \left[ A_{x/y}^{\text{CD}}(t_n) \left( 2\mathcal{P}_{xx/yy}(t_n) + \mathcal{P}_{yy/xx}(t_n) \right) + A_{y/x}^{\text{CD}}(t_n) \mathcal{P}_{xy/yx}(t_n) \right], \quad (5.12)$$

where  $\mathcal{P}_{xx/yy}(t_n)$  and  $\mathcal{P}_{xy/yx}(t_n)$  are obtained as moving averages composed of  $N$  taps, replacing  $J_0$  by  $J'_0(n) = \{j : n - \lceil \frac{N}{2} \rceil + 1 \leq j \leq n + \lfloor \frac{N}{2} \rfloor\}$  in (5.9a) and (5.9b).

### 5.1.2 Time domain iFWM equalizer

Expression 5.12 provides an approximate time domain equivalent for the simVSNE{0} filter derived in Chapter 4. We will now proceed with the derivation of the time domain equivalents for the additional simVSNE{K} filters, responsible for iFWM equalization. Let us then rewrite the simVSNE{K} equalizer of expressions (4.28) and (4.29) in the following form,

$$\begin{aligned} \tilde{A}_{x/y}^{\text{iFWM},(K)}(\omega_n) = \kappa H_{\text{CD}}(\omega_n) & \left[ \tilde{A}_{x/y}(\omega_{n+K}) \left( 2\tilde{\mathcal{P}}_{xx/yy}^{(K)}(\omega_n) + \tilde{\mathcal{P}}_{yy/xx}^{(K)}(\omega_n) - \tilde{\chi}^{(K)}(\omega_n) \right) \right. \\ & \left. + \tilde{A}_{y/x}(\omega_{n+K}) \tilde{\mathcal{P}}_{xy/yx}^{(K)}(\omega_n) \right], \end{aligned} \quad (5.13)$$

$$\begin{aligned} \tilde{A}_{x/y}^{\text{iFWM},(-K)}(\omega_n) = \kappa H_{\text{CD}}(\omega_n) & \left[ \tilde{A}_{x/y}(\omega_{n-K}) \left( 2\tilde{\mathcal{P}}_{xx/yy}^{*(K)}(\omega_{n-K}) + \tilde{\mathcal{P}}_{yy/xx}^{*(K)}(\omega_{n-K}) - \tilde{\chi}^{(-K)}(\omega_n) \right) \right. \\ & \left. + \tilde{A}_{y/x}(\omega_{n-K}) \tilde{\mathcal{P}}_{xy/yx}^{*(K)}(\omega_{n-K}) \right], \end{aligned} \quad (5.14)$$

where the  $\tilde{\mathcal{P}}_{xx/yy}^{(K)}$ ,  $\tilde{\mathcal{P}}_{xy/yx}^{(K)}$  terms represent the cross power between the  $x$  and  $y$  polarization components with a  $K\Delta\omega$  frequency-shift, with  $\Delta\omega$  being the digital frequency resolution,

$$\tilde{\mathcal{P}}_{xx/yy}^{(K)}(\omega_n) = \sum_{j \in J_K(n)} \tilde{A}_{x/y}(\omega_j) \tilde{A}_{x/y}^*(\omega_{j+K}), \quad (5.15a)$$

$$\tilde{\mathcal{P}}_{xy/yx}^{(K)}(\omega_n) = \sum_{j \in J_K(n)} \tilde{A}_{x/y}(\omega_j) \tilde{A}_{y/x}^*(\omega_{j+K}), \quad (5.15b)$$

where  $J_K$  aggregates the  $J_U$  and  $J_L$  summation intervals of expressions (4.16) and (4.17) as,

$$\begin{aligned} J_K(n) = \left\{ \text{if } K \geq 0, j : 1 \leq j \leq n-K-1 \vee n+2K \leq j \leq N-K \right. \\ \left. \text{else, } j : 1 \leq j \leq n-K \vee n+2K \leq j \leq N-K \right\}, \end{aligned} \quad (5.16)$$

## 5.1. Analytical Formulation

---

and  $\tilde{\chi}^{(K)}(\omega_n)$  includes the overlapping degenerate iFWM contributions, similarly to the iSPM overlap of (5.6),

$$\tilde{\chi}^{(K)}(\omega_n) = \tilde{\mathbf{P}}^{(n+2K, n+K)} = \tilde{A}_x(\omega_{n+K})\tilde{A}_x^*(\omega_{n+2K}) + \tilde{A}_y(\omega_{n+K})\tilde{A}_y^*(\omega_{n+2K}). \quad (5.17)$$

The resulting nonlinearly equalized optical field,  $\tilde{A}_{x/y}^{\text{NL},(N_k)}$ , is finally obtained as

$$\tilde{A}_{x/y}^{\text{NL},(N_k)}(\omega_n, z-h) = \sum_{K=-N_k}^{N_k} \tilde{A}_{x/y}^{\text{iFWM},(K)}(\omega_n, z), \quad (5.18)$$

with  $\tilde{A}_{x/y}^{\text{iFWM},(0)}(\omega_n) = \tilde{A}_{x/y}^{\text{iXPM}}(\omega_n)$ , as can be verified by evaluating equation (5.13) for  $K = 0$ . Neglecting the  $\tilde{\chi}^{(K)}(\omega_n)$  terms and replacing the  $J_K$  interval by  $J_0$ , the inverse Fourier transform of (5.13) and (5.14) yields,

$$A_{x/y}^{\text{iFWM},(K)}(t_n) \simeq \kappa \left[ A_{x/y}^{\text{CD},(K)}(t_n) \left( 2\mathcal{P}'_{xx/yy}{}^{(K)}(t_n) + \mathcal{P}'_{yy/xx}{}^{(K)}(t_n) \right) + A_{y/x}^{\text{CD},(K)}(t_n) \mathcal{P}'_{xy/yx}{}^{(K)}(t_n) \right], \quad (5.19)$$

and

$$A_{x/y}^{\text{iFWM},(-K)}(t_n) \simeq \kappa \left[ A_{x/y}^{\text{CD},(-K)}(t_n) \left( 2\mathcal{P}'_{xx/yy}{}^{*(-K)}(t_n) + \mathcal{P}'_{yy/xx}{}^{*(-K)}(t_n) \right) + A_{y/x}^{\text{CD},(-K)}(t_n) \mathcal{P}'_{yx/xy}{}^{*(-K)}(t_n) \right], \quad (5.20)$$

where  $A_{x/y}^{\text{CD},(K)}(t_n)$  is given by (using linear convolution),

$$\begin{aligned} A_{x/y}^{\text{CD},(K)}(t_n) &= \mathcal{F}^{-1} \left\{ \tilde{A}_{x/y}(\omega_{n+K}) H_{\text{CD}}(\omega_n) \right\} \\ &= A_{x/y}(t_n) \exp \left( i2\pi \frac{n}{N} K \right) \otimes h_{\text{CD}}(t_n), \end{aligned} \quad (5.21)$$

where  $h_{\text{CD}}(t_n)$  is the impulse response function for CD compensation and  $\otimes$  represents the linear convolution operation,

$$f(t_n) \otimes g(t_n) = \sum_{j \in J'_0(n)} f(t_j) g(t_{n-j}). \quad (5.22)$$

Finally, the  $\mathcal{P}'_{xx/yy}{}^{(K)}$  and  $\mathcal{P}'_{xy/yx}{}^{(K)}$  terms are obtained from (5.15a) and (5.15b), using the frequency-shift property of Fourier transform, yielding

$$\mathcal{P}'_{xx/yy}{}^{(K)}(t_n) = \frac{1}{N} \sum_{j \in J'_0(n)} |A_{x/y}(t_j)|^2 \exp \left( -i2\pi \frac{j}{N} K \right), \quad (5.23a)$$

$$\mathcal{P}'_{xy/yx}{}^{(K)}(t_n) = \frac{1}{N} \sum_{j \in J'_0(n)} A_{x/y}(t_j) A_{y/x}^*(t_j) \exp \left( -i2\pi \frac{j}{N} K \right). \quad (5.23b)$$

Similarly to (5.18), the final nonlinearly equalized optical field,  $A_{x/y}^{\text{NL},(N_k)}$ , is obtained as

$$A_{x/y}^{\text{NL},(N_k)}(t_n, z - h) = \sum_{K=-N_k}^{N_k} A_{x/y}^{\text{iFWM},(K)}(t_n, z), \quad (5.24)$$

yielding the TD-simVSNE, henceforth abbreviated for simplicity as TD-VSNE. Conversely, the initial FD-simVSNE equalizer giving rise to expressions (5.19), (5.20) and (5.24) will be henceforth abbreviated as FD-VSNE, in order to simplify the notation.

Note that, by ignoring the gaps in the non-contiguous power summation interval,  $J_K$ , we avoid computing complex time domain terms based on convolutions, which require high computational load. On the other hand, this approximation is expected to yield some performance penalty, relatively to the exact formulation. The impact of this penalty will be thoroughly analyzed in section 5.3. A full derivation of the TD-iFWM filters of expressions (5.19) and (5.20) is provided in Appendix C, where the neglected terms can be consulted.

### 5.1.3 Weighted VSNE

In [5], a simple modification on the DBP-SSFM has been proposed to improve its computational efficiency. The modified method, the so-called weighted SSFM (W-SSFM), is based on the insertion of an adjustable time window within the nonlinear step, creating a power weighting effect. By these means, the originally instantaneous nonlinear step is modified to include finite memory, thus accounting for the dispersion-induced distribution of optical power between neighboring symbols. Thereby, the W-SSFM enables to increase the DBP step-size, consequently reducing the computational effort and latency. Figure 5.1 illustrates the numerical implementation of the W-SSFM, obtained by modifying the DBP-SSFM implementation diagram of Figure 3.4 with the insertion of an accumulator block after the power operator. Note that the number of samples to be considered for power weighting can be easily adjusted by setting the summation interval in the accumulator block, without requiring any additional multiplications.

The TD-iXPM and TD-iFWM filters of expressions (5.12), (5.19) and (5.20), obtained through inverse Fourier analysis of their frequency domain counterparts, maintain a fixed power weighting window of  $N$  samples, as per definition of the frequency domain formulation. This ensures the equivalency between the simVSNE formulations in time and frequency domains. Nevertheless, the optical power summation intervals of equations (5.9) and (5.23) can be adjusted to optimize performance, similarly to the power weighting technique proposed in [5] for the W-SSFM. Applying an adjustable power weighting time window, the TD-VSNE described by equations (5.12), (5.19), (5.20) and (5.24) yields the weighted VSNE (W-VSNE) by simply redefining the  $J'_0$  interval as

$$J'_0(n) = \left\{ j: n - \left\lceil \frac{N_{\text{NL}}}{2} \right\rceil + 1 \leq j \leq n + \left\lfloor \frac{N_{\text{NL}}}{2} \right\rfloor \right\}, \quad (5.25)$$

and substituting  $N$  by  $N_{\text{NL}}$  in the exponential factors of (5.21) and (5.23), where  $N_{\text{NL}}$  is the adjustable time window depth to be considered in the nonlinear power weighting

## 5.1. Analytical Formulation

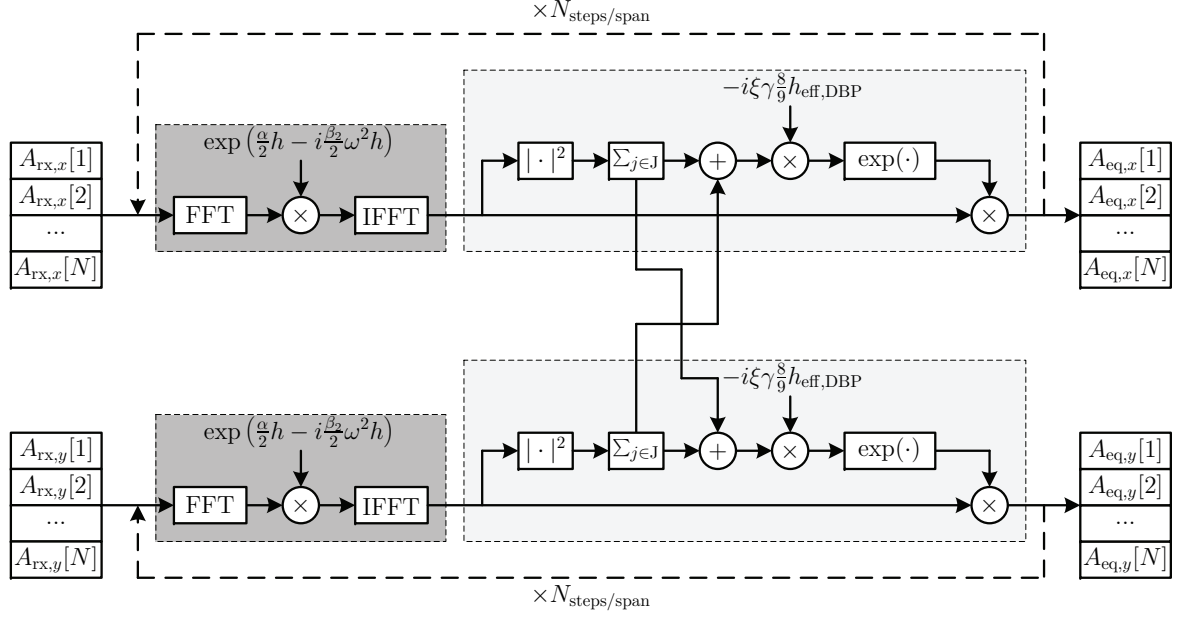


**Figure 5.1:** Numerical implementation of the dual-polarization W-SSFM for a single fiber span and a single FFT block. The implementation architecture is modified from that of Figure 3.4 by the introduction of an accumulator block after the  $|\cdot|^2$  operation.

terms. When  $N_{\text{NL}} = N$  the W-VSNE coincides with the TD-VSNE. Note that the equivalent frequency domain formulation for this adjustable power weighting requires the use of convolution operations, which are computationally intensive. In contrast, the W-VSNE approach does not imply any additional complexity, since the length of the time window can be straightforwardly controlled in hardware by an accumulator block, similarly to the W-SSFM of Figure 5.1.

To maintain coherence with the notation of Chapter 4, we will refer to the  $K$ -th TD-VSNE filter branch, defined by expression (5.19) and (5.20), as TD-VSNE $\{K\}$ . The TD-iXPM equalizer corresponds to the zeroth order TD-VSNE, TD-VSNE $\{0\}$ . The full TD-VSNE filter array, as defined by equation (5.24), will be denoted as TD-VSNE $[N_k]$ . Conversely, the W-VSNE individual filters and the  $N_k$  filter array will be denoted as W-VSNE $\{K\}$  and W-VSNE $[N_k]$ .

The implementation of the W-VSNE $[N_k]$  in parallel with CDE, is illustrated in Figure 5.2. Each W-VSNE $\{K\}$  filter branch is independently implemented, providing  $A_{x/y}^{\text{iFWM},(K)} + A_{x/y}^{\text{iFWM},(-K)}$  output signals that are summed together to obtain  $A_{x/y}^{\text{NL},(N_k)}$ . Note that for simplicity, the  $A_{x/y}^{\text{CD},(\pm K)}$  input signals are not explicitly represented in Figure 5.2. These signals can be obtained directly from the input optical field in time domain, as given by equation (5.21), or alternatively in frequency domain by applying a circular shift to the input field,  $\tilde{A}_{x/y}$ , and then calculating the IFFT of  $\tilde{A}_{x/y}(\omega_{n+K})H_{\text{CD}}(\omega_n)$ , as described in equation (5.21) and illustrated in Figure 5.3. As it is commonly accepted in the literature, FD-CDE is generally preferable from an implementation point of view, since it yields lower complexity when compared to time domain FIR filtering [9]. Nevertheless, from a conceptual ground, the W-VSNE algorithm can be implemented using either a

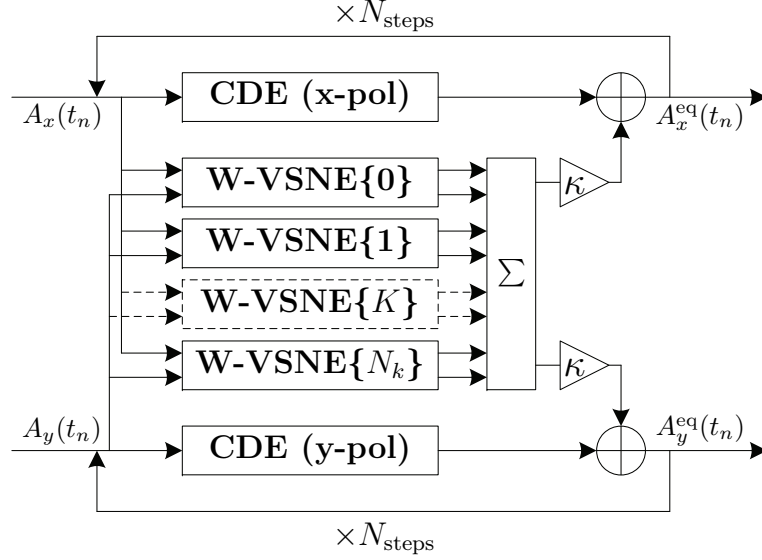


**Figure 5.2:** Schematic diagram for the implementation of DBP using the W-VSNE $[N_k]$  filter array in parallel with CDE. The equalized signal,  $A_{x/y}^{\text{eq}}(t_n)$ , is obtained from the input signal,  $A_{x/y}(t_n)$ , after an  $N_{\text{steps}}$ -DBP procedure, where the W-VSNE $[N_k]$  filter array is applied in parallel with dedicated CDE for each polarization tributary.

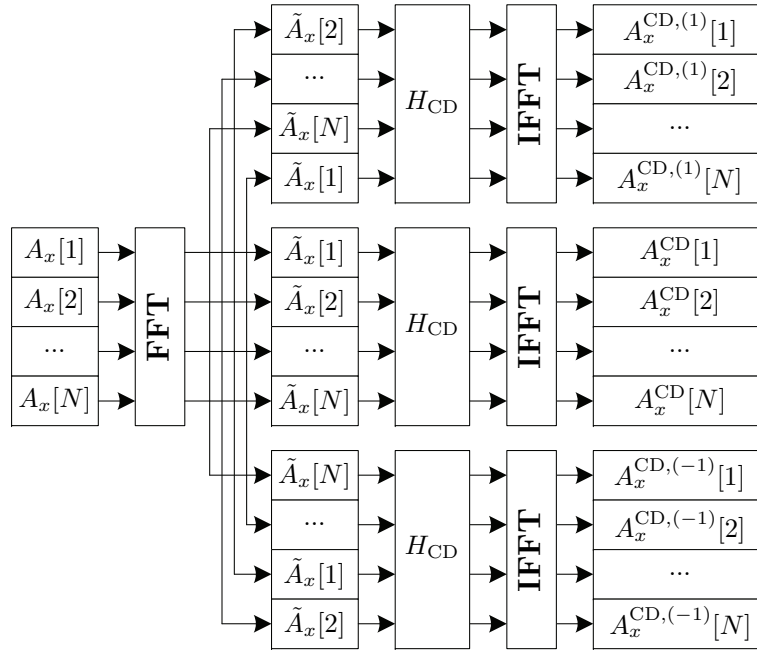


**Figure 5.3:** Frequency domain implementation of CDE in the  $x$  polarization and calculation of the corresponding  $A_x^{\text{CD},(\pm 1)}$  signals, required for the W-VSNE $\{1\}$  filter.

full time domain implementation or an hybrid time/frequency domain implementation, similarly to the SSFM.

The final equalized signal is obtained in a DBP fashion by applying a given number of steps,  $N_{\text{steps}}$ , from the output to the input of the filter. The W-VSNE algorithm

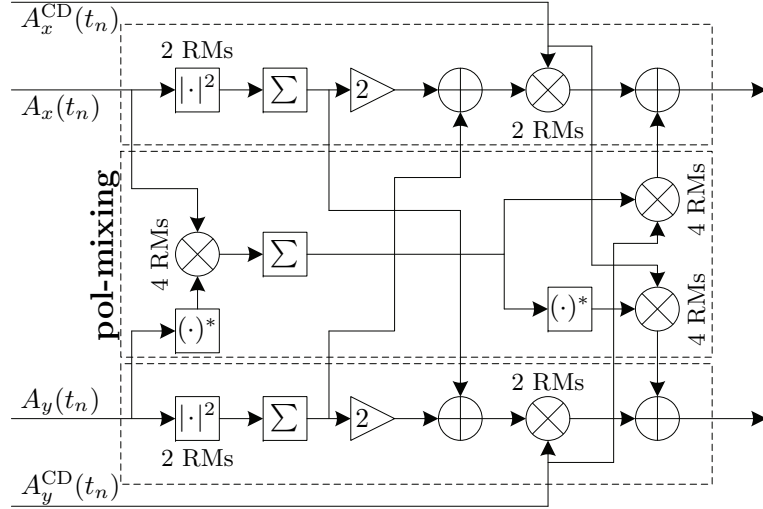


**Figure 5.4:** Implementation detail of the W-VSNE $\{0\}$  filter branch, indicating the number of real multiplications.

maintains the high granularity of the FD-VSNE, with each filter branch being applied in parallel, enabling to control the overall complexity by adjusting the filter dimension,  $N_k$ .

## 5.2 Implementation Complexity

A detailed implementation diagram of the W-VSNE $\{0\}$  filter branch is shown in Figure 5.4, with the indication of the number of RMs involved in each step. A total of 20 RMs per step is required by the W-VSNE $\{0\}$  filter, with 60% of this complexity being allocated for the computation of the coherent polarization mixing terms. Note that the structure of the W-VSNE $[0]$  algorithm closely resembles that of the W-SSFM, in that it is also based on the separate application of linear and nonlinear steps. However, the W-VSNE $[0]$  structure of Figure 5.4 unveils that the linear and nonlinear operations can be partially implemented in parallel, with the respective outputs being summed together as in a perturbative approach. Given this parallel implementation, the W-VSNE $[0]$  can also be classified as a kind of parallel split-step method [6]. To emphasize this similitude, both the complexity and performance of the W-VSNE $[0]$  and W-SSFM algorithms have been shown to be approximately equivalent [4, 6, 7].

By inspection of equations (5.19) and (5.20), a similar complexity analysis can be performed for the other W-VSNE $\{K\}$  filters, yielding a total of 52 RMs per sample, from which 20 RMs are required for the calculation of the power weighting terms ( $\mathcal{P}'^{(K)}_{xx/yy}$  and  $\mathcal{P}'^{(K)}_{xy/yx}$ ) and 32 RMs are due to the multiplication by  $A_{x/y}^{\text{CD},(\pm K)}$ . The added complexity relatively to W-VSNE $\{0\}$  is justified by the presence of the exponential function in (5.23) and by the fact that each W-VSNE $\{K\}$  filter is actually a composite of the two individual filters described by (5.19) and (5.20). To avoid replication of operations, we have moved the  $\kappa$  coefficient to multiply for the W-VSNE $[N_k]$  output,  $A_{x/y}^{\text{NL},(N_k)}$ .

In each iteration, the number of RMs per sample required by the W-VSNE $[N_k]$  filter

array, disregarding the CDE components, is then given by

$$M_{\text{W-VSNE}}^{\text{NL}}(N_k) = 24 + 52N_k, \quad (5.26)$$

where the 4 additional RMs per step are due to the multiplication by  $\kappa$  in Figure 5.2.

The complexity required by the parallel CDE will depend on the method used for equalization (e.g. time or frequency domain). Assuming a frequency domain implementation, and disregarding the overlap-add/overlap-save overhead, the CDE complexity per step is then given by

$$M_{\text{W-VSNE}}^{\text{CDE}}(N, N_k) = 2 \left[ 4 + 2M_{\text{FFT}}(N) + 2N_k M_{\text{FFT}}(N) + 8N_k \right], \quad (5.27)$$

where  $M_{\text{FFT}}$  refers to the FFT complexity given by (3.10). The multiplication of the signal by the CDE transfer function requires 4 RMs per sample. The  $2N_k M_{\text{FFT}}(N) + 8N_k$  term accounts for the calculation of  $A_{x/y}^{\text{CD},(\pm K)} = \mathcal{F}^{-1} \left\{ \tilde{A}_{x/y}(\omega_{n \pm K}) H_{\text{CD}}(\omega_n) \right\}$ , as detailed in Figure 5.3. The factor of 2 accounts for the two polarization tributaries, which are processed independently.

The overall complexity associated with DBP using the W-VSNE[ $N_k$ ] algorithm is then given by

$$M_{\text{W-VSNE}}^{\text{DBP}}(N_k, N) = N_{\text{steps}} \left[ M_{\text{W-VSNE}}^{\text{NL}}(N_k) + M_{\text{W-VSNE}}^{\text{CDE}}(N, N_k) \right]. \quad (5.28)$$

In terms of latency, measured in number of serial RMs, the W-VSNE benefits from the fact that the linear and nonlinear operators are partially applied in parallel. Indeed, observing Figures 5.2 and 5.4 it can be observed that only 2 real multiplication blocks (1 RM in the W-VSNE{ $K$ } filter and 1 RM to multiply by  $\kappa$ ) are applied after obtaining the CDE outputs in time domain. Therefore, the overall latency of the W-VSNE algorithm can be quantified as

$$\tau_{\text{W-VSNE}}^{\text{DBP}} = N_{\text{steps}} (\tau_{\text{CDE}} + 2), \quad (5.29)$$

where  $\tau_{\text{CDE}} = 2 \log_2(N) + 1$  represents the latency associated with each CDE step, including the FFT/IFFT pairs. To obtain expression (5.29) it is assumed that the latency of FD-CDE is always larger than the latency of the W-VSNE{ $K$ } filter branches, which is a valid assumption for practical values of  $N$ .

A thorough analysis of the performance/complexity trade-off of the W-VSNE and W-SSFM techniques will be carried out in the following section, supported by simulation results.

### 5.3 Numerical Assessment

To assess the performance of the proposed TD-VSNE and W-VSNE algorithms, we performed a comprehensive numerical analysis for a 224 Gb/s PM-16QAM transmission system, similar to the simulation setup of section 4.3, which is illustrated in Figure 4.7. Signal generation and propagation over  $24 \times 80$  km of SSMF has been performed in VPItransmissionMaker9.0. Each SSMF span is characterized by  $\alpha = 0.2$  dB/km,  $\beta_2 = -20.4$  ps<sup>2</sup>/km and  $\gamma = 1.3$  W<sup>-1</sup>km<sup>-1</sup>. The fiber attenuation is compensated by an

optical amplifier with 5 dB noise figure and 16 dB gain, to exactly restore the launched optical power in each fiber span. All the receiver-side DSP is then fully implemented in MATLAB with an oversampling ratio of 2. In order to mimic the analog bandwidth of a coherent receiver and to limit the aliasing effect of the initial downsampling stage, we have applied a third-order Butterworth low-pass filter with cutoff frequency at 22.4 GHz. The static equalization subsystem is implemented in time/frequency domain, using FIR/FFT-based CD equalization in parallel with the VSNE-based equalizers. Dynamic equalization of polarization-dependent effects is implemented by a  $2 \times 2$  FIR filter driven by a multi-radii CMA [10]. Since laser phase noise and the local oscillator frequency mismatch have been neglected for simplicity, the carrier recovery subsystem is implemented by a simple fixed phase rotation. Finally, the system performance is assessed through the BER measured over  $2^{17}$  bits.

### 5.3.1 Performance of TD-VSNE versus FD-VSNE

In order to validate the TD-VSNE derivation, we initiate our numerical analysis in Figure 5.5 by comparing the equalization performance of the derived TD-VSNE with its frequency domain counterpart, considering the exact and approximated formulations, corresponding to the use of the  $J_K$  or  $J_0$  summation intervals in (4.15), respectively. In Figure 5.5a it is shown that the FD-VSNE[0] and TD-VSNE[0], that are responsible for iXPM equalization, yield approximately the same performance, confirming the validity of expression (5.12). Indeed, the removal of the iSPM term in the TD-VSNE[0] yields negligible penalty and the tiny gap between both curves is mostly due to numerical effects caused by the replacement of circular (FD-VSNE) by linear (TD-VSNE) convolution. The same observation applies for the comparison between TD-VSNE[8] and FD-VSNE[8]<sub>approx</sub>, where the *approx* subscript stands for the use of the approximated formulation ( $J_0$  replacing  $J_K$  in (5.13) and (5.14) and neglecting the  $\tilde{\chi}^{(K)}(\omega_n)$  terms). The penalty caused by this approximation is revealed by the higher performance of the FD-VSNE[8] curve. For the considered transmission system, Figure 5.5a shows that the TD-VSNE penalty over the exact FD-VSNE is only significant for input powers larger than 1 dBm. This penalty tends to increase when the system is pushed further into the nonlinear regime, reaching approximately 0.75 dB in  $Q^2$  factor for the optimum input power (for TD-VSNE equalization) of 3 dBm, as further detailed in Figures 5.5b and 5.5c. Complementarily, Figures 5.5b and 5.5c show that the TD-VSNE and the approximated FD-VSNE yield equivalent performance for any value of  $N_k$  and  $N_{\text{steps}}$ . In addition, it is shown that the 0.75 dB penalty shown in Figure 5.5a for  $N_k = 8$  and  $N_{\text{steps}} = 24$  is actually the maximum obtained penalty and that the evolution of performance with  $N_k$  and  $N_{\text{steps}}$  is similar for the TD-VSNE and FD-VSNE. Indeed, the performance of both algorithms tends to saturate for  $N_k \geq 3$  and  $N_{\text{steps}} \geq 12$ . Focusing on the  $1 \times 10^{-3}$  BER limit, additional simulations have revealed that the minimum effort FD-VSNE implementation is obtained for  $N_k = 3$  and  $N_{\text{steps}} = 8$  (see Figure 5.12), whereas the corresponding TD-VSNE implementation requires  $N_k = 5$  and  $N_{\text{steps}} = 8$ .

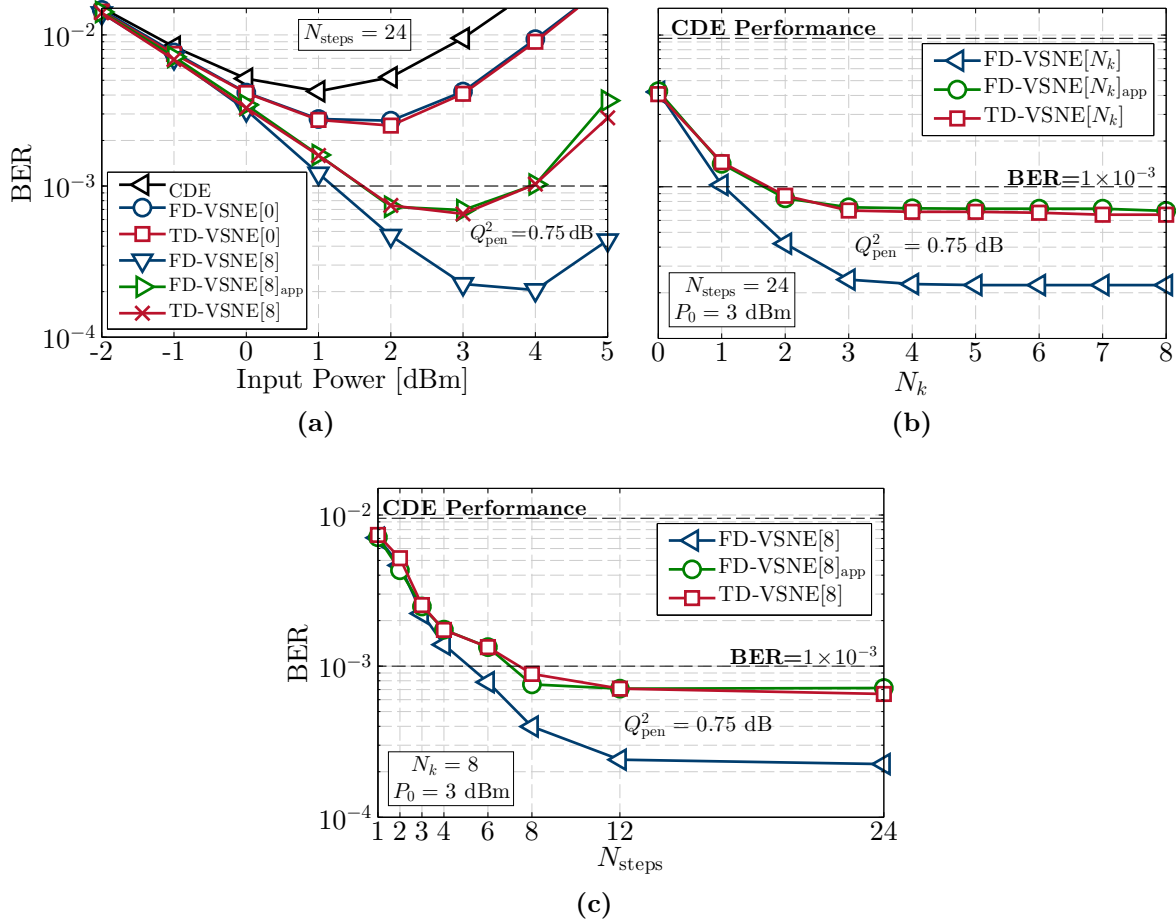


**Figure 5.5:** Performance comparison between the FD-VSNE and TD-VSNE algorithms, employing the exact and approximated formulations. a) BER as a function of input power for a fixed number of steps (1 step per span); b) BER as a function of  $N_k$  for a fixed input power of 3 dBm and 1 step per span; c) BER as a function of  $N_{\text{steps}}$  for an input power of 3 dBm and  $N_k = 8$ .

### 5.3.2 Performance of the W-VSNE

As indicated by expression (5.25), a simple modification can be added to the TD-VSNE algorithm in order to optimize the weighting of its optical power terms, through a nonlinear memory parameter,  $N_{\text{NL}}$ , in a similar way to the W-SSFM. Note that, in this work we assume a simple rectangular window profile for the power weighting of both the W-SSFM and W-VSNE algorithms. This approach leads to the lowest implementation complexity, since the rectangular window can be implemented as a multiplierless moving average. The optimization of  $N_{\text{NL}}$  for the W-SSFM and W-VSNE algorithms is shown in Figure 5.6, considering a fixed input optical power of 3 dBm. In general, it is shown that the nonlinear equalization performance can be substantially enhanced by optimizing  $N_{\text{NL}}$ , which depends on the number of steps,  $N_{\text{steps}}$ , to be considered. For large  $N_{\text{steps}}$ , the equalizer step-size is small, reducing the amount of

### 5.3. Numerical Assessment

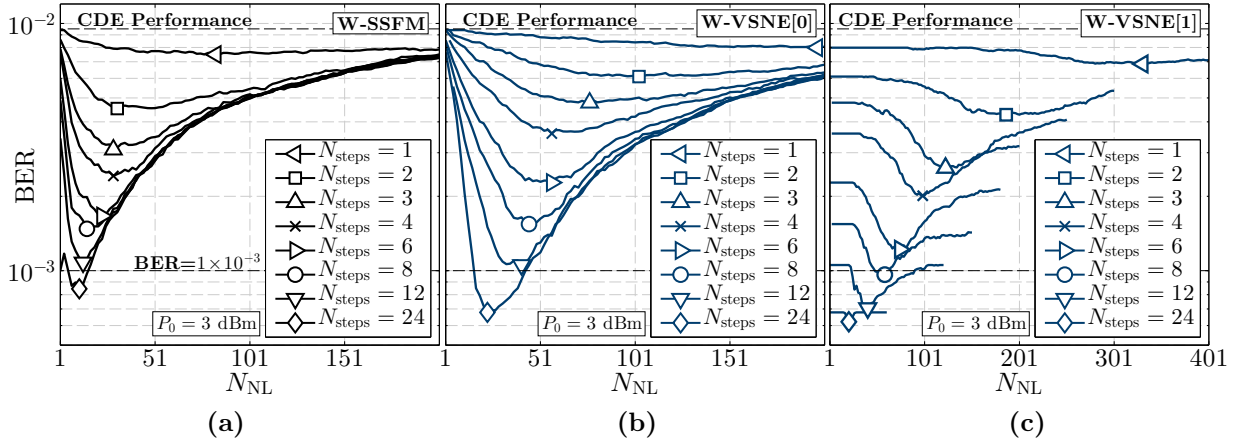


**Figure 5.6:** Optimization of the nonlinear memory parameter,  $N_{NL}$ , for the a) W-SSFM, b) W-VSNE[0] and c) W-VSNE[1] algorithms. The optimum  $N_{NL}$  for each  $N_{steps}$  value is signaled by open markers. Input power is 3 dBm.

accumulated CD to be inverted in each step. In this case, the interaction between dispersive linear and instantaneous nonlinear effects is less significant, and hence the optimum  $N_{NL}$  is also reduced. In contrast, low  $N_{steps}$  causes very large amounts of accumulated CD to be processed in each step, in which case the interaction between linear and nonlinear effects significantly spreads in time, consequently leading to large  $N_{NL}$ . However, when  $N_{NL}$  is increased far beyond its optimum value, the nonlinear equalization performance is severely reduced because the optical power is effectively averaged out, and the nonlinear interactions are lost. This effect is associated with the use of a rectangular power weighting filter profile along with a very large  $N_{NL}$ , thus yielding the average optical received power. A direct comparison between Figures 5.6a and 5.6b further reveals that the optimum nonlinear memory associated with the W-VSNE[0] is significantly larger than the correspondent W-SSFM (2-3 $\times$  larger). This different behavior can be explained by the fact that the W-VSNE has been derived from a Volterra series model, which inherently considers the existence of memory in the linear/nonlinear interactions. On the contrary, the W-SSFM is obtained from a modification of the SSFM algorithm, in which the nonlinear step is originally formulated as a memoryless operator. Therefore, the memory depth of linear/nonlinear interactions that is tolerated by the W-SSFM tends to be smaller. The  $N_{NL}$  optimization for the W-VSNE{1} filter is shown in Figure 5.6c, considering the overall BER performance for the W-VSNE[1] filter array. To perform this optimization we have fixed the  $N_{NL}$  of W-VSNE{0} to the optimum values found in Figure 5.6b, enabling to individually optimize the  $N_{NL}$  of the W-VSNE{1} branch. Although this approach does not guarantee to obtain the absolute optimum performance, it avoids resorting to a complex multivariable optimization, which may be unfeasible to perform in real-time. Following this gradual optimization procedure, a real-time receiver can start operating with an initially estimated  $N_{NL}$  value for W-VSNE[0], which is then adaptively optimized using a simple decision-feedback algorithm. Once the optimum  $N_{NL}$  is found for W-VSNE[0], and if additional equalization performance is required, other

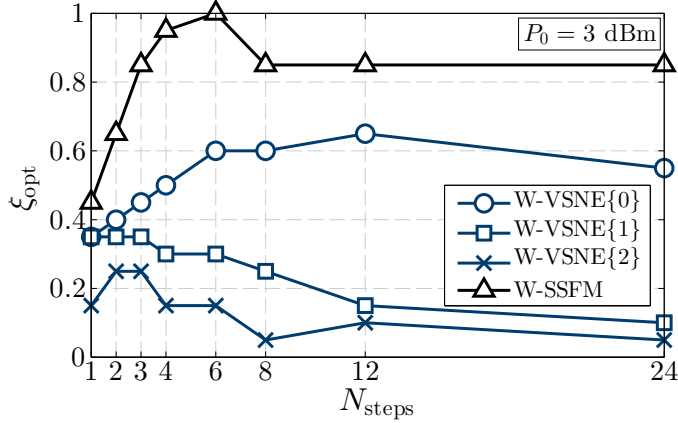


**Figure 5.7:** Optimization of the  $\xi$  parameter for the W-VSNE and W-SSFM algorithms as a function of  $N_{\text{steps}}$ . Input power has been fixed to 3 dBm.

parallel W-VSNE $\{K\}$  filters can be implemented, with the correspondent  $N_{\text{NL}}$  being optimized using a similar approach. Through the analysis of Figure 5.6c we observe that the benefit of W-VSNE[1] over W-VSNE[0] is more significant for  $2 < N_{\text{steps}} < 12$ , and it tends to vanish for higher spatial resolutions. In addition, the optimum nonlinear memory for the W-VSNE{1} filter branch tends to be higher than that of the W-VSNE{0}, which demonstrates that the introduction of additional W-VSNE $\{K\}$  filters enables to capture longer-term nonlinear interactions.

Note that every data point in Figure 5.6 has been obtained after optimizing the  $\xi$  parameter in (5.7), by individually trying all values of  $\xi$ , between 0 and 1, with a resolution of 0.05. The results of this optimization are shown in Figure 5.7. For both the W-SSFM and W-VSNE[0] it can be observed that the optimum  $\xi$  values,  $\xi_{\text{opt}}$ , tends to decrease for coarser spatial resolution, as a consequence of DBP inaccuracy with very large step-sizes. It is also shown that the  $\xi_{\text{opt}}$  for the W-VSNE{0} is typically lower than that of the W-SSFM, mostly because the W-VSNE{0} is only a single filter from an array of  $N_k$  complementary filters, whose outputs are additive. Also, it can be observed that the  $\xi_{\text{opt}}$  values quickly drop for increasing  $K$  filters, indicating that the added benefit of W-VSNE $\{K\}$  filters tends to vanish for relatively small  $K$ .

Considering the above described  $N_{\text{NL}}$  and  $\xi$  optimization procedure, in Figure 5.8 we compare the performance of the W-VSNE with the TD-VSNE and SSFM-based algorithms. As shown in Figure 5.8a, the W-VSNE algorithm achieves the highest performance, when applied with 1 step per span ( $N_{\text{steps}} = 24$ ). The large gain over TD-VSNE[0] can be explained by the fact that the W-VSNE[0] is no longer an iXPM-only equalizer. Indeed, the time domain windowing of the optical power terms in the W-VSNE corresponds in frequency domain to a series of double convolutions, generating the frequency mixing that will emulate iFWM components. Let us now focus on the performance comparison between the W-VSNE and W-SSFM at their optimum power, which in both cases is of 3 dBm. As depicted in Figure 5.8c, the performance gain of the W-VSNE[0] over TD-VSNE[0] reaches a peak of  $\sim 2$  dB in  $Q^2$  factor for  $N_{\text{steps}} = 12$ . This gain then tends to decrease with decreasing  $N_{\text{steps}}$ , accompanying the overall BER

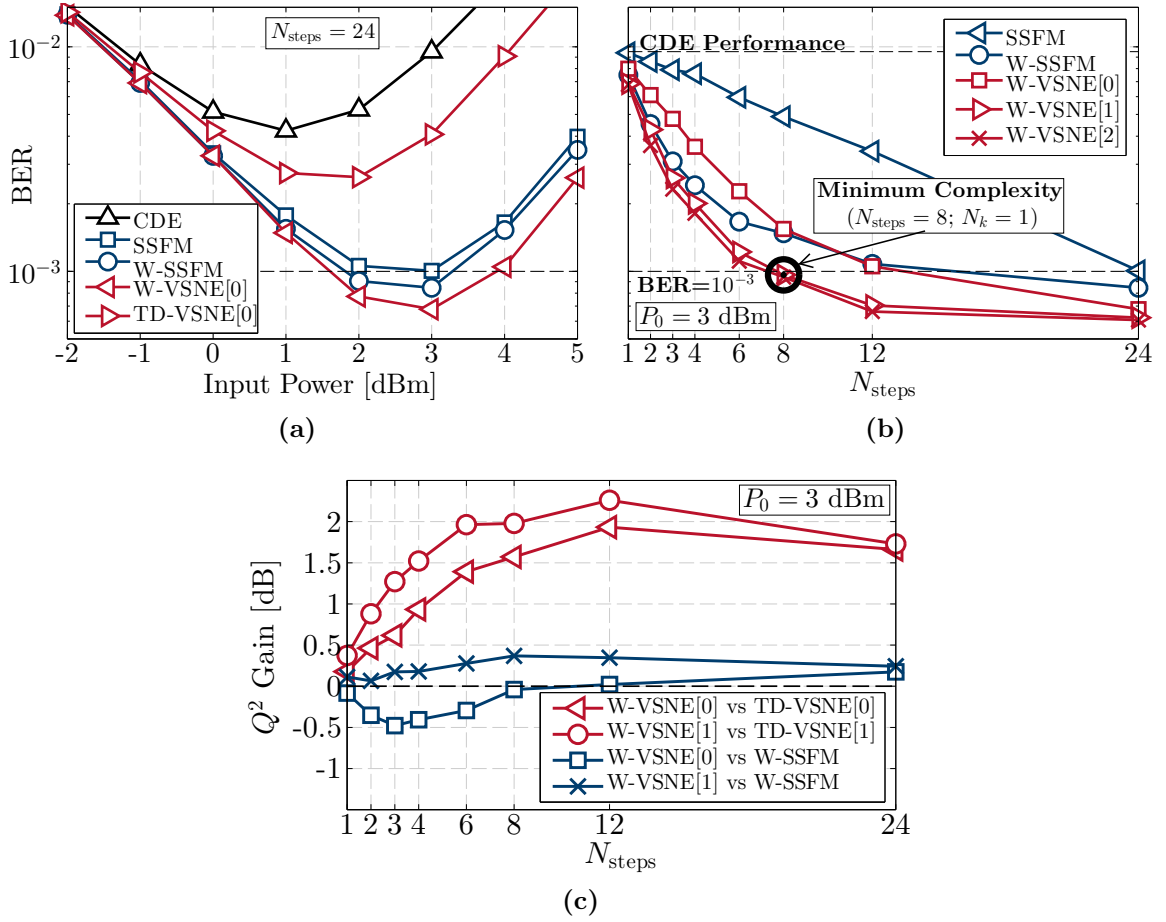


**Figure 5.8:** Performance of the W-VSNE and direct comparison with the TD-VSNE and W-SSFM. a)  $Q^2$  as a function of input power, considering 1 iteration per span; b)  $Q^2$  gain over CDE as a function of  $N_{\text{steps}}$  for a fixed input power of 3 dBm; c)  $Q^2$  gain of the W-VSNE over the TD-VSNE and W-SSFM.

degradation due to insufficient spatial resolution. A direct comparison with the W-SSFM, as shown in Figures 5.8b and 5.8c reveals that the W-VSNE[0] and W-SSFM algorithms yield similar performances. The W-SSFM tends to be more advantageous for  $N_{\text{steps}} < 8$ , reaching a peak gain of 0.5 dB, whereas the W-VSNE[0] shows a  $\sim 0.2$  dB advantage for  $N_{\text{steps}} = 24$ . Nevertheless, the W-VSNE performance can be substantially enhanced by adding an additional filter branch, W-VSNE[1], enabling to surpass the W-SSFM performance for all the considered  $N_{\text{steps}}$ . Considering the  $1 \times 10^{-3}$  BER limit, this benefit opens the possibility of reducing the number of steps by 3 fold (from 24 to 8). Also in Figure 5.8b, it is shown that the W-VSNE[2] only provides a small incremental performance relatively to W-VSNE[1]. This is in contrast with the TD-VSNE and FD-VSNE algorithms, for which the equalization performance has been found to saturate for significantly larger  $N_k$ , as previously illustrated in Figure 5.5b and discussed in Chapter 4. Besides the iFWM-emulation capabilities of the W-VSNE[0], this faster W-VSNE performance saturation with  $N_k$  can also be understood by the fact that

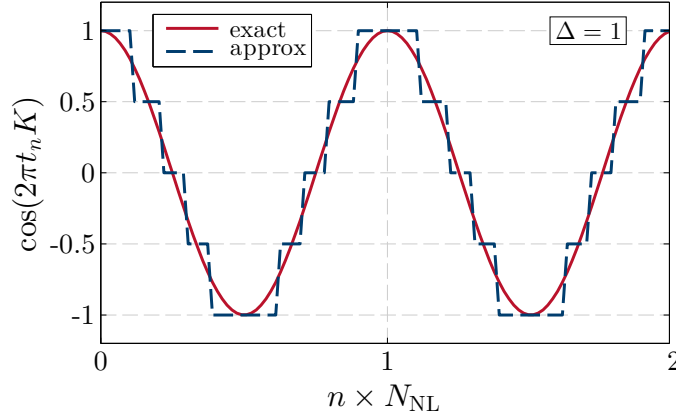


**Figure 5.9:** Application of the power-of-two approximation to the real part of the exponential factor in (5.23), considering  $\Delta = 1$  and  $K = 1$ .

the power weighting terms in the W-VSNE $\{K\}$  filter are modulated by a frequency  $\frac{K}{N_{\text{NL}}}f_s$ , as described in equation (5.23), where  $f_s$  is the sampling rate. Thereby, the optimized  $N_{\text{NL}}$  not only controls the nonlinear memory depth, but also sets the frequency separation of the emulated iFWM triplets. In contrast with the spectrum scanning approach in the FD/TD-VSNE algorithm, this approach will automatically seek for the most relevant uncompensated iFWM distortions, thus accelerating convergence to the optimum performance.

### 5.3.3 Complexity reduction for hardware implementation

Targeting the real-time implementation of the W-VSNE algorithm, in this section we will explore complexity reduction strategies without compromising performance. From the analytical derivation and complexity assessment of the W-VSNE algorithm in sections 5.1 and 5.2, it can be observed that the exponential functions required for calculating the power weighting terms of the  $K$ -th order filters in expression (5.23) are an important source of added complexity. Indeed, to obtain the computational effort expressions (5.26) and (5.28) we have considered that the multiplication by the exponential factor in (5.23) requires a total of 12 RMs per processed sample ( $\mathcal{P}'_{xy}{}^{(K)}$  and  $\mathcal{P}'_{yx}{}^{(K)}$  require 4 RMs each;  $\mathcal{P}'_{xx}{}^{(K)}$  and  $\mathcal{P}'_{yy}{}^{(K)}$  require 2 RMs each). However, this complexity can be avoided by a simple power-of-two approximation of the exponential factor, as shown in Fig. 5.9. For this purpose we define a quantization factor,  $\Delta$ , so that

$$f'(t_n) = \frac{\lfloor f(t_n)2^{\Delta} \rfloor}{2^{\Delta}}, \quad (5.30)$$

where  $f(t_n)$  is any function of  $t_n$  and  $f'(t_n)$  represents its power-of-two approximation. The  $\lfloor \cdot \rfloor$  operator defines the nearest integer operation. Using such an approach, all multiplications are decomposed into hardware efficient shift-and-add operations. Note that for the illustrated case of  $\Delta = 1$ , the only involved operations are a logical right shift to multiply by 0.5 and a bit inversion to multiply by -1. Under this approximation,

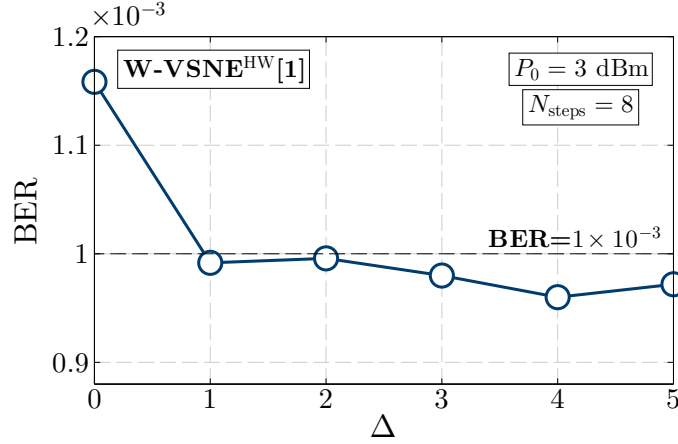


**Figure 5.10:** Impact of the complexity reduction approximations of (5.30) and (5.32) on the performance of the minimum effort W-VSNE[1] ( $N_{\text{steps}} = 8$ ).

the complexity of the hardware optimized W-VSNE implies to redefine expression (5.26) as

$$M_{\text{W-VSNE}}^{\text{NL}}(N_k) = 24 + 40N_k, \quad (5.31)$$

where all RMs due to the exponential factors are eliminated.

Another important source of computational effort is the calculation of the  $A_{x/y}^{\text{CD},(\pm K)}$  terms in frequency domain, as illustrated in Figure 5.3. To avoid the additional CD transfer functions and IFFTs we propose the following time domain approximation,

$$A_{x/y}^{\text{CD},(K)}(t_n) \simeq A_{x/y}^{\text{CD}}(t_{n+d_{\text{opt}}}) \exp\left(i(2\pi t_n K + \phi_{\text{opt}})\right), \quad (5.32)$$

where  $d_{\text{opt}}$  and  $\phi_{\text{opt}}$  are scalar optimization parameters. Employing this time domain approximation jointly with the power-of-two approximation for the exponential factor enables to obtain  $A_{x/y}^{\text{CD},(\pm K)}(t_n)$  directly from  $A_{x/y}^{\text{CD}}(t_{n \pm d_{\text{opt}}})$ , avoiding the use of RM operations. The complexity of the hardware optimized W-VSNE is therefore obtained by redefining (5.28) as

$$M_{\text{W-VSNE}}^{\text{DBP}}(N_k, N) = N_{\text{steps}} \left[ M_{\text{W-VSNE}}^{\text{NL}}(N_k) + M_{\text{W-VSNE}}^{\text{CDE}}(N, 0) \right], \quad (5.33)$$

where the extra complexity required for the  $A_{x/y}^{\text{CD},(\pm K)}$  calculation has been removed. Henceforth, we will refer to the W-VSNE using the hardware efficient approximations of expressions (5.31) and (5.33) as W-VSNE<sup>HW</sup>. Note that the W-VSNE and W-VSNE<sup>HW</sup> differ only for  $N_k > 0$ .

To assess the performance penalty incurred by the approximations of expressions (5.30) and (5.32), Figure 5.10 shows the evolution of BER as a function of the quantization factor,  $\Delta$ , for the minimum effort W-VSNE[1] obtained in Figure 5.8b that yields a BER below the  $1 \times 10^{-3}$  threshold, corresponding to  $N_{\text{steps}} = 8$ . It is shown that the system operation below the BER threshold is maintained for values of  $\Delta$  down to 1, corresponding to the quantization process depicted in Figure 5.9.

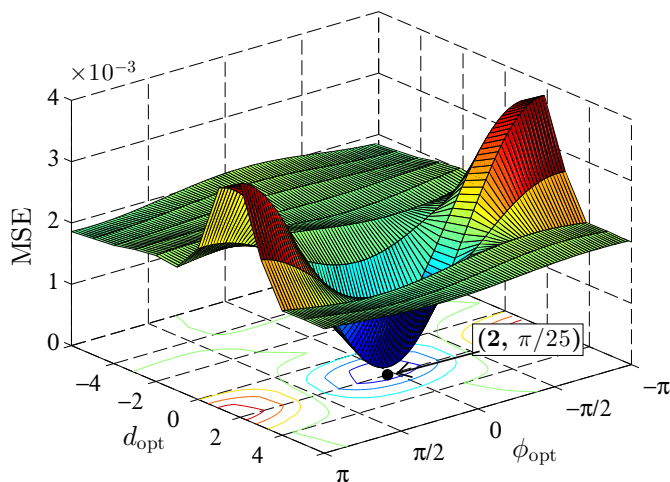


**Figure 5.11:** Two-dimensional optimization procedure associated with the approximation of expression (5.32) to obtain  $A_{x/y}^{\text{CD},(1)}$ .

Finally, in Fig. 5.11 we provide a detail of the two-dimensional optimization procedure of equation (5.32). It can be observed that the best approximation for  $A_{x/y}^{\text{CD},(1)}$  has been obtained with  $d_{\text{opt}} = 2$  and  $\phi_{\text{opt}} = \pi/25$ , for which the MSE between the true and approximated  $A_{x/y}^{\text{CD},(1)}$  signal is minimized. It is important to note that this optimization only depends on the CD equalization transfer function,  $H_{\text{CD}}$ , and therefore it can be pre-computed or performed offline on system initialization. The associated complexity and latency can therefore be neglected.

### 5.3.4 Computational effort analysis

In this section we evaluate the computational effort of the W-VSNE algorithm by determining the minimum complexity required to achieve the BER threshold of  $1 \times 10^{-3}$ .

**Table 5.1:** Computational effort and latency of the W-VSNE, FD-VSNE and W-SSFM corresponding to the results in Figure 5.8b and Figure 5.12.

$N_{\text{steps}}$		24	12	8	6
$N$		128	256	256	512
W-VSNE[0]	$N_{\text{RMs}}$	<b>2112</b>	1152	768	624
	$\tau$	<b>384</b>	216	144	120
W-VSNE[1]	$N_{\text{RMs}}$	5088	2736	<b>1824</b>	1464
	$\tau$	384	216	<b>144</b>	120
W-VSNE <sup>HW</sup> [1]	$N_{\text{RMs}}$	3072	1632	<b>1088</b>	864
	$\tau$	384	216	<b>144</b>	120
FD-VSNE[3]	$N_{\text{RMs}}$	4226	2163	<b>1463</b>	1125
	$\tau$	86	52	<b>40</b>	36
W-SSFM	$N_{\text{RMs}}$	<b>1992</b>	1092	728	594
	$\tau$	<b>456</b>	252	168	138

The corresponding number of RMs per sample,  $N_{\text{RMs}}$ , and latency,  $\tau$ , required by the W-VSNE, FD-VSNE and W-SSFM algorithms, considering different filter configurations is summarized in Table 5.1. The complexity of the W-VSNE and W-VSNE<sup>HW</sup> algorithms is calculated through expressions (5.28) and (5.33), whereas the FD-VSNE complexity is calculated from expression (4.36), derived in Chapter 4. The  $N_{\text{RMs}}$  and  $\tau$  values corresponding to the minimum implementation complexity that enables to achieve the  $1 \times 10^{-3}$  BER threshold are indicated in bold font. Complementarily, using W-SSFM as a benchmark, Table 5.2 summarizes the gains in computational efficiency and latency of the minimum effort W-VSNE and FD-VSNE implementations.

From Figure 5.8b it can be observed that at least 24 steps (1 steps per span) are required by both the W-VSNE[0] and W-SSFM to achieve the  $1 \times 10^{-3}$  BER threshold. In Tables 5.1 and 5.2 it is shown that the W-VSNE[0] yields approximately the same computational effort as the W-SSFM ( $\sim 6\%$  more RMs) with a  $\sim 15\%$  lower latency. Nevertheless, as shown in Figure 5.8c, for this direct comparison the W-VSNE[0] algorithm benefits from  $\sim 0.2$  dB of  $Q^2$  gain over the W-SSFM. Using the W-VSNE[1], the minimum number of steps can be reduced to 8, resulting in 1824 RMs per sample, which roughly corresponds to  $\sim 8\%$  complexity reduction relatively to the W-SSFM. Additionally, this corresponds to a latency reduction of  $\sim 70\%$ . Employing the hardware optimized W-VSNE<sup>HW</sup>, the minimum number of steps remains  $N_{\text{steps}} = 8$  (as shown in Figure 5.10) yielding 1088 RMs per sample, which corresponds to a complexity reduction of approximately 45% relatively to the W-SSFM.

In order to allow a direct comparison with the previously proposed FD-VSNE algorithm, Figure 5.12 shows the best performance (after  $\xi$  optimization) obtained by the FD-VSNE. The minimum effort FD-VSNE configuration that ensures operation below the BER threshold is obtained with  $N_{\text{steps}} = 8$  and  $N_k = 3$  (signaled in Figure 5.12 by an open black circle). It is shown that the FD-VSNE remains the most advantageous algorithm in terms of latency, with  $\sim 90\%$  reduction relatively to the W-SSFM. This stems from the fact that the FD-VSNE is entirely implemented in frequency domain, thus not requiring FFT/IFFT pairs within each step, which are the largest source of processing latency. In contrast, the proposed implementation for the W-VSNE and W-SSFM algorithms is based on an hybrid time/frequency domain processing, where the nonlinear step is implemented in time domain and the linear step is implemented in frequency domain to reduce the overall computational effort. It should be noted however, that both the W-VSNE and W-SSFM can also be entirely implemented in time domain, which would minimize the latency at the expense of increased computational effort. In

**Table 5.2:** Comparison of computational effort and latency with the benchmark W-SSFM implementation.

	$N_{\text{RMs}}$	$\tau$
W-VSNE[0]	+6%	-15.8%
W-VSNE[1]	-8.4%	-68.4%
W-VSNE <sup>HW</sup> [1]	<b>-45.4%</b>	-68.4%
FD-VSNE[3]	-26.6%	<b>-91.2%</b>

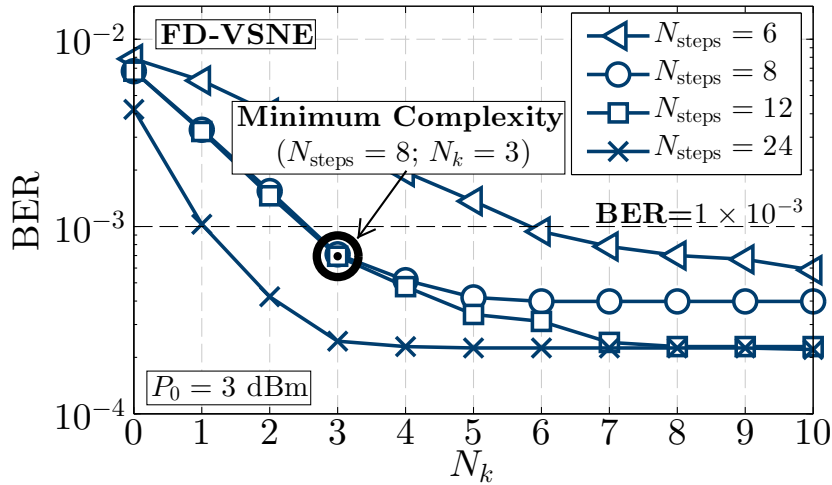


**Figure 5.12:** Performance of the FD-VSNE as a function of  $N_{\text{steps}}$  and  $N_k$ .

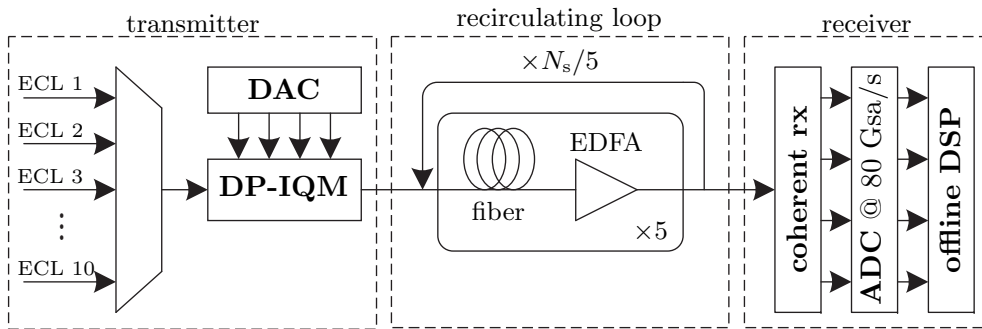


**Figure 5.13:** Laboratorial setup for the experimental validation of the W-VSNE technique. The WDM ultra-long-haul transmission system is composed of  $10 \times 400\text{G}$  signals in a dual-carrier ( $2 \times 31.5$  Gbaud) PM-16QAM configuration.

terms of complexity, the minimum effort FD-VSNE requires 1463 RMs, approximately 20% lower than the W-VSNE[1] but  $\sim 35\%$  larger than the W-VSNE<sup>HW</sup>.

## 5.4 Experimental Validation

The experimental validation of the W-VSNE technique has been carried out in collaboration with Centro de Pesquisa e Desenvolvimento em Telecomunicações (CPqD), in Campinas, São Paulo, Brazil. All results have been obtained in the laboratorial facilities of CPqD during a 1-month research visit partially financed by Fundação para a Ciência e a Tecnologia (FCT) and by CPqD.

### 5.4.1 Laboratorial setup and DSP subsystems

A simplified scheme of the laboratorial setup used for the experimental validation of the W-VSNE technique is depicted in Figure 5.13. A similar configuration is employed in

Chapter 6 for the experimental validation of inter-subcarrier nonlinear compensation in 400G transmission systems, where a more detailed description of the laboratorial setup is provided. At the transmitter side, 10 ECLs with linewidth of 100 kHz were used to generate the WDM optical subcarriers. The WDM comb is composed of five 400G superchannels consisting of two PM-16QAM subcarriers modulated at 31.5 Gbaud, thus generating a gross data-rate of 504 Gb/s. Each superchannel is assigned to a 75 GHz slot, yielding a net SE of 5.33 b/s/Hz. Each I and Q component in the  $x/y$  polarizations is randomly generated by a DAC operating at 63 Gsa/s, with an electrical bandwidth of  $\sim 14$  GHz. After Nyquist pulse shaping with a roll-off factor of 0.1, the DAC analog signal sequence is fed into the dual-polarization (DP) IQ modulator (IQM) for optical modulation. The generated 400G superchannel signal is sent to the recirculating loop, which is composed of 5 spans of 50 km of ultra-low-loss (ULL) fiber, characterized by  $\alpha = 0.162$  dB/km,  $D = 20.4$  ps/(nm·km) and effective area of  $112 \mu\text{m}^2$ . EDFA-only optical amplification is applied with 6 dB noise figure. At the receiver side, a wideband coherent receiver with electrical bandwidth of  $\sim 40$  GHz is used to detect the two superchannel subcarriers. The signal is sampled by a real-time oscilloscope operating at 80 Gsa/s, with an analog bandwidth of  $\sim 35$  GHz, being followed by offline processing in MATLAB. Post-detection DSP starts with the compensation of the receiver frontend impairments. Then, static linear and nonlinear equalization is performed by DBP-based SSFM, W-SSFM and W-VSNE. A multi-radii CMA is then applied for linear adaptive equalization. An additional 25-taps ISI adaptive equalizer is applied after the carrier recovery subsystems. Finally, the BER is measured over  $2^{19}$  received bits.

### 5.4.2 Performance of nonlinear equalization

Similarly to section 5.3.2, the W-VSNE performance analysis is initiated by the optimization of the nonlinear memory parameter,  $N_{\text{NL}}$ . In order to reduce the computation time, the optimization of the  $N_{\text{NL}}$  and  $\xi$  parameters has been performed in different stages, instead of the simultaneous optimization procedure carried out in section 5.3. The multi-variable W-VSNE optimization procedure adopted in this section has been performed as follows:

- i) the impact of the nonlinear memory on the W-VSNE[0] performance is tested for a wide range of  $N_{\text{NL}}$  values, considering empiric initial values for the  $\xi$  parameter. The value of  $N_{\text{NL}}$  yielding the maximum performance,  $N_{\text{NL,opt}}$ , is stored in memory;
- ii) using the best  $N_{\text{NL}}$  values found in i), the optimization proceeds with the assessment of the  $\xi$  parameter within the interval  $0 \leq \xi \leq 1$  (in step-sizes of 0.1). The  $\xi$  value yielding the maximum W-VSNE[0] performance,  $\xi_{\text{opt}}$ , is stored in memory. The optimization of the W-VSNE[0] is concluded, and its maximum performance is assumed to be obtained with the determined  $N_{\text{NL,opt}}$  and  $\xi_{\text{opt}}$  values;
- iii) the following W-VSNE[K] filters are independently optimized by repeating procedures i) and ii).

The same procedure is followed to optimize the performance of the W-SSFM, at the exception of point iii), since the W-SSFM does not include additional parallel filters.

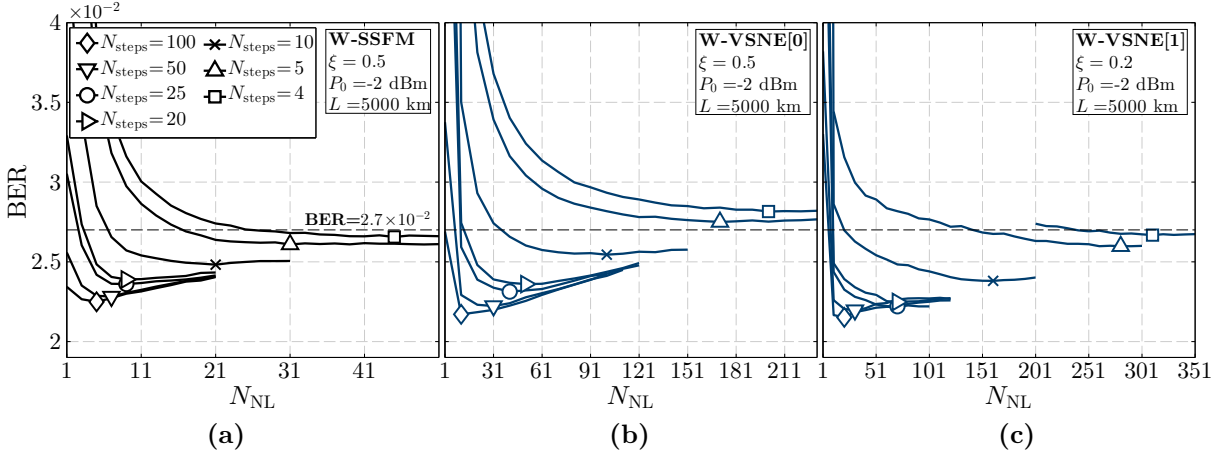


**Figure 5.14:** Optimization of the nonlinear memory,  $N_{NL}$ , for the a) W-SSFM, b) W-VSNE[0] and c) W-VSNE[1] algorithms, in the 400G ULH transmission system under test. The optimum  $N_{NL}$  for each  $N_{steps}$  value is signaled by open markers. Input power is -2 dBm and the propagation distance is 5000 km.

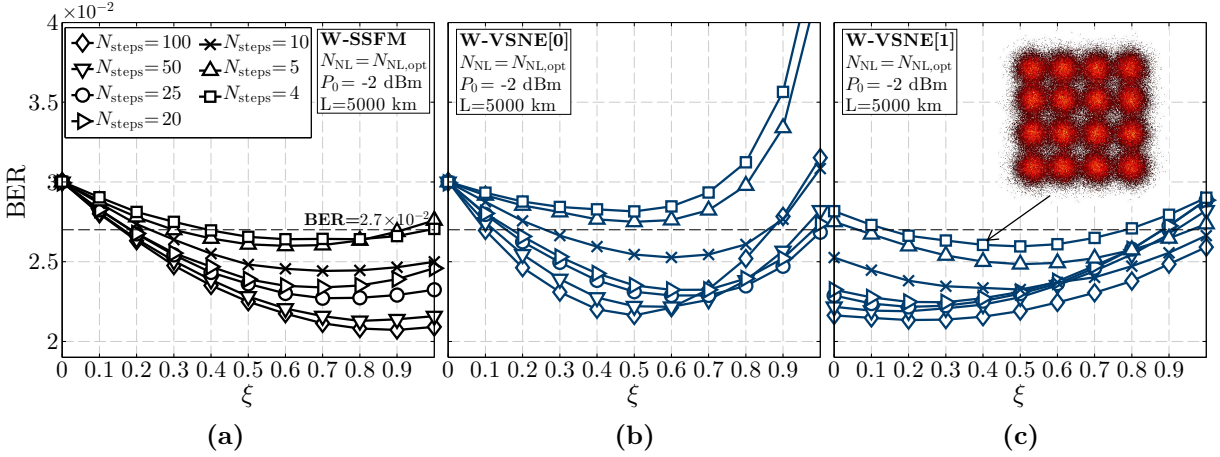


**Figure 5.15:** Optimization of  $\xi$  for the a) W-SSFM, b) W-VSNE[0] and c) W-VSNE[1] algorithms, in the 400G ULH transmission system under test. Input power is -2 dBm and the propagation distance is 5000 km.

Figure 5.14 shows the initial optimization of  $N_{NL}$  for a fixed input power of -2 dBm and a fixed signal reach of 5000 km. The subsequent optimization of  $\xi$  is shown in Figure 5.15. The minimum considered DBP step-size is of 50 km, corresponding to 1 step per span and 100 steps in total. Not shown for simplicity in Figures 5.14 and 5.15, the same optimization procedure has been carried out for the remaining input optical powers. Similarly to the numerical results of Figure 5.6, the obtained experimental results demonstrate that the optimum  $N_{NL}$  tends to increase with decreasing  $N_{steps}$ , due to the higher accumulated dispersion per DBP step. The longer-term memory requirements of the W-VSNE are also experimentally confirmed, with the W-VSNE[0] and W-VSNE[1]

## 5.4. Experimental Validation

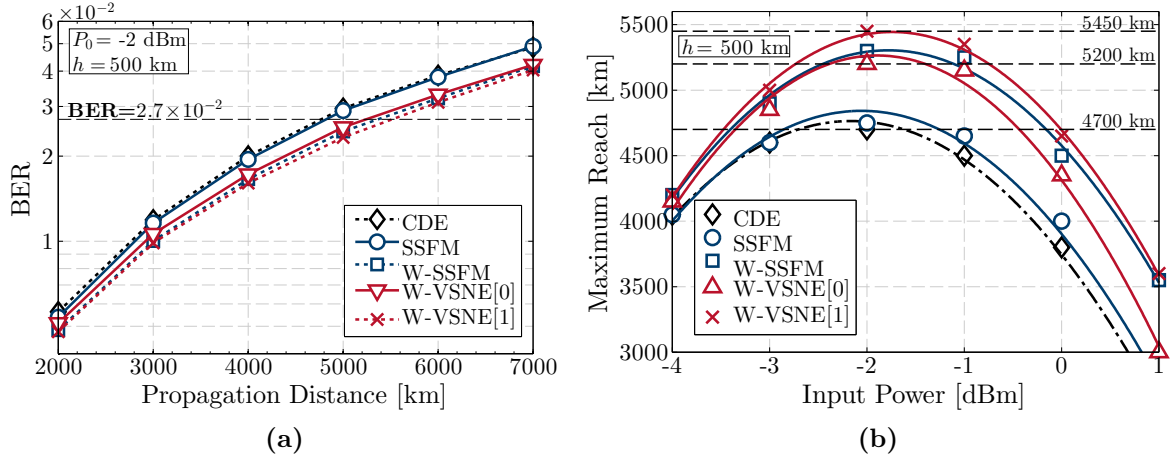


**Figure 5.16:** Performance of the W-VSNE algorithm for nonlinear compensation in the ULH 400G transmission system under test, considering a fixed step-size of 500 km. a) BER versus propagation distance for an input power of -2 dBm; b) estimated maximum reach as a function of the input power.

requiring approximately  $5\times$  and  $7\times$  larger  $N_{\text{NL}}$  than the W-SSFM. This confirms the W-VSNE capability of capturing nonlinear interactions that spread over longer time windows.

The equalization performance of the W-VSNE algorithm in the considered ULH 400G transmission system is shown in Figure 5.16, both in terms of distance-dependency of BER (see Figure 5.16a) and maximum signal reach (see Figure 5.16b) for a fixed step-size of 500 km. The results in Figure 5.16a, corresponding to the optimum input power of -2 dBm, show that the standard DBP-SSFM only brings a marginal gain in BER over CDE, due to the relatively large step-size ( $h = 500$  km). In contrast, the W-SSFM is shown to provide a significant gain in BER. As an example, for a transmission distance of 5000 km, the CDE-enabled BER of  $\sim 3 \times 10^{-2}$  is reduced to approximately  $2.4 \times 10^{-2}$ . This BER improvement enables an extended reach of approximately 600 km, corresponding to a  $\sim 12.5\%$  gain in the transmission distance at the FEC threshold of  $2.7 \times 10^{-2}$ , as can be confirmed in Figure 5.16b.

The results illustrated by Figures 5.16a and 5.16b also show that the W-VSNE[0] and W-VSNE[1] are comparable to the W-SSFM in terms of performance. While the W-VSNE[0] shows a slight disadvantage, the W-VSNE[1] provides the lowest BER for all propagation distances considered in Figure 5.16a. The estimated maximum reach results presented in Figure 5.16b are obtained by repeating the analysis of Figure 5.16a for other optical input powers, ranging from -4 dBm up to 1 dBm, and by performing a cubic interpolation of the measured transmission distances into multiples of the span length (50 km). For the optimum input power of -2 dBm, the maximum reach enabled by CDE is 4700 km. Using intra-channel nonlinear compensation, this distance can be increased up to 5200 km with the W-VSNE[0], 5300 km with the W-SSFM, and 5450 km with the W-VSNE[1].

The previous analysis was extended for several DBP step-sizes ranging from 12.5 km

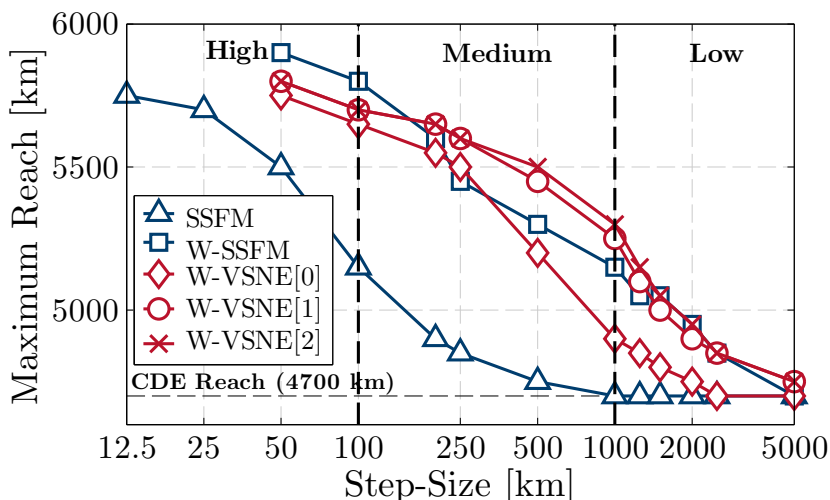


**Figure 5.17:** Estimated maximum reach as a function of the DBP step-size using the SSFM, W-SSFM and W-VSNE methods for the ULH 400G transmission system under test.

(4 steps per span) up to 5000 km (100 spans per step), with the aim to determine the best performance/complexity tradeoff for each nonlinear compensation method. The obtained results are shown in Figure 5.17, where we define three distinct regions of operation:

- i) a high complexity region, where the system reach can be increased by more than 1000 km, but requiring a large number of DBP steps are therefore high complexity ( $h \leq 100$  km);
- ii) a medium complexity region, where a significant reach gain (between 500 km and 1000 km) can be achieved even using DBP step-sizes of several spans per step ( $100 < h \leq 1000$  km);
- iii) a low complexity region, where the reach improvement is lower than 500 km, but DBP is applied with the lowest complexity using very large step-sizes ( $h > 1000$  km).

In accordance with the numerical simulations of section 5.3, the standard SSFM is shown not to be adequate for low complexity DBP, since its performance tends to quickly degrade for step-sizes larger than the span length. On the contrary, both the W-SSFM and the W-VSNE are able to tolerate much longer step-sizes without severely compromising the performance. In the high complexity region, the W-SSFM and W-VSNE are able to approximately reach the same performance as the SSFM with  $4\times$  fewer steps. In fact, the DBP-SSFM requires a minimum of 2 steps per span in order to achieve a reach improvement of  $> 1000$  km, whereas both the W-SSFM and W-VSNE can operate at 2 spans per step. This demonstrates the W-VSNE capability to work at high performance with much lower complexity than the standard SSFM. It is however worth of referring that the enhanced reach provided by the W-VSNE[1] over W-VSNE[0] in the high complexity region is of a mere 50 km, clearly not justifying the additional parallel filter. The W-VSNE gain over the DBP-SSFM is further increased within the medium complexity region, enabling an extended reach between 750 km and

950 km ( $\sim 15 - 20\%$ ) for  $200 \leq h \leq 500$ , corresponding to approximately 10-25 DBP steps in total. The benefit of the additional W-VSNE{1} filter begins to clearly pay off for step-sizes larger than 250 km. For a step-size of 1000 km (20 spans per step), the extended reach provided by the W-VSNE[1] over W-VSNE[0] is of 350 km, which may justify the added complexity of the W-VSNE{1} parallel filter. An additional 50 km of estimated reach are provided by the W-VSNE[2], demonstrating the previously reported performance saturation of the W-VSNE for  $K \geq 2$ . Still considering the step-size of 1000 km, the extended reach over CDE is of 600 km for the W-VSNE[2], 550 km for the W-VSNE[1] and 450 km for the W-SSFM, at the expense of only 6 DBP steps in total, thus demonstrating the feasibility of low-complexity but efficient DBP for ULH 400G transmission systems.

## 5.5 Summary

Following the frequency domain DBP techniques proposed in Chapters 3 and 4, in this chapter we have performed an inverse Fourier analysis of the simVSNE algorithm, yielding a closed-form formulation for time domain Volterra-based equalization of nonlinear fiber impairments in long-haul optical communication systems. Taking advantage of the time domain formulation, we have introduced a power weighting time window into the TD-VSNE, yielding the W-VSNE, which enables to significantly reduce the spatial resolution and filter dimension without significantly penalizing the performance. The equivalency between the frequency and time domain formulations has been proved through numerical simulation, which has also demonstrated the performance advantage of the W-VSNE over the previously proposed W-SSFM when both algorithms are applied with the same number of steps. Leveraged by these advantages and employing simple complexity reduction approximations, we were able to approximately halve the computational effort relatively to the W-SSFM, simultaneously enabling a latency reduction by  $\sim 70\%$ .

Besides the demonstrated complexity reduction, the W-VSNE algorithm shows other important advantages over the FD-VSNE in terms of implementation manageability:

- i) the simplifications made to the summation intervals in the W-VSNE enable an easier hardware implementation. Indeed, the calculation of the  $\tilde{\mathcal{P}}$  terms in the FD-VSNE is performed over  $J_K(n)$ , which is a non-contiguous,  $n$ -dependent and  $K$ -dependent interval. On the contrary, all W-VSNE{ $K$ } filters operate over contiguous  $J'_0(n)$  intervals, which can be implemented as simple moving averages;
- ii) the introduction of the power weighting time window in the W-VSNE has significantly reduced the number of required parallel filters to achieve the same performance as the FD-VSNE. The obtained results show that the W-VSNE performance tends to saturate for  $K > 1$ , whereas significantly larger  $K$  is required for the FD-VSNE algorithm. This W-VSNE property also simplifies the hardware implementation, given the lower number of optimization parameters.

The experimental validation carried out in this chapter has clearly demonstrated the applicability of the proposed W-VSNE algorithm for low-complexity DBP, providing

---

sizeable maximum reach improvement for ULH transmission systems. Note that all the discussed experimental results have been obtained by intra-carrier nonlinear compensation in a  $5 \times 400\text{G}$  WDM transmission system with high spectral efficiency (5.33 b/s/Hz). Despite of the uncompensated inter-channel nonlinearities, we demonstrate that intra-channel nonlinear compensation resorting to advanced DBP algorithms can provide significant benefits in terms of reach, even when applied with low spatial resolution. The potential benefit of inter-channel nonlinear compensation remains an open research topic, which we will address in detail in Chapter 6.

## References

- [1] Y. Gao, F. Zhang, L. Dou, Z. Chen, and A. Xu, “Intra-channel nonlinearities mitigation in pseudo-linear coherent QPSK transmission systems via nonlinear electrical equalizer,” *Optics Communications*, vol. 282, no. 12, pp. 2421 – 2425, 2009.
- [2] J. Pan and C.-H. Cheng, “Nonlinear electrical compensation for the coherent optical OFDM system,” *J. Lightw. Technol.*, vol. 29, no. 2, pp. 215 –221, Jan 2011.
- [3] Z. Pan, B. Chatelain, M. Chagnon, and D. V. Plant, “Volterra filtering for nonlinearity impairment mitigation in DP-16QAM and DP-QPSK fiber optic communication systems,” in *Proc. Optical Fiber Communication Conf. and Exposition (OFC)*, paper JThA40, 2011.
- [4] F. P. Guiomar, S. B. Amado, C. S. Martins, and A. N. Pinto, “Time domain Volterra-based digital backpropagation for coherent optical systems,” *J. Lightw. Technol.*, vol. 15, no. 33, pp. 3170–3181, Aug. 2015.
- [5] D. Rafique, M. Mussolin, M. Forzati, J. Mårtensson, M. N. Chughtai, and A. D. Ellis, “Compensation of intra-channel nonlinear fibre impairments using simplified digital back-propagation algorithm,” *Opt. Express*, vol. 19, no. 10, pp. 9453–9460, May 2011.
- [6] F. P. Guiomar, S. B. Amado, C. S. Martins, and A. N. Pinto, “Parallel split-step method for digital backpropagation,” in *Proc. Optical Fiber Communication Conf. and Exposition (OFC)*, paper Th2A.28, 2015.
- [7] S. B. Amado, F. P. Guiomar, N. J. Muga, J. D. Reis, S. M. Rossi, A. Chiuchiarelli, J. R. F. Oliveira, A. L. Teixeira, and A. N. Pinto, “Experimental demonstration of the parallel split-step method in ultra-long-haul 400G transmission,” in *Proc. 41st European Conf. Optical Communication (ECOC)*, paper Th.2.6.2, 2015.
- [8] F. P. Guiomar and A. N. Pinto, “Simplified Volterra series nonlinear equalizer for polarization-multiplexed coherent optical systems,” *J. Lightw. Technol.*, vol. 31, no. 23, pp. 3879–3891, 2013.

## References

---

- [9] B. Spinnler, “Equalizer design and complexity for digital coherent receivers,” *IEEE J. Sel. Topics Quantum Electron.*, vol. 16, no. 5, pp. 1180–1192, 2010.
- [10] F. P. Guiomar, S. B. Amado, A. Carena, G. Bosco, A. Nespola, A. L. Teixeira, and A. N. Pinto, “Fully-blind linear and nonlinear equalization for 100G PM-64QAM optical systems,” *J. Lightw. Technol.*, vol. 33, no. 7, pp. 1265–1274, 2015.



## Chapter 6

# Nonlinear Equalization of 400G Superchannels

In the previous chapters, the application of DBP has been restricted to intra-channel nonlinear compensation. Indeed, due to the electronic limitations in the receiver in terms of available electrical bandwidth and sampling rate, the vast majority of recent experimental works only consider the use of DBP on an intra-channel basis [1–6]. However, being only capable of partially compensating for the impact of SPM, the maximum performance of intra-channel DBP is strongly limited, with typical reported reach enhancement of  $< 30\%$ , when applied to WDM transmission systems [4–6]. Although multi-carrier (MC) DBP techniques have been proposed and numerically assessed in several pioneering works [7–13], the added complexity required for practical implementation has proven to be a major difficulty, preventing MC-DBP to unleash its full performance until very recently. The first experimental demonstrations of MC-DBP considered relatively low symbol-rates [14] or the use of synchronized sampling oscilloscopes [15]. However, the use of MC-DBP was still regarded as being unpractical in real optical networks, mostly due to the dynamic add and drop of optical channels, which would create a time-varying uncertainty on the data-dependent inter-channel nonlinear impairments. The recent introduction of the concept of optical superchannels [16], which are composed of several subcarriers that are routed through the network as a single entity, has created a new opportunity for the application of MC-DBP. Following this opportunity, several recent experimental works have demonstrated the benefit of MC-DBP on the performance and reach of 400G and terabit superchannels [17–20]. These works make use of state-of-the-art wideband receivers and high sampling rate oscilloscopes to coherently detect the entire superchannel and employ DBP over the total received field, as if it were a single channel. Although this total-field (TF) DBP strategy apparently provides a straightforward implementation, all reported experimental works so far invariably require tens of DBP steps per span and very high sampling rate [17–20], resulting in unpractical DSP complexity [19].

In this chapter, we experimentally assess the performance and complexity of MC-DBP for nonlinear compensation of 400G superchannels based on PM-16QAM and PM-64QAM modulation, considering dual- and triple-carrier superchannel configurations [21]. The

performance and complexity of TF-DBP is compared to that of a coupled equations (CE) DBP approach, demonstrating that CE-DBP is an attractive solution for metro and ultra-long-haul 400G transmission, delivering high equalization performance associated with a lower complexity and enhanced robustness to electrical bandwidth limitations. The organization of this chapter is as follows. The theoretical formulation of MC-DBP based on the CE and TF approaches is addressed in section 6.1, along with the numerical adaptation of the DBP-SSFM technique. Section 6.2 describes the laboratorial setup for 400G superchannel transmission, detailing the considered superchannel configurations and required DSP subsystems. The performance of 400G superchannels composed of PM-16QAM subcarriers for ultra-long-haul propagation is assessed in section 6.3, whereas the metro propagation performance based on PM-64QAM modulation is analyzed in section 6.4. Finally, the main conclusions are summarized in section 6.5.

## 6.1 Multi-Carrier Digital Backpropagation

### 6.1.1 Coupled NLSE for WDM optical signals

Let us start by rewriting the inverse Manakov equation of (3.3) governing backpropagation in polarization-multiplexed optical systems,

$$\frac{\partial A_{x/y}}{\partial(-z)} = \frac{\alpha}{2} A_{x/y} + i \frac{\beta_2}{2} \frac{\partial^2 A_{x/y}}{\partial t^2} - i \xi \frac{8}{9} \gamma \left( |A_x|^2 + |A_y|^2 \right) A_{x/y}, \quad (6.1)$$

where  $A_{x/y}$  represents the optical field envelope of the propagating signal in the  $x/y$  polarization states. So far, we have considered that the backpropagated optical field is only composed of a single channel. Nevertheless, equation (6.1) equally holds for the case of an optical signal composed of  $N_{\text{ch}}$  independent channels, such that

$$A_{x/y} = \sum_{m=-\frac{N_{\text{ch}}-1}{2}}^{\frac{N_{\text{ch}}-1}{2}} A_{x/y}^{(m)} \exp(-im\Delta\omega t), \quad (6.2)$$

where  $A_{x/y}^{(m)}$  represents the optical field envelope corresponding to carrier index  $m$  and  $\Delta\omega$  is the inter-channel spacing in rad/s, as depicted in Fig. 6.1. Considering an odd number of carriers, the central channel is represented by  $A_{x/y}^{(0)}$ . Also note that, in the adopted formalism, the carrier index for an even number of backpropagated channels is a non-integer number, as evidenced in Fig. 6.1a.

The comb of  $N_{\text{ch}}$  WDM channels can be backpropagated using the inverse Manakov equation of (6.1), provided that enough spatial and temporal resolution are applied in its numerical implementation. This approach, commonly designated as total-field (TF) DBP, enables to ideally remove all deterministic fiber impairments, including intra-channel (SPM) and inter-channel (XPM and FWM) nonlinearities [13]. Since it uses the inverse Manakov equation as the underlying analytical model, TF-DBP can be numerically applied resorting to the same DBP algorithms addressed in the previous chapters. However, the practical application of TF-DBP poses a set of critical challenges in terms of hardware and DSP complexity:

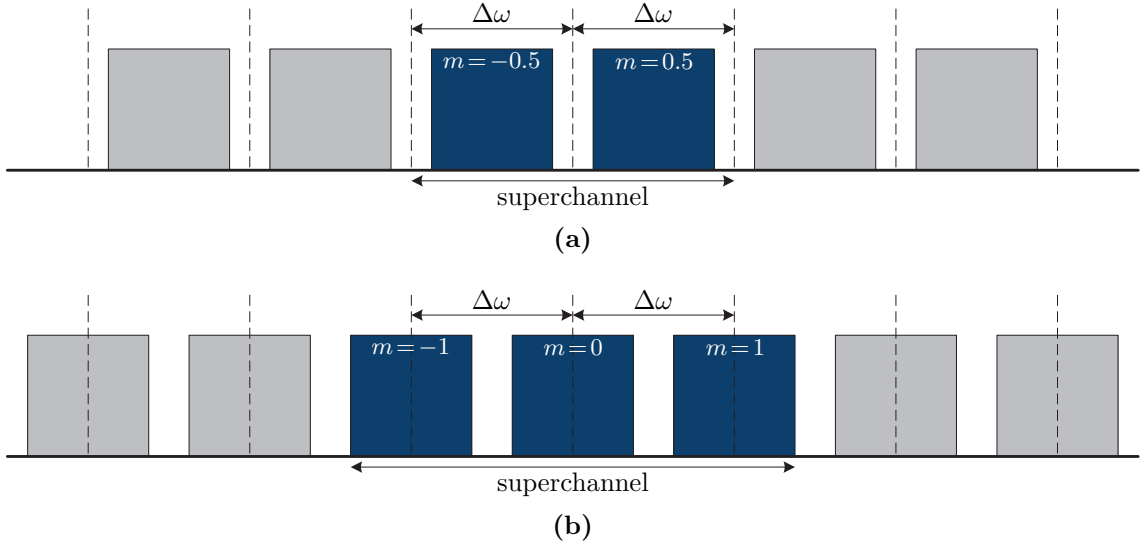


**Figure 6.1:** Schematic illustration of a WDM spectrum, in which DBP is applied over a a) dual- and b) triple-carrier superchannel. Each backpropagated subcarrier is identified by an index  $m$  and the inter-subcarrier spacing is denoted by  $\Delta\omega$ .

- i) high sampling rate requirements, in order to digitally represent the entire WDM spectrum and to avoid aliasing of newly generated FWM components [9, 12];
- ii) short step-size requirements, in order capture the interaction between chromatic dispersion and nonlinear distortions generated at high frequencies;
- iii) the relative phase between all WDM channels must be preserved, in order to allow for FWM compensation. This requires either to use a set of phase-locked LOs [9], which may be unfeasible in practice, or the detection of all backpropagated WDM channels in the same coherent receiver [17–20], which poses critical requirements in terms of electrical bandwidth and sampling rate.

Alternatively, the inverse Manakov equation describing TF-DBP can be split into a set of  $N_{\text{ch}}$  coupled equations. Considering that the signal fed to DBP is composed of  $N_{\text{ch}}$  evenly spaced channels (or subcarriers of a superchannel, as illustrated in Fig. 6.1), and neglecting the inter-channel coherent terms (FWM) and the coherent polarization mixing terms, the following system of coupled equations can be obtained [13],

$$\frac{\partial A_{x/y}^{(m)}}{\partial(-z)} = \frac{\alpha}{2} A_{x/y}^{(m)} + m\beta_2\Delta\omega \frac{\partial A_{x/y}^{(m)}}{\partial t} + i\frac{\beta_2}{2} \frac{\partial^2 A_{x/y}^{(m)}}{\partial t^2} - i\frac{8}{9}\gamma \left( C_{\text{SPM}}^{(m)} + C_{\text{XPM},x/y}^{(m,q)} \right) A_{x/y}^{(m)}, \quad (6.3)$$

where the  $C_{\text{SPM}}^{(m)}$  and  $C_{\text{XPM},x/y}^{(m,q)}$  terms are responsible for the SPM and XPM effects on the  $m$ -th subcarrier, and are respectively given by

$$C_{\text{SPM}}^{(m)} = \xi_{\text{SPM}}^{(m)} \left( |A_x^{(m)}|^2 + |A_y^{(m)}|^2 \right), \quad (6.4)$$

and

$$C_{\text{XPM},x/y}^{(m,q)} = \sum_{\forall q \neq m} \xi_{\text{XPM}}^{(m,q)} \left( 2|A_{x/y}^{(q)}|^2 + |A_{y/x}^{(q)}|^2 \right), \quad (6.5)$$

where  $\xi_{\text{SPM}}^{(m)}$  and  $\xi_{\text{XPM}}^{(m,q)}$  are free parameters that allow for an independent optimization of the SPM and XPM compensation for each subcarrier. Besides the XPM term, equation (6.3) also includes a new  $m\beta_2\Delta\omega\frac{\partial A_{x/y}^{(m)}}{\partial t}$  term, which accounts for the temporal walk-off between subcarriers whose central frequency is separated by  $m\Delta\omega$ . Isolating the walk-off term in equation (6.3) one obtains,

$$\frac{\partial A_{x/y}^{(m)}(t, z)}{\partial z} = -m\beta_2\Delta\omega\frac{\partial A_{x/y}^{(m)}(t, z)}{\partial t}, \quad (6.6)$$

where, for clarity, we have reintroduced the  $(t, z)$  dependence of the optical field envelope. Applying a Fourier transform, the following frequency domain differential equation is obtained,

$$\frac{\partial \tilde{A}_{x/y}^{(m)}(\omega, z)}{\partial z} = -i\omega m\beta_2\Delta\omega\tilde{A}_{x/y}^{(m)}(\omega, z), \quad (6.7)$$

which can be easily solved, yielding a closed-form frequency domain transfer function,

$$\tilde{A}_{x/y}^{(m)}(\omega, z+h) = \exp(-i\omega m\beta_2\Delta\omega h)\tilde{A}_{x/y}^{(m)}(\omega, z). \quad (6.8)$$

Finally, applying an inverse Fourier transform, the following time domain relationship is obtained,

$$A_{x/y}^{(m)}(t, z+h) = A_{x/y}^{(m)}(t - m\beta_2\Delta\omega h, z), \quad (6.9)$$

clearly exposing the temporal delay between the superchannel subcarriers caused by the walk-off effect, which is proportional to the inter-subcarrier frequency separation,  $\Delta\omega$  and to the propagated distance,  $h$ .

Being based on a set of  $N_{\text{ch}}$  coupled equations (CE), the backpropagation approach of equation (6.3) is typically designated as CE-DBP. Since it neglects all phase-sensitive inter-channel effects, the CE-DBP does not require phase coherency between the received subcarriers [9]. Instead, the application of CE-DBP can be based on a set of time-synchronized receivers without any phase coherence requirements [15].

### 6.1.2 Adaptation of the DBP-SSFM

As previously discussed, the numerical implementation of the TF-DBP technique can be straightforwardly generalized from the single-channel case, by simply adjusting the temporal and spatial resolution in order to fit the requirements of the entire WDM spectrum to be backpropagated. In contrast, due to the introduction of XPM coupled terms, the numerical implementation of the CE-DBP technique requires to properly adapt the single-channel DBP algorithms discussed in the previous chapters. In the framework of this chapter, we will address the extension of the asymmetric DBP-SSFM algorithm for the numerical implementation of the CE-DBP technique.

Considering a frequency domain implementation, the linear step of the CE-DBP-SSFM algorithm can be written as,

$$\begin{aligned} \hat{\mathcal{D}}_{\text{SSFM}}^{\text{CE}}\left(A_{x/y}^{(m)}(t, z)\right) &= \mathcal{F}^{-1}\left\{\exp\left(-h\hat{\mathcal{D}}(\omega)\right)\exp\left(-h\hat{\mathcal{W}}^{(m)}(\omega)\right)\mathcal{F}\left\{A_{x/y}^{(m)}(t, z)\right\}\right\} \\ &= \mathcal{F}^{-1}\left\{\exp\left(\frac{\alpha}{2}h - i\omega m\beta_2\Delta\omega h - i\frac{\beta_2}{2}\omega^2 h\right)\mathcal{F}\left\{A_{x/y}^{(m)}(t, z)\right\}\right\}, \quad (6.10) \end{aligned}$$

where  $\hat{\mathcal{D}}(\omega)$  accounts for effect of chromatic dispersion and attenuation, as given by expression (2.40), rewritten here for clarity,

$$\hat{\mathcal{D}}(\omega) = -\frac{\alpha}{2} + i\frac{\beta_2}{2}\omega^2, \quad (6.11)$$

and  $\hat{\mathcal{W}}^{(m)}(\omega)$  accounts for the walk-off experienced by the  $m$ -th subcarrier relatively to the central subcarrier ( $m = 0$ ) of the backpropagated superchannel,

$$\hat{\mathcal{W}}^{(m)}(\omega) = i\omega m\beta_2\Delta\omega. \quad (6.12)$$

Note that the  $\hat{\mathcal{W}}^{(m)}$  operator vanishes for  $m = 0$ , corresponding to the central subcarrier, which sets the reference group velocity of the backpropagated signal. Although the frequency domain implementation of the walk-off operator may be advantageous, since expressions (6.11) and (6.12) can be easily merged to originate a single linear transfer function, an alternative time domain implementation can also be considered, applying the time delay correspondence of expression (6.9). In both cases however, one must bear in mind that the application of non-integer delay to discrete time signals requires a prior interpolation stage. In order to avoid the additional complexity of  $2(N_{\text{ch}} - 1)$  interpolation operations (for an odd number of channels) in each DBP step, a walk-off parameter,  $W_{\text{off}}$ , can be defined as an integer number of delayed samples,

$$W_{\text{off}}^{(m)} = \left\lfloor \frac{m\beta_2\Delta\omega h}{T} \right\rfloor, \quad (6.13)$$

where  $T$  is the sampling period and  $\lfloor \cdot \rfloor$  represents the nearest integer operator. The walk-off operator for discrete time processing is then redefined as,

$$\hat{\mathcal{W}}^{(m)}(\omega_n) = iW_{\text{off}}^{(m)}\frac{\omega T}{h}, \quad (6.14)$$

which now introduces an integer delay in frequency domain. However, the rounding operation in (6.13) introduces a fixed approximation error on the walk-off compensation that accumulates with each SSFM step. In order to avoid this error accumulation, which may prevent a correct application of CE-DBP, the procedure described by Algorithm 1 can be applied, where a periodic correction for the integer walk-off approximation,  $W_c$ , prevents the time delay error to be larger than the sampling period.

In turn, the nonlinear step,  $\hat{\mathcal{N}}_{\text{SSFM}}^{\text{CE}}$ , can be efficiently implemented in time domain as,

$$\begin{aligned} \hat{\mathcal{N}}_{\text{SSFM}}^{\text{CE}}\left(A_{x/y}^{(m)}(t, z)\right) = \exp\left(-h_{\text{eff, DBP}}\left[\hat{\mathcal{N}}_{\text{SPM}}^{(m)}\left(A_{x/y}^{(m)}(t, z)\right)\right.\right. \\ \left.\left.+ \hat{\mathcal{N}}_{\text{XPM}}^{(m,q)}\left(A_{x/y}^{(q)}(t, z)\right)\right]\right)A_{x/y}^{(m)}(t, z), \end{aligned} \quad (6.15)$$

where  $\hat{\mathcal{N}}_{\text{SPM}}^{(m)}$  accounts for the SPM distortion on subcarrier  $m$ , and is given by

$$\hat{\mathcal{N}}_{\text{SPM}}^{(m)}\left(A_{x/y}^{(m)}(t, z)\right) = i\frac{8}{9}\gamma\xi_{\text{SPM}}^{(m)}\left(|A_x^{(m)}(t, z)|^2 + |A_y^{(m)}(t, z)|^2\right), \quad (6.16)$$

**Algorithm 1** Correction for the integer approximation of non-integer walk-off experienced by the  $m$ -th subcarrier.

---

```

 $W_c = 0$ 
for  $n = 1 : N_{\text{steps/span}} N_s$  do
     $W_{\text{off}}^{(m)} = \lfloor \frac{m\beta_2\Delta\omega h}{T} \rfloor$ 
     $W_c \leftarrow W_c + (\frac{m\beta_2\Delta\omega h}{T} - W_{\text{off}}^{(m)})$ 
    if  $|W_c| > 1$  then
         $W_{\text{off}}^{(m)} \leftarrow W_{\text{off}}^{(m)} + \lfloor W_c \rfloor$ 
         $W_c \leftarrow W_c - \lfloor W_c \rfloor$ 
    end if
     $A(t, L - nh) = \mathcal{F}^{-1} \left\{ \mathcal{F} \{ A(t, L - (n-1)h) \} \exp \left( -iW_{\text{off}}^{(m)} T \omega \right) \right\}$ 
end for
    
```

---

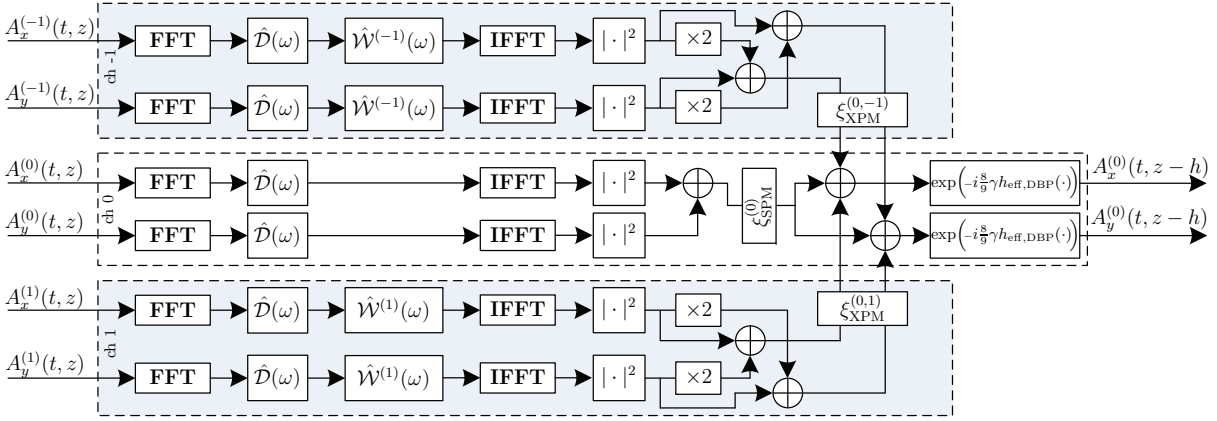


**Figure 6.2:** Numerical implementation of a single step of the asymmetric dual-polarization CE-DBP-SSFM, considering a backpropagated signal composed of 3 channels. For simplicity, only the compensation of the central channel is fully illustrated.

and  $\hat{\mathcal{N}}_{\text{XPM}}^{(m,q)}$  accounts for the XPM distortion incurred by the remaining backpropagated subcarriers on the  $m$ -th channel,

$$\hat{\mathcal{N}}_{\text{XPM}}^{(m,q)} \left( A_{x/y}^{(q)}(t, z) \right) = i \frac{8}{9} \gamma \sum_{\forall q \neq m} \xi_{\text{XPM}}^{(m,q)} \left( 2 |A_{x/y}^{(q)}(t, z)|^2 + |A_{y/x}^{(q)}(t, z)|^2 \right). \quad (6.17)$$

The numerical implementation of a single step of the CE-DBP-SSFM algorithm is schematically represented in Figure 6.2, considering the backpropagation of three subcarriers (or equivalently, three independent WDM channels, provided that they propagate together in the fiber link). Note that the implementation complexity remains very similar to that of an intra-channel compensation of each subcarrier. Regarding the linear step, the  $\hat{\mathcal{D}}$  and  $\hat{\mathcal{W}}^{(m)}$  operators can be easily integrated into a single transfer function, maintaining the computational effort of intra-channel compensation. In turn, the nonlinear step does not imply the computation of any additional  $|\cdot|^2$  or  $\exp(\cdot)$  terms. Instead, it only requires simple  $2 \times (\cdot)$  operations to calculate the XPM coupling terms

## 6.2. Laboratorial Setup

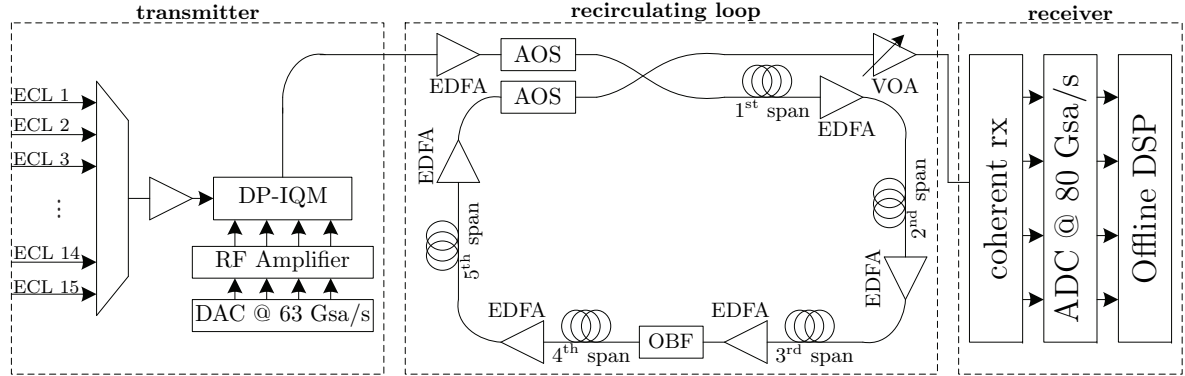


**Figure 6.3:** Laboratorial setup for the experimental assessment of 400G superchannel transmission in metro and ultra-long-haul transmission systems.

that can be easily implemented using bit shifts. The only marginal added complexity lies on the optimization of the  $\xi_{\text{XPM}}^{(m,q)}$  free parameters, which in a real-time implementation can be updated using a decision-feedback strategy [22]. With a similar complexity per step, the comparison of computational effort generated by the intra-channel DBP-SSFM and the inter-channel CE-DBP-SSFM can be assessed by the number of steps required by each algorithm to achieve a given target performance. The same observation applies to the TF-DBP, where the possibility of applying a single DBP-SSFM chain for the entire backpropagated signal comes at the expense of an increased sampling rate. The complexity/performance trade-off and other implementation issues will be thoroughly assessed in the following sections, resorting to experimental data obtained for various 400G superchannel configurations.

## 6.2 Laboratorial Setup

A simplified schematic representation of the implemented laboratorial setup is depicted in Figure 6.3. At the transmitter-side, up to 15 ECLs with 100 kHz linewidth are utilized to modulate the individual subcarriers of the WDM comb centered at 1550 nm. Prior to modulation the optical carriers are then passed through an optical booster in order to maximize the SNR of the transmitted signal. The digital I and Q components for both signal polarizations are independently and randomly generated in a 4-channel DAC prototype manufactured by Fujitsu, operating at 63 Gsample/s with 8-bits of resolution and  $\sim 14$  GHz electrical bandwidth. The digital bit stream is mapped into the corresponding QAM symbols, upsampled to match the DAC sampling rate and filtered by a raised-cosine filter with a roll-off factor of 0.1. Digital pre-emphasis of high frequencies is carried out by a 1<sup>st</sup>-order Gaussian filter, partially compensating for the bandwidth limitations in the DAC. The DAC electrical outputs are sent to a linear quad-driver radio frequency (RF) amplifier (maximum input voltage of 200 mV; maximum output voltage of 5 V) with  $\sim 35$  GHz of electrical bandwidth and finally fed to the DP-IQM to modulate the optical carriers. The resulting 400G superchannels are sent to an optical recirculating loop, composed of 5 spans of ULL fiber (Corning Vascade<sup>®</sup> EX2000) with

50 km each. Optical amplification is solely performed by EDFAs with  $\sim 6$  dB noise figure. A configurable optical bandpass filter (OBF) (Finisar's WaveShaper 4000S) is placed within the recirculating loop to attenuate the out-of-band ASE noise. Before the receiver, an optical pre-amplifier and a VOA are utilized to adjust the optical power arriving at the photodiodes. The wideband digital coherent super-receiver with 40 GHz of electrical bandwidth is responsible for the detection of all subcarriers composing the superchannel. The electrical I and Q components in both polarization tributaries are then digitized by a 80 Gsample/s real-time sampling oscilloscope with 34 GHz of analogue bandwidth. The main parameters of the laboratorial setup are summarized in Table 6.1.

### 6.2.1 Superchannel configurations

Figure 6.4 shows the considered superchannel configurations for 400G transmission based on dual- and triple-carrier PM-16QAM and PM-64QAM modulation. For simplicity, an exact Nyquist bandwidth is assumed for each subcarrier, although in practice a roll-off factor of 0.1 has been adopted. The PM-16QAM 400G superchannel configurations depicted in Figures 6.4a and 6.4b fit a gross data-rate of 504 Gb/s in a 75 GHz slot. The gross data-rate of 504 Gb/s enables to allocate a 20% FEC overhead, leading to a pre-FEC BER threshold of  $2.7 \times 10^{-2}$  for soft-decision decoding. For the WDM scenario, five independent 400G superchannels are transmitted in a 75 GHz WDM grid, compliant with the latest ITU-T G.694.1 recommendation for a flexible frequency grid with 12.5 GHz granularity and yielding a net spectral efficiency of 5.33 b/s/Hz. This represents a  $\sim 33\%$  spectral efficiency improvement relatively to other dual-wavelength 400G PM-16QAM approaches resorting to the allocation of two individual 50 GHz slots for each subcarrier [23]. Alternatively to this PM-16QAM 400G solution, which is a strong candidate for long-haul and ULH transmission, Figure 6.4c shows a triple-carrier PM-64QAM 400G superchannel, fitting the same gross data-rate of 504 Gb/s in a 50 GHz frequency slot, yielding an enhanced SE of 8 b/s/Hz. This PM-64QAM is especially designed for high-SE transmission in metro networks, with propagation distances of up to 1000 km.

**Table 6.1:** Main set of parameters associated with the laboratorial setup of Figure 6.3.  $\Delta\nu$  - laser linewidth;  $f_s$  - sampling rate;  $P_{\max}$  - maximum output power of the ECLs; BW - electrical bandwidth;  $\alpha_{\text{roll-off}}$  - roll-off factor of the raised-cosine filter;  $A_{\text{eff}}$  - effective area of the fiber core;  $F_n$  - noise figure of the EDFAs.

Transmitter		Recirculating Loop		Receiver	
ECL	$\Delta\nu = 100$ kHz	Fiber	$\alpha = 0.16$ dB/km	LO	$\Delta\nu = 100$ kHz
	$P_{\max} = 16$ dBm		$\beta_2 = -3.29$ ps <sup>2</sup> /km	Photodiodes	BW = 40 GHz
DAC	$f_s = 63$ Gsample/s	EDFA	$\gamma = 2.01$ W <sup>-1</sup> km <sup>-1</sup>	Oscilloscope	$f_s = 80$ Gsample/s
	BW = 14 GHz		$A_{\text{eff}} = 112$ $\mu\text{m}^2$		BW = 34 GHz
	$\alpha_{\text{roll-off}} = 0.1$		$F_n = 6$ dB		

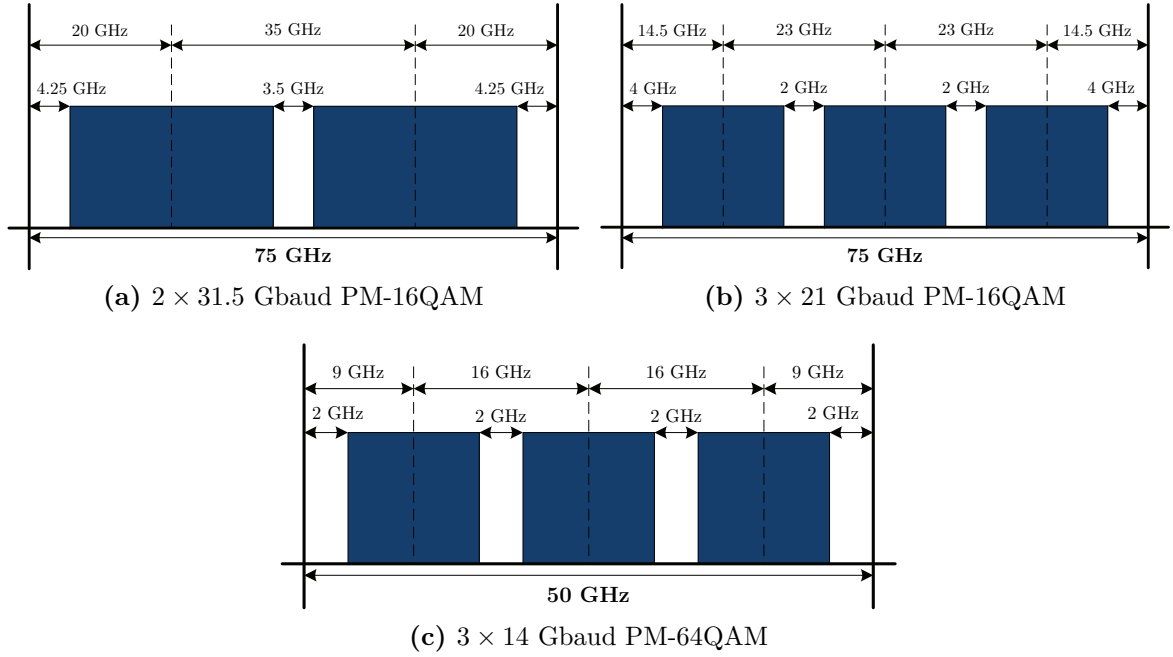


**Figure 6.4:** 400G superchannel configurations for metro and ULH transmission based on a) dual-carrier PM-16QAM, b) triple-carrier PM-16QAM and c) triple-carrier PM-64QAM.

### 6.2.2 DSP subsystems

After coherent detection, all DSP subsystems are implemented offline in MATLAB, as depicted in Figure 6.5. In order to correct for the optical frontend imperfections, the first DSP subsystems include deskew and orthonormalization functions, enabling to roughly compensate for the time and amplitude mismatch between the digitized I and Q signal components. An additional post-emphasis filter is applied to partially compensate for the electrical bandwidth limitations of the coherent receiver. This subsystem will be of critical importance for the application of total-field DBP, correcting the profile of the received spectrum to be digitally backpropagated. Depending on the configuration of the static equalization block (total-field or coupled equations DBP), the remaining sequence of DSP subsystems needs to be slightly adjusted. In the case of TF-DBP, the static equalization block is preceded by a digital resampling stage, which sets the sampling rate utilized for backpropagation. Thereafter, the individual superchannel subcarriers are separated by means of band-pass filtering and downconverted to baseband. A second digital resampling stage is then applied to adjust the sampling rate to a fixed number of 2 samples per symbol. In turn, when the static equalization block includes only CD compensation or CE-DBP, each superchannel subcarrier is firstly downconverted to baseband and directly resampled to 2 samples per symbol. The dynamic equalization block, which is responsible for the compensation of polarization-dependent effects, is based on complex  $2 \times 2$  FIR filter with 31 taps, driven by a multi-radii CMA feedback error function adjusted for PM-16QAM or PM-64QAM modulation, depending on the superchannel configuration. After downsampling to 1 sample per symbol, digital carrier recovery includes a 4<sup>th</sup>-

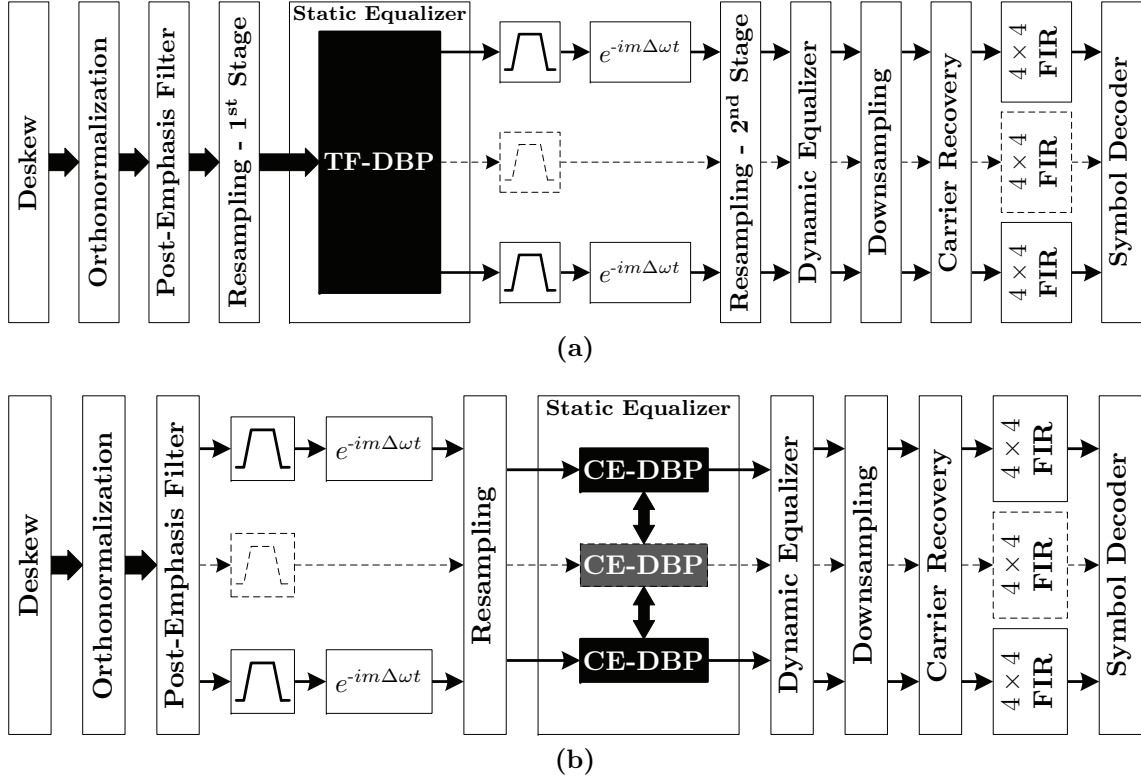


**Figure 6.5:** Sequence of post-detection DSP subsystems for offline processing of 400G superchannels including a) total-field DBP and b) coupled-equations DBP. The dashed arrows and blocks represent the processing of the central subcarrier, only for superchannels composed of an odd number of subcarriers.

order spectral-based frequency estimation [24] and modified Viterbi & Viterbi phase estimation [25]. For the case of PM-64QAM modulation, a second phase recovery stage is applied, using a 40-taps DD maximum likelihood phase estimation algorithm [26], similarly to what has been done in the experimental validation section of Chapter 4. A 25-taps decision-directed  $4 \times 4$  equalizer with separate treatment of real and imaginary signal components is then applied at the symbol-rate to fine tune the linear adaptive equalization, also allowing for residual compensation of IQ skew [27]. Finally, after symbol decoding the BER is individually counted over  $2^{19}$  bits for each subcarrier. The superchannel performance is assessed by the average BER in all subcarriers.

### 6.2.3 Back-to-back characterization

Figure 6.6 illustrates the back-to-back (B2B) characterization for the  $2 \times 31.5$  Gbaud,  $3 \times 21$  Gbaud and  $3 \times 14$  Gbaud superchannel configurations, considering both single-channel and WDM transmission. The SNR (in dB) is calculated from the measured OSNR as,

$$\text{SNR} = \text{OSNR} - 10 \log_{10} \left( \frac{R_s}{\Delta f} \right), \quad (6.18)$$

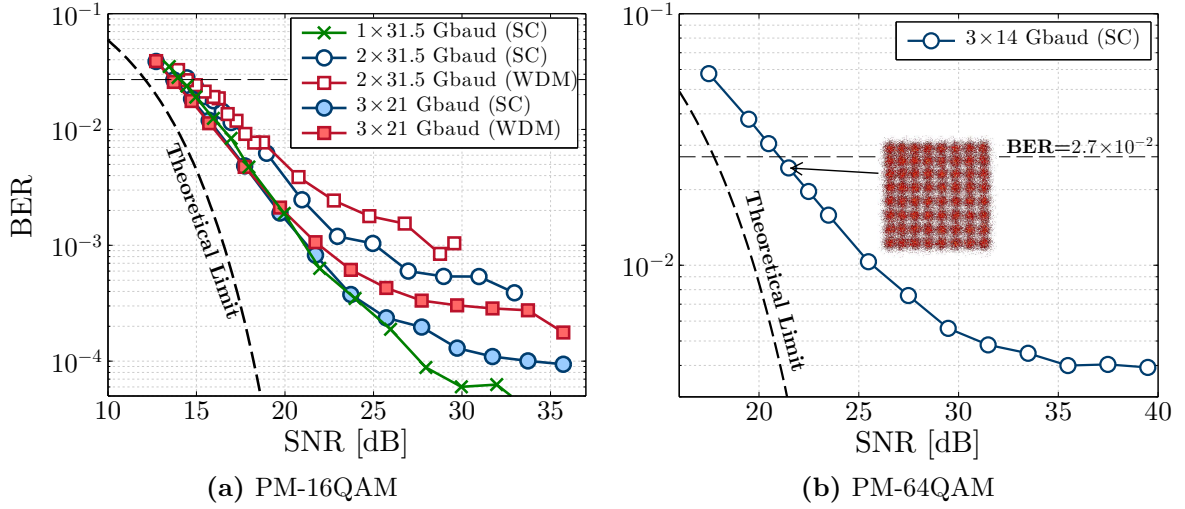


**Figure 6.6:** Back-to-back characterization of single-channel and WDM transmission of 400G superchannels based on a) PM-16QAM and b) PM-64QAM modulation.

where  $R_s$  is the symbol-rate and  $\Delta f$  is the OSNR measurement bandwidth (0.1 nm).

Let us start by analyzing the B2B characterization of the  $2 \times 31.5$  Gbaud 400G superchannel, presented in Figure 6.6a. In order to assess the impact of the receiver limitations in terms of bandwidth and effective number of bits (ENOB) on the B2B performance, a single 31.5 Gbaud wavelength has also been tested. It can be observed that the dual-carrier configurations show a significant BER penalty in the high SNR region. This penalty is caused by three main limiting aspects:

- i) the analog bandwidth of the receiver, which affects more seriously the dual-carrier configurations, since they occupy higher frequencies;
- ii) the degradation of ENOB in the higher frequencies, which reduces the accuracy of the digitization process for the dual-carrier configurations;
- iii) the linear inter-subcarrier crosstalk.

An additional penalty is obtained between the WDM and single-channel configurations, which is mainly caused by the linear crosstalk between transmitted superchannels. Nevertheless, despite of these penalties on the high SNR region, the B2B performance near the established FEC limit of  $2.7 \times 10^{-2}$  is very similar for all the considered scenarios, indicating that the impact of the aforementioned limitations on the maximum signal reach is expected to be only marginal<sup>1</sup>. Indeed, the estimated SNR penalty at the FEC limit is of  $\sim 2$  dB for the single-carrier configuration and  $\sim 2.3$  dB for the dual-carrier configurations, relatively to the theoretical required SNR of  $\sim 12.1$  dB.

A direct comparison between the B2B performance of the  $2 \times 31.5$  Gbaud and  $3 \times 21$  Gbaud configurations reveals that the BER floor in the high SNR region tends to

<sup>1</sup>Note however, that other propagation phenomena, mostly due to Kerr nonlinearity, are expected to play a key role. This aspect will be thoroughly discussed further ahead.

improve by reducing the symbol rate. This is mostly caused by electrical bandwidth limitations on the DAC that generates each subcarrier independently. Indeed, the 14 GHz DAC bandwidth imposes a strong limitation on the achievable symbol-rate, which cannot be fully compensated by the pre-emphasis filter. Due to the improved DAC performance, the SNR penalty at the FEC limit is also reduced to approximately 1.6 dB, thus yielding a practical SNR margin of  $\sim 0.7$  dB over the  $2 \times 31.5$  Gbaud configuration (required SNRs of  $\sim 14.4$  dB and  $\sim 13.7$  for the  $2 \times 31.5$  Gbaud and  $3 \times 21$  Gbaud configurations, respectively). Note that this SNR margin tends to increase for lower BER thresholds. As an example, for an hypothetical BER limit of  $3.8 \times 10^{-3}$ , the SNR penalty of the dual-carrier over the triple-carrier configuration is increased to approximately 2.5 dB. This improved B2B performance and increased OSNR margin will play an important role on the maximum signal reach in ultra-long-haul fiber links, as it will be thoroughly discussed in the following sections.

Finally, the B2B performance of the triple-carrier PM-64QAM solution is presented in Figure 6.6b, for which we have obtained an OSNR penalty of  $\sim 3.3$  dB. Although this penalty is larger than that obtained for the PM-16QAM superchannels, it is well within the state-of-the-art of PM-64QAM transmission, which is more severely affected by critical implementation bottlenecks such as limited ENOB of the DAC and ADCs, degraded electrical amplification due to the higher peak-to-average power ratio and the non-ideal response of the optical modulator.

## 6.3 Ultra-Long-Haul Propagation Performance

The use of PM-16QAM modulation has been shown to enable ultra-long-haul transmission with a spectral efficiency of  $>5$  b/s/Hz [28, 29]. In the following subsections, we experimentally assess the maximum propagation reach of the dual- and triple-carrier 400G superchannels configurations proposed in Figure 6.4. The main focus is given to the performance comparison of MC-DBP for both scenarios.

### 6.3.1 Performance and complexity of multi-carrier DBP

The spatial resolution optimization of MC-DBP in terms of the required number of steps per span,  $N_{\text{steps}/\text{span}}$ , is presented in Figure 6.7 for the two considered ultra-long-haul 400G solutions. The performance of MC-DBP is assessed for a fixed propagation distance of 6000 km and for the optimum input power through the  $Q^2$  improvement obtained over CDE, defined as

$$Q_{\text{gain}}^2[\text{dB}] = 20 \log_{10} \left( \frac{\text{erfc}^{-1}(2 \times \text{BER}_{\text{DBP}})}{\text{erfc}^{-1}(2 \times \text{BER}_{\text{CDE}})} \right), \quad (6.19)$$

where  $\text{BER}_{\text{DBP}}$  and  $\text{BER}_{\text{CDE}}$  are the bit error rates obtained with DBP and CDE equalization, respectively, and  $\text{erfc}^{-1}(\cdot)$  represents the inverse complementary error function. The numerical implementation of all DBP techniques is based on the W-SSFM algorithm. Three different DBP implementations are considered:

### 6.3. Ultra-Long-Haul Propagation Performance

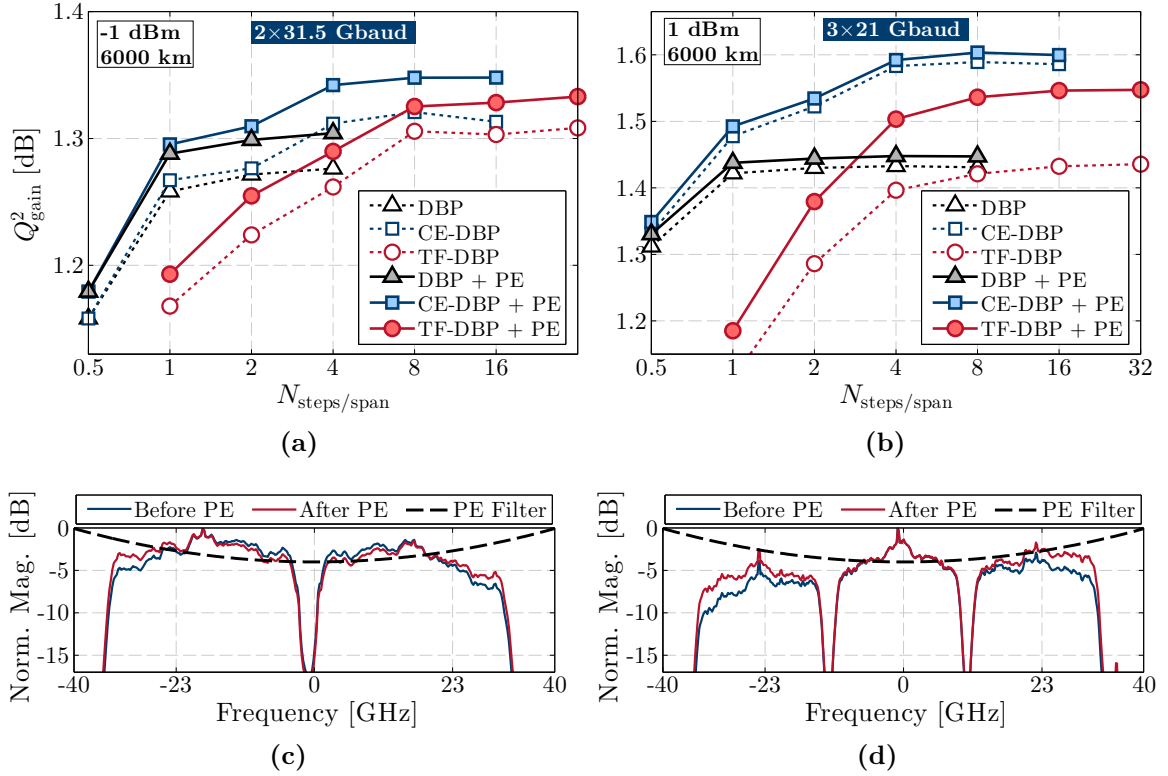


**Figure 6.7:** Performance and spatial resolution requirements of MC-DBP for ultra-long-haul 400G transmission based on a) dual-carrier and b) triple-carrier PM-16QAM modulation. The electrical spectrum and the profile of the post-emphasis (PE) filter applied before DBP is shown in c) and d), for the dual- and triple-carrier configurations, respectively.

- i) independent intra-subcarrier DBP (henceforth simply denoted as DBP, for simplicity) performed over each 400G subcarrier;
- ii) joint backpropagation of all 400G subcarriers as a single entity, using TF-DBP;
- iii) coupled digital backpropagation using CE-DBP, after band-pass filtering and downconverting each subcarrier to baseband.

In addition, a post-emphasis (PE) filter is also optionally applied prior to DBP in order to counteract the attenuation of high frequencies caused by the electrical bandwidth limitations on the receiver ( $\sim 35$  GHz), as depicted in Figures 6.7c and 6.7d. The PE filter has a Gaussian profile (order 1) and cutoff frequency of 35 GHz.

For both the dual- and triple-carrier 400G solutions, the performance of intra-subcarrier DBP is shown to approximately saturate with 1 step per span. In contrast, nonlinear compensation based on TF-DBP is shown to require approximately 8 steps per span in order to converge to its optimum performance. This result is in agreement with other recent works employing TF-DBP, which report the need for tens of steps per span [17–20]. The obtained results also show that the application of TF-DBP with  $N_{\text{steps/span}} < 4$  actually leads to worse performance than simple intra-subcarrier

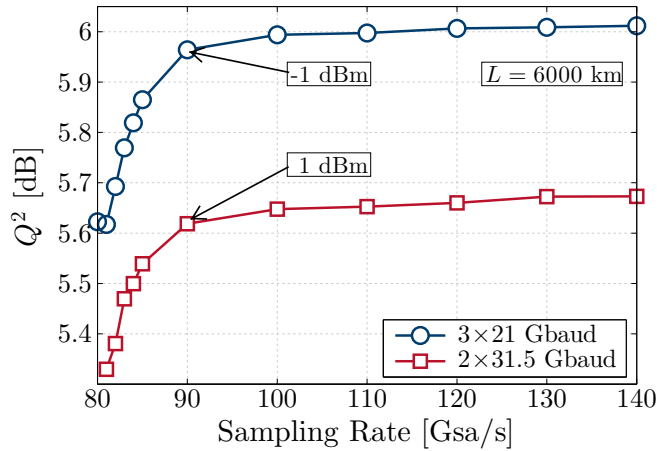


**Figure 6.8:** Sampling rate requirements of TF-DBP for the dual- and triple-carrier 400G configurations. The backpropagated signal corresponds to a transmission distance of 6000 km at the optimum input power.

DBP. The need for such high spatial resolution is tightly intertwined with the broader backpropagated spectrum which requires finer temporal resolution (higher sampling rate). In fact, it has been shown that, in order to avoid aliasing caused by the out-of-band FWM components generated in each SSFM-based TF-DBP step, a substantial oversampling ratio is required [8, 9]. Figure 6.8 exposes the dependence of TF-DBP performance on the sampling rate of the backpropagated digital signal. The obtained results for both 400G configurations show that a minimum sampling rate of 100 Gsa/s is required for TF-DBP to deliver its maximum performance. Note that, in the experimental realization, the sampling rate of the oscilloscope is limited to 80 Gsa/s. The test of higher sampling rates illustrated in Figure 6.8 makes use of a digital resampling stage, as previously discussed and depicted in Figure 6.5a. Therefore, although partially avoiding the aliasing generation of DBP-SSFM, this oversampling stage also introduces some interpolation noise that may affect the performance of TF-DBP.

The results of Figure 6.7 also show the key role played by the PE filter to unleash the performance of TF-DBP, especially for the triple-carrier scenario. Note that the attenuation of high frequency components at the receiver end generates an inaccurate representation of the temporal signal profile that is fed to DBP. Consequently, each nonlinear step incurs an error on the applied nonlinear phase-shift, which depends on the temporal power profile, thus degrading the performance of DBP. By partially correcting for the low-pass filtering imposed by the receiver, the PE filter allows to reduce the error between the true received optical signal and its digital baseband representation, thereby enhancing the accuracy of DBP. As depicted in Figure 6.7d, the impact of the PE filter is more pronounced for the outer subcarriers in the triple-carrier 400G configuration, causing a strong impact on the performance of TF-DBP. Indeed, without the aid of the PE filter, the maximum TF-DBP performance is only approximately matched with that of intra-subcarrier DBP.

As an alternative MC-DBP approach, Figure 6.7 also shows the performance of

CE-DBP, for both the dual- and triple-carrier configurations. Since CE-DBP only accounts for SPM and XPM compensation, a small performance loss would be expectable relatively to TF-DBP, which also applies FWM compensation. Counterintuitively, a slight performance improvement was obtained with CE-DBP, which can be attributed to the following main factors:

- i) the impact of FWM is known to be relatively weak for dispersion unmanaged ultra-long-haul propagation at high symbol-rates [30]. In addition, the FWM compensation performed by the TF-DBP in the considered scenarios is quite limited, due to the low number of backpropagated subcarriers [19]. The penalty incurred by avoiding FWM compensation, is then expected to be small;
- ii) although reducing the aliasing generation between multiple steps, the digital upsampling stage before TF-DBP also introduces noise into the time domain signal, contributing as a source of backpropagated added noise. To avoid this issue, a higher sampling rate on the ADCs should be considered, similarly to the work of [19], where a received signal occupying approximately 73 GHz is digitized by 160 GSa/s ADCs. This however comes at the expense of more costly and complex hardware;
- iii) as clearly shown in Figure 6.7b, the reduced impact of the PE filter on CE-DBP reveals its higher robustness against receiver bandwidth limitations. This can be understood by noting that, prior to CE-DBP, each subcarrier is downconverted to baseband and individually normalized to the estimated input optical power, thus partially eliminating the power unbalance between subcarriers. Consequently, part of the observed TF-DBP penalty over CE-DBP can be attributed to the non-ideal match between the utilized PE filter profile and the low-pass profile of the receiver.

Besides the improved performance under practical conditions, CE-DBP also shows another important advantage: since the inter-subcarrier coupling terms can be individually optimized through the  $\xi_{\text{XPM}}$  factors, its minimum performance is set by intra-subcarrier DBP. This allows to relax the spatial resolution requirements without incurring an abrupt performance loss, as experienced by TF-DBP. As a consequence, the complexity reduction achieved by CE-DBP is associated both with lower sampling rate requirements and larger tolerated step-sizes. Finally, the results of Figure 6.7 already allow to preliminarily conclude that MC-DBP yields higher performance for the triple-carrier 400G configuration, as in general MC-DBP is expected to become more effective with an increasing number of backpropagated subcarriers. This result will be confirmed by the nonlinear system performance analyzed in the following section.

#### 6.3.2 Maximum signal reach

After optimizing intra- and inter-subcarrier DBP, the system performance was extensively analyzed for a wide set of input optical powers<sup>2</sup> and a propagation distance

---

<sup>2</sup>Here we define the input optical power as the launched power per superchannel.

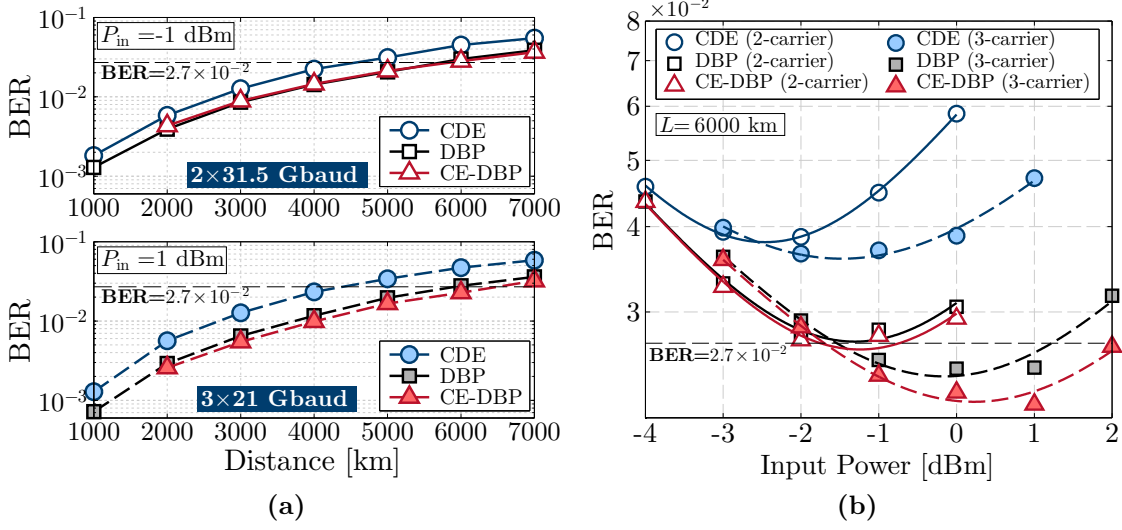


**Figure 6.9:** Ultra-long-haul 400G propagation performance as a function of the transmission distance and input power per superchannel, considering the optimum input power and a propagation length of 6000 km. a) BER versus distance at the optimum input power; b) BER versus input power after propagation over 6000 km.

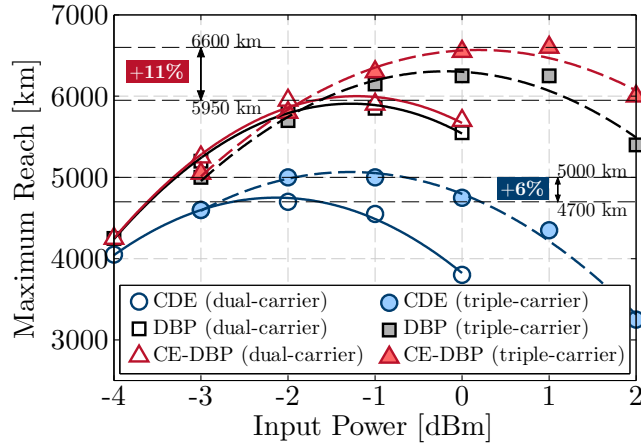


**Figure 6.10:** Estimated maximum signal reach of 400G transmission based on dual- and triple-carrier PM-16QAM modulation, after linear and nonlinear compensation.

ranging from 250 km (1 recirculation) up to 7000 km (28 recirculations). Intra-subcarrier DBP is applied with 1 step per span, whereas inter-subcarrier nonlinear compensation is applied by the CE-DBP with 4 steps per span. The obtained performance in terms of BER versus distance (at the optimum power) and BER versus input power (for a fixed distance of 6000 km) is summarized in Figure 6.9.

From the obtained measurements, the optimum power per superchannel for the triple-carrier configuration is estimated to be approximately 0.5-1 dB higher than that of the dual-carrier 400G superchannel. This increased optimum power for 400G transmission at lower baud-rate is in good agreement with other recent results exploiting the impact

of baud-rate on dispersion unmanaged ultra-long-haul transmission [31, 32]. Noteworthy, after nonlinear compensation with CE-DBP, the optimum power gap between the two 400G solutions is increased to  $\sim 2$  dB, reflecting the higher DBP performance provided by the triple-carrier configuration. In contrast with the case of dual-carrier 400G, where inter-subcarrier DBP provides only a marginal benefit, an additional nonlinear tolerance of 0.5-1 dB is provided by CE-DBP for the triple-carrier 400G, after propagation over 6000 km. This allows to conclude that the use of inter-subcarrier nonlinear compensation in standard dual-carrier 400G superchannels may be of negligible benefit. In contrast, decreasing the baud-rate and increasing the number of subcarriers creates stronger inter-subcarrier nonlinear distortions, enhancing the role of inter-subcarrier DBP.

The previous analysis has been repeated for all captured propagation distances and input powers, giving rise to Figure 6.10, which shows the estimated maximum reach of dual- and triple-carrier 400G, obtained by interpolating the processed results of BER versus distance into multiples of the span length (50 km). Considering only CD compensation, the estimated maximum signal reach is of 4700 km and 5000 km for the dual and triple-carrier 400G superchannels, respectively. This corresponds to an increased reach of  $\sim 6\%$  for the triple-carrier configuration, which is in good agreement with other previously reported theoretical predictions [33], as well numerical and experimental results [31, 32]. The same ratio is roughly preserved after intra-subcarrier DBP, with an estimated maximum reach of 5850 km and 6250 km for the dual- and triple-carrier 400G, respectively. Notably, the reach improvement obtained with the triple-carrier 400G superchannel is increased to  $\sim 11\%$  after CE-DBP, corroborating the well-known enhanced performance of MC-DBP with increasing number of backpropagated subcarriers [8, 9, 19]. The overall extended reach over CDE is of 1250 km ( $\sim 26\%$ ) and 1600 km (32%) for the dual- and triple-carrier 400G superchannels, respectively.

## 6.4 Metro Propagation Performance

With the aim to extend the previous ultra-long-haul analysis to shorter reach transmission systems with higher SE, in this section we experimentally assess the performance of a 400G solution based on triple-carrier PM-64QAM modulation, configured according to Figure 6.4c. This solution delivers a net SE of 8 b/s/Hz at the expense of a higher constellation cardinality, reducing the maximum signal reach. It can be therefore an interesting option for high-capacity optical metro networks with transmission distance up to 1000 km. For simplicity, in this work we restrict the analysis of this solution to a single-superchannel scenario composed of three subcarriers, thus providing an upper bound for the performance of digital nonlinear compensation in such systems. In fact, the main aim of this extended analysis is to study the potential benefit of inter-subcarrier DBP for higher SE and shorter transmission distances.

### 6.4.1 Triple-carrier PM-64QAM

The optimization of the MC-DBP spatial resolution for the triple-carrier PM-64QAM 400G superchannel is shown in Figure 6.11, for a fixed input power per superchannel of

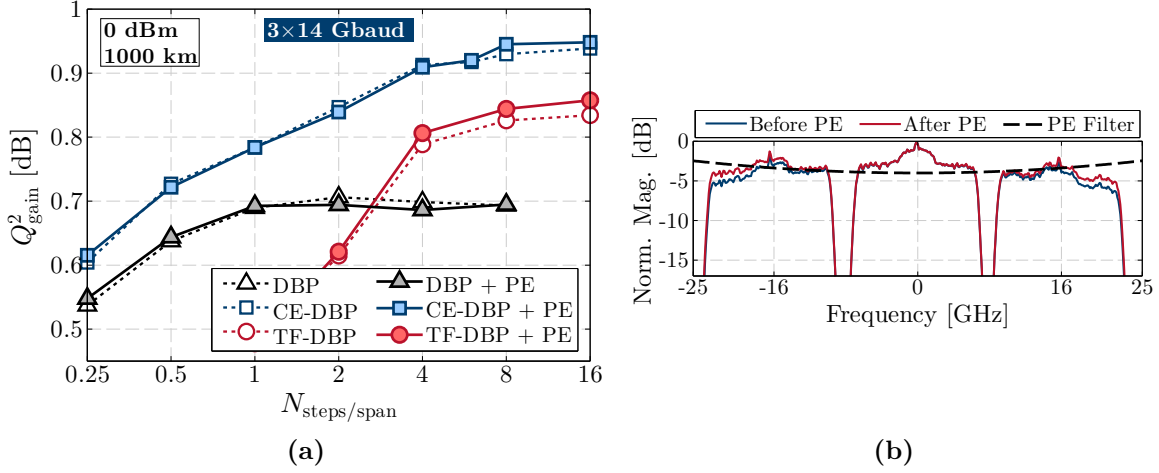


**Figure 6.11:** Performance and spatial resolution requirements of MC-DBP for metro 400G transmission based on triple-carrier PM-64QAM modulation, considering an input power of 0 dBm and a propagation length of 1000 km. The electrical spectrum and the profile of the PE filter applied before DBP is shown in b).

0 dBm and after propagation over 1000 km. Similarly to the previously discussed PM-16QAM results, the CE-DBP is shown to deliver the highest  $Q^2$  gain over CDE, with intra-subcarrier DBP setting the minimum achievable CE-DBP performance. On the contrary, TF-DBP requires at least 4 steps per span in order to surpass the performance of intra-subcarrier DBP. The optimum DBP step-sizes are found to be similar to those of ultra-long-haul transmission. Note that the impact of the PE filter on triple-carrier 400G is now much smaller, as can be seen by comparing the gaps between the TF-DBP curves in Figures 6.11a and 6.7b. Due to its higher SE, the PM-64QAM superchannel occupies a smaller frequency range, thus being more robust to the electrical bandwidth limitation of the utilized receiver. This effect is clearly visible by comparing the spectra of Figures 6.11b and 6.7d.

After DBP optimization, the performance of the PM-64QAM superchannel has been analyzed for a wide range of input powers (per superchannel) and a propagation distance ranging from 250 km to 2000 km (in steps of 250 km, or 1 recirculation). The obtained results are summarized in Figure 6.12, considering the performance dependence on the propagation distance for a fixed input power (0 dBm) and on the input power for a fixed propagation distance (1500 km).

The performance advantage provided by XPM compensation through the CE-DBP algorithm is clearly visible both in terms of achievable transmission reach below the FEC threshold (see Figure 6.12a) and enhanced nonlinear tolerance (see Figure 6.12b). It can be concluded that the maximum signal reach with CE-DBP is over 1750 km for an optimum input power of 0 dBm per superchannel<sup>3</sup>.

Finally, repeating the previously described procedure to obtain the results of Figure 6.10, the estimated maximum signal reach of the triple-carrier PM-64QAM 400G

<sup>3</sup>It is worth reemphasizing here that these results correspond to a single superchannel experiment.

#### 6.4. Metro Propagation Performance

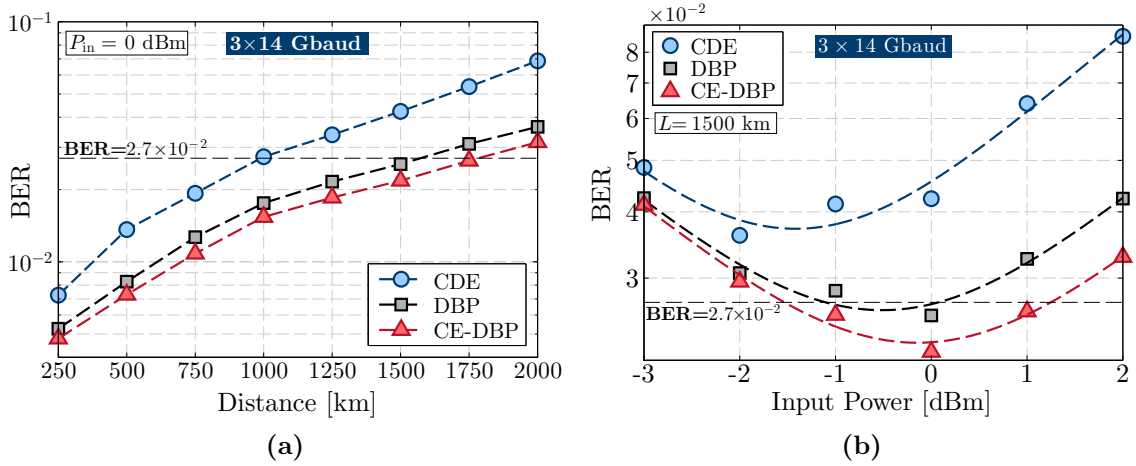


**Figure 6.12:** Metro 400G propagation performance as a function of the transmission distance and input power per superchannel. a) BER versus distance at the optimum input power; b) BER versus input power after propagation over 1500 km.

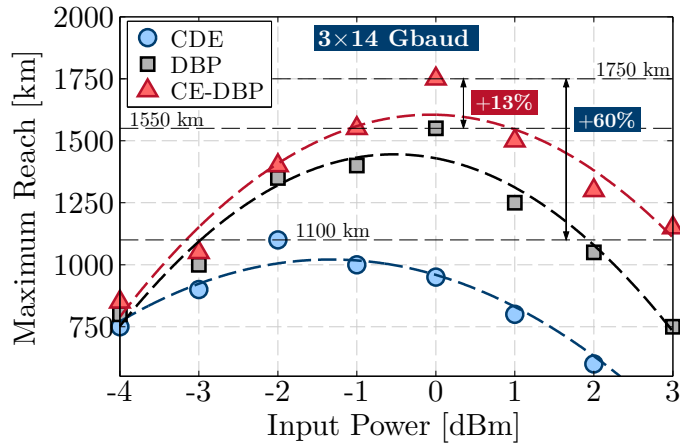


**Figure 6.13:** Estimated maximum signal reach of 400G transmission based on triple-carrier PM-64QAM modulation, after linear and nonlinear compensation.

superchannel is presented in Figure 6.13. The maximum signal reach of 1750 km after CE-DBP is confirmed, representing approximately a 60% reach improvement relatively to the linearly equalized signal (1100 km). In addition, the improvement over the estimated intra-subcarrier DBP reach (1550 km) is of approximately 13%. These results confirm that MC-DBP may play an important role to extend the maximum signal reach of high-SE optical signals, whose OSNR requirements are very strict, being therefore strongly impacted by nonlinear distortions.

## 6.5 Summary

In this chapter, we have experimentally analyzed the issue of inter-channel nonlinear equalization within the context of 400G superchannels for ultra-long-haul and metro transmission systems. In order to tackle the high complexity of TF-DBP, we have experimentally demonstrated the CE-DBP approach for dual- and triple-carrier superchannel configurations. Due to the electronic limitations in terms of analog bandwidth and sampling rate, the CE-DBP approach was shown to deliver the highest performance, simultaneously enabling to reduce the processing rate and requiring fewer DBP steps than the widely used TF-DBP. Through the introduction of simple coupling terms between the intra-subcarrier DBP equalizers, CE-DBP is shown to provide significant gains in terms of signal reach at the expense of marginal added complexity.

Building from the widely proposed dual-carrier 400G superchannel based on PM-16QAM modulation, and motivated by the recently published analytical results that demonstrate the benefit of symbol-rate optimization [33], we have tested an alternative triple-carrier 400G solution for ultra-long-haul transmission and verified a  $\sim 6\%$  extended reach relatively to its dual-carrier counterpart. Notably, this benefit is increased to approximately 11% after nonlinear compensation of both 400G solutions using CE-DBP, which reflects the enhanced MC-DBP performance with increasing number of backpropagated subcarriers. Note that these results were obtained in a WDM configuration composed of 5 independent superchannels placed in contiguous 75 GHz slots, thus demonstrating that intra- and inter-subcarrier DBP can provide significant benefits in realistic propagation scenarios with strong inter-channel interference. These results also support the idea that an evolution towards subcarrier multiplexing can be beneficial for ultra-long-haul transmission, both in terms of signal propagation and multi-carrier nonlinear equalization performance.

In order to extend the study to shorter-reach and high SE optical links, we have also tested the performance of a triple-carrier PM-64QAM 400G superchannel placed in a single 50 GHz frequency slot. Using CE-DBP, we demonstrate a reach improvement of  $\sim 60\%$  over conventional CD equalization, proving that intra- and inter-subcarrier nonlinear equalization can be a crucial enabling technology for high-SE optical metro networks.

## References

- [1] D. S. Millar, S. Makovejs, C. Behrens, S. Hellerbrand, R. I. Killey, P. Bayvel, and S. J. Savory, "Mitigation of fiber nonlinearity using a digital coherent receiver," *IEEE J. Sel. Topics Quantum Electron.*, vol. 16, no. 5, pp. 1217–1226, 2010.
- [2] Y. Gao, J. C. Cartledge, J. D. Downie, J. E. Hurley, D. Pikula, and S. S.-H. Yam, "Nonlinearity compensation of 224 Gb/s dual-polarization 16-QAM transmission over 2700 km," *IEEE Photon. Technol. Lett.*, vol. 25, no. 1, pp. 14–17, 2013.
- [3] F. P. Guiomar, J. D. Reis, A. Carena, G. Bosco, A. L. Teixeira, and A. N. Pinto, "Experimental demonstration of a frequency-domain Volterra series nonlinear

- equalizer in polarization-multiplexed transmission,” *Opt. Express*, vol. 21, no. 1, pp. 276–288, 2013.
- [4] S. J. Savory, G. Gavioli, E. Torrenco, and P. Poggiolini, “Impact of interchannel nonlinearities on a split-step intrachannel nonlinear equalizer,” *IEEE Photon. Technol. Lett.*, vol. 22, no. 10, pp. 673–675, 2010.
- [5] D. Lavery, C. Behrens, S. Makovejs, D. Millar, R. Killey, S. Savory, and P. Bayvel, “Long-haul transmission of PS-QPSK at 100 Gb/s using digital backpropagation,” *IEEE Photon. Technol. Lett.*, vol. 24, no. 3, pp. 176–178, feb.1, 2012.
- [6] F. P. Guiomar, S. B. Amado, A. Carena, G. Bosco, A. Nespola, A. L. Teixeira, and A. N. Pinto, “Fully-blind linear and nonlinear equalization for 100G PM-64QAM optical systems,” *J. Lightw. Technol.*, vol. 33, no. 7, pp. 1265–1274, 2015.
- [7] X. Li, X. Chen, G. Goldfarb, E. Mateo, I. Kim, F. Yaman, and G. Li, “Electronic post-compensation of WDM transmission impairments using coherent detection and digital signal processing,” *Opt. Express*, vol. 16, no. 2, pp. 880–888, Jan 2008.
- [8] E. Mateo, L. Zhu, and G. Li, “Impact of XPM and FWM on the digital implementation of impairment compensation for WDM transmission using backward propagation,” *Opt. Express*, vol. 16, no. 20, pp. 16 124–16 137, Sep 2008.
- [9] E. F. Mateo and G. Li, “Compensation of interchannel nonlinearities using enhanced coupled equations for digital backward propagation,” *Appl. Opt.*, vol. 48, no. 25, pp. F6–F10, Sep 2009.
- [10] F. Yaman and G. Li, “Nonlinear impairment compensation for polarization-division multiplexed WDM transmission using digital backward propagation,” *IEEE Photonics Journal*, vol. 1, no. 2, pp. 144–152, 2009.
- [11] E. F. Mateo, F. Yaman, and G. Li, “Efficient compensation of inter-channel nonlinear effects via digital backward propagation in WDM optical transmission,” *Opt. Express*, vol. 18, no. 14, pp. 15 144–15 154, Jul 2010.
- [12] E. F. Mateo, X. Zhou, and G. Li, “Improved digital backward propagation for the compensation of inter-channel nonlinear effects in polarization-multiplexed WDM systems,” *Opt. Express*, vol. 19, no. 2, pp. 570–583, Jan 2011.
- [13] ———, “Selective post-compensation of nonlinear impairments in polarization-division multiplexed WDM systems with different channel granularities,” *IEEE J. Quantum Electron.*, vol. 47, no. 1, pp. 109–116, 2011.
- [14] L. Zhu, F. Yaman, and G. Li, “Experimental demonstration of XPM compensation for WDM fibre transmission,” *Electron. Lett.*, vol. 46, no. 16, pp. 1140–1141, 2010.
- [15] E. Ip, Y.-K. Huang, E. Mateo, Y. Aono, Y. Yano, T. Tajima, and T. Wang, “Interchannel nonlinearity compensation for  $3\lambda\times 114$ -Gb/s DP-8QAM using three

- synchronized sampling scopes,” in *Proc. Optical Fiber Communication Conf. and Exposition (OFC)*, paper OM3A.6, March 2012.
- [16] G. Bosco, V. Curri, A. Carena, P. Poggiolini, and F. Forghieri, “On the performance of Nyquist-WDM Terabit superchannels based on PM-BPSK, PM-QPSK, PM-8QAM or PM-16QAM subcarriers,” *J. Lightw. Technol.*, vol. 29, no. 1, pp. 53–61, Jan 2011.
- [17] N. Fontaine, X. Liu, S. Chandrasekhar, R. Ryf, S. Randel, P. Winzer, R. Delbue, P. Pupalaiakis, and A. Sureka, “Fiber nonlinearity compensation by digital backpropagation of an entire 1.2-Tb/s superchannel using a full-field spectrally-sliced receiver,” in *Proc. 39th European Conference on Optical Communication (ECOC)*, paper Mo.3.D.5, Sept 2013.
- [18] R. Maher, L. Galdino, M. Sato, T. Xu, K. Shi, S. Kilmurray, S. Savory, B. Thomsen, R. Killey, and P. Bayvel, “Linear and nonlinear impairment mitigation in a Nyquist spaced DP-16QAM WDM transmission system with full-field DBP,” in *Proc. 40th European Conference on Optical Communication (ECOC)*, paper P.5.10, Sept 2014.
- [19] R. Maher, T. Xu, L. Galdino, M. Sato, A. Alvarado, K. Shi, S. J. Savory, B. C. Thomsen, R. I. Killey, and P. Bayvel, “Spectrally shaped DP-16QAM super-channel transmission with multi-channel digital back-propagation,” *Scientific Reports*, vol. 5, no. 8214, pp. 1 – 8, 2015.
- [20] R. Maher, D. Lavery, D. Millar, A. Alvarado, K. Parsons, R. Killey, and P. Bayvel, “Reach enhancement of 100% for a DP-64QAM super-channel using MC-DBP,” in *Proc. Optical Fiber Communication Conf. and Exposition (OFC)*. Optical Society of America, 2015, p. Th4D.5.
- [21] F. P. Guiomar, S. B. Amado, J. D. Reis, S. M. Rossi, A. Chiuchiarelli, J. R. F. Oliveira, A. L. Teixeira, and A. N. Pinto, “Ultra-long-haul 400G superchannel transmission with multi-carrier nonlinear equalization,” in *Proc. 41st European Conf. Optical Communication (ECOC)*, paper Th.2.2.4, 2015.
- [22] A. Napoli, M. Kuschnerov, C.-Y. Lin, B. Spinnler, M. Bohn, D. Rafique, V. A. Sleiffer, and B. Schmauss, “Adaptive digital back-propagation for optical communication systems,” in *Optical Fiber Communication Conference*. Optical Society of America, 2014, p. M3C.4.
- [23] B. Lavigne, O. Bertran-Pardo, C. Bresson, M. Lefrançois, E. Balmeffre, M. L. Monnier, L. Raddatz, and L. Suberini, “400Gb/s trials on commercial systems using real-time bit-rate-adaptive transponders for next generation networks,” in *Proc. Optical Fiber Communication Conf. and Exposition (OFC)*. Optical Society of America, 2015, p. W3E.1.
- [24] S. Hoffmann, S. Bhandare, T. Pfau, O. Adamczyk, C. Wordehoff, R. Peveling, M. Porrmann, and R. Noe, “Frequency and phase estimation for coherent QPSK

- transmission with unlocked DFB lasers,” *IEEE Photon. Technol. Lett.*, vol. 20, no. 18, pp. 1569–1571, 2008.
- [25] I. Fatadin, D. Ives, and S. Savory, “Blind equalization and carrier phase recovery in a 16-QAM optical coherent system,” *J. Lightw. Technol.*, vol. 27, no. 15, pp. 3042–3049, 2009.
- [26] X. Zhou, “An improved feed-forward carrier recovery algorithm for coherent receivers with M-QAM modulation format,” *IEEE Photon. Technol. Lett.*, vol. 22, no. 14, pp. 1051–1053, 2010.
- [27] M. Paskov, D. Lavery, and S. Savory, “Blind equalization of receiver in-phase/quadrature skew in the presence of Nyquist filtering,” *IEEE Photon. Technol. Lett.*, vol. 25, no. 24, pp. 2446–2449, 2013.
- [28] H. Zhang, J.-X. Cai, H. G. Batshon, M. Mazurczyk, O. Sinkin, D. Foursa, A. Pilipetskii, G. Mohs, and N. Bergano, “200 Gb/s and dual wavelength 400 Gb/s transmission over transpacific distance at 6 b/s/Hz spectral efficiency,” in *Proc. Optical Fiber Communication Conf. and Exposition (OFC)*, paper PDP5A.6, 2013.
- [29] T. Rahman, D. Rafique, A. Napoli, E. de Man, B. Spinnler, M. Bohn, C. Okonkwo, A. Koonen, and H. de Waardt, “Ultralong haul 1.28-Tb/s PM-16QAM WDM transmission employing hybrid amplification,” *J. Lightw. Technol.*, vol. 33, no. 9, pp. 1794–1804, May 2015.
- [30] A. Mecozzi and R. Essiambre, “Nonlinear Shannon limit in pseudolinear coherent systems,” *J. Lightw. Technol.*, vol. 30, no. 12, pp. 2011–2024, 2012.
- [31] A. Bononi, N. Rossi, and P. Serena, “Performance dependence on channel baud-rate of coherent single-carrier WDM systems,” in *Proc. 39th European Conf. Optical Communication (ECOC)*, paper Th.1.D.5, Sept 2013.
- [32] M. Qiu, Q. Zhuge, X. Xu, M. Chagnon, M. Morsy-Osman, and D. V. Plant, “Subcarrier multiplexing using DACs for fiber nonlinearity mitigation in coherent optical communication systems,” in *Proc. Optical Fiber Communication Conf. and Exposition (OFC)*, paper Tu3J.2, 2014.
- [33] P. Poggiolini, Y. Jiang, A. Carena, G. Bosco, and F. Forghierir, “Analytical results on system maximum reach increase through symbol rate optimization,” in *Proc. Optical Fiber Communication Conf. and Exposition (OFC)*, paper Th3D.6, 2015.



# Chapter 7

## Conclusions and Future Work

Potentiated by coherent detection and high-speed DSP technologies, digital equalization of nonlinear fiber impairments has been recently proposed as way of extending the linear propagation regime in installed optical fibers [1], thereby delaying the upcoming capacity crunch [2–4]. However, the high computational effort imposed by state-of-the-art nonlinear equalization techniques remains a major challenge for its practical deployment. With the primary goal of optimizing the complexity/performance tradeoff, novel equalization algorithms have been proposed in the framework of this thesis for the post-compensation of intra- and inter-channel nonlinear fiber impairments in metro, long-haul and ultra-long-haul optical transmission systems. All developed techniques have been extensively assessed through numerical simulations and validated by offline processing of experimental data. The new scientific contributions generated in the framework of this thesis, namely in terms of novel equalization techniques and obtained experimental results, can be an important step forward for the commercial deployment of post-detection nonlinear compensation technologies. In this final chapter, the most relevant conclusions are summarized and envisioned future research topics are discussed.

### 7.1 Conclusions

The first major contribution of this thesis is presented in Chapter 3, where an inverse VSTF is derived from the NLSE [5] and truncated to third-order, originating a matrix-based VSNE [6], which is numerically assessed for single-polarization transmission [7]. The VSNE is then extended to PM optical systems and experimentally demonstrated for 100G transmission systems based on PM-QPSK modulation [8, 9]. By these means, the VSNE is shown to enable high performance nonlinear equalization with relaxed requirements in terms of spatial and temporal resolution, in comparison with the benchmark DBP-SSFM technique.

Although enabling an highly parallel implementation, the  $N$ -by- $N$  matrix-based operations in the VSNE are shown to require  $O(N^2)$  complexity per processed sample, hindering its application for optical links with large accumulated dispersion. In order to tackle the complexity minimization problem, a comprehensive analysis of the third-order

VSNE kernel is carried out in Chapter 4, leading to the development of a symmetric kernel reconstruction technique, yielding the symVSNE algorithm [10]. Further complexity reduction is achieved by employing a frequency-flat approximation, giving rise to the simVSNE technique [11], whose complexity is shown to be independent of the Fourier transform block-size,  $N$ . The symVSNE and simVSNE algorithms are experimentally demonstrated in a 100G transmission system based on PM-64QAM modulation [12, 13], proving significant advantages over legacy DBP-SSFM compensation, both in terms of latency and number of real multiplications per sample. In addition, the symVSNE and simVSNE techniques benefit from an highly modular structure, easily enabling to control the performance/complexity tradeoff by simply adjusting the number of parallel filters to be considered for nonlinear compensation. This may be a crucial advantage for the real-time implementation of DBP, also enabling reduce the power consumption of the chip during periods of lower required performance.

Aiming to identify new potential sources of complexity minimization, an inverse Fourier analysis of the simVSNE technique is carried out in Chapter 5, leading to the development of the W-VSNE algorithm [14], whose nonlinear step is entirely formulated in time domain. On the contrary of the W-SSFM, the W-VSNE is based on a perturbative approach, enabling to partially apply the linear and nonlinear steps in parallel, thus reducing the overall processing latency. In addition, it shows the advantage of avoiding the use of exponential functions in the nonlinear step, thus resorting only to basic hardware operations [15]. The high performance and low-complexity of the W-VSNE technique is demonstrated through a comprehensive numerical and experimental assessment, providing significant gains over the widely used W-SSFM algorithm. The performance/complexity tradeoff is thoroughly analyzed for a dual-carrier 400G ultra-long-haul transmission system, revealing the possibility of obtaining an extended reach of more than 500 km by using less than 10 DBP steps in total. These results may put intra-channel DBP on the edge of being commercially deployed for the first time [16].

Finally, the issue of inter-channel nonlinear compensation is addressed in Chapter 6, within the context of 400G superchannel transmission for metro and ultra-long-haul. In order to tackle the enormous complexity associated with the recently reported TF-DBP approaches, an alternative CE-DBP has been experimentally assessed for dual- and triple-carrier 400G superchannels, which has revealed significant advantages in terms of required sampling rate, spatial resolution and robustness to electrical bandwidth limitations in the receiver [17]. In addition, the direct comparison between dual- and triple-carrier 400G solutions has confirmed the advantage associated with the baud-rate reduction that has been recently suggested by analytical [18], simulation [19] and experimental results [20]. Furthermore, inter-subcarrier nonlinear compensation was found to significantly boost this advantage, unveiling the enhanced DBP performance with increasing number of backpropagated subcarriers. These results confirm that the recently proposed baud-rate optimization [18] can provide substantial performance benefits both in terms of signal propagation and nonlinear post-compensation.

## 7.2 Future Work

In a research field strongly dominated by SSFM-based techniques, the novel Volterra-based equalizers proposed in this thesis have opened new possibilities and research directions to approach the issue of nonlinear impairment compensation in coherent optical fiber systems. Resulting from the efforts of this work, several research directions remain as open and challenging topics, from which we highlight the following:

- In the framework of this thesis, the issue of nonlinear equalization has been addressed exclusively from the receiver-side, employing post-detection digital equalizers. Nevertheless, several pre-compensation techniques have also been proposed, mostly employing SSFM-based DBP pre-distortion [21–23]. In fact, before the mass adoption of coherent detection, the first studied DBP-based techniques were based on pre-distortion [21, 22]. The application of the developed Volterra-based algorithms as pre-compensation techniques remains an open topic. Taking advantage of the recent progress on high-speed and high-resolution DACs, a comprehensive experimental analysis can be carried out exploiting the optimum balance between pre- and post-compensation DBP in terms of performance and complexity. Note that a partial pre-compensation of linear and nonlinear impairments may not only relax the step-size requirements of post-detection DBP, as it may also produce a strong influence efficiency of nonlinear impairments during signal propagation;
- In dispersion unmanaged fiber links, it has been demonstrated that nonlinear impairments tends to produce much more impact in the first few fiber spans after signal transmission, in which the signal is not yet completely *gaussianized* [24]. This property can be used to minimize the DBP-VSTF complexity by reducing the number of iFWM elements in the third-order Volterra kernel for the first few DBP steps, where iFWM efficiency is lower. As the DBP steps get closer to the transmitter, the number of iFWM terms should be increased to compensate for the enhanced iFWM efficiency. The same approach may also be used to control the number of parallel symVSNE/simVSNE filters.
- All nonlinear compensation algorithms proposed and assessed in the scope of this thesis assume a full knowledge of the propagation link, namely in terms of the fiber parameters ( $\alpha$ ,  $\beta_2$  and  $\gamma$ ) and the link length,  $L$ . However, with the current trend of migration into more dynamic optical networks, these parameters may be difficult to know *a priori*, or may even be time-varying. In fact, even for static point-to-point optical links, we may find deviations from the ideal fiber parameters, which should be taken into account in order to maximize the digital equalization performance. This problematic requires an adaptive equalization of nonlinear fiber impairments, capable of dealing with unknown, uncertain or time-varying fiber parameters. Although some pioneer works on adaptive nonlinear equalization can be found in the literature [25–28], these make use of very long data-aided training sequences to estimate the key parameters for nonlinear equalization, drastically increasing the implementation complexity and requiring large overheads. A potentially interesting

---

solution, yet to be explored, could be the use of a static nonlinear equalization stage, in which the majority of the estimated nonlinear impairments is blindly compensated, followed by an adaptive equalization stage capable of fine tuning the nonlinear equalizer performance. This is a similar approach to the one currently used for linear compensation, in which the estimated CD is statically equalized with low-complexity algorithms, whereas the dynamic polarization effects and residual uncompensated/overcompensated CD is removed by a subsequent adaptive equalization block (commonly resorting to CMA-based adaptation);

- The issue of multi-carrier nonlinear compensation has been addressed in Chapter 6, but only considering SSFM-based DBP. The extension of Volterra-based DBP for multi-carrier compensation thus remains an open research topic. It can be particularly interesting to investigate the properties of the simVSNE algorithm when applied in association with a coupled equations approach. As discussed in Chapter 6, the main disadvantage of CE-DBP over TF-DBP lies on the required number of FFT/IFFT pairs, which scales with the number of backpropagated channels. Since it is entirely applied in the frequency domain, the simVSNE avoids the replication of FFTs in each DBP step, and thus it can be a very advantageous technique for low-complexity CE-DBP. In addition, as shown in Figures 4.4 and 4.5 presented in Chapter 4, the error associated with the simVSNE frequency-flat approximation tends to decrease for lower symbol-rates, which opens the door for a successful application in subcarrier multiplexing systems, in which DBP must be applied over a large number of subcarriers.

## References

- [1] E. Ip, P. Ji, E. Mateo, Y.-K. Huang, L. Xu, D. Qian, N. Bai, and T. Wang, “100G and beyond transmission technologies for evolving optical networks and relevant physical-layer issues,” *Proc. IEEE*, vol. 100, no. 5, pp. 1065–1078, 2012.
- [2] P. P. Mitra and J. B. Stark, “Nonlinear limits to the information capacity of optical fibre communications,” *Letters to Nature*, vol. 411, pp. 1027–1030, 2001.
- [3] R. W. Tkach, “Scaling optical communications for the next decade and beyond,” *Bell Labs Technical Journal*, vol. 14, no. 4, pp. 3–9, 2010.
- [4] R. Essiambre and R. W. Tkach, “Capacity trends and limits of optical communication networks,” *Proc. IEEE*, vol. 100, no. 5, pp. 1035–1055, 2012.
- [5] F. P. Guiomar, J. D. Reis, A. L. Teixeira, and A. N. Pinto, “Digital postcompensation using Volterra series transfer function,” *IEEE Photonics Technology Letters*, vol. 23, no. 19, pp. 1412–1414, 2011.
- [6] —, “Mitigation of intra-channel nonlinearities using a frequency-domain Volterra series equalizer,” *Opt. Express*, vol. 20, no. 2, pp. 1360–1369, Jan 2012.

- [7] —, “Mitigation of intra-channel nonlinearities using a frequency-domain Volterra series equalizer,” in *Proc. 37th European Conf. Optical Communication (ECOC)*, paper Tu.6.B.1, 2011.
- [8] F. P. Guiomar, J. D. Reis, A. Carena, G. Bosco, A. L. Teixeira, and A. N. Pinto, “Experimental demonstration of a frequency-domain Volterra series nonlinear equalizer in polarization-multiplexed transmission,” in *Proc. 38th European Conf. Optical Communication (ECOC)*, paper Th.1.D.1, 2012.
- [9] —, “Experimental demonstration of a frequency-domain Volterra series nonlinear equalizer in polarization-multiplexed transmission,” *Opt. Express*, vol. 21, no. 1, pp. 276–288, 2013.
- [10] F. P. Guiomar and A. N. Pinto, “Simplified Volterra series nonlinear equalizer for polarization-multiplexed coherent optical systems,” *J. Lightw. Technol.*, vol. 31, no. 23, pp. 3879–3891, 2013.
- [11] F. P. Guiomar, S. B. Amado, N. J. Muga, J. D. Reis, A. L. Teixeira, and A. N. Pinto, “Simplified Volterra series nonlinear equalizer by intra-channel cross-phase modulation oriented pruning,” in *Proc. 39th European Conf. Optical Communication (ECOC)*, paper We.3.C.6, Sept 2013.
- [12] F. P. Guiomar, S. B. Amado, A. Carena, G. Bosco, A. Nespola, and A. N. Pinto, “Transmission of PM-64QAM over 1524 km of PSCF using fully-blind equalization and Volterra-based nonlinear mitigation,” in *Proc. 40th European Conf. Optical Communication (ECOC)*, paper We.3.3.3, 2014.
- [13] F. P. Guiomar, S. B. Amado, A. Carena, G. Bosco, A. Nespola, A. L. Teixeira, and A. N. Pinto, “Fully-blind linear and nonlinear equalization for 100G PM-64QAM optical systems,” *J. Lightw. Technol.*, vol. 33, no. 7, pp. 1265–1274, 2015.
- [14] F. P. Guiomar, S. B. Amado, C. S. Martins, and A. N. Pinto, “Time domain Volterra-based digital backpropagation for coherent optical systems,” *J. Lightw. Technol.*, vol. 15, no. 33, pp. 3170–3181, Aug. 2015.
- [15] —, “Parallel split-step method for digital backpropagation,” in *Proc. Optical Fiber Communication Conf. and Exposition (OFC)*, paper Th2A.28, 2015.
- [16] V. Parahyba, J. Reis, S. Ranzini, E. Schneider, E. Rosa, F. Simes, J. Diniz, L. Carvalho, E. Filho, J. Oliveira, and J. Oliveira, “Performance against implementation of digital backpropagation for high-speed coherent optical systems,” *Electronics Letters*, vol. 51, no. 14, pp. 1094–1096, July 2015.
- [17] F. P. Guiomar, S. B. Amado, J. D. Reis, S. M. Rossi, A. Chiuchiarelli, J. R. F. Oliveira, A. L. Teixeira, and A. N. Pinto, “Ultra-long-haul 400G superchannel transmission with multi-carrier nonlinear equalization,” in *Proc. 41st European Conf. Optical Communication (ECOC)*, paper Th.2.2.4, 2015.

- 
- [18] P. Poggiolini, Y. Jiang, A. Carena, G. Bosco, and F. Forghieri, “Analytical results on system maximum reach increase through symbol rate optimization,” in *Proc. Optical Fiber Communication Conf. and Exposition (OFC)*, paper Th3D.6, 2015.
- [19] A. Bononi, N. Rossi, and P. Serena, “Performance dependence on channel baud-rate of coherent single-carrier WDM systems,” in *Proc. 39th European Conf. Optical Communication (ECOC)*, paper Th.1.D.5, Sept 2013.
- [20] M. Qiu, Q. Zhuge, X. Xu, M. Chagnon, M. Morsy-Osman, and D. V. Plant, “Subcarrier multiplexing using DACs for fiber nonlinearity mitigation in coherent optical communication systems,” in *Proc. Optical Fiber Communication Conf. and Exposition (OFC)*, paper Tu3J.2, 2014.
- [21] R.-J. Essiambre, P. J. Winzer, X. Q. Wang, W. Lee, C. A. White, and E. C. Burrows, “Electronic predistortion and fiber nonlinearity,” *IEEE Photon. Technol. Lett.*, vol. 18, no. 17, pp. 1804–1806, 2006.
- [22] K. Roberts, C. Li, L. Strawczynski, M. O’Sullivan, and I. Hardcastle, “Electronic precompensation of optical nonlinearity,” *IEEE Photon. Technol. Lett.*, vol. 18, no. 2, pp. 403–405, 2006.
- [23] S. Zhang, L. Xu, P. Y. Kam, C. Yu, and T. Wang, “Performance investigation of the joint SPM compensation in a long-haul coherent dual-polarization QPSK system,” in *Proc. 36th European Conf. Optical Communication (ECOC)*, paper P3.15, Sept 2010.
- [24] A. Carena, V. Curri, G. Bosco, P. Poggiolini, and F. Forghieri, “Modeling of the impact of nonlinear propagation effects in uncompensated optical coherent transmission links,” *J. Lightw. Technol.*, vol. 30, no. 10, pp. 1524–1539, 2012.
- [25] Y. Gao, F. Zhang, L. Dou, Z. Chen, and A. Xu, “Intra-channel nonlinearities mitigation in pseudo-linear coherent QPSK transmission systems via nonlinear electrical equalizer,” *Optics Communications*, vol. 282, no. 12, pp. 2421 – 2425, 2009.
- [26] F. Zhang, Y. Gao, Y. Luo, J. Li, L. Zhu, L. Li, Z. Chen, and A. Xu, “Experimental demonstration of intra-channel nonlinearity mitigation in coherent QPSK systems with nonlinear electrical equaliser,” *Electron. Lett.*, vol. 46, no. 5, pp. 353–355, 2010.
- [27] J. Pan and C.-H. Cheng, “Nonlinear electrical compensation for the coherent optical OFDM system,” *J. Lightw. Technol.*, vol. 29, no. 2, pp. 215 –221, Jan 2011.
- [28] —, “Nonlinear electrical predistortion and equalization for the coherent optical communication system,” *J. Lightw. Technol.*, vol. 29, no. 18, pp. 2785 –2789, Sept 2011.
-

# Appendices



# Appendix A

## Frequency Domain NLSE

This appendix presents a detailed analytical derivation of the frequency domain NLSE described by equation (2.10). Let us start by rewriting the time domain scalar NLSE of equation (2.9),

$$\frac{\partial A(t, z)}{\partial z} = -\frac{\alpha}{2}A(t, z) - i\frac{\beta_2}{2}\frac{\partial^2 A(t, z)}{\partial t^2} + i\gamma|A(t, z)|^2 A(t, z). \quad (\text{A.1})$$

Using the Fourier transform definition of expression (2.11), the linear terms in (A.1) can be readily transformed into frequency domain through the following Fourier transform pairs,

$$\mathcal{F}\{A(t, z)\} = \tilde{A}(\omega, z), \quad (\text{A.2a})$$

$$\mathcal{F}\left\{\frac{\partial A(t, z)}{\partial z}\right\} = \frac{\partial \tilde{A}(\omega, z)}{\partial z}, \quad (\text{A.2b})$$

$$\mathcal{F}\left\{\frac{\partial^2 A(t, z)}{\partial t^2}\right\} = -\omega^2 \tilde{A}(\omega, z). \quad (\text{A.2c})$$

$$(\text{A.2d})$$

In turn, the Fourier transform of the nonlinear term,  $i\gamma|A(t, z)|^2 A(t, z)$ , requires to make use of the convolution theorem in two steps. First, let us determine the Fourier transform of  $|A(t, z)|^2$ :

$$\begin{aligned} \mathcal{F}\{A(t, z)A^*(t, z)\} &= \int_{-\infty}^{\infty} A(t, z)A^*(t, z) \exp(i\omega t) dt \\ &= \int_{-\infty}^{\infty} \left[ \frac{1}{2\pi} \int_{-\infty}^{\infty} \tilde{A}(\omega_1, z) \exp(-i\omega_1 t) d\omega_1 \right] A^*(t, z) \exp(i\omega t) dt \\ &= \frac{1}{2\pi} \int_{-\infty}^{\infty} \tilde{A}(\omega_1, z) \left[ \int_{-\infty}^{\infty} A^*(t, z) \exp(-i\omega_1 t) \exp(i\omega t) dt \right] d\omega_1 \\ &= \frac{1}{2\pi} \int_{-\infty}^{\infty} \tilde{A}(\omega_1, z) \left[ \int_{-\infty}^{\infty} A^*(t, z) \exp(i(\omega - \omega_1)t) dt \right] d\omega_1 \\ &= \frac{1}{2\pi} \int_{-\infty}^{\infty} \tilde{A}(\omega_1, z) \tilde{A}^*(\omega_1 - \omega, z) d\omega_1 = \tilde{A}(\omega, z) \otimes \tilde{A}^*(-\omega, z), \quad (\text{A.3}) \end{aligned}$$

where  $\otimes$  defines the convolution integral,

$$X(\omega) \otimes Y(\omega) = \frac{1}{2\pi} \int_{-\infty}^{\infty} X(\omega_1) Y(\omega - \omega_1) d\omega_1. \quad (\text{A.4})$$

Also note the use of the complex conjugation property of Fourier transform,  $\mathcal{F}\{x(t)\} = X(\omega) \Rightarrow \mathcal{F}\{x^*(t)\} = X(-\omega)$ , in the final step of expression (A.3). Finally, using again the convolution theorem, we may determine  $\mathcal{F}\{|A(t, z)|^2 A(t, z)\} = \mathcal{F}\{A(t, z) A^*(t, z)\} \otimes \mathcal{F}\{A(t, z)\}$  as,

$$\begin{aligned} \mathcal{F}\{A(t, z) A^*(t, z)\} \otimes \mathcal{F}\{A(t, z)\} &= \tilde{A}(\omega, z) \otimes \tilde{A}^*(-\omega, z) \otimes \tilde{A}(\omega, z) \\ &= \frac{1}{2\pi} \int_{-\infty}^{\infty} \left[ \frac{1}{2\pi} \int_{-\infty}^{\infty} \tilde{A}(\omega_1, z) \tilde{A}^*(\omega_1 - \omega_2, z) d\omega_1 \right] \tilde{A}(\omega - \omega_2) d\omega_2 \\ &= \frac{1}{4\pi^2} \int_{-\infty}^{\infty} \int_{-\infty}^{\infty} \tilde{A}(\omega_1, z) \tilde{A}^*(\omega_1 - \omega_2, z) \tilde{A}(\omega - \omega_2) d\omega_1 d\omega_2. \end{aligned} \quad (\text{A.5})$$

Performing the substitution  $\omega_1 - \omega_2 \rightarrow \omega_2$ , the following expression is obtained,

$$\mathcal{F}\{|A(t, z)|^2 A(t, z)\} = \frac{1}{4\pi^2} \iint \tilde{A}(\omega_1, z) \tilde{A}^*(\omega_2, z) \tilde{A}(\omega - \omega_1 + \omega_2, z) d\omega_1 d\omega_2. \quad (\text{A.6})$$

Taking all the previously defined Fourier transform pairs, and making use of the linearity property of Fourier transform, the frequency domain NLSE is finally written as

$$\begin{aligned} \frac{\partial \tilde{A}(\omega, z)}{\partial z} &= -\frac{\alpha}{2} \tilde{A}(\omega, z) + i \frac{\beta_2}{2} \omega^2 \tilde{A}(\omega, z) \\ &\quad + \frac{i\gamma}{4\pi^2} \iint \tilde{A}(\omega_1, z) \tilde{A}^*(\omega_2, z) \tilde{A}(\omega - \omega_1 + \omega_2, z) d\omega_1 d\omega_2. \end{aligned} \quad (\text{A.7})$$

# Appendix B

## Multi-Span VSTF

This appendix presents a detailed analytical derivation for the multi-span VSTF of equation (2.58). Using a two-spans base case, we prove by induction that equation (2.58) holds for any number of fiber spans. To initiate the analytical derivation, it is useful to first rewrite equation (2.55),

$$\begin{aligned} \tilde{A}(\omega, z + L_s) &= H_1(\omega, L_s) \tilde{A}(\omega, z) \\ &+ i\gamma H_1(\omega, L_s) \iint H_3(\omega, \omega_1, \omega_2, L_s) \tilde{A}(\omega_1, z) \tilde{A}^*(\omega_2, z) \tilde{A}(\omega - \omega_1 + \omega_2, z) d\omega_1 d\omega_2. \end{aligned} \quad (\text{B.1})$$

Let us consider now the calculation of  $\tilde{A}(\omega, z + 2L_s)$ , using  $\tilde{A}(\omega, z + L_s)$  as the VSTF input,

$$\begin{aligned} \tilde{A}(\omega, z + 2L_s) &= H_1(\omega, L_s) \exp\left(\frac{\alpha}{2}L_s\right) \tilde{A}(\omega, z + L_s) + i\gamma H_1(\omega, L_s) \exp\left(\frac{3}{2}\alpha L_s\right) \\ &\times \iint H_3(\omega, \omega_1, \omega_2, L_s) \tilde{A}(\omega_1, z + L_s) \tilde{A}^*(\omega_2, z + L_s) \tilde{A}(\omega - \omega_1 + \omega_2, z + L_s) d\omega_1 d\omega_2, \end{aligned} \quad (\text{B.2})$$

where the  $\exp\left(\frac{\alpha}{2}L_s\right)$  factors account for the optical gain in between fiber spans. Substituting (B.1) in the first RHS term (linear term) of (B.2) yields,

$$\begin{aligned} \tilde{A}^{\text{LI}}(\omega, z + 2L_s) &= H_1^2(\omega, L_s) \exp\left(\frac{\alpha}{2}L_s\right) \tilde{A}(\omega, z + L_s) + i\gamma H_1^2(\omega, L_s) \exp\left(\frac{\alpha}{2}L_s\right) \\ &\times \iint H_3(\omega, \omega_1, \omega_2, L_s) \tilde{A}(\omega_1, z) \tilde{A}^*(\omega_2, z) \tilde{A}(\omega - \omega_1 + \omega_2, z) d\omega_1 d\omega_2. \end{aligned} \quad (\text{B.3})$$

Substituting (B.1) in the second RHS term (nonlinear term) of (B.2) yields,

$$\begin{aligned}
 \tilde{A}^{\text{NL}}(\omega, z + 2L_s) &= i\gamma H_1(\omega, L_s) \exp\left(\frac{3}{2}\alpha L_s\right) \iint H_3(\omega, \omega_1, \omega_2, L_s) \left[ H_1(\omega_1, L_s) \tilde{A}(\omega_1, z) \right. \\
 &\quad \left. + i\gamma H_1(\omega_1, L_s) \iint H_3(\omega_1, \omega'_1, \omega'_2, L_s) \tilde{A}(\omega'_1, z) \tilde{A}^*(\omega'_2, z) \tilde{A}(\omega_1 - \omega'_1 + \omega'_2, z) d\omega'_1 d\omega'_2 \right] \\
 &\quad \times \left[ H_1(\omega_2, L_s) \tilde{A}(\omega_2, z) \right. \\
 &\quad \left. + i\gamma H_1(\omega_2, L_s) \iint H_3(\omega_2, \omega'_1, \omega'_2, L_s) \tilde{A}(\omega'_1, z) \tilde{A}^*(\omega'_2, z) \tilde{A}(\omega_2 - \omega'_1 + \omega'_2, z) d\omega'_1 d\omega'_2 \right]^* \\
 &\quad \times \left[ H_1(\omega - \omega_1 + \omega_2, L_s) \tilde{A}(\omega - \omega_1 + \omega_2, z) \right. \\
 &\quad \left. + i\gamma H_1(\omega - \omega_1 + \omega_2, L_s) \iint H_3(\omega - \omega_1 + \omega_2, \omega'_1, \omega'_2, L_s) \tilde{A}(\omega'_1, z) \tilde{A}^*(\omega'_2, z) \right. \\
 &\quad \left. \times \tilde{A}(\omega - \omega_1 + \omega_2 - \omega'_1 + \omega'_2, z) d\omega'_1 d\omega'_2 \right] d\omega_1 d\omega_2 \tag{B.4}
 \end{aligned}$$

Removing all higher-order terms (order higher than 3) in (B.4) one obtains,

$$\begin{aligned}
 \tilde{A}^{\text{NL}}(\omega, z + 2L_s) &= i\gamma H_1(\omega, L_s) \exp\left(\frac{3}{2}\alpha L_s\right) \iint H_3(\omega, \omega_1, \omega_2, L_s) H_1(\omega_1, L_s) H_1^*(\omega_2, L_s) \\
 &\quad \times H_1(\omega - \omega_1 + \omega_2, L_s) \tilde{A}(\omega_1, z) \tilde{A}^*(\omega_2, z) \tilde{A}(\omega - \omega_1 + \omega_2, z) d\omega_1 d\omega_2, \tag{B.5}
 \end{aligned}$$

where  $H_1(\omega_1, L_s) H_1^*(\omega_2, L_s) H_1(\omega - \omega_1 + \omega_2, L_s)$  is equivalent to

$$\begin{aligned}
 H_1(\omega_1, L_s) H_1^*(\omega_2, L_s) H_1(\omega - \omega_1 + \omega_2, L_s) &= \\
 &= \exp\left(-\frac{3}{2}\alpha L_s + i\frac{\beta_2}{2}\omega_1^2 L_s - i\frac{\beta_2}{2}\omega_2^2 L_s + i\frac{\beta_2}{2}(\omega - \omega_1 + \omega_2)^2 L_s\right) \\
 &= \exp\left(-\frac{3}{2}\alpha L_s + i\frac{\beta_2}{2}\omega^2 L_s + i\beta_2(\omega_1 - \omega)(\omega_1 - \omega_2)L_s\right) \\
 &= \exp(-\alpha L_s) H_1(\omega, L_s) \exp(i\beta_2(\omega_1 - \omega)(\omega_1 - \omega_2)). \tag{B.6}
 \end{aligned}$$

Substituting (B.6) into (B.5) and summing the  $\tilde{A}^{\text{LI}}$  and  $\tilde{A}^{\text{NL}}$  terms of (B.3) and (B.5) yields

$$\begin{aligned}
 \tilde{A}(\omega, z + 2L_s) &= H_1^2(\omega, L_s) \exp\left(\frac{\alpha}{2}L_s\right) \tilde{A}(\omega, z) + i\gamma H_1^2(\omega, L_s) \exp\left(\frac{\alpha}{2}L_s\right) \\
 &\quad \times \iint \left[1 + \exp(i\beta_2(\omega_1 - \omega)(\omega_1 - \omega_2)L_s)\right] H_3(\omega, \omega_1, \omega_2, L_s) \tilde{A}(\omega_1, z) \tilde{A}^*(\omega_2, z) \\
 &\quad \times \tilde{A}(\omega - \omega_1 + \omega_2, z) d\omega_1 d\omega_2, \tag{B.7}
 \end{aligned}$$

---

where

$$H_1^2(\omega, L_s) \exp\left(\frac{\alpha}{2}L_s\right) = H_1^{\text{MS}}(\omega, 2L_s), \quad (\text{B.8})$$

and

$$\left[1 + \exp(i\beta_2(\omega_1 - \omega)(\omega_1 - \omega_2)L_s)\right] H_3(\omega, \omega_1, \omega_2, L_s) = H_3^{\text{MS}}(\omega, \omega_1, \omega_2, 2L_s). \quad (\text{B.9})$$

Substituting (B.8) and (B.9) into (B.7) finally yields a multi-span VSTF of the form of equation (2.58), for the specific case of two fiber spans,

$$\begin{aligned} \tilde{A}(\omega, z + 2L_s) &= H_1^{\text{MS}}(\omega, 2L_s)\tilde{A}(\omega, z) + i\gamma H_1^{\text{MS}}(\omega, 2L_s) \\ &\quad \times \iint H_3^{\text{MS}}(\omega, \omega_1, \omega_2, 2L_s)\tilde{A}(\omega_1, z)\tilde{A}^*(\omega_2, z)\tilde{A}(\omega - \omega_1 + \omega_2, z) d\omega_1 d\omega_2. \end{aligned} \quad (\text{B.10})$$

Expression (B.10) can be easily generalized for an optical link composed of  $N_s$  fiber spans, by recursively repeating this procedure. The simplification made from equation (B.4) to (B.5), where the higher-order terms are neglected, clearly exposes the inter-span error accumulation of the third-order multi-span VSTF.



## Appendix C

# Full Derivation of the iFWM Filters in the TD-VSNE

This appendix provides a full derivation of equations (5.19) and (5.20) in Chapter 5, yielding the TD-iFWM filters. For simplicity we will only detail the derivation of equation (5.19), from which equation (5.20) can be readily obtained by analogy. Applying the inverse discrete Fourier transform to equation (5.13), we obtain

$$\begin{aligned}
 \mathcal{F}^{-1}\left\{\tilde{A}_{x/y}^{\text{iFWM},(K)}(\omega_n)\right\} = & \kappa \left[ 2\mathcal{F}^{-1}\left\{H_{\text{CD}}(\omega_n)\tilde{A}_{x/y}(\omega_{n+K})\right\} \otimes \mathcal{F}^{-1}\left\{\tilde{\mathcal{P}}_{xx/yy}^{(K)}(\omega_n)\right\} \right. \\
 & + \mathcal{F}^{-1}\left\{H_{\text{CD}}(\omega_n)\tilde{A}_{x/y}(\omega_{n+K})\right\} \otimes \mathcal{F}^{-1}\left\{\tilde{\mathcal{P}}_{yy/xx}^{(K)}(\omega_n)\right\} \\
 & - \mathcal{F}^{-1}\left\{H_{\text{CD}}(\omega_n)\tilde{A}_{x/y}(\omega_{n+K})\right\} \otimes \mathcal{F}^{-1}\left\{\tilde{\chi}^{(K)}(\omega_n)\right\} \\
 & \left. + \mathcal{F}^{-1}\left\{H_{\text{CD}}(\omega_n)\tilde{A}_{y/x}(\omega_{n+K})\right\} \otimes \mathcal{F}^{-1}\left\{\tilde{\mathcal{P}}_{xy/yx}^{(K)}(\omega_n)\right\} \right], \quad (\text{C.1})
 \end{aligned}$$

where the  $\mathcal{F}^{-1}\left\{\tilde{A}_{x/y}^{\text{CD}}(\omega_{n+K})\right\}$  terms are given by expression (5.21). To calculate the  $\mathcal{F}^{-1}\left\{\tilde{\mathcal{P}}_{xy}^{(K)}(\omega_n)\right\}$  terms it is useful to first rewrite (5.15) as,

$$\begin{aligned}
 \tilde{\mathcal{P}}_{xy}^{(K)}(\omega_n) = & \underbrace{\sum_{j=1}^N \tilde{A}_x(\omega_j)\tilde{A}_y^*(\omega_{\text{mod}(j+K,N)})}_{\tilde{P}'_{xy}(K)} - \underbrace{\sum_{j=n-K+1}^{n+K-1} \tilde{A}_x(\omega_j)\tilde{A}_y^*(\omega_{j+K})}_{\tilde{P}''_{xy}(K)(\omega_n)} \\
 & - \underbrace{\sum_{j=N-K+1}^N \tilde{A}_x(\omega_j)\tilde{A}_y^*(\omega_{j-N+K})}_{\tilde{P}'''_{xy}(K)(\omega_n)}, \quad (\text{C.2})
 \end{aligned}$$

where  $\text{mod}(j, N)$  denotes the modulo  $N$  operation applied to the  $j$  index. Note that the first term corresponds to a full summation with circular shifting over the  $N$ -samples FFT

block. We can therefore apply Parseval's theorem to obtain,

$$\mathcal{F}^{-1}\{\tilde{P}'_{xy}(K)\} = \frac{1}{N} \sum_{j=1}^N A_x(t_j) A_y^*(t_j) \exp\left(-i2\pi \frac{j}{N} K\right) = \mathcal{P}'_{xy}(K), \quad (\text{C.3})$$

In contrast with the simple time domain equivalent of equation (C.3), the inverse Fourier transform of the remaining terms in (C.2) yields more complex expressions,

$$\begin{aligned} \mathcal{F}^{-1}\{\tilde{P}''_{xy}(K)(\omega_n)\} &= \sum_{j=n-K+1}^{n+K-1} \mathcal{F}^{-1}\{\tilde{A}_x(\omega_j) \tilde{A}_y^*(\omega_{j+K})\} \\ &= \sum_{j=-K+1}^{K-1} \mathcal{F}^{-1}\{\tilde{A}_x(\omega_{n+j}) \tilde{A}_y^*(\omega_{n+j+K})\} \\ &= \sum_{j=-K+1}^{K-1} A_x(t_n) \exp\left(i2\pi \frac{n}{N} j\right) \otimes A_y^*(-t_n) \exp\left(i2\pi \frac{n}{N} (j+K)\right) \\ &= \frac{1}{N} \sum_{j=-K+1}^{K-1} \sum_{p=1}^N \sum_{m=-\infty}^{\infty} A_x(t_p) A_y^*(-t_{n-p-mN}) \exp\left(i2\pi \frac{(n-mN)(j+K) - pK}{N}\right) \\ &= \mathcal{P}''_{xy}(K)(t_n), \end{aligned} \quad (\text{C.4})$$

and

$$\begin{aligned} \mathcal{F}^{-1}\{\tilde{P}'''_{xy}(K)(\omega_n)\} &= \sum_{j=N-K+1}^N \mathcal{F}^{-1}\{\tilde{A}_x(\omega_j) \tilde{A}_y^*(\omega_{j-N+K})\} \\ &= \sum_{j=1}^K \mathcal{F}^{-1}\{\tilde{A}_x(\omega_{N-K+j}) \tilde{A}_y^*(\omega_j)\} \\ &= \frac{1}{N^2} \sum_{j=1}^K \left[ \sum_{m=1}^N A_x(t_m) \exp\left(i \frac{2\pi(N-K+j-1)(m-1)}{N}\right) \right. \\ &\quad \left. \times \sum_{m=1}^N A_y^*(t_m) \exp\left(i \frac{2\pi(j-1)(m-1)}{N}\right) \right] \\ &= \mathcal{P}'''_{xy}(K)(t_n). \end{aligned} \quad (\text{C.5})$$

The complete inverse discrete Fourier transform of  $\tilde{\mathcal{P}}_{xy}(K)(\omega_n)$  is then given by

$$\mathcal{P}_{xy}(K)(t_n) = \mathcal{F}^{-1}\{\tilde{\mathcal{P}}_{xy}(K)(\omega_n)\} = \mathcal{P}'_{xy}(K) + \mathcal{P}''_{xy}(K)(t_n) + \mathcal{P}'''_{xy}(K)(t_n). \quad (\text{C.6})$$

The inverse Fourier transform of the degenerate iFWM contribution,  $\tilde{\chi}^{(K)}(\omega_n)$ , is

---

given by

$$\begin{aligned}
\mathcal{F}^{-1}\{\tilde{\chi}^{(K)}(\omega_n)\} &= \mathcal{F}^{-1}\{\tilde{A}_x(\omega_{n+K})\tilde{A}_x^*(\omega_{n+2K})\} + \mathcal{F}^{-1}\{\tilde{A}_y(\omega_{n+K})\tilde{A}_y^*(\omega_{n+2K})\} \\
&= A_x(t_n) \exp\left(i2\pi\frac{n}{N}K\right) \otimes A_x^*(-t_n) \exp\left(i2\pi\frac{n}{N}2K\right) \\
&\quad + A_y(t_n) \exp\left(i2\pi\frac{n}{N}K\right) \otimes A_y^*(-t_n) \exp\left(i2\pi\frac{n}{N}2K\right) \\
&= \chi^{(K)}(t_n).
\end{aligned} \tag{C.7}$$

Using expressions (C.1) to (C.7), the exact inverse Fourier transform of  $\tilde{A}_{x/y}^{\text{iFWM},(K)}(\omega_n)$  can be obtained as

$$\begin{aligned}
A_{x/y}^{\text{iFWM},(K)}(t_n) &= \kappa \left[ 2A_{x/y}^{\text{CD},(K)}(t_n) \otimes \mathcal{P}_{xx/yy}^{(K)}(t_n) + A_{x/y}^{\text{CD},(K)}(t_n) \otimes \mathcal{P}_{yy/xx}^{(K)}(t_n) \right. \\
&\quad \left. - A_{x/y}^{\text{CD},(K)}(t_n) \otimes \chi^{(K)}(t_n) + A_{y/x}^{\text{CD},(K)}(t_n) \otimes \mathcal{P}_{xy/yx}^{(K)}(t_n) \right].
\end{aligned} \tag{C.8}$$

Finally, neglecting the  $\mathcal{P}_{xy}''^{(K)}(t_n)$ ,  $\mathcal{P}_{xy}'''^{(K)}(t_n)$  and  $\chi^{(K)}(t_n)$  contributions, equation (C.8) can be simplified to

$$A_{x/y}^{\text{iFWM},(K)}(t_n) = \kappa \left[ A_{x/y}^{\text{CD},(K)}(t_n) \left( 2\mathcal{P}_{xx/yy}'^{(K)} + \mathcal{P}_{yy/xx}'^{(K)} \right) + A_{y/x}^{\text{CD},(K)}(t_n) \mathcal{P}_{xy/yx}'^{(K)} \right], \tag{C.9}$$

and conversely,

$$A_{x/y}^{\text{iFWM},(-K)}(t_n) = \kappa \left[ A_{x/y}^{\text{CD},(-K)}(t_n) \left( 2\mathcal{P}_{xx/yy}'^{*(K)} + \mathcal{P}_{yy/xx}'^{*(K)} \right) + A_{y/x}^{\text{CD},(-K)}(t_n) \mathcal{P}_{yx/xy}'^{*(K)} \right]. \tag{C.10}$$

Note that besides the inherent complexity of expressions (C.4), (C.5) and (C.7) the  $n$  dependency of the  $\mathcal{P}_{xy}''^{(K)}(t_n)$ ,  $\mathcal{P}_{xy}'''^{(K)}(t_n)$  and  $\chi^{(K)}(t_n)$  terms requires to keep the circular convolutions in expression (C.1). In contrast, the  $\mathcal{P}_{xy}'^{(K)}$  terms are obtained by a much simpler computational process and are  $n$ -independent, which allows to simplify the circular convolution into a simple multiplication. This is the reasoning for neglecting  $\mathcal{P}_{xy}''^{(K)}(t_n)$ ,  $\mathcal{P}_{xy}'''^{(K)}(t_n)$  and  $\chi^{(K)}(t_n)$  in the approximated TD-iFWM equalizer of equations (5.19) and (5.20).

